



THE UNIVERSITY OF QUEENSLAND  
AUSTRALIA

**Development and Application of Multiphysics Simulation Tools  
for Foil Thrust Bearings Operating with Carbon Dioxide**

Kan Qin  
Master of Engineering

*A thesis submitted for the degree of Doctor of Philosophy at*

*The University of Queensland in 2017*

*School of Mechanical and Mining Engineering,  
Queensland Geothermal Energy Centre of Excellence*

## Abstract

Foil bearings can enable different turbomachinery architecture. The use of the cycle's working fluid within the bearings results in an oil-free and compact turbomachinery system. Using CO<sub>2</sub> as the operating fluid for a foil bearing creates new operating and new modelling challenges. These include turbulent flow within the film, non-negligible inertia forces, high windage losses, non-ideal gas behaviour and reduced rotordynamic damping. Since the flow phenomena within foil bearings are complex, involving fluid flow, structural deformation and heat transfer, use of the conventional Reynolds equation is not proven to be suitable for foil bearings with CO<sub>2</sub> as the operating fluid. To address these modelling issues, a multi-physics multi-timescale simulation tool including fluid, structure and thermal solvers was developed to predict the performance of foil bearings and to create insight on their operations with CO<sub>2</sub>. New flow physics and operation challenges for foil thrust bearings with CO<sub>2</sub> were built and described in details next.

To model the fluid flow within foil bearings, the modifications of the in-house computational fluid dynamics solver are first presented to enable laminar simulations within foil bearings. To reduce the computational cost for turbulent simulations, a compressible wall function is implemented. The checker-boarding effect, due to the high aspect ratio cell is eliminated by a fourth-order artificial dissipation term, while maintaining the second order spatial accuracy. These modifications result in a fast and stable solver for turbulent simulations of CO<sub>2</sub> foil thrust bearings without contaminating the flow field. For the fluid-structure simulation, the in-house computational fluid dynamics solver is modified by implementing a moving grid capability. This capability is validated with inviscid, viscous and turbulent flow cases. A separate bespoke finite difference code based on the Kirchhoff plate equation for the circular thin plate is developed in Python to solve the structural deformation within foil thrust bearings. A fluid-structure coupling strategy and the corresponding mapping algorithm are employed for steady state and time-accurate transient simulations.

Using the developed fluid-structure simulation tool, the steady state performances of foil thrust bearings with CO<sub>2</sub> are investigated. The centrifugal inertia effects are found to be significant for foil thrust bearings with CO<sub>2</sub>. In the ramp region, they generate an additional inflow close to the rotor inner edge, resulting in a higher peak pressure. Contrary in the flat region, the inertia force creates

a rapid mass loss through the bearing outer edge, which reduces pressure in this region. These different flow fields alter bearing performance compared to conventional air foil bearings. Conventional Reynolds equation cannot account for the irregular radial velocity profiles that are driven by strong inertial effects. In addition, the turbulence effects increase load capacity and power loss simultaneously. The steady state simulations indicate that both load and power loss increase linearly with the decreasing rotor to top foil separations and the increasing rotational speeds. A slower rate is observed for power loss. The rotational speed has a larger effect on power loss compared than the rotor to top foil separations.

Finally, a heat conduction solver is added to the fluid-structure simulation tool. This results in a multi-physics multi-timescale tool for the fluid-structure-thermal simulation. The coupling strategy is then proposed and validated with different test cases. The heat transfer models of the solid structures within foil thrust bearings are discussed. Numerical simulations of foil thrust bearings with air and CO<sub>2</sub> are performed at the same load condition. It is found that foil thrust bearings with CO<sub>2</sub> significantly benefit from increased convective cooling on the rear surface of the rotor, if the rotor operates in a high pressure CO<sub>2</sub> environment. The centrifugal pumping that naturally occurs in CO<sub>2</sub> bearings due to the high fluid density provides a new and effective cooling mechanism for the CO<sub>2</sub> bearing. The fluid-structure modelling approach is found to applicable at the rotational speed less than 30 000 rpm. However, the thermal solver has to be included when foil bearings are operating at higher rotational speeds. This is due to the large deflection caused by thermal stresses.

This project is the first work of its kind to use the high fidelity multi-physics multi-timescale simulation tool to simulate foil thrust bearings with CO<sub>2</sub>. The results reveal new flow physics, steady state performances of foil bearings at different operating conditions.

## **Declaration by Author**

This thesis is composed of my original work, and contains no material previously published or written by another person except where due reference has been made in the text. I have clearly stated the contribution by others to jointly-authored works that I have included in my thesis.

I have clearly stated the contribution of others to my thesis as a whole, including statistical assistance, survey design, data analysis, significant technical procedures, professional editorial advice, and any other original research work used or reported in my thesis. The content of my thesis is the result of work I have carried out since the commencement of my research higher degree candidature and does not include a substantial part of work that has been submitted to qualify for the award of any other degree or diploma in any university or other tertiary institution. I have clearly stated which parts of my thesis, if any, have been submitted to qualify for another award.

I acknowledge that an electronic copy of my thesis must be lodged with the University Library and, subject to the policy and procedures of The University of Queensland, the thesis be made available for research and study in accordance with the Copyright Act 1968 unless a period of embargo has been approved by the Dean of the Graduate School.

I acknowledge that copyright of all material contained in my thesis resides with the copyright holder(s) of that material. Where appropriate I have obtained copyright permission from the copyright holder to reproduce material in this thesis

## Publications during candidature

### Journal Articles

1. **Qin, K.**, Gollan, R. and Jahn, I.H., Application of a Wall Function to Simulate Turbulent Flows in Foil Bearings at High Rotational Speeds, *Tribology International* 115, 2017, 546-556.
2. Qi, J., Reddell, T., **Qin, K.**, Hooman, K. and Jahn, I.H., Supercritical CO<sub>2</sub> Radial Turbine Design Performance as a Function of Turbine Size Parameters, *ASME Journal of Turbomachinery* 139(8), 2017, 081008.
3. **Qin, K.**, Jahn, I.H. and Jacobs, P.A., Effect of Operating Conditions on the Elasto-hydrodynamic Performance of Foil Thrust Bearings for Supercritical CO<sub>2</sub> Cycles. *ASME Journal of Engineering for Gas Turbines and Power*. 139(4), 2016, 042505.
4. **Qin, K.**, Jahn, I.H., Gollan, R.J. and Jacobs, P.A., Development of a Computational Tool to Simulate Foil Bearings for Supercritical CO<sub>2</sub> Cycles. *ASME Journal of Engineering for Gas Turbines and Power*. 138(9), 2016, 092503.
5. **Qin, K.**, Jahn, I.H., and Jacobs, P.A.. Development of a Fluid-Structure Model for Gas-Lubricated Bump-Type Foil Thrust Bearings. *Applied Mechanics and Materials*. 846, 2016, 169-175.

### Conference Papers

1. **Qin, K.**, Jacobs, P.A., Keep, J.A. and Jahn, I.H.. A Three-dimensional Fluid-Structure-Thermal Simulation of Bump-Type Foil Thrust Bearings. 1st Global Power and Propulsion Forum, Zürich, Switzerland. GPPF-2017-22, 2017.
2. **Qin, K.**, Jahn, I.H., and Jacobs, P.A.. Prediction of Dynamic Characteristics of Foil Thrust Bearing Using Computational Fluid Dynamics. 20th Australasian Fluid Mechanics Conference, Perth, Australia. 2016.

3. **Qin, K.**, Jahn, I.H., and Jacobs, P.A.. Effect of Operating Conditions on the Elasto-hydrodynamic Performance of Foil Thrust Bearings for Supercritical CO<sub>2</sub> Cycles. ASME Turbo Expo 2016, Seoul, South Korea. 2016.
4. Qi, J., Reddell, T., **Qin, K.**, Hooman, K. and Jahn, I.H., Supercritical CO<sub>2</sub> Radial Turbine Design Performance as a Function of Turbine Size Parameters. ASME Turbo Expo 2016, Seoul, South Korea. 2016.
5. **Qin, K.**, Jahn, I.H. and Jacobs, P.A., Validation of a Three-dimensional CFD Analysis of Foil Bearings with Supercritical CO<sub>2</sub>. 19th Australasian Fluid Mechanics Conference, Melbourne, Australia. 2014.

### **Technical Reports**

1. **Qin, K.** and Jahn, I.H., Structural Deformation of a Circular Thin Plate with Combinations of Fixed and Free Edges. School of Mechanical and Mining Engineering, The University of Queensland. 2015/05.
2. Jahn, I.H. and **Qin, K.**, e3prepToFoam: a Mesh Generator for OpenFOAM. School of Mechanical and Mining Engineering, The University of Queensland. 2015/04.

### **Publications included in this thesis**

As allowed by the University of Queensland Policy 4.60.07 (Alternate Thesis Format Options), this thesis partly comprises of publications. These publications form the main parts of the thesis. Four of them (Chapter 3, 4, 5 and 7) have been published in peer reviewed publications with the statements of authorship and contribution provided, and the rest one (Chapter 6) will be submitted to a peer-reviewed journal.

**Qin, K.**, Gollan, R. and Jahn, I.H., Application of a Wall Function to Simulate Turbulent Flows in Foil Bearings at High Rotational Speeds. *Tribology International*. 115, 2017, 546-556. – Incorporated in Chapter 3.

Contributor	Statement of contribution
Kan Qin	Problem specification (70 %) Numerical simulations (100 %) Result analysis (80 %) Drafting and writing (70 %)
Ingo Jahn	Problem specification (30 %) Result analysis (20 %) Drafting and writing (25 %)
Rowan Gollan	Drafting and writing (5 %)

**Qin, K.**, Jahn, I.H. and Jacobs, P.A., Effect of Operating Conditions on the Elaso-hydrodynamic Performance of Foil Thrust Bearings for Supercritical CO<sub>2</sub> Cycles. *ASME Journal of Engineering for Gas Turbines and Power*. 139(4), 2016, 042505. – Incorporated in Chapter 5.

Contributor	Statement of contribution
Kan Qin	Problem specification (50 %) Numerical simulations (100 %) Result analysis (80 %) Drafting and writing (70 %)
Ingo Jahn	Problem specification (50 %) Result analysis (20 %) Drafting and writing (25 %)
Peter Jacobs	Drafting and writing (5 %)

**Qin, K.**, Jacobs, P.A., Keep, J.A. and Jahn, I.H.. A Three-dimensional Fluid-Structure-Thermal Simulation of Bump-Type Foil Thrust Bearings. 1st Global Power and Propulsion Forum, Zürich, Switzerland. GPPF-2017-22, 2017. – Incorporated in Chapter 7.

Contributor	Statement of contribution
Kan Qin	Problem specification (50 %)
	Numerical simulations (100 %)
	Result analysis (80 %)
	Drafting and writing (70 %)
Peter Jacobs	Drafting and writing (5 %)
Joshua Keep	Drafting and writing (5 %)
Ingo Jahn	Problem specification (50 %)
	Result analysis (20 %)
	Drafting and writing (20 %)

**Qin, K.,** Jahn, I.H., and Jacobs, P.A.. Prediction of Dynamic Characteristics of Foil Thrust Bearing Using Computational Fluid Dynamics. 20th Australasian Fluid Mechanics Conference, Perth, Australia. 2016. – Incorporated in Chapter 6.

Contributor	Statement of contribution
Kan Qin	Problem specification (50 %)
	Numerical simulations (100 %)
	Result analysis (80 %)
	Drafting and writing (70 %)
Ingo Jahn	Problem specification (50 %)
	Result analysis (20 %)
	Drafting and writing (25 %)
Peter Jacobs	Drafting and writing (5 %)

**Qin, K.,** Jahn, I.H., Gollan, R.J. and Jacobs, P.A., Development of a Computational Tool to Simulate Foil Bearings for Supercritical CO<sub>2</sub> Cycles. ASME Journal of Engineering for Gas Turbines and Power. 138(9), 2016, 092503. – Incorporated in Chapter 4.

Contributor	Statement of contribution
Kan Qin	Problem specification (30 %)
	Numerical simulations (100 %)
	Result analysis (80 %)
	Drafting and writing (70 %)
Ingo Jahn	Problem specification (50 %)
	Result analysis (20 %)
	Drafting and writing (25 %)
Rowan Gollan	Result analysis (5 %)
	Drafting and writing (5 %)
Peter Jacobs	Problem specification (20 %)
	Drafting and writing (5 %)

**Qin, K.**, Jahn, I.H., and Jacobs, P.A.. Development of a Fluid-Structure Model for Gas-Lubricated Bump-Type Foil Thrust Bearings. Applied Mechanics and Materials. 846, 2016, 169-175. – Incorporated in Chapter 4.

Contributor	Statement of contribution
Kan Qin	Problem specification (50 %) Numerical simulations (100 %) Result analysis (80 %) Drafting and writing (70 %)
Ingo Jahn	Problem specification (50 %) Result analysis (20 %) Drafting and writing (25 %)
Peter Jacobs	Drafting and writing (5 %)

**Contribution by others to the thesis**

Dr. Ingo Jahn, Dr. Rowan Gollan and Dr. Peter Jacobs are the co-authors of the publications incorporated in this thesis.

**Statement of parts of the thesis submitted to qualify for the award of another degree**

None.

## Acknowledgements

I want to express my deepest and most sincere gratitude to my principle supervisor, Dr. Ingo Jahn. Thanks for your guidance and constant encouragement throughout this project, for sharing your knowledge and passion for science and research, for constantly providing new ideas and insights. Finally, thanks for always making time!

I would like to gratefully acknowledge my associate supervisor Dr. Peter Jacobs for offering the opportunity to start my PhD candidature with this interesting project and for his technical guidance of his CFD code: Eilmer.

I thank Dr. Rowan Gollan for giving me advice in debugging code and proposing many inspiring suggestions for future work. Thanks also go to Dr. Paul Petrie-Repar for sharing his experience in writing CFD code and many discussions on damping. I would like to thank Dr. Wilson Chan for the valuable discussion on the  $k-\omega$  turbulence model. Also, I would like to thank Dr. Carlos Ventura for valuable suggestions at weekly meeting during the early stage of my candidature and Dr. Andrew Rowlands for his help during my PhD application.

This project is not possible without the support from the Australian Solar Thermal Research Initiative (ASTRI), a project supported by Australian Government. I acknowledge the China Scholarship Council, The University of Queensland and the Queensland Geothermal Energy Centre of Excellence for the financial support.

The simulations detailed on this thesis were undertaken with the assistance of resources from the University of Queensland High Performance Computing Facility's Barrine and Tinaroo clusters, the National Computational Infrastructure (NCI), which is supported by the Australian Government, and the Pawsey Supercomputing Centre, funded by from the Australian Government and the Government of Western Australia.

Thanks to all my other good buddies at UQ, Yuchen Dai, Peixing Dong, Xiaoxiao Li, Yu Liu, Suoying He, Jacob Hess, Xin Kang, Joshua Keep, Mohsen Modirshanechi, Mostafa Odabae, Yubiao Sun, Phil Swann, Jianhui Qi, Jianyong Wang, Xurong Wang, Han Wei, Mohd Fairuz Zakariya; thanks for all the coffee breaks, BBQ, laughs, parties and discussions. Thanks for making my time at UQ so enjoyable.

Finally and most importantly, the biggest thanks of all goes to my grandparents, parents and Yujiao. Thanks for your encouragement and support, for believing in me and for your love.

## **Keywords**

Computational Fluid Dynamics, Multi-physics Simulations, Foil Thrust Bearings, Supercritical CO<sub>2</sub> Cycles, Turbulent Flow, Centrifugal Inertia Effects

## **Australian and New Zealand Standard Research Classifications (ANZSRC)**

091307 Numerical Modelling and Mechanical Characterisation, 50%

091309 Tribology, 50%

## **Fields of Research (FoR) Classification (FOR)**

0913 Mechanical Engineering, 100%

---

# Contents

---

<b>List of Figures</b>	<b>xvii</b>
<b>List of Tables</b>	<b>xxvi</b>
<b>Nomenclature</b>	<b>xxviii</b>
<b>1 Introduction</b>	<b>1</b>
1.1 Motivation . . . . .	1
1.2 Aims and Objectives . . . . .	6
1.3 Thesis Overview . . . . .	7
<b>2 Literature Review</b>	<b>9</b>
2.1 Introduction . . . . .	9
2.2 Background on Supercritical CO <sub>2</sub> Power Cycle . . . . .	9
2.2.1 Components for Supercritical CO <sub>2</sub> Cycles . . . . .	13
2.3 Experimental Work on Foil Thrust Bearings . . . . .	18
2.4 Fluid Simulation for Gas Bearings . . . . .	21
2.4.1 Classical Reynolds Equation . . . . .	21
2.4.2 Turbulent Reynolds equation . . . . .	25
2.4.3 Computational Fluid Dynamics . . . . .	27
2.5 Structural model . . . . .	29
2.6 Thermal Performance . . . . .	35
2.7 Gap in Literature . . . . .	39
<b>3 Fluid Simulations</b>	<b>41</b>
3.1 Introduction . . . . .	41

3.2	Description of Fluid Solver . . . . .	41
3.3	Modification of Fluid Solver for Laminar Simulations of Foil Bearings . . . . .	42
3.3.1	Moving Wall Boundary Condition . . . . .	42
3.3.2	Periodic Boundary Condition . . . . .	43
3.3.3	Reconstruction . . . . .	43
3.3.4	Taylor-Couette Flow . . . . .	43
3.3.5	Hydrostatic Air Thrust Bearing . . . . .	46
3.3.6	Wavy Thrust Bearing . . . . .	49
3.4	Modification of Fluid Solver for Turbulent Simulations of Foil Bearings . . . . .	54
3.4.1	Wilcox's 2006 $k$ - $\omega$ model . . . . .	55
3.4.2	Wall Modelled Turbulence Model for Foil Bearing Applications . . . . .	57
3.4.3	Stabilisation Method for Turbulent Simulations . . . . .	70
3.5	Conclusions . . . . .	77
<b>4</b>	<b>Fluid-Structure Coupled Simulations</b>	<b>79</b>
4.1	Introduction . . . . .	79
4.2	Moving Grid . . . . .	79
4.2.1	Convective Flux Update with Moving Grid . . . . .	80
4.2.2	Viscous Flux Update with Moving Grid . . . . .	83
4.3	Fluid-Structure Simulation: Test Cases . . . . .	83
4.3.1	Random Grid Motion . . . . .	84
4.3.2	Constant Velocity Piston . . . . .	84
4.3.3	Projectile in Tube . . . . .	86
4.3.4	Pitching NACA0012 Airfoil . . . . .	87
4.3.5	Oscillating Plate . . . . .	92
4.3.6	Pitching NACA64A010 Airfoil (Turbulent) . . . . .	94
4.4	Structural Deformation Solver . . . . .	97
4.4.1	Top Foil Model . . . . .	97
4.4.2	Bump Foil Model . . . . .	101
4.5	Fluid-Structure Simulation: Coupling Strategy . . . . .	102
4.6	Conclusions . . . . .	106

<b>5</b>	<b>Foil Bearing Steady State Performance</b>	<b>109</b>
5.1	Introduction . . . . .	109
5.2	Steady State Performance Evaluation . . . . .	109
5.3	Validation for Steady State Performance . . . . .	110
5.4	Selection of Gas Models . . . . .	112
5.5	Comparison Between Reynolds Equation and Eilmer . . . . .	113
5.6	Effect of Operating Conditions . . . . .	125
5.6.1	Selection of Operating Conditions . . . . .	125
5.6.2	Centrifugal Effects . . . . .	127
5.6.3	Turbulence Effects . . . . .	135
5.7	Revisit of Computational Domain: Steady State Performance . . . . .	136
5.8	Steady State Performance . . . . .	139
5.9	Conclusions . . . . .	143
<b>6</b>	<b>Foil Bearing Dynamic Performance</b>	<b>145</b>
6.1	Introduction . . . . .	145
6.2	Dynamic Performance Evaluation . . . . .	145
6.3	Verification of Dynamic Analysis Capability . . . . .	148
6.4	Revisit of Computational Domain: Dynamic Performance . . . . .	149
6.5	Conclusions . . . . .	151
<b>7</b>	<b>Fluid-Structure-Thermal Simulations</b>	<b>153</b>
7.1	Introduction . . . . .	153
7.2	Computational Framework . . . . .	153
7.2.1	Heat Conduction Solver . . . . .	153
7.2.2	Coupling Method: Fluid-Thermal . . . . .	154
7.2.3	Conjugate Couette Flow . . . . .	156
7.2.4	Conjugate Nozzle Flow . . . . .	157
7.2.5	Coupling Method: Fluid-Structure-Thermal . . . . .	158
7.3	Application to Foil Thrust Bearings . . . . .	159
7.3.1	Heat Transfer Model for Rotor . . . . .	160

7.3.2	Heat Transfer Model for Stator . . . . .	161
7.4	Comparison Between Air and CO <sub>2</sub> Foil Thrust Bearings . . . . .	165
7.5	Preliminary Performance Investigation . . . . .	172
7.6	Conclusions . . . . .	179
<b>8</b>	<b>Conclusions and Future Work</b>	<b>181</b>
8.1	Conclusions . . . . .	181
8.2	Recommendations for Foil Bearing Designs . . . . .	184
8.3	Future Research . . . . .	184
	<b>References</b>	<b>187</b>
<b>A</b>	<b>Discretisation of Reynolds equation</b>	<b>207</b>
<b>B</b>	<b>Description of Eilmer</b>	<b>211</b>
<b>C</b>	<b>Source Code</b>	<b>215</b>
C.1	Moving Wall Boundary Condition . . . . .	215
C.2	Periodic Boundary Condition . . . . .	216
C.3	Reconstruction . . . . .	217
<b>D</b>	<b>Description of Wilcox's 2006 <math>k-\omega</math> model</b>	<b>219</b>

---

# List of Figures

---

1.1	Schematic of sCO <sub>2</sub> turbo-alternator-compressor, taken from Ref. [8]. . . . .	2
1.2	Schematic diagram of a hydrostatic bearing, taken from Ref. [10]. . . . .	3
1.3	Schematic diagram of a tapered-land bearing, taken from Ref. [12]. . . . .	4
1.4	Tilting pad bearing, taken from Ref. [15]. . . . .	4
1.5	Metal mesh bearing, taken from Ref. [21]. . . . .	5
1.6	Schematic of foil thrust bearing, taken from Ref. [23]. . . . .	6
2.1	Plant layout of a sCO <sub>2</sub> Brayton cycle, taken from Ref. [31]. . . . .	10
2.2	(a) operating conditions at SNL and (b) projected system operation by Dostal et al. [4], taken from Ref. [31]. . . . .	11
2.3	Direct normal irradiation in Australia, taken from Ref. [35]. . . . .	11
2.4	Test rig by Singh [39]; (a): System layout; (b): Control element. . . . .	12
2.5	Photograph of the SNL sCO <sub>2</sub> Brayton loop [42]. . . . .	13
2.6	Sandia sCO <sub>2</sub> centrifugal compressor rotating at 75 000 rpm, taken from Ref. [7]. . . . .	14
2.7	Variation of thermophysical properties of CO <sub>2</sub> : dynamic viscosity $\mu$ ((a), solid line); thermal conductivity $\kappa$ ((a), dash line); density $\rho$ ((b), solid line); and specific heat capacity $C_p$ ((b), dash line) of CO <sub>2</sub> as a function of temperature at a pressure of 8 MPa, taken from Ref. [49]. . . . .	15
2.8	Bulk film temperature (averaged over film thickness) of loaded bearing overlapped on the pressure profiles for CO <sub>2</sub> with real gas effect at 40 000 rpm, taken from Ref. [71].	17
2.9	Prototype bearing with one top foil removed, taken from Ref. [23]. . . . .	18
2.10	Nomenclature for foil thrust bearings, taken from Ref. [76]. . . . .	19
2.11	Torque versus load at 23 000 rpm, taken from Ref. [23]. . . . .	19
2.12	Measured trailing edge temperature gradients, taken from Ref. [77]. . . . .	20

2.13	Coordinate system for small perturbations, taken from Ref. [84]. . . . .	22
2.14	Comparison between Reynolds equation and experiment, taken from Ref. [76]. . . . .	23
2.15	Non-dimensional pressure distribution of foil thrust bearings obtained from Reynolds equation, taken from Ref. [76]. . . . .	24
2.16	Load and torque of foil thrust bearings obtained from Reynolds equation, taken from Ref. [76]. . . . .	24
2.17	A plot of the $G'$ functions for each of the Ng and Pan [87], Constantinescu [88], and Hirs [89] turbulence models as a function of rotational Reynolds number, taken from Ref. [24]. . . . .	25
2.18	Non-dimensional pressure distribution of foil thrust bearings obtained from turbulent Reynolds equation, taken from Ref. [8]. . . . .	27
2.19	Load and power loss of foil thrust bearings obtained from turbulent Reynolds equation, taken from Ref. [8]. . . . .	28
2.20	Pressure distribution in a long slider bearing using Reynolds equation and CFD, taken from Ref. [91]. . . . .	30
2.21	Nomenclature for bump strips, taken from Ref. [76]. . . . .	31
2.22	Bump deflection for various load distributions, taken from Ref. [97]. . . . .	33
2.23	Bump deflection for various load distributions, taken from Ref. [100]. . . . .	34
2.24	Structural stiffness and damping, taken from Ref. [75]. . . . .	35
2.25	Vertical deflection of the bump top points for friction coefficients 0.0 and 0.2 (right), taken from Ref. [108]. . . . .	36
2.26	(a): Thermal resistance at the bump contacts to the top foil and the bearing housing, along with the thermal resistance model of a bump arc, (b): simplified CFD model of an inlet mixing chamber, taken from Ref. [109]. . . . .	37
2.27	Simplified thermal domains of the surrounding structures around the radial foil bearing close to turbine and thermal boundary conditions, taken from Ref. [111]. . . . .	38
3.1	Computational domain for Taylor-Couette flow, taken from Ref. [122]. . . . .	43
3.2	Comparison of temperature (a) and axially averaged velocity (b) profiles in radial direction at low pressure condition. . . . .	45

3.3	Comparison of temperature (a) and axially averaged velocity (b) profiles in radial direction at intermediate pressure condition. . . . .	46
3.4	Parameters variation of Taylor-Couette Flow at high pressure condition; (a): pressure; (b): temperature. . . . .	47
3.5	Temperature and velocity for Taylor-vortices case. . . . .	48
3.6	Schematic of hydrostatic air thrust bearing geometry, taken from Ref. [127]. . . . .	49
3.7	Steady state pressure distribution in an inward pressurised bearing for different bearing numbers: (a): wide bearing; (b): narrow bearing. . . . .	50
3.8	Comparison of zero radial velocity line at different bearing number. . . . .	50
3.9	Schematic of the geometry (a) and coordinate (b) of the wavy thrust bearings, taken from Ref. [128]. . . . .	51
3.10	Schematic of symmetric wavy film thickness and comparison of pressure at center radius between Eilmer and Reynolds equation. . . . .	52
3.11	Schematic of a 4:1 wavy film thickness and comparison of pressure at center radius between Eilmer and Reynolds equation. . . . .	53
3.12	(a) Experimental apparatus (taken from Ref. [134]) and (b) schematic diagram of the simulation domain for Couette and Poiseuille flows, dimensions in mm. . . . .	56
3.13	(a) Velocity distribution for turbulent plane Couette flow, (b) Comparison with the law of the wall. . . . .	58
3.14	Schematic diagram of the simulation domain for flat plate, in mm. . . . .	61
3.15	Performance comparison with different grid spacings for adiabatic walls, (a) friction coefficient; (b) law of the wall. 380 mm from leading edge, $Re_x=2.39 \times 10^6$ . . . . .	63
3.16	Performance comparison with different grid spacings for constant temperature walls, (a) friction coefficient; (b) heat flux. . . . .	65
3.17	Law of the wall and temperature, 380 mm from leading edge, $Re_x=2.39 \times 10^6$ . . . . .	66
3.18	Performance comparison with different grid spacings for various cases. . . . .	68
3.19	Comparison of different turbulence models for case 5. . . . .	70
3.20	Convergence history of norms based on turbulent kinetic energy for different mesh sizes: a) $L_2$ norms, b) $L_\infty$ norms. . . . .	72
3.21	(a) Norms and (b) observed order of accuracy. . . . .	73

3.22	Pressure contour of the rigid foil thrust bearings, rotational speed: 30 000 rpm, rotor to top foil separation: 22 $\mu\text{m}$ . . . . .	74
3.23	Velocity contour of the rigid foil thrust bearings, rotational speed: 30 000 rpm, rotor to top foil separation: 22 $\mu\text{m}$ . . . . .	75
3.24	Comparison of tangential and radial velocities at a circumferential angle of 44.46°. . . . .	75
4.1	Schematic diagram for the moving interface. $A_n, B_n, C_n, D_n$ are the vertices at time $n$ , $A_{n+1}, B_{n+1}, C_{n+1}, D_{n+1}$ is the vertices at time $n + 1$ . $A_{if}, B_{if}, C_{if}, D_{if}$ are the effective vertices at time $n + 1$ , used to calculate the swept volume $V_{if}$ . $W_A, W_B, W_C, W_D$ grid-velocities associated with the vertices. . . . .	81
4.2	Ghost cell configuration for a slip wall condition. . . . .	82
4.3	Schematic diagram for tangential moving velocity. . . . .	83
4.4	(a) Initial two-dimensional mesh for random grid motion, (b) final two-dimensional mesh. . . . .	85
4.5	Comparison results of Eilmer and analytical solution, (a) density, (b) pressure, (c) temperature, (d) velocity. . . . .	86
4.6	Schematic diagram of projectile in tube, dimensions in mm. . . . .	87
4.7	Comparison of pressure at end wall and piston face. . . . .	88
4.8	Comparison of results between Eilmer, L1D, and ideal solution, (a) simulation time and piston position, (b) piston velocity and piston position. . . . .	88
4.9	Computational domain for NACA0012 airfoil. . . . .	90
4.10	Grid convergence study for pitching NACA0012. . . . .	90
4.11	Instantaneous pressure coefficient, (a) $0.52^\circ$ , $\downarrow$ , downward stroke, (b) $-0.54^\circ$ , $\uparrow$ , upward stroke, (c) $-2.00^\circ$ , $\uparrow$ , upward stroke, (d) $2.01^\circ$ , $\downarrow$ , downward stroke, (e) $2.34^\circ$ , $\downarrow$ , downward stroke, (f) $-2.41^\circ$ , $\downarrow$ , downward stroke. . . . .	91
4.12	Comparison between Eilmer and experiment, (a) normal force coefficient, (b) moment coefficient. . . . .	92
4.13	Computational domain for the oscillating plate. . . . .	93
4.14	Grid convergence study of oscillating plate: (a) velocity distribution at 1 ms, (b) Friction coefficient over the fine mesh in terms of representative cell size at 1 ms. . . . .	94

4.15	Comparison of results between Eilmer and analytical solution, (a) velocity profile at different phase angles, (b) local skin friction coefficient. . . . .	95
4.16	Grid convergence study for the pitching NACA64A010 airfoil. . . . .	96
4.17	Comparison of results between Eilmer and experiment [161], (a) lift force coefficient $C_l$ vs angle of attack $\alpha$ , (b) moment coefficient $C_m$ vs angle of attack $\alpha$ . . . . .	96
4.18	Schematic diagram for forces and moments. . . . .	98
4.19	(a) Schematic diagram of top foil in foil bearings, (b) deformation comparison between ANSYS and the Kirchhoff plate structural deformation code at different radii. . . . .	99
4.20	Grid convergence study: (a) & (b) local deflection, (c) & (d) maximum deflection. . .	101
4.21	Flow chart of the bump foil model, taken from [100]. . . . .	103
4.22	Structural damping coefficient, $C_B$ . . . . .	104
4.23	Stencil for mapping method at the fluid-structure interface, (a): from Eilmer to the structure solver, (b): from the structure solver to Eilmer. . . . .	105
4.24	Pressure and deflection contours at the fluid-structure interface, the mapping process is (a)→(b)→(c)→(d). . . . .	107
4.25	Comparison of deflection by the structure solver and mapped deflection for Eilmer. .	108
5.1	Side view of foil thrust bearings, not to scale. . . . .	110
5.2	Computational domain for foil thrust bearings, not to scale. . . . .	111
5.3	Grid convergence study for foil thrust bearings: (a) local deflection at the medium radius, (b) pressure at the medium radius. . . . .	112
5.4	Comparison of measurements and numerical simulation at fixed rotational speed of 21 000 rpm. . . . .	112
5.5	Comparison of maximum deformation between Eilmer and numerical results from Ref. [26]. . . . .	113
5.6	Pressure-Enthalpy diagram for CO <sub>2</sub> . . . . .	114
5.7	Comparison of thermodynamic properties at the medium radius with the rotational speed of 30000 rpm: (a) Pressure, (b) Compressibility factor, (c) Density, (d) Temperature, (e) Dynamic viscosity, (f) Thermal conductivity. . . . .	115

5.8	Comparison between Eilmer-laminar and Reynolds equation, (a) Pressure (in Pa) contour for low density condition, (b) Pressure (in Pa) contour for high density condition, (c) Pressure (in Pa) contour for low density condition, (d) Pressure (in Pa) contour for high density condition, (e) & (f) Comparison of pressure at the medium radius. . . . .	117
5.9	Pressure increase contour for foil thrust bearings, (a) CO <sub>2</sub> , rotational speed: 60 000 rpm, (b) Air, rotational speed: 60 000 rpm. . . . .	118
5.10	Comparison of non-dimensional pressure distribution at the medium radius between Eilmer and Reynolds equation. . . . .	120
5.11	Ramp region: pressure increase, radial and tangential velocity at different circumferential angles. Rotational speed: 60 000 rpm, ramp ends at 15°, (Rotor at top, stator at bottom). . . . .	122
5.12	Flat region: pressure increase, radial and tangential velocity at different circumferential angles. Rotational speed: 60 000 rpm, flat starts at 15°, (Rotor at top, stator at bottom). . . . .	123
5.13	Approximate streamlines at 90% (rotor) and 10% (stator) film thickness (radial component is exaggerated). . . . .	124
5.14	The architecture of a supercritical CO <sub>2</sub> turbomachinery system. . . . .	125
5.15	Density (solid line, in $kg/m^3$ ) and dynamic viscosity (dashed line, in $\times 10^6 kg/ms$ ) at different operating conditions. . . . .	126
5.16	Rotational Reynolds number at different operating conditions (based on 5 $\mu m$ initial gap and 50 000 rpm). . . . .	127
5.17	Performance comparison at different operating conditions from laminar fluid solver, solid line: load capacity in N, dashed line: torque in Nmm, Eilmer-laminar. Rotational speed: 50 000 rpm. . . . .	128
5.18	Pressure increase ( $p - p_a$ ) at the different operating pressures. Operating temperature fixed at 400 K, Eilmer-laminar. Rotational speed: 50 000 rpm. . . . .	128
5.19	Radial velocity profile in the ramp region (circumferential angle: 5°) for different operating conditions, bold line: $V_r = 0$ , Eilmer-laminar. . . . .	129

5.20	Radial velocity profile in the ramp region (circumferential angle: $25^\circ$ ) for the different operating conditions, bold line: $V_r = 0$ . Note, the inner radius velocity profile are so small that they are difficult to see, Eilmer-laminar. . . . .	130
5.21	Streamlines and radial velocity close to stator and rotor. Operating condition: 0.1 MPa and 400 K, $\rho=1.33 \text{ kg m}^{-3}$ . the rotational direction is anti-clockwise, Eilmer-laminar.	132
5.22	Streamlines and radial velocity close to stator and rotor. Operating condition: 1.4 MPa and 400 K, $\rho=19.01 \text{ kg m}^{-3}$ , the rotational direction is anti-clockwise, Eilmer-laminar.	133
5.23	Local deflection (in $\mu\text{m}$ ) for two operating conditions, rotational direction: anti-clockwise, Eilmer-laminar. . . . .	134
5.24	Performance comparison for different flow regimes, the operating temperature is fixed as 400 K. . . . .	135
5.25	Local deflection (in $\mu\text{m}$ ) at an operating pressure of 1.4 MPa and operating temperature of 400 K. . . . .	136
5.26	Comparison of tangential velocity profile at laminar and turbulent flow at the medium radius with the circumferential angle of $24.20^\circ$ . . . . .	137
5.27	Pressure and radial velocity close to stator and rotor. Operating condition: 4.0 MPa and 400 K, the rotational direction in anti-clockwise, Eilmer-turbulent. . . . .	138
5.28	Schematic diagram of different computational domains for foil thrust bearings. . . .	139
5.29	Comparison of pressure distribution at different computational domains, rotational speed is 40 000 rpm and load is 200 N, notable differences in pressure at start of ramp and end of flat regions. . . . .	140
5.30	Gauge Pressure (unit in kPa) and deflection (unit in $\mu\text{m}$ ) contours at different rotor to top foil separation, rotational speed of 30 000 rpm. . . . .	142
5.31	Steady state performance of foil thrust bearings under different rotational speed and initial film thickness. . . . .	143
6.1	Schematic diagram of rotor perturbation motion. . . . .	146
6.2	History plot of reaction force and rotor motion. . . . .	148
6.3	Comparison of the calculated stiffness and damping coefficient at different cycles. . .	149
6.4	Comparison of the calculated stiffness and damping coefficient at different parameters.	150

6.5	Comparison of CFD and numerical results from San Andrés [26], rotational speed: 21 000 rpm. . . . .	150
6.6	Comparison of foil thrust bearings performance at different computational domain, (a): synchronous stiffness; (b): synchronous damping. . . . .	151
7.1	Schematic diagram for conjugate Couette flow. . . . .	156
7.2	Comparison of temperature distribution between fluid-thermal simulation and analytical solution. . . . .	156
7.3	Boundary conditions for conjugate nozzle flow, coloured by temperature. . . . .	157
7.4	(a) Temperature distribution along outer wall of nozzle [178], used as the nonuniform temperature boundary condition for numerical simulation, (b) comparison of temperature distribution along inner wall of nozzle between numerical simulation and experiment [178]. . . . .	158
7.5	Schematic diagram for fluid-structure-thermal simulations. . . . .	159
7.6	Schematic diagram for layout of foil thrust bearings. . . . .	160
7.7	Computational domain for the rotor. . . . .	160
7.8	Computational domain for the stator, (a): Stator in three dimensional, (b): Stator with top foil removed in three dimensional. . . . .	162
7.9	Schematic diagram of heat transfer from top foil to thrust plate. . . . .	163
7.10	Schematic diagram of the additional geometry to account for the contact resistance. . . . .	164
7.11	Schematic diagram of the deflection of the bump foil. . . . .	164
7.12	Schematic diagram of computational mesh of stator. . . . .	165
7.13	Computational domain of a foil thrust bearing. . . . .	166
7.14	Air foil thrust bearings interface temperatures, (a): rotor; (b): stator; (c): heat flow chart for complete bearing. . . . .	168
7.15	CO <sub>2</sub> foil thrust bearings interface temperatures, (a): rotor; (b): stator; (c): heat flow chart for complete bearing. . . . .	169
7.16	Comparison of streamline between air and CO <sub>2</sub> thrust bearings in the groove, (a) air; (b) CO <sub>2</sub> . . . . .	171
7.17	Comparison of (a) heat flow and maximum top foil temperature (b) for different convection coefficients within the bump channels. . . . .	172

7.18 Comparison of rotor temperature (in K) at power loss, (a) 318 N and 417 W, (b) 100 N and 352 W, rotational speed is 30 000 rpm. . . . . 173

7.19 Comparison of rotor deflection (in m) at different power loss, (a) 318 N and 417 W, (b) 100 N and 352 W, rotational speed is 30 000 rpm. . . . . 174

7.20 Temperature and deflection at the rotor, load of 318 N, power loss of 417 W, rotational speed is 30 000 rpm. . . . . 174

7.21 Comparison of stator temperature (in K) at different load and power loss, (a) 318 N and 417 W, (b) 100 N and 352 W, rotational speed is 30 000 rpm. . . . . 175

7.22 Comparison of stator deflection (in m) at different power loss, (a) 318 N and 417 W, (b) 100 N and 352 W, rotational speed is 30 000 rpm. . . . . 175

7.23 Comparison of rotor temperature (in K) at different rotational speed, (a) 40 000 rpm, load is 275 N, power loss is 815 W, (b) 50 000 rpm, load is 318 N, power loss is 1273 W. 176

7.24 Comparison of rotor deflection (in m) due to thermal stress at different rotational speed, (a) 40 000 rpm, load is 275 N, power loss is 815 W, (b) 50 000 rpm, load is 318 N, power loss is 1273 W. . . . . 177

7.25 Comparison of rotor temperature (in K) at different rotational speed, (a) 40 000 rpm, load is 275 N, power loss is 815 W, (b) 50 000 rpm, load is 318 N, power loss is 1273 W. 177

7.26 Comparison of stator deflection (in m) due to thermal stress at different rotational speed, (a) 40 000 rpm, load is 275 N, power loss is 815 W, (b) 50 000 rpm, load is 318 N, power loss is 1273 W. . . . . 178

7.27 Comparison of bearing performance for different modelling approaches. . . . . 178

---

## List of Tables

---

2.1	Geometry and physical parameters for thrust foil bearings in Ref. [26, 73]. . . . .	19
2.2	The Ng and Pan turbulent coefficients for various critical Reynolds numbers. Applicable to Equations 2.8 and 2.9. . . . .	26
3.1	Parameters for simulations, used match the experimental conditions as reported in Ref. [122]. . . . .	44
3.2	Rotational speed (in rpm) for different bearing speed parameter for perfect air and dense air. . . . .	48
3.3	Wavy thrust bearing physical and operational characteristics. . . . .	51
3.4	Comparison results of load (in N) and friction torque (in Nmm) obtained from Reynolds equation and Eilmer. . . . .	53
3.5	Operating condition of foil thrust bearings from SNL's test loop [8]. . . . .	54
3.6	Details of El Telbany and Reynolds tests. . . . .	67
3.7	Comparison of frictional velocity (in m/s) at different grid spacings. The low stress wall is the moving wall in cases 1,2,3 and 5. . . . .	69
3.8	Comparison of time step used by different modeling approaches. . . . .	74
3.9	Matrix of rotational speeds and minimum rotor to top foil separation to show trends in $k_4$ required to stabilise simulations. . . . .	77
4.1	Operating condition of foil thrust bearings from SNL's test loop [8]. . . . .	100
4.2	Comparison of pressure force between Eilmer and the structure solver. . . . .	106
5.1	Performance comparison of foil thrust bearings with different computational meshes. . . . .	111
5.2	Performance comparison of the fixed geometry thrust bearings between Eilmer-laminar and Reynolds equation. . . . .	116

5.3 Operating conditions for CO<sub>2</sub> and air. . . . . 118

7.1 Geometry and parameters for the foil thrust bearing. . . . . 166

---

# Nomenclature

---

## Acronyms

2D	Two dimensional
3D	Three dimensional
AGARD	Advisory Group for Aerospace Research and Development
AUSM	Advection Upstream Splitting Method
CFD	Computational Fluid Dynamics
CFL	Courant-Friedrichs-Lewy
CST	Concentrated Solar Thermal
CTDNS	Compressible Temporal Direct Numerical Simulation
DNS	Direct Numerical Simulation
DSMC	Direct Simulation Monte Carlo
EFM	Equilibrium Flux Method
FDM	Finite Difference Method
LES	Large Eddy Simulation
NACA	National Advisory Committee for Aeronautics
NASA	National Aeronautics and Space Administration
RANS	Reynolds-averaged Navier–Stokes
Re	Reynolds number.
REFPROP	Reference Fluid Thermodynamic and Transport Properties Database
sCO <sub>2</sub>	Supercritical CO <sub>2</sub>
SNL	Sandia National Laboratories

## Greek Symbols

$\alpha$	Angle of attack.
----------	------------------

$\alpha_0$	Pitching range.
$\alpha_m$	Mean angle of attack.
$\beta$	Under-relaxation factor.
$\kappa$	Reduced frequency.
$\mu$	Dynamic viscosity.
$\nu$	Poisson's ratio.
$\omega$	Rotational speed.
$\phi$	Scalar quantity.
$\rho$	Density.
$\tau_{wall}$	Wall shear stress.
$\theta$	Angle.

## Roman Symbols

$\Delta U$	Change of conserved flow quantities $U$ .
$\Delta t$	Time step.
$\hat{\mathbf{n}}$	Outward-facing unit normal of the control surface.
$\hat{\mathbf{t}}$	Tangential unit-vector associated with a boundary interface.
$\mathbf{F}_i$	Convective flux.
$\mathbf{F}_v$	Viscous flux.
$\mathbf{L}$	Momentum flux.
$\mathbf{Q}$	An array of source terms.
$\mathbf{U}$	An array of conserved flow quantities per unit volume.
$\mathbf{u}$	Flow velocity vector.
$\mathbf{w}_a$	Interface grid-velocity obtained by averaging the velocity of four vertices.
$\mathbf{w}_{if}$	Effective interface moving velocity.
$A$	Area of the control face.
$A_{if}$	Interface area.
$C$	Equivalent damping.
$c$	Chord length.
$C_B$	Structural damping.

$C_b$	Fluid film damping.
$C_f$	Skin friction coefficient.
$C_l$	Lift force coefficient.
$C_m$	Momentum coefficient.
$D$	Stiffness of thin plate.
$D_T$	Diffusivity of solid materials.
$E$	Total energy.
$F$	Lift force.
$G$	Mass flux.
$H$	Energy flux.
$h$	Thickness.
$K$	Equivalent stiffness.
$K_B$	Structural stiffness.
$K_b$	Fluid film stiffness.
$M$	Momentum.
$p$	Pressure acting on the thin plate.
$p_a$	Ambient pressure.
$r$	Radius.
$S$	Bounding surface.
$T$	Friction torque.
$u^+$	Non-dimensional velocity.
$V$	Cell volume.
$w$	Deflection.
$y^+$	Non-dimensional distance.

## Subscripts

$f$	Fluid.
$i$	Interface.
$s$	Solid.

# Introduction

---

## 1.1 Motivation

The sCO<sub>2</sub> power cycle is considered a promising next generation power cycle. It has the potential to offer better overall economics due to a higher thermal conversion efficiency and lower capital cost. Feher [1] designed the first sCO<sub>2</sub> power cycles at last 60s. At the same time, Angelino [2, 3] proposed a liquid phase compression gas turbine. The system efficiency was larger than that of regenerative Brayton cycles and the approximately same with that of regenerative Rankine cycles.

CO<sub>2</sub> is an abundant, non-toxic, stable and relatively inert working fluid with a critical temperature close to ambient temperature in many locations (31 °C). Therefore, sCO<sub>2</sub> cycles do not require low temperature cooling fluid, which is not available at many places, especially at places with abundant solar energy. Supercritical CO<sub>2</sub> Brayton cycle can offer higher efficiency compared to steam cycles at temperatures larger than 550 °C [4]. This cycle also has a compact architecture compared to Rankine cycles due to the higher density fluid. This also reduces the cost of maintenance, installation, and operation [5].

sCO<sub>2</sub> turbomachinery system is a critical component operating at high speeds with the support from bearings. Figure 1.1 shows the schematic diagram of the sCO<sub>2</sub> turbomachinery commissioned at SNL. Two journal bearings and one thrust bearing are used to support axial and radial loads, respectively. In sCO<sub>2</sub> turbomachinery, thrust loads arise from the unequal axial pressure distribution on rotors, while radial loads are from the radial force on rotors and the shaft weight. The thrust load from a 100 kW sCO<sub>2</sub> turbine designed at QGECE is approximately 1000 N due to high absolute pressure and pressure difference across turbine, and the shaft rotational speed can be 160 000 rpm to ensure a higher total-to-static efficiency [6]. This presents critical challenges to the bearing operating

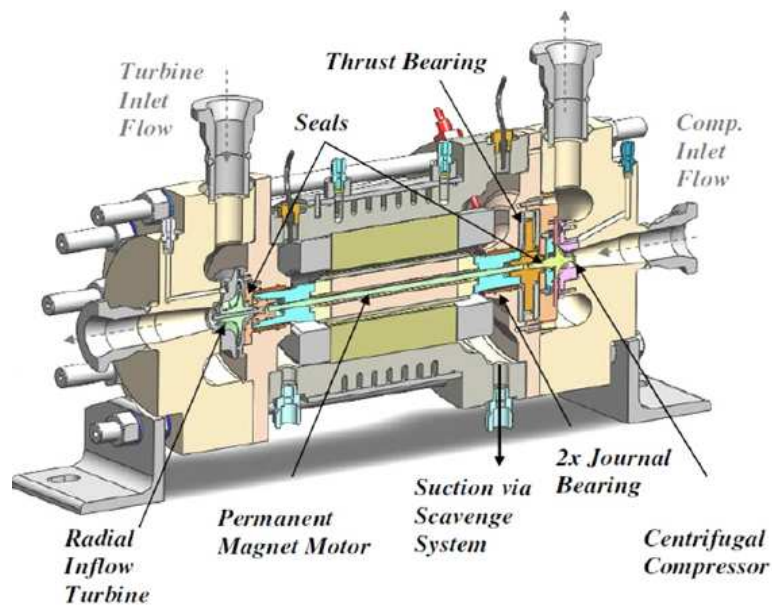


**Figure 1.1:** Schematic of sCO<sub>2</sub> turbo-alternator-compressor, taken from Ref. [8].

conditions. Many early tests of sCO<sub>2</sub> turbomachinery at SNL [7] used ball bearings. However ball bearings are limited to a lifetime between 20 hours and 2000 hours [7]. This is too short for practical applications with targeted lives greater than 20 000 hours.

Other alternatives to rolling-element bearings are fluid bearings. Long operation life is not a problem for fluid bearings compared to rolling-element bearings. Also, the need for additional oil supply systems is removed, since the cycle fluid (CO<sub>2</sub> for sCO<sub>2</sub> power cycles) is used as the working fluid for the bearings. Fluid bearings are typically used in high load and high rotational speed conditions, where conventional rolling-element bearings would have short life (as encountered at the small sCO<sub>2</sub> cycle test rig at SNL [7]) [9]. Fluid bearings are bearings in which the load is supported by a thin layer of rapidly moving pressurised liquid or gas between the rotor and stator. Because of no contact between moving objectives, the sliding friction is minimised, allowing fluid bearings to have lower friction, wear and vibration than many other types of bearings. Fluid bearings can be further classified into two types depending on pressurisation types, hydrostatic and hydrodynamic bearings.

Hydrostatic bearings refer to a configuration where the lubricant with high pressure is fed into the bearings by an external pump. Therefore, the formed load capacity is used to compensate loads from turbines and compressors. The schematic diagram of a hydrostatic bearing is depicted in Figure 1.2. The orifice in the recess connects the high pressure fluid from the external pump with the bearing

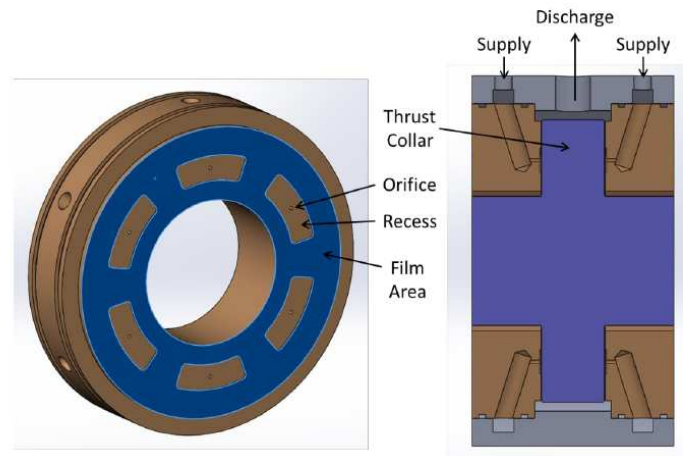


**Figure 1.2:** Schematic diagram of a hydrostatic bearing, taken from Ref. [10].

chamber. In hydrostatic bearings, mechanical contact and wear can be avoided, even at the very low rotational speed and lightly load. The second advantage is good stiffness. High stiffness is maintained under different loads and rotational speeds [9]. However, the drawback is that auxiliary components are needed to enable its operation. The cost and system complexity increase accordingly.

On the contrary to hydrostatic bearings, hydrodynamic bearings rely on a high speed rotor to pressurise the fluid. The pressure in the fluid film is increased due to a wedge shape formed by the rotor and stator. The increased pressure provides forces to compensate the load from turbines or compressors. Compared to hydrostatic bearings, hydrodynamic bearings do not require the external pressurisation and experience weight reduction due to the elimination of the additional oil supply system, and substantial savings in maintenance costs [11]. Depending on the support structure at the stator, fluid bearings can be further divided into fixed-geometry bearings (e.g. tapered-land bearings) and flexible supporting bearings (e.g. tilting pad, bump-type, and metal mesh bearings).

Tapered-land bearings are simple and compact fixed geometry bearings, which are able to operate reliably for long periods [13]. Their schematic diagram is shown in Figure 1.3. The geometry forms the ramp and flat regions between the rotor and stator. The pressure is increased due to the convergent shape in the ramp region. Since the tapered-land bearings are sensitive to load, speed and working fluid, a custom design is commonly required for the specific operating conditions [14].

One challenge of the aforementioned fixed-geometry bearing are manufacturing uncertainties [16]. This results in a large performance uncertainty during operation. Therefore, flexible supporting bear-

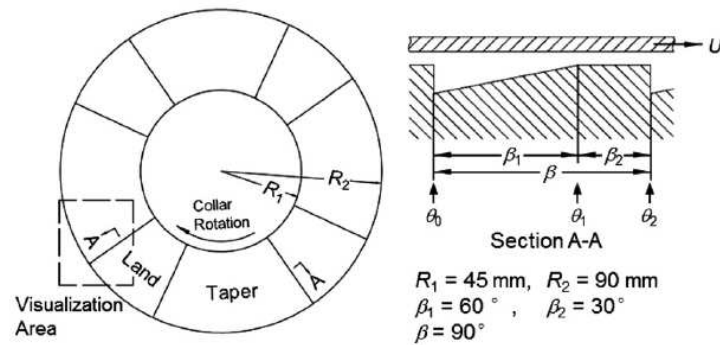


**Figure 1.3:** Schematic diagram of a tapered-land bearing, taken from Ref. [12].

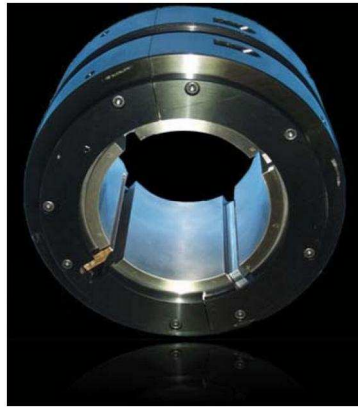


**Figure 1.4:** Tilting pad bearing, taken from Ref. [15].

ings are introduced, which are able to increase tolerance with respect to deformations of the rotor and stator and to manufacturing variation. Flexible bearings consist of tilting pad bearing [15], bump-type foil bearings [11], metal mesh foil bearings [17] or the hybrid bump and metal mesh bearings that is recently proposed by Feng et al. [18]. Tilting pad bearings usually have a multiple number of pads. A four pad bearing is shown in Figure 1.4. Each pad is able to rotate about a pivot freely. For tilting pad bearings, destabilising forces are minimal. Thus, the bearings are not the effect of rotordynamic instability [15]. Tilting pad bearings are utilised as the fluid-film bearing for high-speed applications [15]. Metal mesh bearings use the ring shaped metal mesh to support the top foil as depicted in Figure 1.5. This bearing was employed as vibration isolaters in gas turbine engines initially [19]. Metal mesh bearings have received increased attention in recent years at Texas A&M University led

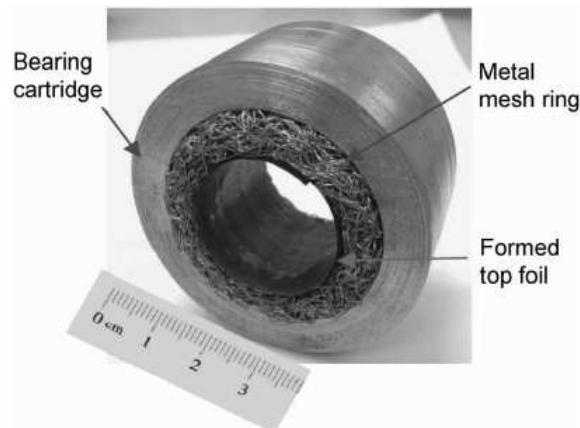


**Figure 1.5:** Metal mesh bearing, taken from Ref. [21].

by San Andrés [17, 20, 21, 22]. However, this metal mesh bearing is still under development and is not widely used in industry so far.

Bump-type foil bearings have been widely investigated in literature for air cycle machines [11]. It was successfully utilised to support the long duration tests for the sCO<sub>2</sub> cycle test rig at SNL [7]. Therefore, this bump-type foil bearings was selected to be investigated in this project. Bump-type gas foil bearings are composed of a smooth top foil and a corrugated bump foil. Each is made from a thin sheet of compliant metal, usually a nickel-based alloy. In a typical configuration, the top foil is affixed to the bearing housing on the upstream side, and on the downstream side it sits at the height of its bump understructure, forming a partially ramped profile as indicated in Figure 1.6. During operation, gas is drawn into the thin region between the rotor collar and top foils, and a self-generated hydrodynamic pressure field reacts to the thrust and radial load acting on the rotor. The bearing geometry and operating conditions, bump foil's mechanical properties, the top foil's material and coating determine the overall static and dynamic performance of the foil bearing.

Foil bearings have various advantages compared to the conventional rolling-element bearings in turbomachinery, including improved reliability, elimination of lubrication systems, and better tolerance to misalignment [24]. The corrugated structure providing stiffness and damping (relative motion) to the system makes the foil bearing unique [25]. A converging wedge is formed between the rotor and the top foil. The application of foil bearings was identified as a revolutionary concept in gas turbine engines. This approach provided a significant performance improvement in efficiency, speed,

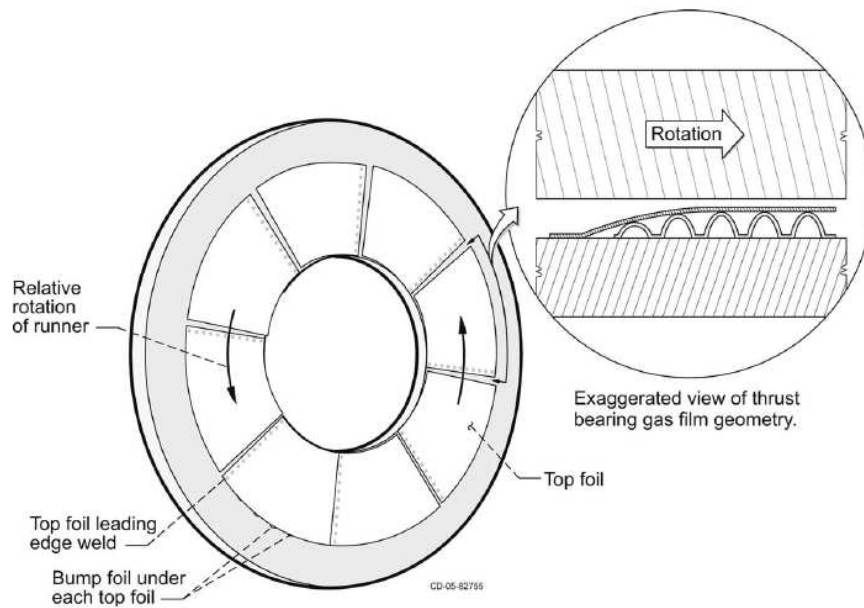


**Figure 1.6:** Schematic of foil thrust bearing, taken from Ref. [23].

and reliability. The typical applications of foil bearings are ranging from the magnetic disk drive read/write heads in personal computers to the air cycle machines (aeroengine and turbochargers) [26].

Even though foil bearings have been successfully used in small  $s\text{CO}_2$  cycle test rigs to allow a longer duration testing [7], the flow behaviour and structural behaviour, including rotordynamic performance, of foil bearings and how it is affected by nonlinear properties and highly dense  $\text{CO}_2$  is not well understood. To date, investigations of  $\text{CO}_2$  foil bearings have been limited [27, 28]. Reynolds equation is widely used to model the pressure distribution within foil bearings. However it is uncertain if Reynolds equation is able to capture the new flow physics within foil bearings when operating with  $\text{CO}_2$ . Additionally, turbulence flow regimes induced by highly dense  $\text{CO}_2$  would result in the significant viscous heating effects. Their thermal performances has to be accurately investigated and properly managed to avoid in operation failures.

## 1.2 Aims and Objectives

Because of the interest in applying foil bearings to future  $s\text{CO}_2$  cycle machines and the lack of analysis capability other than Reynolds equation based approaches, this thesis sets out to develop a higher fidelity simulation tool. The tool developed in this thesis has the capability to perform transient fluid-

structure-thermal predictions of foil bearings. The simulation tool is presently developed for foil thrust bearings but the methodology is transferable to foil journal bearings. The objectives of this PhD project are:

1. To develop a high fidelity multi-physics multi-timescale simulation tool to analyse the performance of foil bearings for a range of working fluids, including high density CO<sub>2</sub>;
2. To provide the new insight to the operation of foil thrust bearings with CO<sub>2</sub>.

## 1.3 Thesis Overview

In this thesis, the aims and objectives outlined in Section 1.2 are achieved using a systematic approach. The thesis starts with discussion of relevant literature to highlight the theoretical basis of the work and experimental studies of foil bearings. This is followed by the development of a multi-physics and multi-timescale computational tool, build on the in-house CFD code Eilmer. This tool is developed and validated progressively until the full fluid-structure-thermal operation of a CO<sub>2</sub> foil thrust bearing can be completed. The gradual increase in complexity with each chapter allows the reader to progress with a logical flow of ideas and conclusions. A brief breakdown of each chapter is given here:

### **Chapter 2** *Literature Review*

An overview of the sCO<sub>2</sub> power cycle is given in this chapter to active the need to design foil thrust bearings. Theoretical and experimental approaches for foil journal and thrust bearings are then discussed to highlight the inadequacy of these approaches for CO<sub>2</sub> foil bearings.

### **Chapter 3** *Fluid Simulations*

Chapter 3 describes the main modifications of the in-house CFD solver Eilmer to allow the simulation of the fluid flow within foil bearings. The modifications allow Eilmer to simulate laminar and turbulent flows in foil bearings. The corresponding verification and validation cases are then presented to test the suitability of the modified CFD solver.

### **Chapter 4** *Fluid-Structure Coupled Simulations*

Chapter 4 documents the inclusion of the moving grid framework into the in-house CFD solver and the development of the structural deformation solver to simulate the deformation of the top and bump foils, followed by the mapping algorithm and coupling strategy. The coupling strategy is then employed to demonstrate the calculation process of the fluid-structure solver to obtain the steady state and dynamic performances.

**Chapter 5** *Foil Bearing Steady State Performance*

Chapter 5 documents the validation of the developed fluid-structure simulation tool for air foil thrust bearings. The gas model is selected for real gas properties of CO<sub>2</sub>. Simulation results for rigid and flexible bearings are compared to highlight the significance of centrifugal inertia and turbulence effects introduced by the high density CO<sub>2</sub>. It is found that centrifugal inertia effects increase the load capacity in the ramp region, while decrease the load capacity at the flat region. Also, turbulence effects largely increase the load and power loss. The computational domain used for foil thrust bearings is then investigated by comparing the steady state performances. Finally, the steady state performance under different rotational speeds and rotor to top foil separations is investigated.

**Chapter 6** *Foil Bearing Dynamic Performance*

Chapter 6 details the procedure to calculate dynamic stiffness and damping coefficients using the developed fluid-structure solver. This is followed by verification cases for air foil thrust bearings. The computational domain is again revisited by comparing the dynamic performances.

**Chapter 7** *Fluid-Structure-Thermal Simulations*

Chapter 7 details the computational framework for the fluid-structure-thermal simulation of foil thrust bearings. Under the same load condition (110 N), the fluid-structure-thermal simulation are performed for foil bearings with air and CO<sub>2</sub>, respectively. It is found that the groove is beneficial to remove viscous heat generation for CO<sub>2</sub> foil bearings due to centrifugal inertia effect. The bearing performance is compared using fluid-structure and fluid-structure-thermal modelling approaches. The fluid-structure simulation is applicable at the low rotational speed. However, fluid-structure-thermal modelling approach is needed at the rotational speed larger than 40 000 rpm.

**Chapter 8** *Conclusions and Future Work*

Chapter 8 summarises the findings of the work and discusses avenues for future research.

# Literature Review

---

## 2.1 Introduction

In the previous chapter, we highlighted the operating requirement and experiment failure from SNL's tests using conventional rolling-element bearings. One solution to enable this promising cycle is to use foil bearings. In this chapter, the background literature of sCO<sub>2</sub> power cycles and major components is described. Experimental studies for foil thrust bearings are then discussed. Reynolds equation, as an effective model for foil bearings, is then reviewed, followed by the modified Reynolds equation for turbulent flows. Next, the CFD approach applied to air bearings is reviewed. This confirms that Reynolds equation is an accurate numerical method to investigate air bearings. The second part focuses on analytical models for structural deformation within foil bearings. This highlights the complexity in predicting bump foil stiffness. In addition, the influence of temperature within foil bearings is reviewed and the effect of deflection due to thermal stresses is highlighted.

## 2.2 Background on Supercritical CO<sub>2</sub> Power Cycle

In more recent years, sCO<sub>2</sub> power cycles have drawn attention in many applications, including, nuclear power [4], coal power [29], and renewable energy [30]. Dostal [4] showed that the sCO<sub>2</sub> cycle has a higher efficiency compared to steam cycles at temperatures above 550 °C. Turchi [30] developed and benchmarked different sCO<sub>2</sub> cycle configurations for CST applications, including, simple Brayton cycle, recompression Brayton cycle with reheat, partial cooling cycle with recompression and reheat, and recompression with main-compression intercooling and reheat. It was concluded that the partial cooling cycles and recompression with main compression intercooling together with reheat are able of achieving greater than 50 % efficiency. These intercooled cycles expanded the temperature dif-



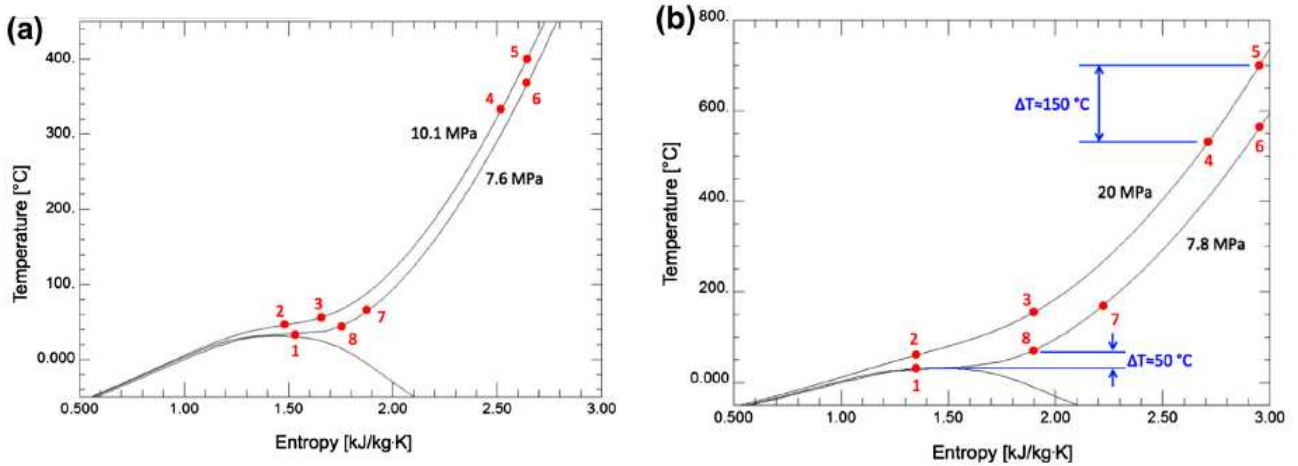


**Figure 2.2:** (a) operating conditions at SNL and (b) projected system operation by Dostal et al. [4], taken from Ref. [31].

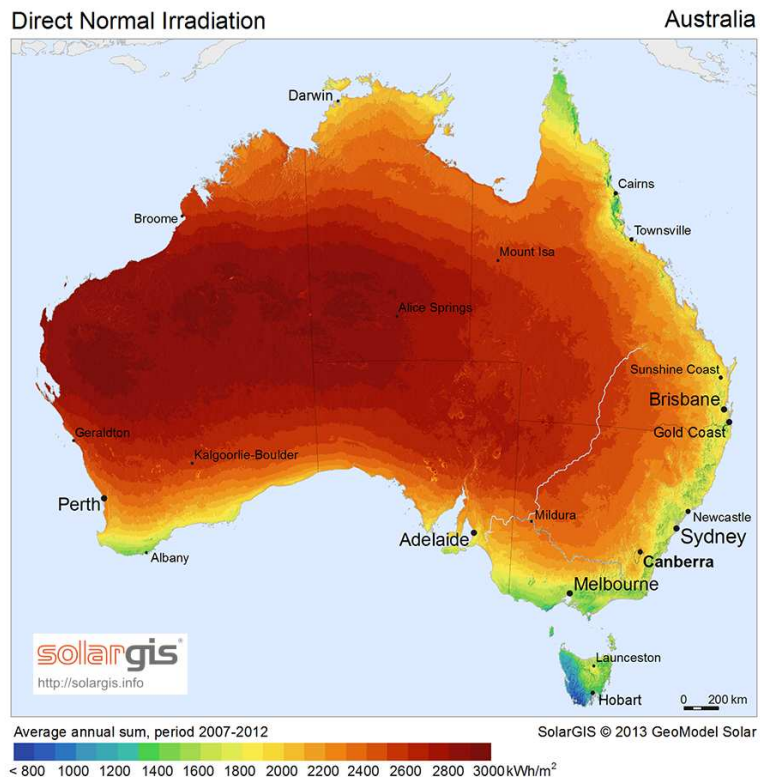


**Figure 2.3:** Direct normal irradiation in Australia, taken from Ref. [35].

In Australia, due to the abundant solar energy resources (see Figure 2.3), there is a growing interest in deploying sCO<sub>2</sub> power cycles for solar power applications. Singh et al. [36, 37, 38] performed

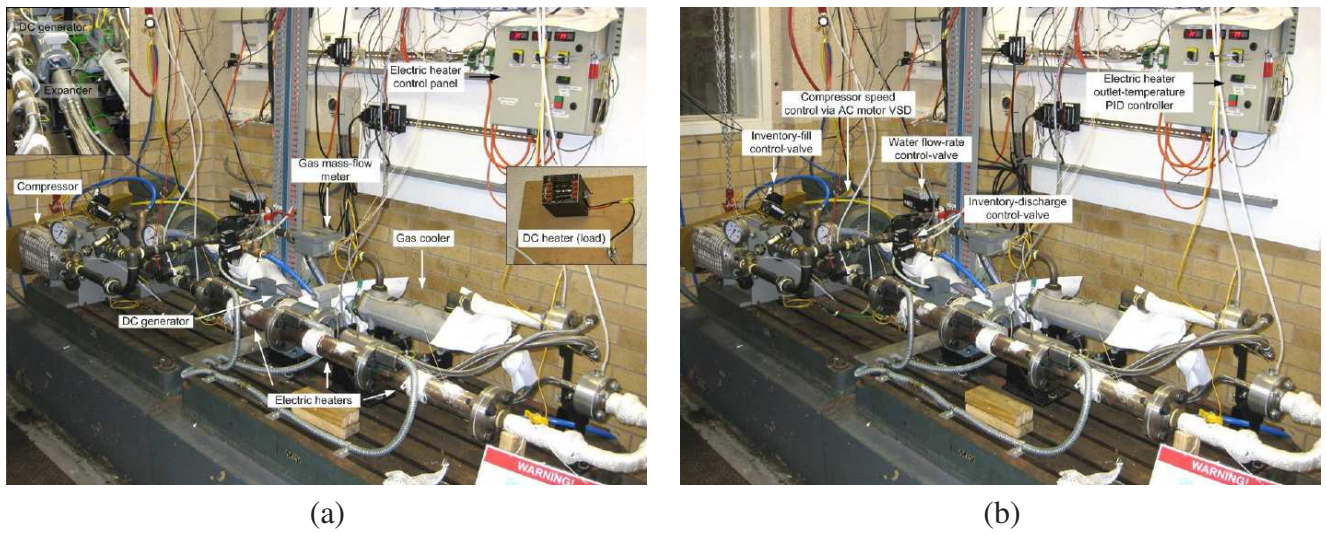


**Figure 2.4:** Test rig by Singh [39]; (a): System layout; (b): Control element.

considerable studies on the dynamic characteristics of direct-heated  $s\text{CO}_2$  Brayton cycle in a solar thermal power plant. The dynamic characteristics was investigated. His work highlighted the potential for mass-flow rate control in summer and control of compressor inlet conditions in winter [36]. The effect of the relative hot-to-cold side volume-ratios was also investigated [37]. Furthermore, an extremum-seeking-control and inventory-control method for closed Brayton cycles was presented by Singh et al. [38]. Simulations indicated that this control method can be achieved with a fixed- $\text{CO}_2$  inventory in both summer and winter. A small test-rig was constructed at the University of Queensland to test the dynamic performance of supercritical  $\text{CO}_2$  cycles [39, 40].

Besides these theoretical studies about the potential application of  $s\text{CO}_2$  power cycles, SNL conducted pioneering work on the experimental operation of  $s\text{CO}_2$  cycles [5, 7, 41, 42]. Figure 2.5 depicts the SNL's Megawatt-scale  $s\text{CO}_2$  split-flow recompression Brayton cycle. This provided preliminary experimental results for  $s\text{CO}_2$  cycles and the performance of critical components using  $s\text{CO}_2$  as the working fluid. These included recuperation and waste heat rejection heat exchangers, turbines, bearings, compressors, seals and heat exchangers. Iverson [41] pointed out that one challenge for solar thermal applications was the transient nature of the solar resource. A dataset for stable  $s\text{CO}_2$  Brayton cycle operation that was used as validation for numerical simulations was also presented.

Besides, Conboy et al. [42] presented experimental results regarding the control of  $s\text{CO}_2$  cycles, especially during the startup and shutdown processes. A protected shutdown in a motor was employed



**Figure 2.5:** Photograph of the SNL sCO<sub>2</sub> Brayton loop [42].

to prevent damage of foil bearings at speeds of less than 25 000 rpm, the lift-off speed for their foil bearings.

### 2.2.1 Components for Supercritical CO<sub>2</sub> Cycles

Before realising sCO<sub>2</sub> cycles, a number of challenges need to be overcome, making this an active area of research. The key components of this cycles, including turbine, compressor, heat exchanger, bearing and seal, need to be re-studied due to the new working fluid and especially the non-linear behaviour and high density exhibited by sCO<sub>2</sub>.

#### Turbine

Both axial and radial turbines are considered as the candidate for sCO<sub>2</sub> power cycles [6, 43, 44]. The high dense CO<sub>2</sub> results in the challenge for the aerodynamic design of turbines and compressor. Low volume flow rate leads to the design point at very low specific speeds and small sizes of turbine and compressor as shown in Figure 2.6. A partial admission axial turbine was considered by Kang et al. [43]. Qi et al. [6] used an automatic preliminary radial inflow design code developed by Ventura et al. [45] to investigate sCO<sub>2</sub> turbines at different power and rotational speeds. It was found that increasing power increased the number of feasible designs. The number of feasible design was limited when the speed is reduced. In Ref. [6], an total-to-static efficiency of 85% was attained under the selected operating conditions. Since the operating point of the sCO<sub>2</sub> turbine is far away from the critical point, Redlich-Kwong-Aungier cubic equation is accurate enough to simulate the sCO<sub>2</sub> turbine [43]. Apart from the aerodynamic design, the forced response of sCO<sub>2</sub> turbines was also of interest [46].

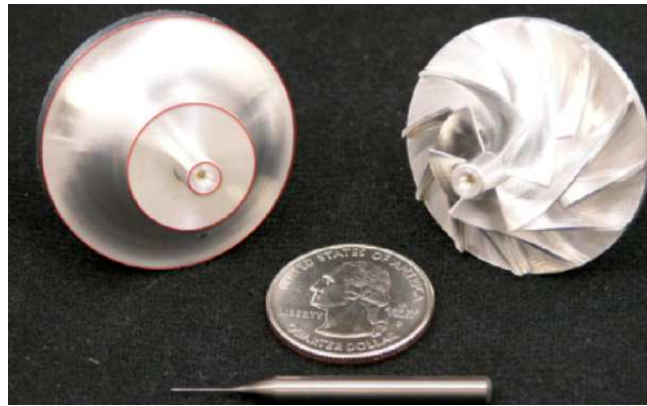


**Figure 2.6:** Sandia sCO<sub>2</sub> centrifugal compressor rotating at 75 000 rpm, taken from Ref. [7].

## Compressor

For CO<sub>2</sub> compressor design, Kus et al. [47] developed a one-dimensional code for preliminary design and performance prediction of oil-free CO<sub>2</sub> compressors. The high speed centrifugal compressor in a hermetic configuration was supported on foil gas bearings, and a wide range of loss mechanisms was considered. Lee et al. [48] developed a mean-line code called KAIST\_TMD for designing supercritical CO<sub>2</sub> compressor and turbine, which was compared to the existing experimental data to verify its capability.

The operating condition of sCO<sub>2</sub> compressors is slightly above the critical point, which introduces the significant non-ideal gas effect [50]. An abrupt property change is observed close to the critical point as shown in Figure 2.7. Additionally, it is possible that the working fluid within the compressors drops into the two phase region. These effects create challenges when designing sCO<sub>2</sub> compressors. Therefore, the standard assumptions might not be applicable when using one dimensional design tools [51]. High-fidelity computational tools were also used to predict the performance of sCO<sub>2</sub> compressors. Furusawa et al. [52] proposed a numerical method to simulate sCO<sub>2</sub> flows with the preconditioning method, in which thermophysical properties of fluids are generated from an in-house software. A nonequilibrium condensation model was also applied. It was found that condensation occurred in regions near the trailing edges. Pecnik et al. [53, 54] presented a three-dimensional computational fluid dynamics analysis of a centrifugal compressor operating with sCO<sub>2</sub> in the region above the critical point. Experimental data from SNL sCO<sub>2</sub> compression loop facility was selected as the validation case. The ideal head coefficient computed from CFD results was higher than the one

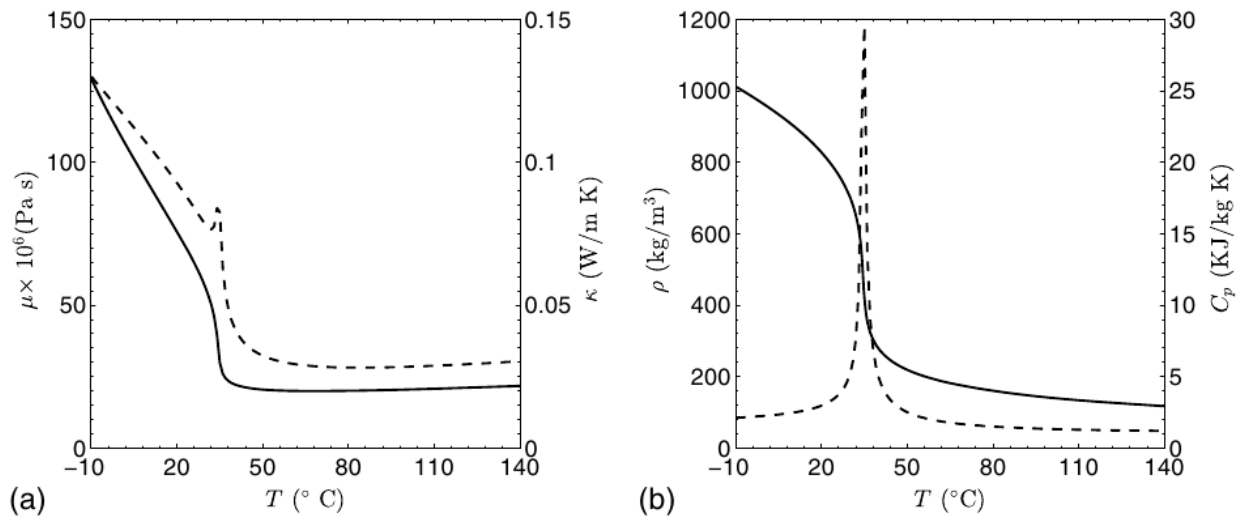


**Figure 2.7:** Variation of thermophysical properties of CO<sub>2</sub>: dynamic viscosity  $\mu$  ((a), solid line); thermal conductivity  $\kappa$  ((a), dash line); density  $\rho$  ((b), solid line); and specific heat capacity  $C_p$  ((b), dash line) of CO<sub>2</sub> as a function of temperature at a pressure of 8 MPa, taken from Ref. [49].

obtained from measurements. Differences are attributed to the simplified geometry adopted in their work. Kim et al. [55] provided CFD investigation of a centrifugal compressor with supercritical CO<sub>2</sub> as working fluid, numerical simulations using the  $k - \omega$  SST model were found to return satisfactory results. Their operating conditions are far from the critical point, however as the sCO<sub>2</sub> compressor operating condition approaches the critical point, deviations from the reference data start to become apparent. In the more challenging case, the disagreement with experimental data might be partially due to the modelling limitations within the two-phase regions. Moreover, RANS models might have the limitation on the investigation of turbulence close to the critical point, where a large local property variation was observed. Alternatively, DNS has been applied to the performance simulation for CO<sub>2</sub> compressors and varying properties [56].

## Heat Exchanger

The development of the sCO<sub>2</sub> heat exchanger including recuperator [57], hot-side [58] and cold-side heat exchangers [59] are of particular interest. Heat exchangers are important to sCO<sub>2</sub> power cycles as they are the main components for heat addition and rejection. Since CO<sub>2</sub> exhibits different behaviours compared to conventional heat transfer fluids [49], the work on the heat exchanger using sCO<sub>2</sub> is primarily focusing on the development of heat transfer correlations theoretical [60, 61] and

experimental [62, 63, 64, 65]. From numerical simulations, it was found by Dang [60] that the low Reynolds number  $k-\epsilon$  model by Jones and Launder showed the best agreement with the experimental data compared to three other models (the mixing length model by Bellmore and Reid, and the low Reynolds number  $k-\epsilon$  models by Launder and Sharma and by Myong and Kasagi). They also showed that the the heat transfer coefficient is not significantly influenced by the turbulent Prandtl number. A more detailed comparison of turbulence models was conducted by He et al. [61]. DNS results were used as a benchmark dataset for model assessment. Among the selected turbulence models (classical  $k-\epsilon$ ,  $k-\epsilon$  Chien,  $k-\omega$  model by Wilcox, Myong and Kasagi, Yang and Shihh and V2F), the V2F model was found to perform best. Given the numerical results, which show a certain amount of deviation with between different turbulence models and experimental data, there is a growing interest in employing DNS to investigate the heat transfer behaviour for sCO<sub>2</sub> [49, 66].

### Seal

Sealing is very important for sCO<sub>2</sub> cycles due to the high operating pressures. Lost gases requires a significant amount of energy for re-injection into the closed loop. For the first sCO<sub>2</sub> cycle at SNL, labyrinth seals were used [7]. Recently, dry gas seals are being considered for sCO<sub>2</sub> power cycles due to their low leakage performance [67, 68, 69, 70]. Zakariya and Jahn [67] investigated the effect of highly dense CO<sub>2</sub> and operation close to the critical point. The centrifugal effect introduced by the highly dense CO<sub>2</sub> was found to be beneficial for seal performance, reducing seal leakage at the expense of opening force. It was implied that the seal operating with CO<sub>2</sub> close to the critical point is not detrimental to seal performance. A further parametric study was performed by Zakariya and Jahn [68]. It was found that dry gas seals with a wide dam are preferred, since the leakage is reduced while the change in the lift force is minimal. Moreover, Bidkar et al. [70] performed a fluid, structural, and thermal analysis for a hydrodynamic face seals. Reynolds equation was found to be not applicable for the modelling of turbulent flow within the CO<sub>2</sub> seal. Only a one-way coupling strategy is implemented in his analysis. Thatte and Dheeradhada [69] performed a coupled analysis of dry gas seal using sCO<sub>2</sub>, including thermal deformations.

### Bearing

In the small sCO<sub>2</sub> cycle test rig at SNL, a seal is positioned upstream of the foil bearing. A scavenge pump at the downstream of the foil bearing maintains constant pressure in the bearing chamber [8]. The resulting operating conditions (see Figure 1.1) for the foil bearing are around 1.4 MPa

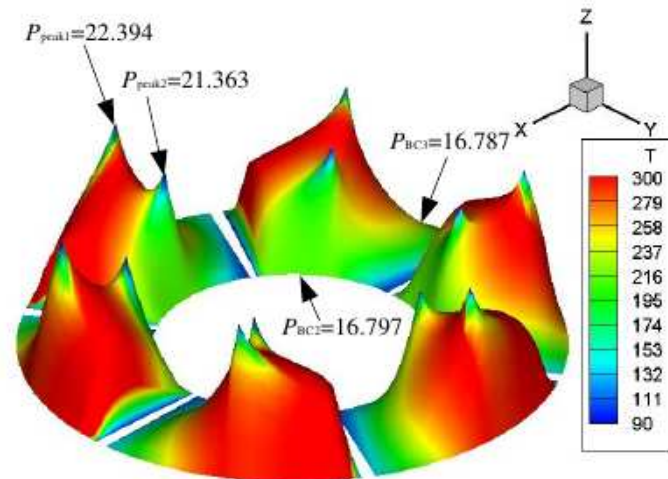


**Figure 2.8:** Bulk film temperature (averaged over film thickness) of loaded bearing overlapped on the pressure profiles for CO<sub>2</sub> with real gas effect at 40 000 rpm, taken from Ref. [71].

and 300 K [7, 8]. It is believed to be a compromise between ensuring a low pressure downstream of the seal, thereby low windage losses and a condition that allows foil bearing design using conventional methods [8]. At this operating condition, CO<sub>2</sub> density is up to 26 kg/m<sup>3</sup>, resulting in Reynolds number larger than 2000 [8], which is different from air bearings (laminar flow). The highly dense gas also results in a larger centrifugal inertia forces compared to air bearing (density is 1.2 kg/m<sup>3</sup>).

Conboy [8] used the modified turbulent Reynolds equation to include real gas effects in foil thrust bearings. They found that turbulent effects can increase the load capacity and friction torque simultaneously. Kim [72] developed a modified three dimensional Reynolds equation for foil journal bearings. Real gas effects, turbulent flow and viscous heating effects are all included in this model, and the performance of foil journal bearings using CO<sub>2</sub> at different rotational speed and conditions was investigated. A more recent work from Xu and Kim [71] investigated the three dimensional performance of a hybrid (hydrostatic and hydrodynamic) thrust foil bearings. Very high temperature increase across the thin film (see Figure 2.8) is obtained when CO<sub>2</sub> is used as the working fluid. This highlighted the importance of accurate thermal prediction.

## 2.3 Experimental Work on Foil Thrust Bearings

Foil bearing are key components for sCO<sub>2</sub> turbomachinery as introduced in Chapter 1. Experiments have been conducted to investigate the steady state and dynamic performances of foil journal and



**Figure 2.9:** Prototype bearing with one top foil removed, taken from Ref. [23].

**Table 2.1:** Geometry and physical parameters for thrust foil bearings in Ref. [26, 73].

Parameters	Magnitude	Parameters	Magnitude
Number of pads	6	Bump foil material	Inconel X-750
Outer diameter	101.6 mm	Bump foil thickness	0.102 mm
Inner diameter	51.0 mm	Bump foil pitch	5.00 mm (averaged)
Pad arc extent	45°	Bump half length	1.60 mm
Pad taper extent	15°	Bump height	0.50 mm
Top foil material	Inconel X-750	Top foil thickness	0.150 mm

thrust bearings. The design, fabrication and performance testing of foil thrust bearings is represented in Ref. [23]. Their prototype foil thrust bearings is shown in Figure 2.9, which consists of six thrust pads. Five non-uniform bump foil strips in the radial direction are mounted underneath the top foil for each pad. The geometry and physical parameters of this prototype are provided in Table 2.1. The side view of one thrust pad is depicted in Figure 2.10. The shape of the runner and the top foil shape form a convergent shape (ramp region), followed by a flat region. The experimentally measured load capacity in terms of friction torque is shown in Figure 2.11. This provides an effective starting point for the development of foil thrust bearings. The prototype is widely used in literature to investigate the performance of foil thrust bearings [73, 74, 75].

Dickman [73] also investigated the steady state performance of foil thrust bearings at different load and rotational speeds. However only repeatability of experiments was assessed, and the uncertainty analysis is missing in his work. The thermal performance of foil thrust bearings was investigated by

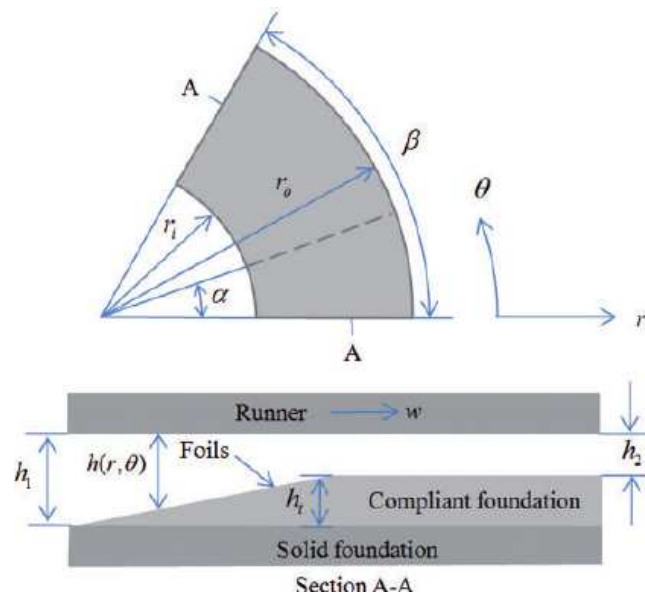


Figure 2.10: Nomenclature for foil thrust bearings, taken from Ref. [76].

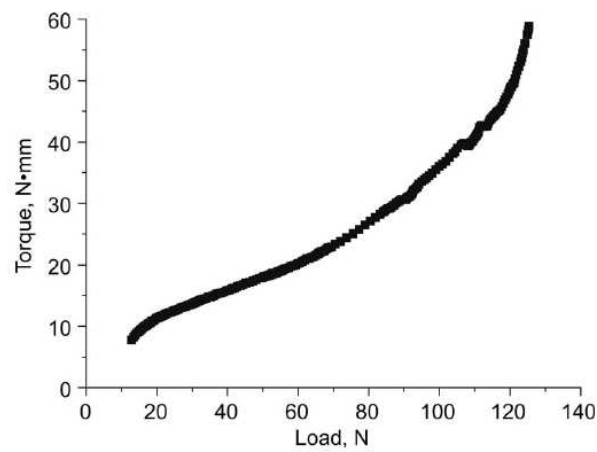
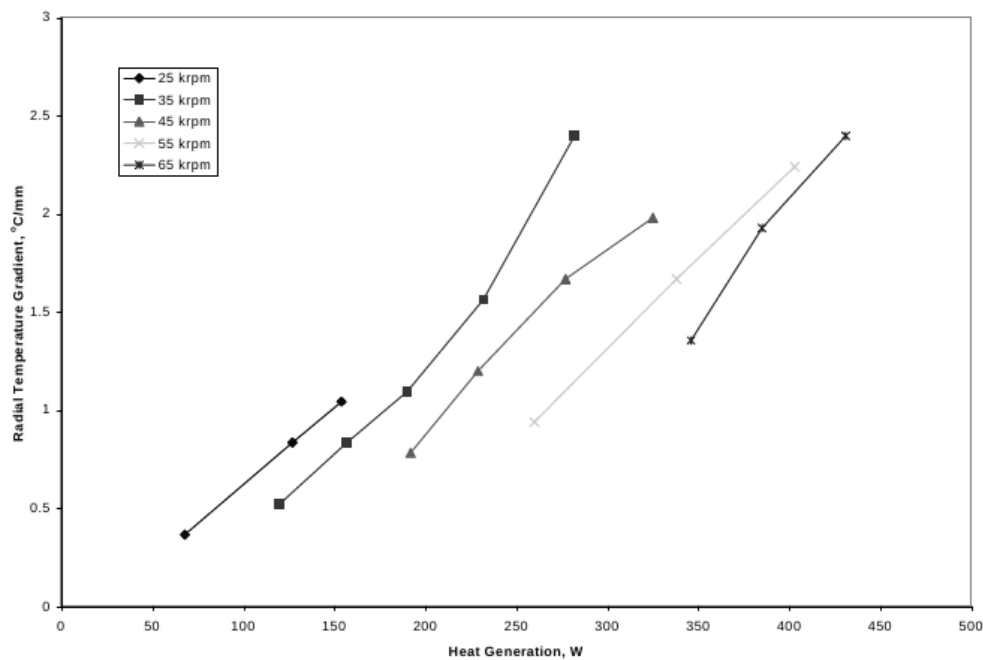


Figure 2.11: Torque versus load at 23 000 rpm, taken from Ref. [23].



**Figure 2.12:** Measured trailing edge temperature gradients, taken from Ref. [77].

Dykas and Radil [77, 78]. Three thermocouples were mounted in a test bearing near the trailing edge at different radial location to calculate the temperature gradient. The results for different rotational speed and heat loss are shown in Figure 2.12. For the experimental work conducted by Dykas et al. [23] and Dickman [73], only the integral values, load capacity and friction torque, were measured. The corresponding bearing clearance, pressure, and temperature distributions are not given. Radil and Zeszotek [79] performed an experimental investigation into the temperature profile of a foil journal bearings. It was found that both journal rotational speed and radial load are factors determining heat generation. The rotational speed played a more significant role on the temperature increase.

Balducci et al. [74] investigated the start-up and shut-down torque, which varies linearly with load and does not depend on the maximum speed. The other important finding from their work is that the thermal regime is significant during the start-up tests. Balducci et al. [75] also studied the dynamic performance of foil thrust bearings by employing an electromagnetic shaker, which was vertically mounted to the upper part of the shaft. The dynamic characteristic of structure and foil bearings were investigated under three different static loads (30 N, 60 N, and 90 N) and excitation frequencies (from 150 Hz to 750 Hz). It was observed that the stiffness increases with the excitation frequency and

static load, while the equivalent viscous damping decreases with the excitation frequency and static load. Kim et al. [80] identified the dynamic characteristic of foil thrust bearings using base excitation. A single degree-of-freedom model was utilised to investigate stiffness, damping, and loss factor (defined by  $\text{damping} \times \text{excitation frequency} / \text{stiffness}$ ) of foil thrust bearings at the different dynamic load and excitation frequency. The same trend of stiffness and damping coefficients with excitation frequency was reported in Ref. [75].

## 2.4 Fluid Simulation for Gas Bearings

Different approaches have been used to simulate gas film. Reynolds equation is widely used to model the fluid flow within foil bearings. This approach has been proven as a suitable tool. In this section, various versions of Reynolds equation and the CFD approach are introduced.

### 2.4.1 Classical Reynolds Equation

Osborne Reynolds was the first to propose a two-dimensional differential equation to solve the pressure distribution within fluid bearings [81]. This equation is a simplified form of the Navier-Stokes equations with several fundamental assumptions:

1. All inertial forces are negligible. This indicates that Reynolds equation is only valid at small Reynolds numbers;
2. The pressure gradient perpendicular to the rotor and stator is small, compared to the axial and circumferential pressure gradients,  $\frac{dP}{dz} = 0$ ;
3. The velocity gradient across the film thickness is largest. Therefore, the velocity gradients in the axial and circumferential direction are neglected,  $\frac{du}{dr} = \frac{du}{d\theta} = 0$ ;
4. The body forces are negligible;
5. The flow is laminar;
6. The fluid density is constant; This assumption holds when oil is the lubricant. However, for gas bearings, the compressible Reynolds equation can be used.
7. The fluid is Newtonian;

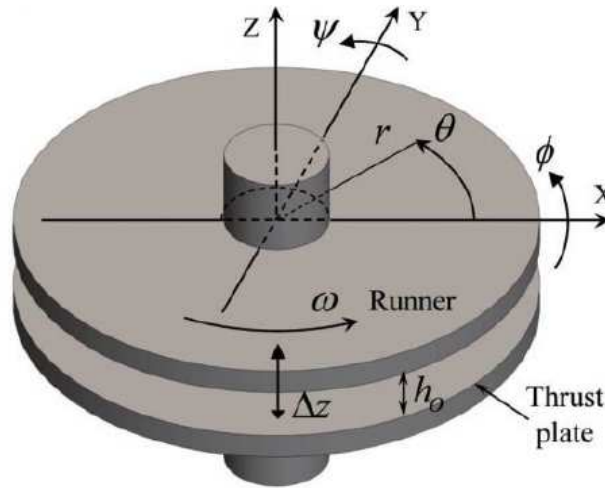


**Figure 2.13:** Coordinate system for small perturbations, taken from Ref. [84].

8. Non-slip boundaries exist at the rotor and stator.

Hence, the three dimensional Navier-Stokes equations are reduced to the two dimensional partial differential Reynolds equation [82],

$$\frac{1}{r} \frac{\partial}{\partial r} \left( r \rho h^3 \frac{1}{\mu} \frac{\partial p}{\partial r} \right) + \frac{1}{r^2} \frac{\partial}{\partial \theta} \left( \rho h^3 \frac{1}{\mu} \frac{\partial p}{\partial \theta} \right) = \Lambda \frac{\partial(\rho h)}{\partial \theta} . \quad (2.1)$$

The detailed derivation process can be found in Bruckner's PhD thesis [82], including equations in Cartesian and Cylindrical coordinates, respectively.

To solve this partial differential equation, the finite difference method is usually utilised. Detailed discretisation procedures can be found in Appendix A. For the iteration procedure, the Gauss-Seidel method, the preconditioned conjugate gradient method, successive over-relaxation method, and the multigrid method can be used. These iteration methods were reviewed and compared by Wang et al. [83]. Once steady state performance is achieved, the load capacity  $F$  and friction torque  $T$  from Reynolds equation are calculated as [84, 85],

$$F = \int_r \int_\theta (p - p_a) dr d\theta , \quad (2.2)$$

$$T = \int_r \int_\theta \left[ \frac{h}{2} \frac{\partial p}{\partial \theta} + \frac{\mu \omega r^2}{h} \right] r dr d\theta . \quad (2.3)$$

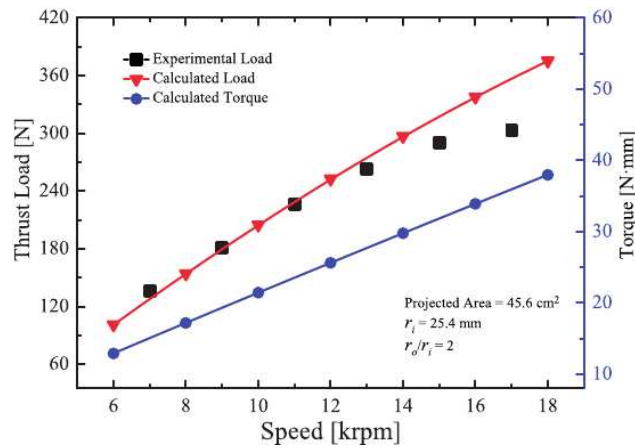


**Figure 2.14:** Comparison between Reynolds equation and experiment, taken from Ref. [76].

For some applications, the dynamic performance of foil bearings including rotordynamic stiffness and damping coefficients is also of interest. The small perturbation approach has been used to obtain dynamic force coefficients [84]. Once the steady state results of pressure distribution and film thickness are obtained, the steady state position of the rotor is perturbed by small translational displacement ( $\Delta z$ ), small rotational displacement ( $\Delta \phi$  and  $\Delta \psi$ ), small translational velocity ( $\Delta \dot{z}$ ), and small rotational velocities ( $\Delta \dot{\phi}$  and  $\Delta \dot{\psi}$ ) as shown in Figure 2.13. The pressure perturbations are then solved. Consequently, the rotordynamic stiffness and damping coefficients are calculated. The detailed procedure can be found in Refs. [84, 86]. In summary, Reynolds equation (Equation 2.1) can be used to calculate the steady state and dynamic performance of foil thrust bearings as long as the flow remains laminar. The comparison of results from Reynolds equation (Equation 2.4.1) and experiment is depicted in Figure 2.14. Good agreement is achieved.

Atmospheric pressure 0.1 MPa and temperature 298 K are usually taken as the operating conditions for air foil thrust bearings [26, 76, 84, 85]. The air density at the operating condition is only  $1.2 \text{ kg/m}^3$ . Reynolds number around 100 is obtained using the bearing geometry in Table 2.1. The non-dimensional pressure distribution (normalised by 0.1 MPa), obtained from Reynolds equation (Equation 2.4.1), is shown in Figure 2.15. The pressure increases due to the convergent shape between the rotor and top foil. The peak pressure occurs at the end of the ramp region. The steady state performance of the foil thrust bearings is shown in Figure 2.16. Under the investigated film thickness and rotational speeds, a maximum load of 200 N is obtained, while the corresponding torque is approximately 28 Nmm (power loss is 147 W). Load and torque have a roughly linear relationship with initial

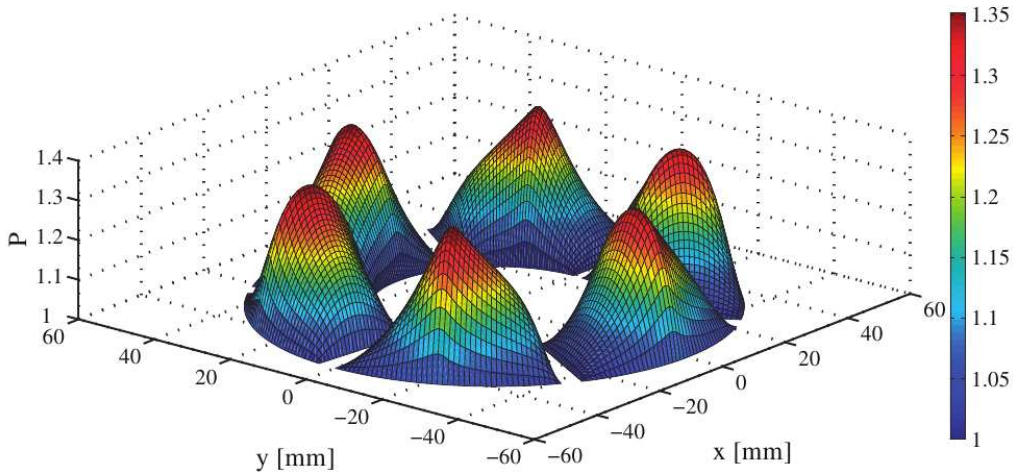


**Figure 2.15:** Non-dimensional pressure distribution of foil thrust bearings obtained from Reynolds equation, taken from Ref. [76].

minimum film thickness as shown in Figure 2.16(a). Both load and friction torque increase with the decreasing film thickness.

## 2.4.2 Turbulent Reynolds equation

The assumptions for Reynolds equation listed in the previous section might not be appropriate for some cases. For example, examination of CO<sub>2</sub> fluid film at SNL reveals Reynolds number above 1600, suggesting turbulent flows. The classical Reynolds equation was modified to include turbulence effect by including the correction factors  $G_r$  and  $G_\theta$ ,

$$\frac{1}{r} \frac{\partial}{\partial r} \left( r G_r \rho h^3 \frac{1}{\mu} \frac{\partial p}{\partial r} \right) + \frac{1}{r^2} \frac{\partial}{\partial \theta} \left( G_\theta \rho h^3 \frac{1}{\mu} \frac{\partial p}{\partial \theta} \right) = \Lambda \frac{\partial(\rho h)}{\partial \theta} . \quad (2.4)$$

Turbulent lubrication is developed from the work of Ng and Pan [87], Constantinescu [88] and Hirs [89]. Constantinescu [88] used the Prandtl mixing length to calculate Reynolds stress tensor. He experimentally showed that at a Reynolds number below 2000, the flow is in a laminar flow regime. For Reynolds numbers (based on film thickness) greater than 2000, turbulence begins to affect the correction factors in an exponential manner, as shown in Figure 2.17. Using the Prandtl mixing length concept, and assuming strong Couette flow, Constantinescu determined the following expressions,

$$G_r = \frac{40.5405}{40.5405 + (k^2 Re_t)^{0.65}} , \quad (2.5)$$

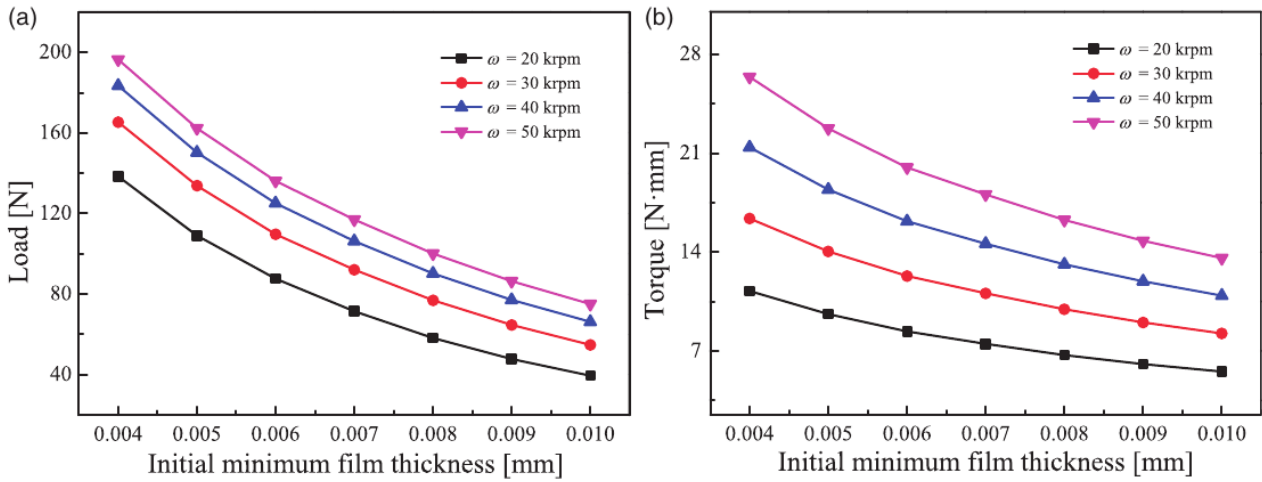


Figure 2.16: Load and torque of foil thrust bearings obtained from Reynolds equation, taken from Ref. [76].

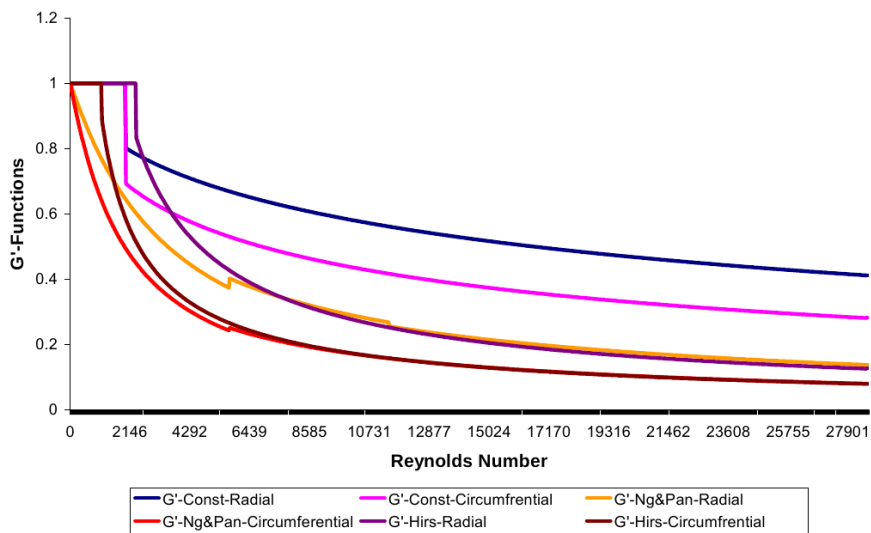


Figure 2.17: A plot of the  $G'$  functions for each of the Ng and Pan [87], Constantinescu [88], and Hirs [89] turbulence models as a function of rotational Reynolds number, taken from Ref. [24].

**Table 2.2:** The Ng and Pan turbulent coefficients for various critical Reynolds numbers. Applicable to Equations 2.8 and 2.9.

Reynolds Number	$K_\phi$	$n_\phi$	$K_r$	$n_r$
$50\,000 < Re_t$	0.0388	0.8	0.213	0.8
$10\,000 < Re_t < 50\,000$	0.025	0.84	0.0136	0.84
$5000 < Re_t < 10\,000$	0.025	0.84	0.0088	0.88
$Re_t < 5000$	0.0039	1.06	0.0021	1.06

$$G_\phi = \frac{22.6415}{22.6415 + (k^2 Re_t)^{0.725}} \quad , \quad (2.6)$$

where:

$$k = 0.125 Re_t^{0.007} \quad . \quad (2.7)$$

Ng and Pan [87] utilised the concept of the law of the wall for turbulent shear flows to calculate turbulent stresses as the function the mean velocity gradient. To obtain the eddy diffusivity, they used Reichardt's formula and experimentally obtained the necessary constants for various critical Reynolds numbers. Ng and Pan's turbulence model is expressed by,

$$G_r = \frac{12}{12 + K_r Re_t^{n_r}} \quad , \quad (2.8)$$

$$G_\phi = \frac{12}{12 + K_\phi Re_t^{n_\phi}} \quad . \quad (2.9)$$

The constants  $K$  and  $n$  are defined as a function of Reynolds numbers, as detailed in Table 2.2.

A further model by Hirs [89] adopts a bulk flow approach that requires no physical representation of the turbulent transport mechanism. One advantage to such an approach is that the unknown coefficients can be determined from bulk-flow measurements without determining the velocity profiles. The Hirs model is expressed below for three different Reynolds number ranges for smooth surfaces,

$$G_r = \frac{306.122}{Re_t^{0.76}} \quad \text{if } Re_t < 10^5 \quad , \quad (2.10)$$

$$G_r = 1.0 \quad \text{if } Re_t < 2060 \quad . \quad (2.11)$$

$$G_\phi = \frac{174.672}{Re_t^{0.75}} \text{ if } Re_t < 10^5, \quad (2.12)$$

$$G_\phi = 1.0 \text{ if } Re_t < 977. \quad (2.13)$$

Among these turbulence correction factors, shown in Figure 2.17, it was experimentally confirmed that the Hirs model is the most accurate [90].

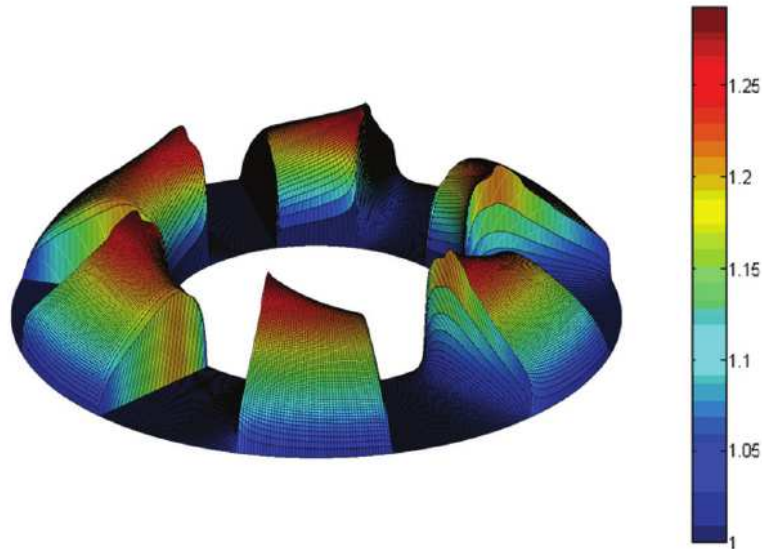
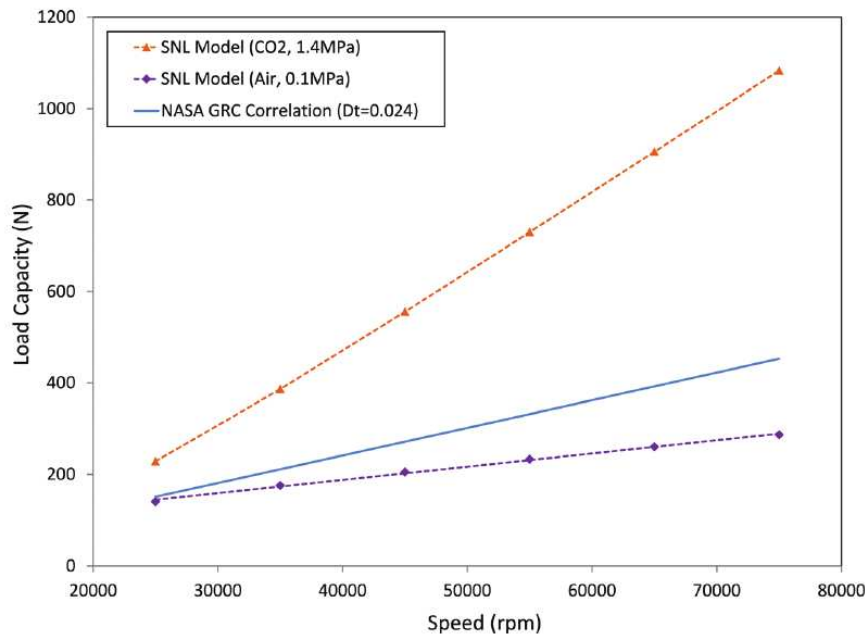


**Figure 2.18:** Non-dimensional pressure distribution of foil thrust bearings obtained from turbulent Reynolds equation, taken from Ref. [8].

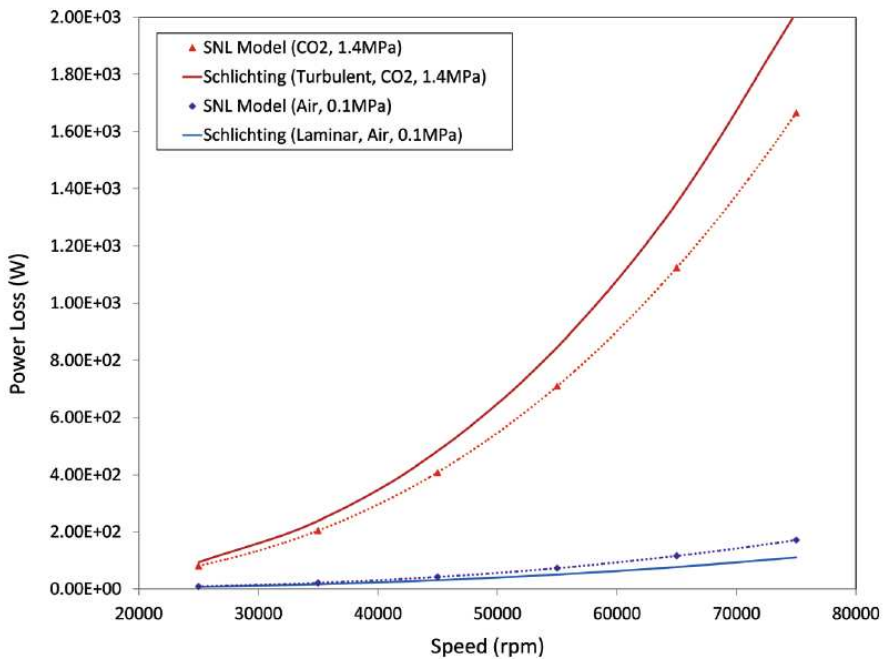
The pressure of 1.4 MPa and temperature of 300 K are used as the ambient condition for foil thrust bearings operating with CO<sub>2</sub> at SNL. The non-dimensional pressure distribution (normalised by 1.4 MPa), using turbulent Reynolds equation, is illustrated in Figure 2.18. A similar pressure distribution is obtained compared to Figure 2.15. Again, the peak pressure occurs at the end of the ramp region. The steady state performance is also plotted in Figure 2.19, including load and power loss. Here, the initial minimum film thickness is set as 5 μm. It is found that the maximum load can be over 1000 N, but a very high power loss, around 1800 W, is obtained.

### 2.4.3 Computational Fluid Dynamics

Due to fluid property of CO<sub>2</sub>, some assumptions for Reynolds equation outlined in Section 2.4.1 might not be appropriate. For example, constant density, negligible inertia forces. It is recommended that a more comprehensive approach like CFD can be utilised to investigate CO<sub>2</sub> foil bearings. Chen and



(a) Load.



(b) Power loss.

**Figure 2.19:** Load and power loss of foil thrust bearings obtained from turbulent Reynolds equation, taken from Ref. [8].

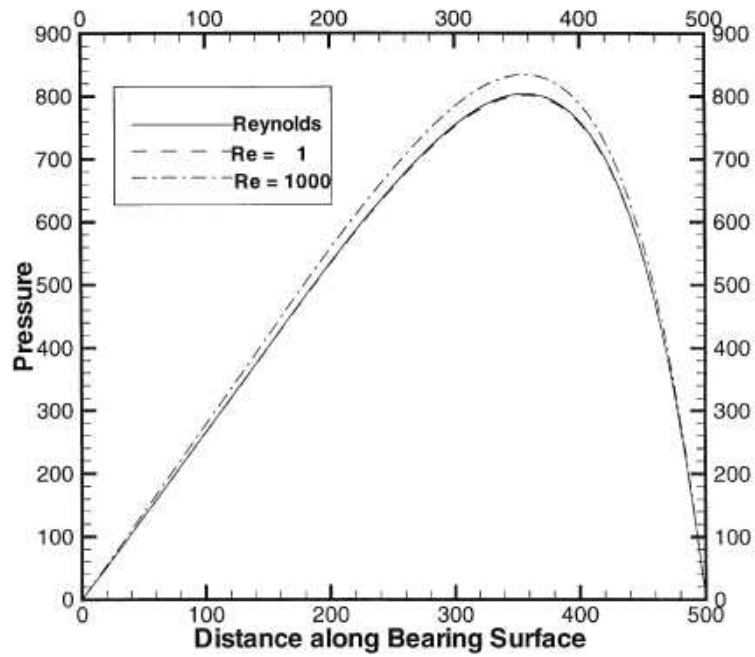
Hahn [91] investigated the suitability of CFD for solving steady state performance of hydrodynamic bearings. Various geometries were investigated including step pad bearings, slider bearings, journal bearings and squeeze-film dampers. The suitability of neglected inertia in the derivation of Reynolds number were investigated, which is found to be appropriate. The results from Ref. [91] for slider and step bearings are shown in Figure 2.20. Good agreement is achieved at the very low Reynolds number of 1, however differences are observed at the high Reynolds number (1000). Brajdic-Mitidieri [92] validated CFD as a suitable tool for predicting the fluid flow in simple converging bearings. Guo et al. [93] applied CFD to investigate the steady state and dynamic performances of hydrodynamic, hydrostatic and hybrid bearings. Reasonable agreement was obtained between CFD and Reynolds equation.

For some cases, the bearing geometry is either too complex or cavitation is presented. Papadopoulos et al. [94] studied the flow pattern and performance of a dimpled parallel thrust bearing by CFD. Zhang et al. [95] designed a hydrodynamic water-lubricated step thrust bearings using CFD in conjunction with the Zwart-Gerber-Belamri cavitation model. Parametric studies were undertaken with different pad dimensions, step heights, step positions, water film thicknesses and rotational speeds.

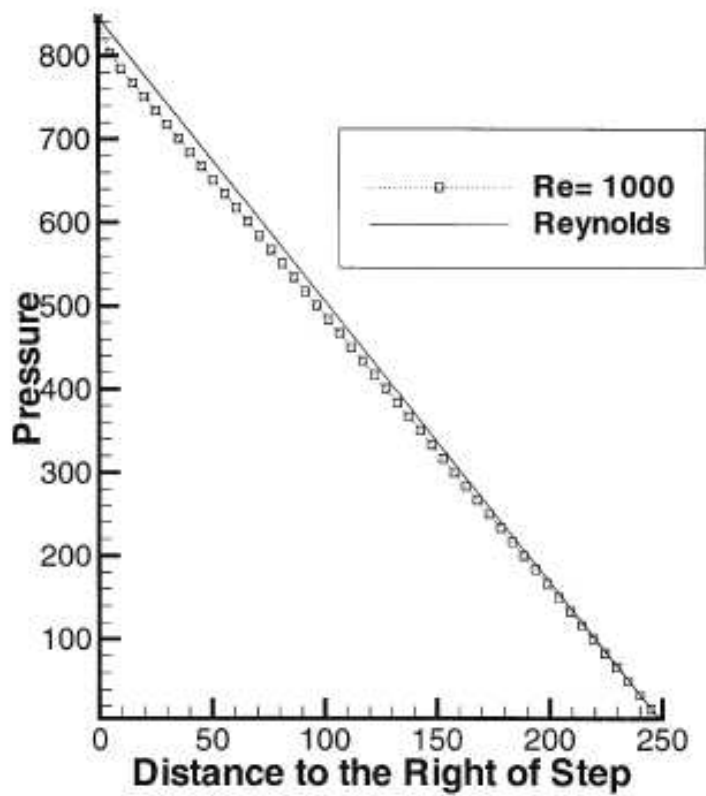
In literature, good agreement is obtained between CFD and Reynolds equation [91, 92] at low Reynolds number (see Figure 2.20). The results also confirmed the assumptions of Reynolds equation and confirmed that Reynolds equation is an adequate approach to investigate gas bearings performance, when the studied bearing geometry is simple. However, the difference between CFD and Reynolds equation is observed at large Reynolds number.

## 2.5 Structural model

In a typical configuration of foil bearings, the top foil is affixed to the bearing housing on one side, and on the opposing side it sits at the height of its bump understructure. A partially ramped profile is formed. During the hydrodynamic action, the initial top foil shape is deflected due to pressure increase within the foil bearing. This deformation has to be modelled since it is a significant fraction compared to the clearance between top foil and stator.



(a) Slider bearings.



(b) Step bearings.

**Figure 2.20:** Pressure distribution in a long slider bearing using Reynolds equation and CFD, taken from Ref. [91].

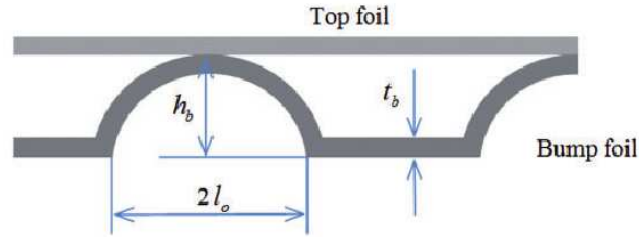


**Figure 2.21:** Nomenclature for bump strips, taken from Ref. [76].

The deforming parts are top and bump foils. A variety of structural deformation models exist in literature for journal and thrust foil bearings. The bump foil is taken as a spring-like structure with a certain stiffness to support the top foil. The nomenclature for a bump strip is depicted in Figure 2.21. Heshmat [11] was among the first researcher to analyse foil bearings, and to propose a simplified method (see Equation 2.14) to calculate the equivalent stiffness of the bump foils. In his model, the entire top foil was regarded as a single element,

$$\alpha = \frac{2 p_a s}{h_b E} \left( \frac{l_0}{t_b} \right)^3 (1 - \nu^2) . \quad (2.14)$$

Iordanoff [96] proposed a more advanced structural model that divided the bump foil into two categories: fixed-free and free-free. For the welded bump, a fixed-free arrangement is assumed, while a free-free end is applied for the free bumps. The local compliance for these two bump types are defined as,

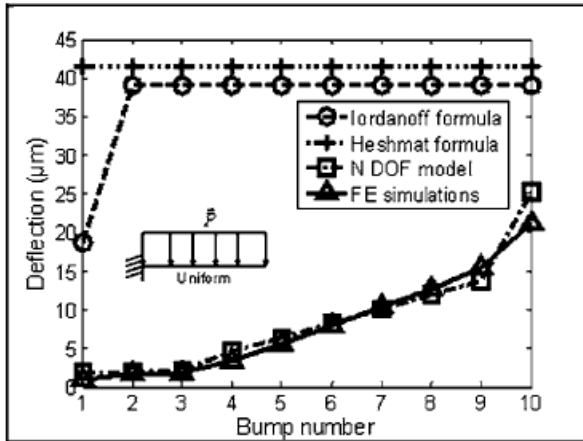
$$\text{Fixed-free end: } s = \frac{12 l_0^3 i J (1 - \nu^2)}{E e^3 \sin^3(\alpha/2)} , \quad (2.15)$$

$$\text{Free-free end: } s = \frac{6 l_0^3 i I (1 - \nu^2)}{E e^3 \sin^3(\alpha/2)} . \quad (2.16)$$

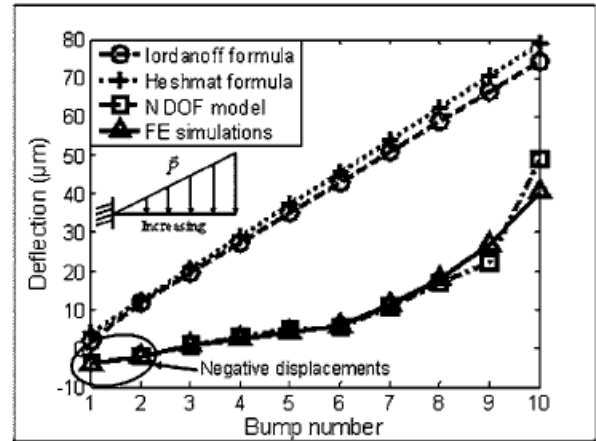
The definition of each parameter can be found in Ref. [96]. This approach is widely used in literature [26]. However, it was found that these models tend to underestimate the magnitude of the bump foil stiffness, since the interactions between bumps are not considered. Le Lez et al. [97] proposed a model that described the foil bump structure as a multi-degree of freedom system of interacting bumps. Good agreement exists when compared with finite element simulations. However, a large difference exists between this model and the previous analytical models presented by Heshmat [11] and

Iordanoff [96] (see Figure 2.22), especially at high load condition. For all test cases in Figure 2.22, the total equivalent force corresponds to a uniform pressure of 200 000 Pa. Hryniewicz et al. [98] proposed a new two-dimensional bump foil model. The model was able to consider the detailed geometry of bump foil structure and the interaction between bumps. Feng et al. [99] developed a link-spring model to calculate the stiffness. Using the link-spring model, each bump was simplified to two rigid links and a horizontally spaced spring. The stiffness was then determined from Castigliano's theorem. Gad et al. [100] also developed a structural stiffness model for Generation II foil thrust bearings. In his study, the lateral deflection of the flat segment between bumps was investigated. His model considers the interaction between bumps and the friction between the bump foil and the surrounding structure was considered. A comparison of the various bump foil models is shown in Figure 2.23 [100]. The analytical model from Gad et al. [100] provides the close agreement with finite element analyses.

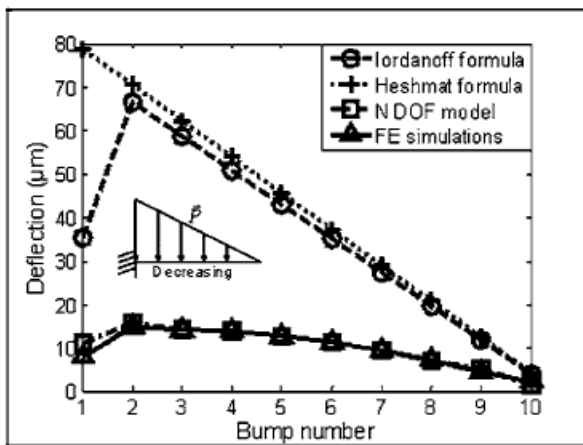
Experiments were also conducted to test the structural stiffness of foil bearings. Rubio and San Andrés [101] tested the structural stiffness of a commercial foil bearing. It was found that the stiffness of a single bump was most sensitive to the dry-friction coefficient, the bump length, and the bump end conditions. Furthermore, the structural stiffness increases as the bump foil deflection increases, which was taken as the hardening effect. These phenomena correspond to the analytical model from Le Lez et al. [97], Hryniewicz et al. [98], Feng et al. [99], and Gad et al. [100]. In addition, bump and top foils provide coulomb damping due to the relative sliding, which is essential for stability of the machine [102]. However, little work has been done to characterise the damping coefficients of bump foils. A theoretical model was firstly developed by Ku and Heshmat [103] to calculate equivalent viscous damping coefficients of a bump foil strip. This coefficient was determined based on the area of a closed hysteresis loop of the journal center motion. The same approach was also applied by Le Lez et al. [104] to investigate the dynamic stiffness and damping of a single bump of the foil structure. Experiments undertaken by Balducchi et al. [75] provided the frequency dependent structure stiffness and damping coefficients at different load conditions as shown in Figure 2.24.



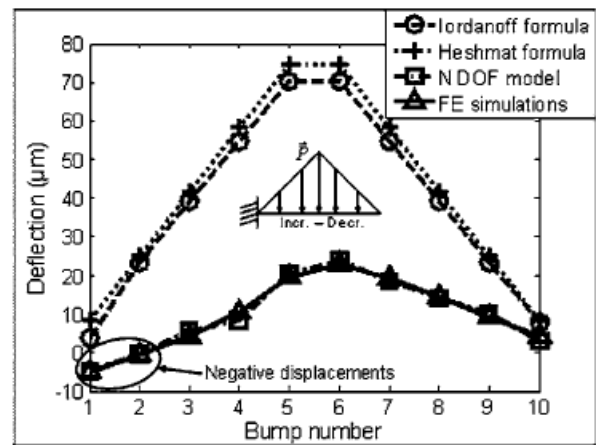
a) Uniform load distribution



b) Increasing load distribution



c) Decreasing load distribution



d) Increasing-decreasing load distribution

Figure 2.22: Bump deflection for various load distributions, taken from Ref. [97].

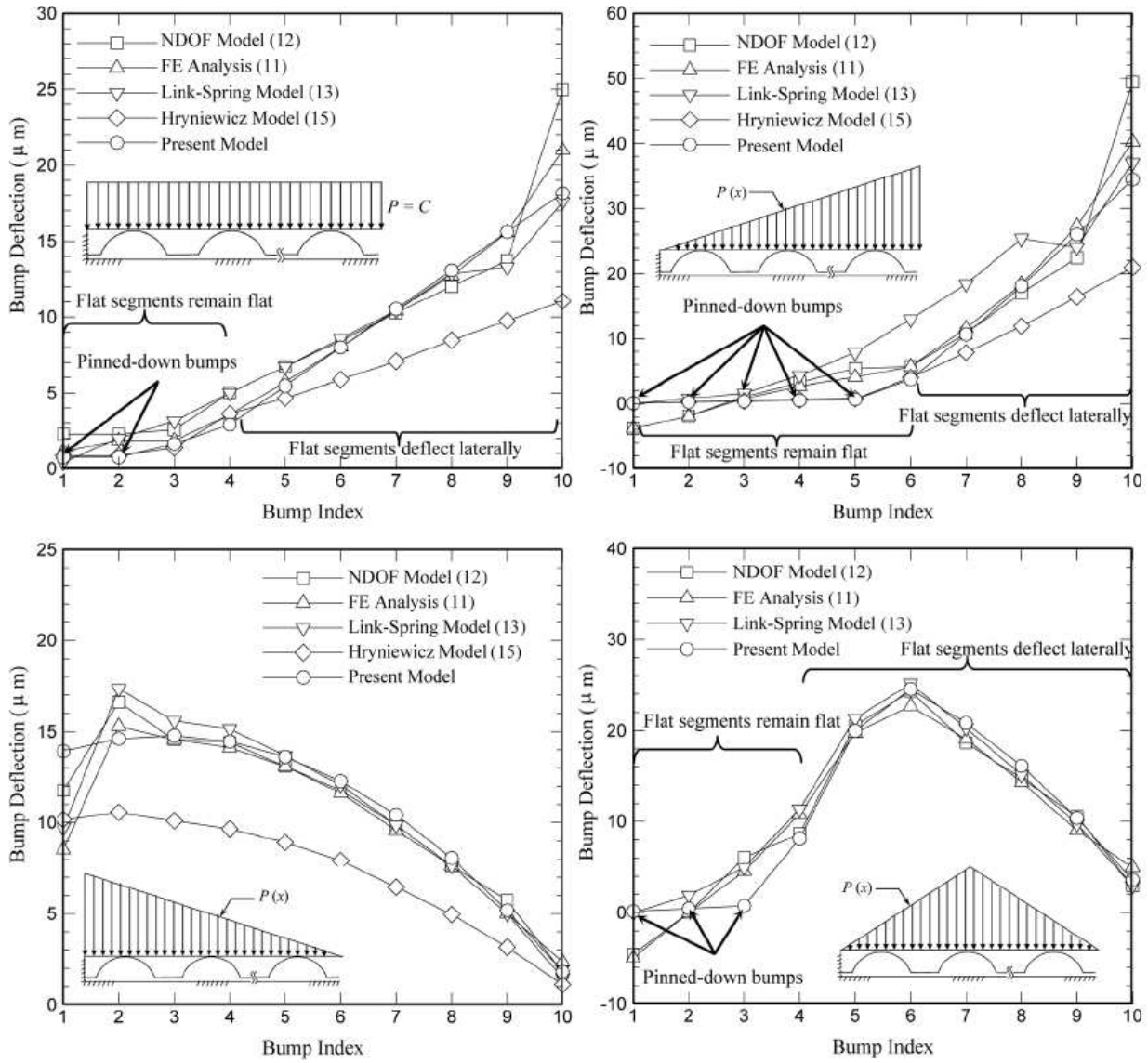
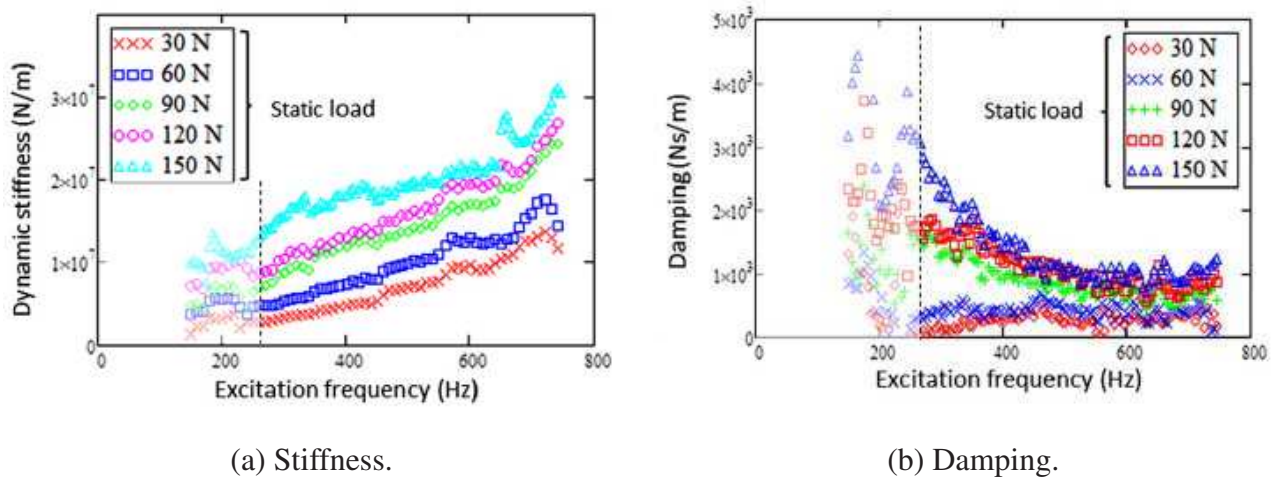


Figure 2.23: Bump deflection for various load distributions, taken from Ref. [100].



**Figure 2.24:** Structural stiffness and damping, taken from Ref. [75].

For the top foil, two-dimensional shell or one-dimensional beam-like models were developed by San Andrés and Kim [105]. These models allowed sagging between bumps. Advanced two-dimensional plate models were applied by Bruckner [82] and Lee and Kim [106] in simulating deformation of thrust bearings. In addition, coupling to the commercial structural-analysis software (ANSYS) was also considered to improve the accuracy of the deformation, but with an associated increase in computational cost [94, 107]. More recently, Lehn et al. [108] proposed a new approach that models top and bump foils as a two-dimensional thick shell. The shear, membrane, and bending effects are all considered. This model provides an accurate prediction for the structural deformation within foil bearings and shows good agreement with finite element simulations as shown in Figure 2.25.

## 2.6 Thermal Performance

While there are many inherent advantages to foil bearings, there are also several limitations. The most important problems during experiments at high speed are high local temperatures and temperature gradients, which causes thermal runaway of foil bearings [7]. This is due to the weak conduction rate of the thin foil structure and low heat capacity of air. The small contact areas between top foil and bump foils and low heat capacity prevent conductive or convective heat removal from the fluid film. Hence, the temperature distribution within foil bearings has to be carefully considered in design, particularly for bearings operating with high rotational speed or high load.

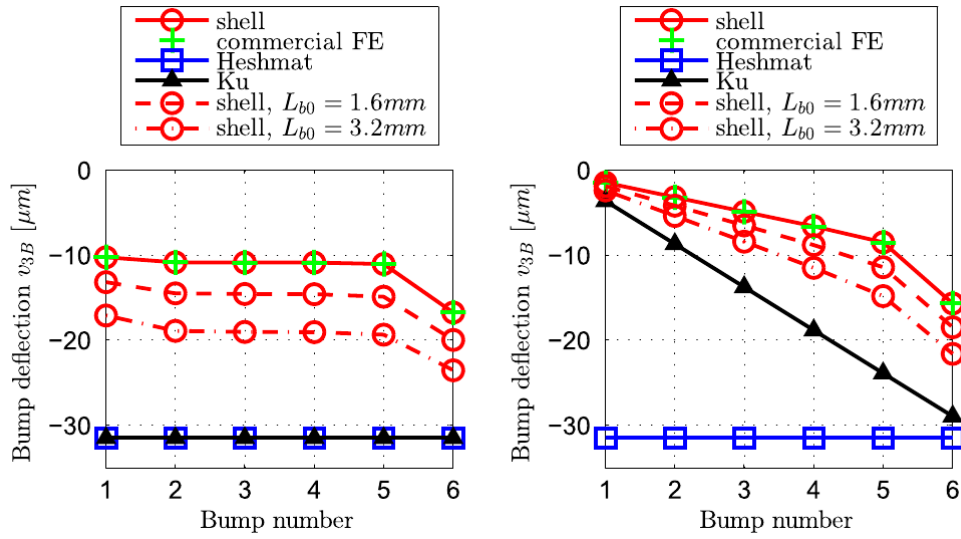
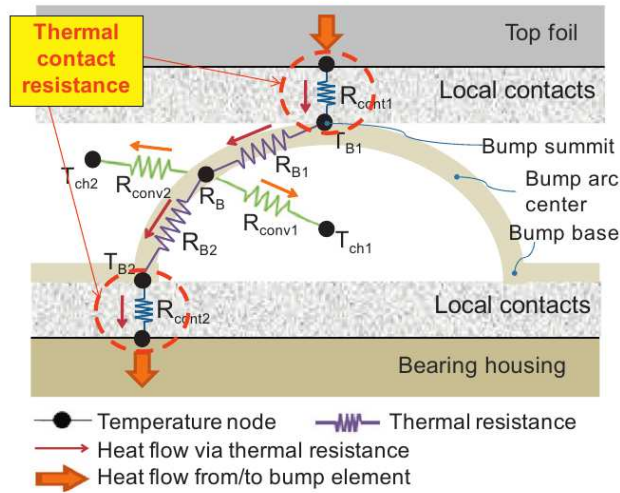


**Figure 2.25:** Vertical deflection of the bump top points for friction coefficients 0.0 and 0.2 (right), taken from Ref. [108].

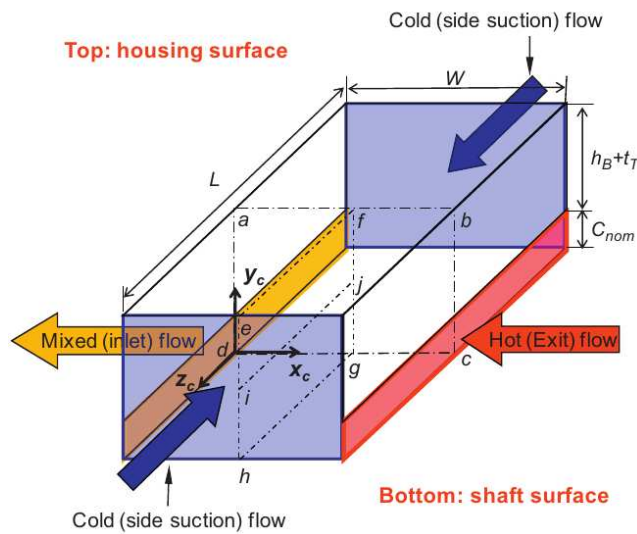
Salehi et al. [110] performed the first study to model and characterise thermal properties of gas foil journal bearings. The Couette flow approximation to the energy equation was implemented with the compressible Reynolds equation. This simplified method provides a reasonable agreement with experimental data, with a maximum over-prediction of 19%. Sim and Kim [109] presented a thermo-hydrodynamic model that accounted for the thermal contact resistance between the top foil, bump foil and bearing housing as shown in Figure 2.26(a). Additional thermal resistances were included between top and bump foils, and bump foil and bearing housing. The mixing effect between the leading and trailing edges of top foils was also investigated. The suction flow mixing ratio at the groove region was obtained and then applied to their model. This suction flow mixing ratio  $\lambda_s$  was defined as the ratio of the cold suction flow rate to the mixed inlet flow rate,

$$\lambda = \frac{\dot{m}_{suc}}{\dot{m}_{inlet}} . \quad (2.17)$$

It was noted that a large mixing ratio provides an effective cooling mechanism in the mixing chamber. The mixing chamber is the groove region between the leading and trailing edges of the top foil. This mixing model was also applied in Ref. [111]. In this paper, the computational domain was expanded to the surrounding structures including two plenums, bearing sleeve, housing, and rotor



(a)



(b)

**Figure 2.26:** (a): Thermal resistance at the bump contacts to the top foil and the bearing housing, along with the thermal resistance model of a bump arc, (b): simplified CFD model of an inlet mixing chamber, taken from Ref. [109].

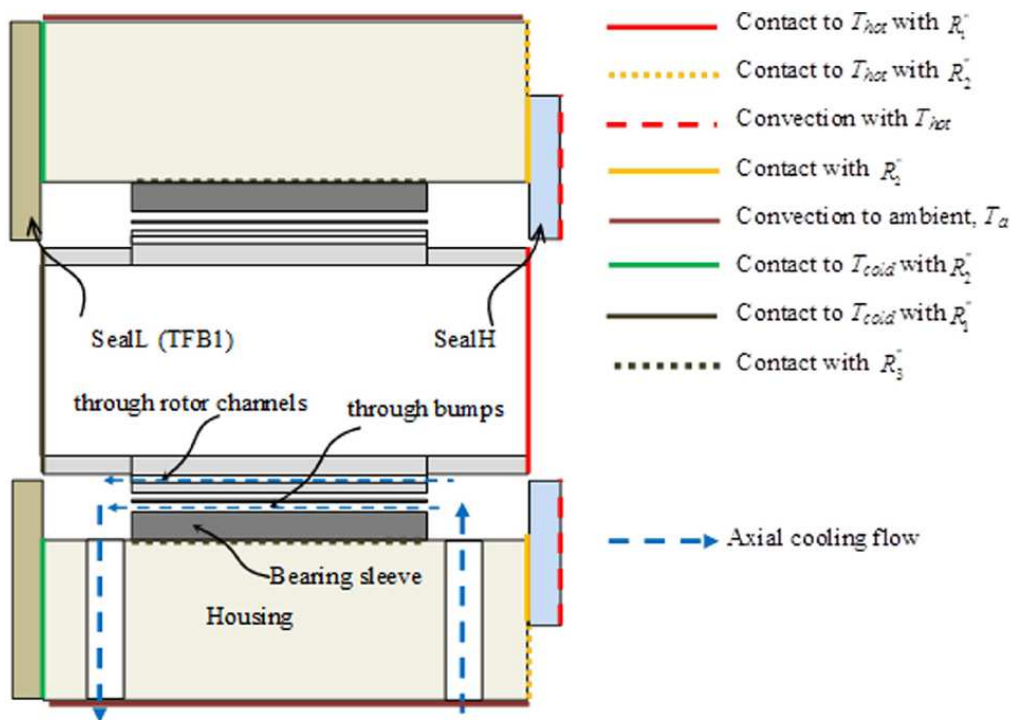


**Figure 2.27:** Simplified thermal domains of the surrounding structures around the radial foil bearing close to turbine and thermal boundary conditions, taken from Ref. [111].

exposed to the plenums shown in Figure 2.27. In order to maintain temperature at the rotor and top foil below 300 °C, cooling air must be provided. The feasibility and effectiveness of radial injection cooling were experimentally tested by Shrestha et al. [112]. They concluded that radial injection cooling can provide a more uniform sleeve temperature in the circumferential direction and a smaller axial gradient of shaft temperature compared to an axial cooling strategy.

The aforementioned work is for the thermo-hydrodynamic modelling of foil journal bearings. Little work had been undertaken to model the temperature field for foil thrust bearings. The Couette flow approximation of the energy equation from Salehi et al. [110] was used by Gad and Kaneko [85] to predict the temperature distribution for air foil thrust bearings. Lee and Kim [113] conducted a three-dimensional thermo-hydrodynamic analysis of Raleigh step air foil thrust bearings with a forced air cooling and the optimum cooling air pressure was found for the reference simulation condition.

DellaCorte et al. [114] reported a reduction of 30 % in load capacity for a tested gas foil bearing when the operating temperature increases from 25 °C to 650 °C. This reduction is attributed to the structural deformation due to thermal stress and centrifugal growth. In this way, this deflection has to

be accounted in accurate performance prediction of foil bearings. Typically, linear thermal expansion theory is applied to calculate the thermal deflection [113, 115, 116].

A numerical thermo-elastohydrodynamic analysis of a novel air radial foil thrust bearing was reported by Lee and Kim [116]. At a rotational speed of 50 000 rpm and a load of 200 N, the maximum temperature rise was approximately 70 K for a case where cooling flow is prescribed. However, for typical foil journal or thrust bearings, there is no pressure gradient between the inner and outer radii, which results in no forced cooling flow through the bump foils. Therefore, the temperature increase in typical foil bearings, recirculating coolant by natural pumping, can be much higher than the value reported in Ref. [113]. The turbulent thermo-elastohydrodynamic analyses of hybrid thrust bearings and journal bearings with CO<sub>2</sub> was conducted by Xu et al. [71] and Kim [28]. A high temperature increase was observed in their simulations. In this case, the thermal effect on the performance of foil thrust bearings has to be considered.

## 2.7 Gap in Literature

At the start of this Chapter we discussed foil bearings as the critical components for sCO<sub>2</sub> turbomachinery systems. We then presented experimental studies and different modelling approaches, including Reynolds equation and its medication for turbulent flow, and CFD for foil bearings. We also highlighted the importance of thermal modelling for the operation of foil bearing. Several research questions remain:

- Is Reynolds equation still applicable for foil bearings with the highly dense CO<sub>2</sub>?
- How does the new working fluid CO<sub>2</sub> influence foil bearing operation, including steady state (load and power loss) and dynamic (stiffness and damping) performances?
- Are temperature distributions affected and what are good cooling strategies?

To close this gap in literature, we now begin investigating the performances of foil thrust bearings with CO<sub>2</sub> using the high-fidelity multiphysics simulation tools. This approach allows us to explore that are not accounted for by Reynolds equation.



# Fluid Simulations

---

## 3.1 Introduction

Despite the strong interest in utilising foil bearings for  $s\text{CO}_2$  cycles, little research has been done on developing bearings for this application. The bearings, at the core of the turbomachinery system, play an essential role for the design of turbomachinery components, and should be carefully studied and designed. When used as the working fluid, high pressure supercritical  $\text{CO}_2$  is far more dense than air, less viscous, and can be a highly non-ideal gas. These factors present challenges when predicting the performance of foil bearings. There is the potential for turbulent flow, highly compressible flow, non-linear thermodynamic properties and significant fluid inertia due to high density and high speed operation. The conventional Reynolds equation, or its modifications, might not be adequate to account for all these effects simultaneously. The simulation of foil bearings is complex, and consists of three aspects: fluid flow, structural deformation and heat conduction. In this Chapter, the development of the in-house fluid solver Eilmer for simulations of flow within foil bearings is described. Section 3.2 describes the basic structure of the in-house CFD code Eilmer [117]. The modifications of Eilmer for laminar and turbulent simulations and the corresponding validation cases are documented in Sections 3.3 and 3.4, respectively.

## 3.2 Description of Fluid Solver

In order to accurately predict the fluid performance within foil bearings for  $s\text{CO}_2$  cycle applications, three dimensional flow simulation is selected over conventional approaches using the two-dimensional Reynolds equation. For the simulation of the fluid domain in foil bearings, the compressible flow solver, Eilmer (written in C++), developed at The University of Queensland [117, 118] is used. For

much of the code's history, it has been used to simulate hypersonic flows and, more recently, it has been extended to turbomachinery flow fields [119]. Eilmer is an integrated collection of programs that solves the compressible Navier-Stokes equations on multi-block structured grids to provide time-accurate flow simulations. The governing equations are expressed in integral form over cell-centred finite-volume cells, with the rate of change of conserved quantities in each cell specified as a summation of the mass, momentum and energy fluxes through the cell interfaces. Detailed description of Eilmer can be found in Appendix B.

The governing equations are closed using equation of state. Eilmer has models for gases with constant specific heat, thermally perfect gases and real gases. For real gas properties of  $\text{sCO}_2$ , a real gas equation of state is implemented directly in the computation. Alternatively, a look-up table approach is also implemented. For the look-up table implementation, a thermodynamic mesh based on temperature  $T$  and density  $\rho$  is generated prior to the simulation with the NIST database REFPROP [120]. During simulation, a bilinear interpolation method is used to calculate the thermodynamic properties from the tabulated data. This reduces the computational cost significantly and was found to be 15 times faster than executing REFPROP equation of state functions directly, with no reduction in solution accuracy.

### 3.3 Modification of Fluid Solver for Laminar Simulations of Foil Bearings

Eilmer was developed for the high-speed compressible flow within the hypersonic regime [117]. To simulate fluid flow with foil bearings using Eilmer, several new features were added into the solver. This section discusses the additions for the laminar simulations of foil bearings.

#### 3.3.1 Moving Wall Boundary Condition

The first part of the work is to implement a moving wall boundary condition for the rotor in foil bearings. This implementation is straightforward, the translational or/and rotational velocities are set at the boundary interfaces directly, while other parameters are the same as for conventional wall boundaries.

### 3.3.2 Periodic Boundary Condition

Foil thrust bearings typically consist of several thrust pads, only one thrust pad is simulated to save on computational cost. In this case, a periodic boundary condition is required to exchange flow conditions. For the scalar variables (pressure and temperature), the parameters are swapped directly between the connected periodic boundary faces. However, for the vector parameters, a helper function is implemented to rotate the vectors.

### 3.3.3 Reconstruction

A non-zero mass flux through wall boundaries is obtained when prescribing the wall boundaries to curved faces. This is identified as a code bug during the reconstruction process. The reconstruction is to obtain the inviscid fluxes at cell interfaces, which is done by evaluating the left and right values at a cell interface in the one-dimensional direction [121]. The non-zero mass flux is attributed to the use of the cell centre data in the global frame of reference. Part of source codes for these modifications can be found in Appendix The bug is fixed by reconstructing in the local frame of reference.

### 3.3.4 Taylor-Couette Flow

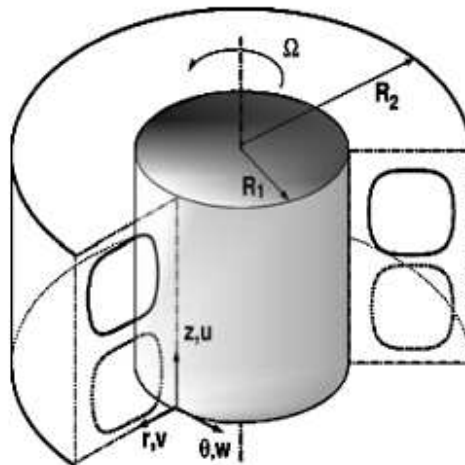


**Figure 3.1:** Computational domain for Taylor-Couette flow, taken from Ref. [122].

Taylor-Couette flow is used as the first test case to verify the moving wall as well as periodic boundary conditions. Several examples of compressible Taylor-Couette flow from Ref. [122], an annulus with inner radius 215.5 mm and gap width 3.1 mm are selected. The axial extent of the

**Table 3.1:** Parameters for simulations, used match the experimental conditions as reported in Ref. [122].

Case	Low pressure	Intermediate pressure	High pressure
Pressure, Pa	10	100	1000
Rotor Temperature, K	344	348	351
Stator Temperature, K	344	350	366
Taylor Number	1.1	12	105

annulus is 5 times the gap width. The computational domain is shown in Figure 3.1. The outer cylindrical surface (the housing) of the annulus is fixed and the inner surface (the rotor) is moving with a rotational speed of 27 600 rpm. Three different pressures are simulated to cover a range of cases, with and without Taylor vortices. Other parameters used for the simulations are summarised in Table 3.1.

Taylor number is commonly used to define different flow states, for incompressible flows in rotating environments, a common form of the Taylor number is,

$$Ta = \frac{U_i d}{\nu} \sqrt{\frac{d}{R_i}}, \quad (3.1)$$

where  $d$  denotes with width of the gap,  $R_i$  the inner radius, and  $U_i$  the peripheral velocity of the inner cylinder.

For the low pressure case with Taylor number less than 41.3 (critical Taylor number), the expected velocity profile is approximately linear across the narrow gap, and the temperature profile has a parabolic shape with maximum temperature near the centre of the gap. Figure 3.2 shows the results of velocity and temperature for different methods. The apparent difference is caused by the slip-wall boundary condition modelled in DSMC method from Ref. [122]. A no-slip boundary condition is used by Eilmer.

For the intermediate pressure case, shown in Figure 3.3, similar results of temperature and tangential velocity exists for Eilmer and other codes [122]. The Taylor number in this case is 12 and no vortices are expected. The profile of tangential velocities is approximately linear and the temperature profile is parabolic. The agreement between numerical schemes is good. In the low-pressure cases, where the Knudsen number is about 0.1, the velocity profiles exhibit increased gradients near the wall

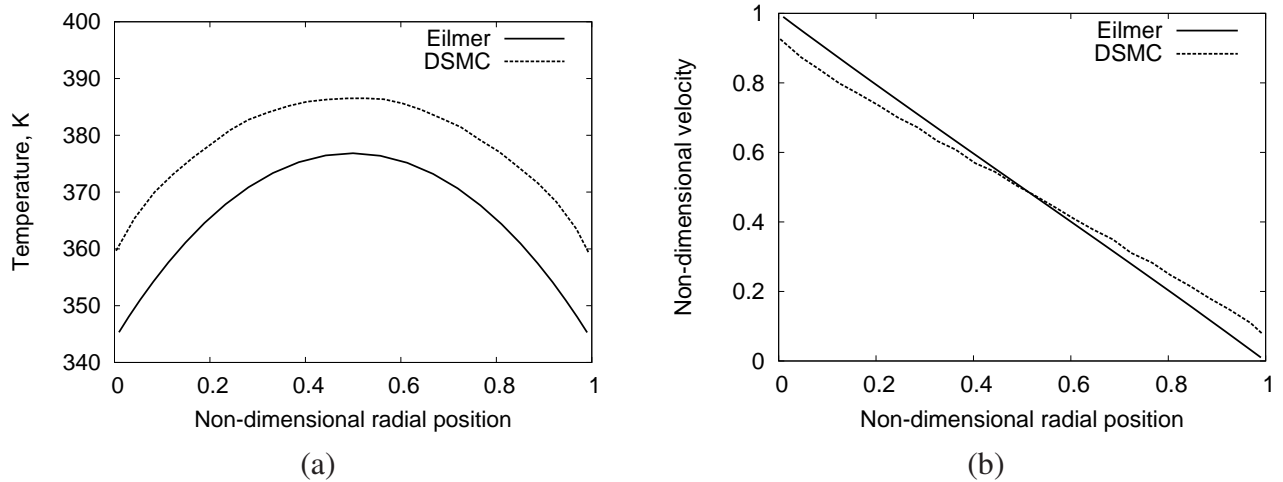


**Figure 3.2:** Comparison of temperature (a) and axially averaged velocity (b) profiles in radial direction at low pressure condition.

surfaces and velocity slip at the 10% level. However, as the Knudsen number decreases to about 0.01 for the intermediate pressure cases, the DSMC simulations show that the velocity profile is nearly linear, and the velocity slip is an order of magnitude less than at the low pressures. This verifies that Eilmer can simulate Taylor-Couette flow with the modifications.

For the high pressure case, the Taylor number has exceeded a critical value, making the flow fully three dimensional. Schlichting [123] suggested that in incompressible flow for Taylor number in ranges between 41.3 and 400, laminar flow with Taylor vortices exists. In this range, the flow can be further characterised as axisymmetric Taylor vortices, wavy Taylor vortices and others. However, the Taylor number for the transition from axisymmetric Taylor vortices to wavy vortices is not firmly established. For instance, the transition is theoretically predicted to occur at  $\frac{T}{T_{crit}} = 1.1$  for aspect ratio  $\eta = 0.85$  for infinitely long cylinders [124, 125], whereas experiments indicate a range of higher values between 1.14 and 1.31 for  $\eta=0.80-0.90$ , depending on experimental conditions [126].

For the high pressure case, the ratio of Taylor number to critical Taylor number is 2.22, and the flow will eventually evolve into unstable wavy vortices as shown in Figure 3.4. The simulation in Ref. [122] is performed with 2D axisymmetry, therefore a stable axisymmetric vortices is obtained. Figure 3.4 recorded temperature and pressure variations at the circumferential angle of  $0^\circ$  with simulation time in Eilmer (three dimensional), where the temperature and pressure will oscillate with a certain frequency, eventually.

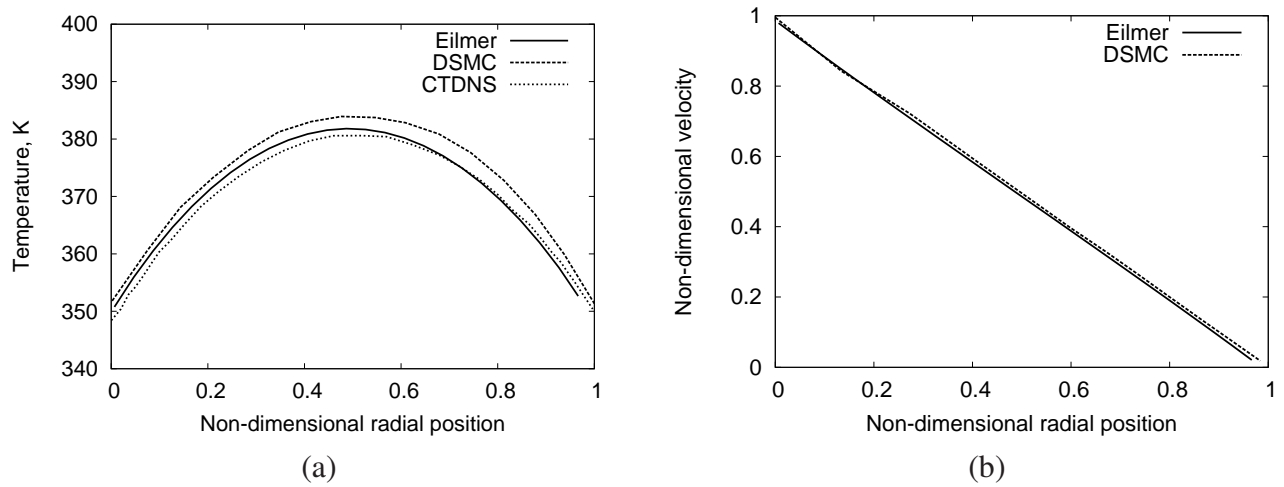


**Figure 3.3:** Comparison of temperature (a) and axially averaged velocity (b) profiles in radial direction at intermediate pressure condition.

If the rotational speed of the rotor is reduced to 18 400 rpm, while the other parameters remain the same with the high pressure case in Ref. [122], the axisymmetric vortices can be simulated. The velocity profile (averaged over the axial direction) has changed to an S-shapes curve as shown in Figure 3.5. This velocity profile characterises a flow with a higher gradient at the walls, due to enhanced radial transport of fluid induced by the vortices. The axially averaged temperature profile is much flatter than the parabolic profile of the lower Taylor number cases. This averaged shape also exhibits steeper gradient at the walls, which induce a high heat flux. Again, these changes are due to the presence of vortices and the associated increase in radial transport of momentum and energy across the gap.

### 3.3.5 Hydrostatic Air Thrust Bearing

With high density  $\text{CO}_2$  as the operating fluid, high centrifugal inertia effects cannot be ignored. A hydrostatic air thrust bearing is used to verify the suitability of Eilmer in simulating thrust bearing as well as modelling the centrifugal inertia force. Garratt et al. [127] considered the centrifugal inertia effects in high-speed hydrostatic air thrust bearings. They used a Reynolds equation modified for compressible flow to model the dynamics of pressurised air bearings in a simplified axisymmetric geometry. The basic air-flow characteristics were analysed for various non-dimensional speed parameters  $\lambda$  under steady-state condition when the bearing faces are fixed at a constant distance. Their

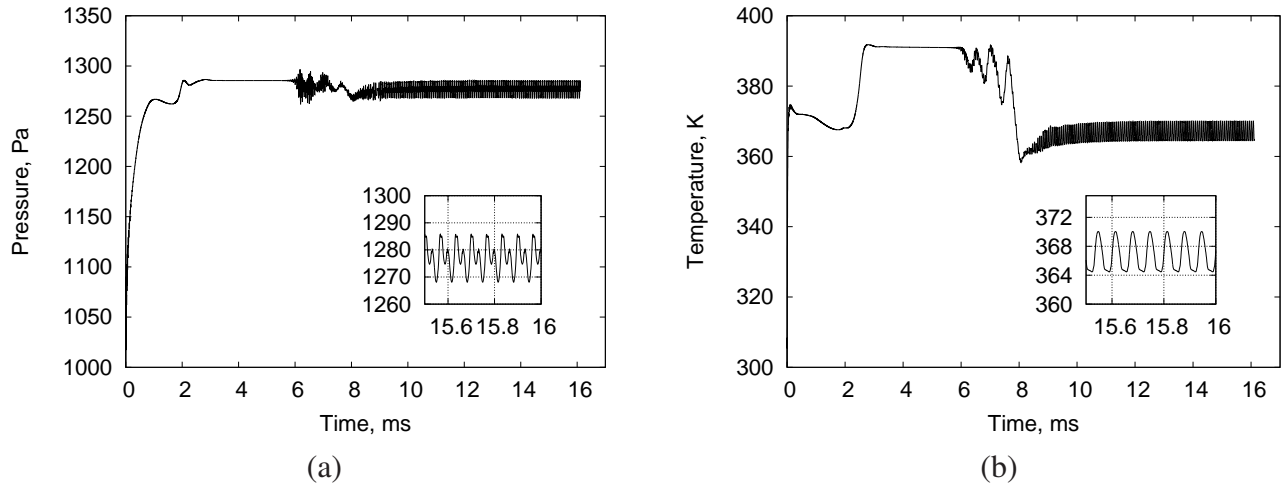


**Figure 3.4:** Parameters variation of Taylor-Couette Flow at high pressure condition; (a): pressure; (b): temperature.

modified Reynolds equation is,

$$\frac{\partial}{\partial r} \left( p r \frac{\partial p}{\partial r} \right) - \lambda \frac{\partial}{\partial r} (r^2 p^2) = 0 . \quad (3.2)$$

The speed parameter  $\lambda$ , which relates to different rotational speed, is defined as,

$$\lambda = \frac{3 \hat{\rho}_a \Omega^2 r_O^2}{10 \hat{p}_a K_s} . \quad (3.3)$$

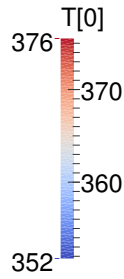
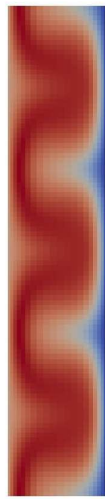
and characterises the magnitude of the inertia effects during high speed operation.  $\hat{\rho}_a$  is air density at atmospheric pressure, and  $K_s$  is the dimensionless parameter relating the air density and pressure in the perfect gas law,

$$p = K_s \rho . \quad (3.4)$$

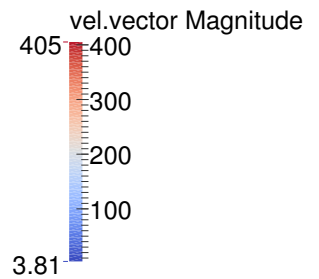
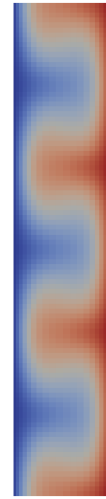
A schematic of their hydrostatic air thrust bearing is shown Figure 3.6. The outer radius is defined as 0.05 m, the size of inner radius will be different based on narrow bearings or wide bearings, and the gap height of the bearing is 10  $\mu\text{m}$ .

The working fluid is dense air with the constant density of 10 kg/m<sup>3</sup>. Using this dense gas can largely reduce the rotational speed at the same bearing number  $\lambda$ , see Table 3.2. The viscous heating effect can be minimised compared to that of using perfect air.

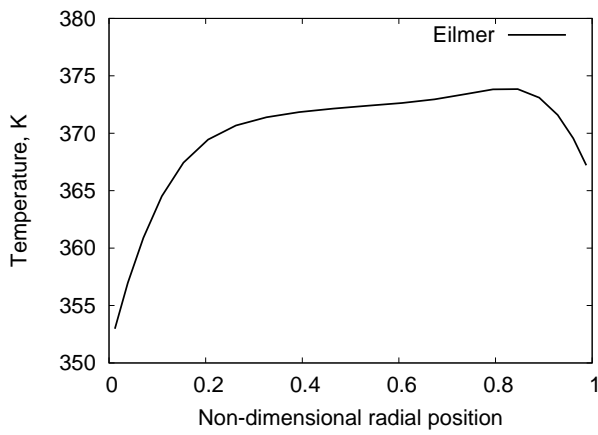
Pressure profiles obtained using Eilmer and the modified Reynolds equation (Equation 3.2) by [127]



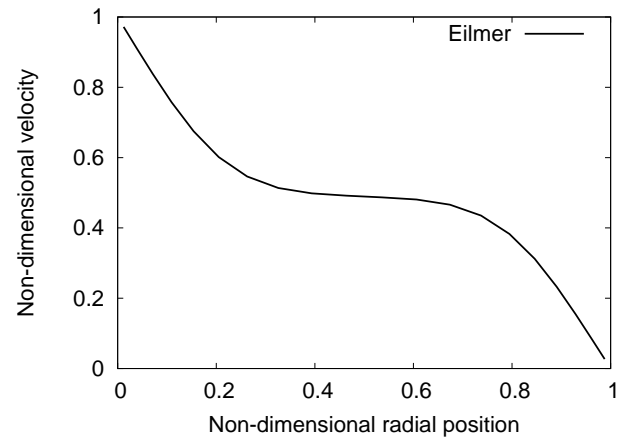
(a) Temperature contour.



(b) Velocity contour.



(c) Averaged temperature profiles in radial direction.



(d) Axially averaged velocity profiles in radial direction.

**Figure 3.5:** Temperature and velocity for Taylor-vortices case.

**Table 3.2:** Rotational speed (in rpm) for different bearing speed parameter for perfect air and dense air.

Case	$\lambda=0$	$\lambda=2$	$\lambda=4$	$\lambda=6$
Perfect air	0	142 994.89	202 225.32	247 674.42
Dense air	0	49 637.97	70 198.70	85 975.49

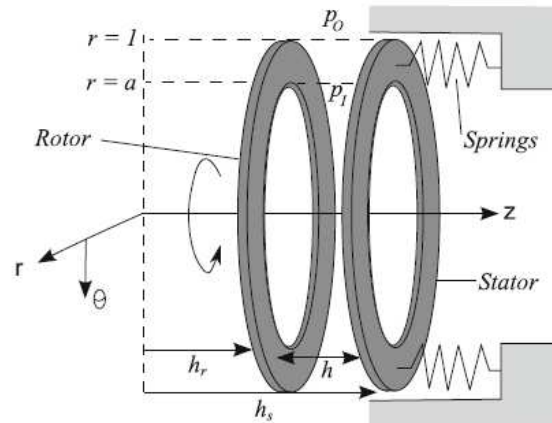


**Figure 3.6:** Schematic of hydrostatic air thrust bearing geometry, taken from Ref. [127].

for an inward pressurised bearing are shown in Figure 3.7, where (a) and (b) correspond to a wide and narrow bearing, respectively. For the wide bearing, at low rotation speeds, the inward pressurisation gives a continuously decreasing pressure from the outer to inner radii. The pressure becomes sub-ambient in the middle of bearing at high speeds. The reason is attributed to the mass loss close to the rotor. For the narrow bearing, the pressure profile remains almost linear for all speed number  $\lambda$ , as shown in Figure 3.7. The pressure distribution from Eilmer shows good agreement against analytical results from the modified Reynolds Equation. Eilmer correctly captures the inertial effects, which are the cause of the dip in pressure observed for the wide bearings.

For inward pressurised bearings, the positive pressure gradient results in a purely inward flow without of high-speed rotation. However, with rotation, the flow near the rotor becomes outwards, and this region of outward flow increases in size for higher rotational speeds. The boundary between the pressure driven inward flow and the outside flow due to centrifugal effects can be monitored by a line of zero radial velocity. Figure 3.8 compares the position of the radial velocity line between Eilmer and the modified Reynolds equation. The results confirm that Eilmer accurately captures the inward and outward flows.

### 3.3.6 Wavy Thrust Bearing

This test case is used to study the suitability of Eilmer to simulate the pressure distribution in bearings with complex pad geometries. The modeling of a wavy thrust bearing has been studied by Zhao et

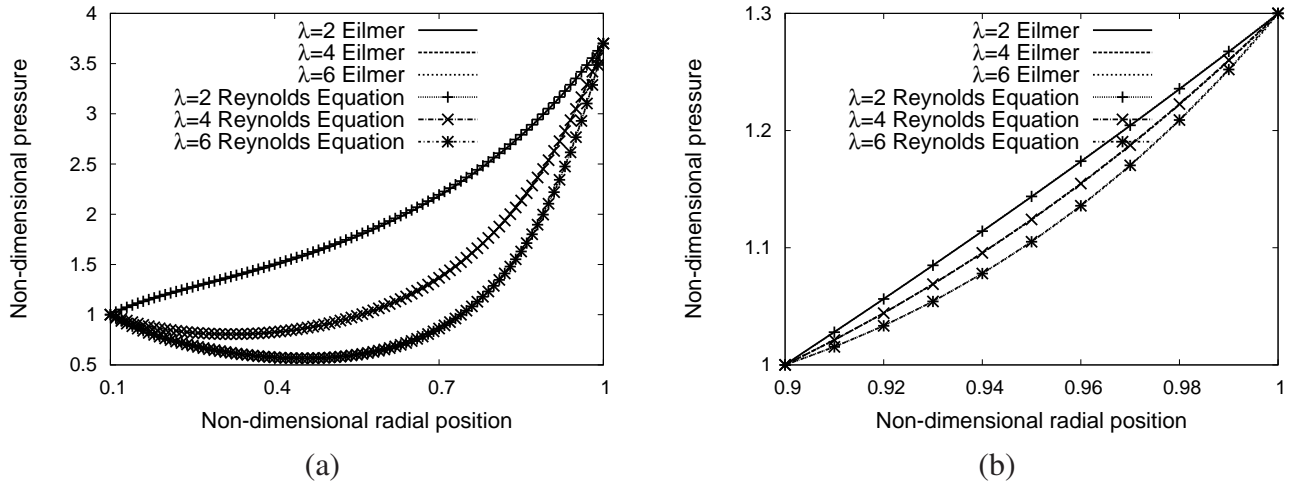


**Figure 3.7:** Steady state pressure distribution in an inward pressurised bearing for different bearing numbers: (a): wide bearing; (b): narrow bearing.

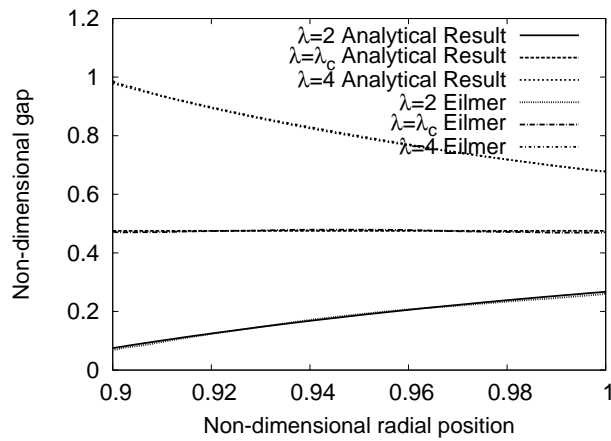


**Figure 3.8:** Comparison of zero radial velocity line at different bearing number.

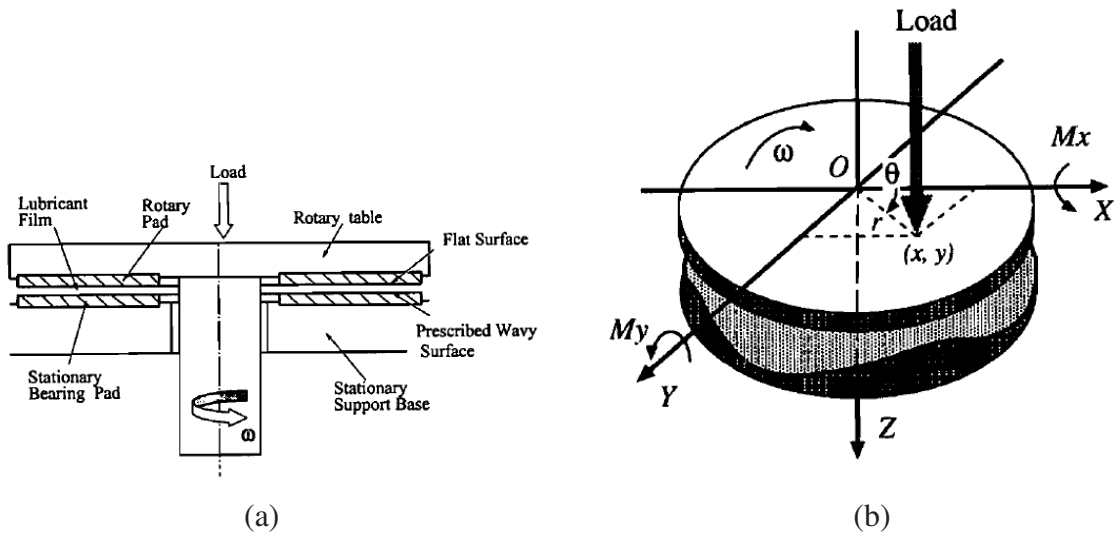


**Figure 3.9:** Schematic of the geometry (a) and coordinate (b) of the wavy thrust bearings, taken from Ref. [128].

al. [128] using Reynolds equation. Their numerical simulation of a self-acting thrust bearing was developed using a system of two circular discs moving relative to each other as shown in Figure 3.9. The Reynolds equation for this system, written in polar coordinate, is,

$$\frac{\partial}{\partial r} \left( \rho h^3 \frac{p}{r} \right) + \frac{1}{r} \rho h^3 \frac{\partial p}{\partial r} + \frac{1}{r^2} \frac{\partial}{\partial \theta} \left( \rho h^3 \frac{p}{\theta} \right) = 6 \eta \omega \frac{\partial \rho h}{\partial \theta} . \quad (3.5)$$

The discretization of Reynolds equation 3.5 is based on Ref. [129] and provided in Appendix A. The solution to the equation is evaluated using the Gauss-Seidel successive under-relaxation method. The computational domain is a single thrust pad. To solve this equation, density and dynamic viscosity of working fluid are calculated from thermo-physical software REFPROP [120].

**Table 3.3:** Wavy thrust bearing physical and operational characteristics.

Outer radius of discs	50.8 mm
Inner radius of discs	25.4 mm
Nominal average clearance, $h_c$	0.010 mm
Wave amplitude, $g$	6.35 $\mu\text{m}$
Rotational speed	25 000 rpm
Pad angular extent	45°
Working fluid	CO <sub>2</sub>

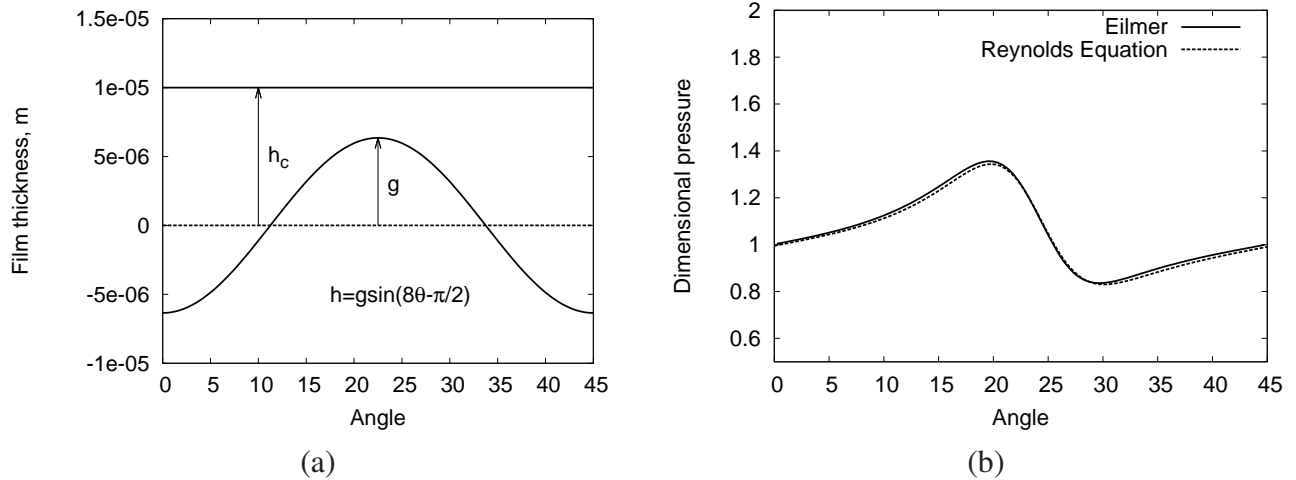


**Figure 3.10:** Schematic of symmetric wavy film thickness and comparison of pressure at center radius between Eilmer and Reynolds equation.

As a first comparison case a wavy bearing with a sinusoidal structure was studied. The geometry is shown in Figure 3.10(a). The remaining geometry and operating parameters are defined in Table 3.3. High pressure CO<sub>2</sub> is used as the working fluid for this case, and the ambient conditions are 1.4 MPa and 300 K, corresponding to SNL's test conditions [8]. The inner and outer surfaces are regarded as fixed pressure boundary condition, while the rotor and pad are modelled as moving and stationary fixed temperature walls, respectively. The other two surfaces are connected with a periodic boundary condition. A grid independence study was conducted for Eilmer as well as the finite difference code for Reynolds equation. Figure 3.10(b) compares the results of pressure distribution at mean radius between Eilmer and Reynolds equation. Good agreement between Reynolds equation and Eilmer demonstrates the ability of Eilmer to correctly simulate wavy bearings.

To study a more foil bearing like geometry, which is characterised by a long compression ramp and followed by an almost instantaneous expansion, case 2 explores the flow in wavy bearing with a skewed sin-wave geometry. The ratio of compression to expansion part is now changed to 4:1 as shown in Figure 3.11(a). The resulting pressure at the bearing mean radius for Reynolds equation and Eilmer are shown in Figure 3.11(b). Good agreement is also achieved.

The results for load and friction torque integrated from Reynolds equation and Eilmer are shown in Table 3.4. The relative error between Eilmer and Reynolds equation for both cases is almost the same, 70 N for load and 14 Nmm for friction torque. The cause of this difference has to be further

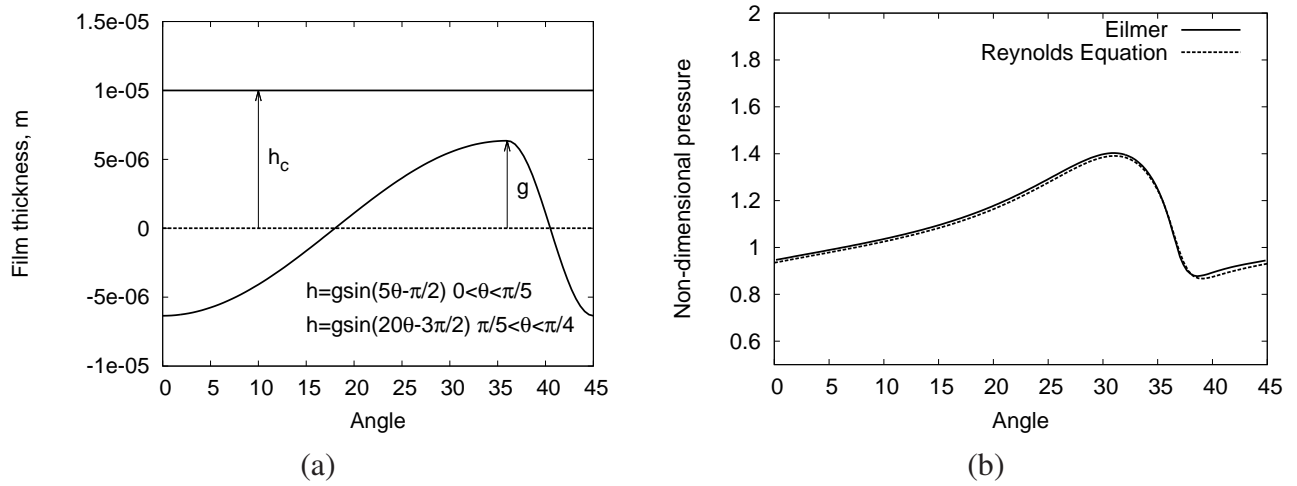


**Figure 3.11:** Schematic of a 4:1 wavy film thickness and comparison of pressure at center radius between Eilmer and Reynolds equation.

**Table 3.4:** Comparison results of load (in N) and friction torque (in Nmm) obtained from Reynolds equation and Eilmer.

Case	Load Eilmer	Load Reynolds equation	Friction torque Eilmer	Friction torque Reynolds equation
1	374.20	308.51	64.41	50.45
2	723.60	650.46	64.35	50.49

**Table 3.5:** Operating condition of foil thrust bearings from SNL's test loop [8].

Parameters	Value
Working fluid	CO <sub>2</sub>
Ambient pressure	1.4 MPa
Ambient temperature	300 K
Inner diameter	50.8 mm
Outer diameter	106 mm
Designed rotational speed	75 000 rpm
Designed minimum film thickness	5 μm

investigated.

### 3.4 Modification of Fluid Solver for Turbulent Simulations of Foil Bearings

We now turn our attention to the case of turbulent flow within the bearing. High Reynolds numbers are likely, due to the high density and low dynamic viscosity of high pressure CO<sub>2</sub>. For foil bearings running without a pressure gradient between inner and outer radii, the fluid flow is pure Couette flow [130], and the transition to turbulence is governed by the rotational Reynolds number,

$$Re = \frac{\rho \omega r h}{\mu} , \quad (3.6)$$

when  $Re < Re_t$ , the bearing flow remains laminar and when  $Re > Re_t$  turbulence appears. Although no experimental study has been undertaken to determine the limits, Souchet [131] recommended the following values:

$$Re_t = 1600 . \quad (3.7)$$

The operating condition for foil bearings tested in the SNL are listed in Table 3.5. These conditions result in a rotational Reynolds number of 2656, which is substantially larger than the critical value recommended by Souchet [131]. Therefore, the flow regime within foil bearings is expected to be turbulent at design condition.

Foil thrust bearings operating with CO<sub>2</sub> exhibit turbulent flow due to the high density and low

viscosity of the working fluid. To close the momentum equations this requires a model for the evaluation of the turbulent shear stress. The Wilcox's 2006 low-Reynolds  $k - \omega$  turbulence model [132] was previously implemented in Eilmer [133]. Section 3.4.1 details the implemented turbulence model and its validation. However, this model has a high computational cost due to the requirement for fine meshes close to wall boundaries and simulation instabilities due to very high aspect ratio cells within the foil thrust bearing geometry. To reduce the computational cost and stabilise turbulent simulations, a compressible wall function and a fourth-order artificial dissipation term are implemented in Eilmer as discussed in Section 3.4.2 and 3.4.3.

### 3.4.1 Wilcox's 2006 $k-\omega$ model

The Favre-averaged mass, momentum and energy conservation equations and the equations defining the Wilcox's 2006  $k-\omega$  model are described in Appendix D.

The most important differences between Wilcox's 2006  $k-\omega$  model and earlier versions are the addition of a "cross diffusion" term and a built-in "stress-limiter" modification. The addition of "cross diffusion" (see  $\sigma_d$  in the  $\omega$  equation) was suggested as a remedy for the original  $k-\omega$  model's sensitivity to the freestream value of  $\omega$ . The "stress-limiter" modification makes the eddy viscosity a function of  $k$ ,  $\omega$  and, effectively, the ratio of turbulence-energy production to turbulence-energy dissipation.

#### Turbulent Couette Flow Using Wall-Resolved Turbulence Model

The  $k-\omega$  turbulence model is already implemented in Eilmer and validated for hypersonic flowfield simulation [133], however, it is yet to be validated for turbulent flow in foil bearings. To validate the turbulence model for the flow in foil bearings, an experiment of turbulent plane Couette flow conducted by El Telbany et al. [134, 135] is selected as the test case. Their test rig [134, 135] was a 2440 mm long parallel walled channel, with the main measurement station at the centre of the channel and 1980 mm from the blowing end. The belt forming the moving floor is 1200 mm wide. To eliminate possible flapping, the belt is supported from underneath by an aluminium-surfaced plate. For their test case, the height between two parallel plates was 66 mm, while the moving speed of the belt was 12.84 m/s. Since the measured region is located at the centre of the whole test rig, the side walls had little influence on the flow regime and a two-dimensional domain can be used for the simulation.

The corresponding experimental apparatus and computational domain is shown in Figure 3.12.

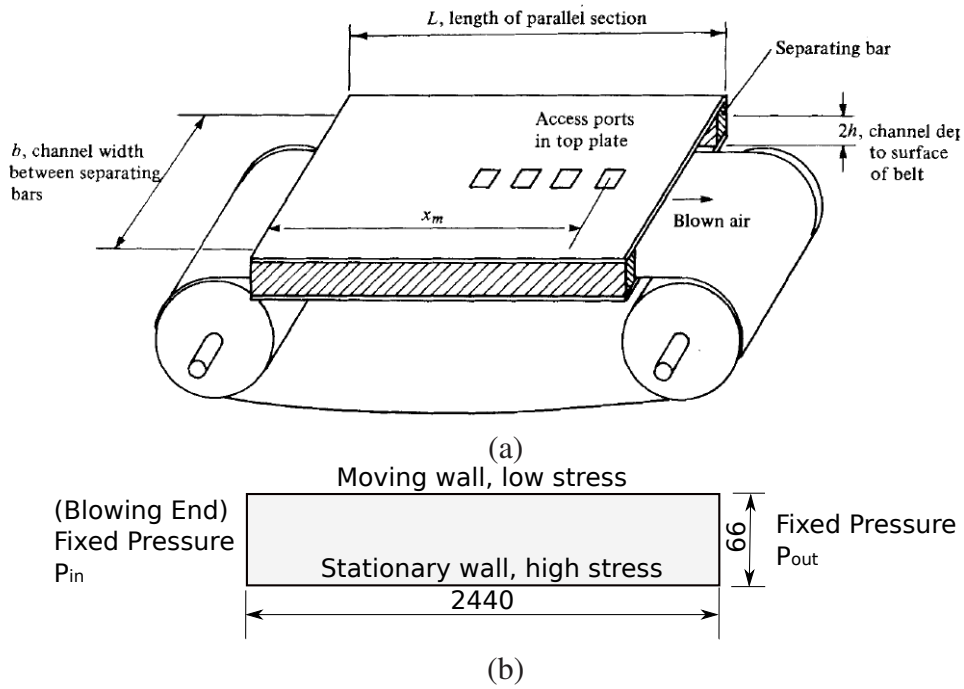


**Figure 3.12:** (a) Experimental apparatus (taken from Ref. [134]) and (b) schematic diagram of the simulation domain for Couette and Poiseuille flows, dimensions in mm.

The top boundary is a stationary fixed temperature wall, the bottom is a fixed temperature wall with fixed translational velocity, and the west and east boundaries of the simulation domain are defined as mixed boundaries. At these mixed boundaries, a fixed pressure is used, while zero gradient is applied for velocities. The turbulence intensity  $I_{turb}$  and turbulent-to-laminar viscosity ratio  $\mu_{turb}/\mu_{lam}$  are set to inflow values if the direction of mass flux is inward, otherwise their values are obtained from the flow cells within the domain and adjacent to the boundary. The values of turbulence kinetic energy  $k$  and specific rate of dissipation  $\omega$  for turbulence model are then computed as,

$$k = \frac{3}{2}(I_{turb} u)^2, \quad (3.8)$$

$$\omega = \rho \frac{k}{\mu_{lam}} \left( \frac{\mu_{lam}}{\mu_{turb}} \right), \quad (3.9)$$

where  $u$  is the velocity of the cell adjacent to the boundary. El Telbany et al. [135] measured the turbulence intensity in the experiment to be approximately 0.1. We used this value and a turbulent-to-laminar viscosity ratio of 1.0 as the inflow values in the simulation.

Three different computational meshes were used. A coarse mesh ( $240 \times 80$  cells), a medium mesh

( $480 \times 160$  cells) and a fine mesh ( $960 \times 320$  cells). For these meshes, cells were clustered to the walls to ensure that the first  $y^+$  value was lower than 1.0 and there were at least 15 cells in the wall-normal direction within the boundary layer. The velocities at points between the two parallel plates were extracted and compared for the different meshes as shown in Figure 3.13(a). The maximum relative error between the coarse and fine mesh was 2.04 %, whereas it was 0.49 % between the medium and fine mesh. The medium mesh was then selected for subsequent analysis.

Figure 3.13(a) compares the velocity profile across the channel between Eilmer and the experiment. The figure shows good agreement, which indicates that the velocity profile between the parallel plates is adequately captured. In addition, it is instructive to replot the data of Figure 3.13(a) in the typical semi-logarithmic manner. This is done in Figure 3.13(b). In the viscous layer [136],  $y^+ < 10$ , the non-dimensional velocity  $u^+$  and distance  $y^+$  have the relationship,

$$u^+ = y^+ . \quad (3.10)$$

and in the overlap layer [136],  $y^+ > 10$ , the logarithmic velocity profile is expected,

$$u^+ = \frac{1}{0.41} \ln y^+ + 5.0 . \quad (3.11)$$

Figure 3.13(b) compares the law of the wall to the simulation data. The  $y^+$  value for the first cell is less than 0.3, which is sufficient for turbulent flow simulation using Eilmer as suggested by Chan et al. [133]. The frictional velocity calculated from Eilmer is 0.292 m/s, and El Telbany et al. [134] experimentally determined the friction velocity to be 0.282 m/s. The relative error is less than 0.3 %, which is also acceptable. Good agreement is achieved between the law of the wall and Eilmer with Wilcox's 2006  $k - \omega$  turbulence model.

### 3.4.2 Wall Modelled Turbulence Model for Foil Bearing Applications

For turbulent simulations, the Wilcox's 2006  $k - \omega$  turbulence model [132] is implemented in Eilmer. As shown by Chan et al. [133], the non-dimensionalised normal distance of the first cell from the wall,  $y^+$ , has a non-trivial effect on the accuracy of surface skin friction and heat flux prediction. For turbulence models that integrate through the viscous sublayer, at least one cell has to be within the viscous sublayer to ensure accurate solutions. This results in very fine cells close to wall boundaries.

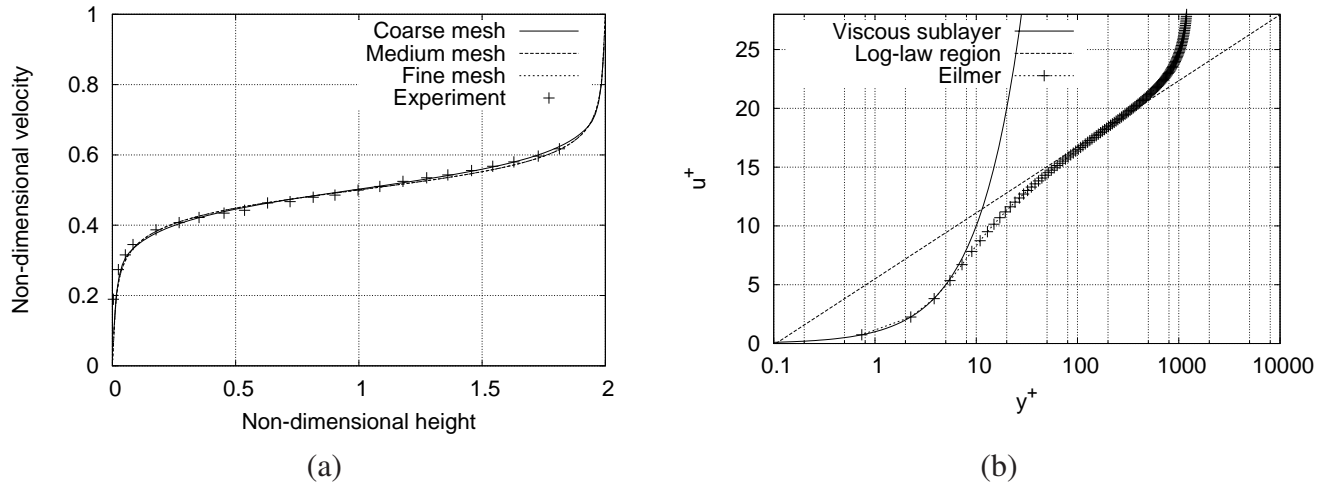


**Figure 3.13:** (a) Velocity distribution for turbulent plane Couette flow, (b) Comparison with the law of the wall.

For explicit time-stepping solvers such as Eilmer [117], these fine cells result in very small time steps due to CFL stability criterion that is imposed.

An alternative is to employ a wall function to model the lower section of the boundary layer. This section describes the implementation of a wall model to avoid having to resolve the viscous sublayer in Eilmer. Since the high-gradient region of the fluid nearest to the wall is modeled with empirical relationships, the first cell center may be placed further away from the wall [137]. This approach reduces the number of cells required to discretise the flowfield and increases the maximum allowable time step.

Wall functions are typically utilised as an efficient approach to reduce computational cost. Several wall functions exist in the literature and are implemented by various CFD codes. Typically a piecewise wall function is utilised [138], and different velocity profiles are activated depends on the local  $y^+$  value at the first cell from the wall. In OpenFOAM [139], an automatic near-wall treatment is used in conjunction with SST  $k - \omega$  turbulence model, and the formulation for the velocity profile near the wall is,

$$u_{\tau}^{vis} = \frac{U}{y^+} \quad (3.12a)$$

$$u_{\tau}^{log} = \frac{U}{\frac{1}{\kappa} \ln(y^+) + C} \quad (3.12b)$$

$$u_{\tau} = [(u_{\tau}^{vis})^4 + (u_{\tau}^{log})^4]^{0.25} \quad (3.12c)$$

However, this does not consider compressibility effects, which become significant especially for high speed flows. The wall function developed by Nichols et al. [137] is able to include these factors, and has been implemented by Gao et al. into their CFD code [140]. This wall function has been demonstrated to provide a virtually grid independent solution when used with the Spalart-Allmaras one-equation model and the  $k - \omega$  model for both attached and separated flows [132, 137]. The assumptions of this wall function are defined by Nichols and Nelson [137]. The wall function uses the unified law of the wall,

$$y^+ = u^+ + y_{white}^+ - e^{-\kappa B} [1 + \kappa u^+ + (\kappa u^+)^2/2 + (\kappa u^+)^3/6] , \quad (3.13)$$

where  $y^+$  is the non-dimensional wall distance,  $u^+$  denotes the non-dimensional velocity,  $y_{white}^+$  is the non-dimensional wall distance for incompressible adiabatic flow,  $\kappa$  and  $B$  are constants, taken as 0.4 and 5.5, respectively. Equation 3.13 ensures that the  $y^+$  value at the first cell can be within different ranges (viscous sublayer, buffer layer and logarithm regions). The effects of compressibility and flow are addressed by the non-dimensional parameter,  $y_{white}^+$  defined as,

$$y_{white}^+ = exp((\kappa/\sqrt{\Gamma})(\sin^{-1}[(2\Gamma u^+ - \beta)/Q] - \phi))e^{-\kappa B} . \quad (3.14)$$

with variables defined as,

$$\Gamma = \frac{\gamma u_\tau^2}{2 c_p T_w} , \quad (3.15)$$

$$\beta = \frac{q_w \mu_w}{\rho_w T_w k_w u_\tau} , \quad (3.16)$$

$$Q = (\beta^2 + 4\Gamma)^{\frac{1}{2}} . \quad (3.17)$$

The non-dimensional parameter  $\Gamma$  models compressibility effects, and the parameter  $\beta$  models heat transfer effects. The temperature distribution within the boundary layer is given by the Crocco-Busemann equation,

$$T = T_w [1 + \beta u^+ - \Gamma (u^+)^2] , \quad (3.18)$$

where  $T$  is the temperature at the first cell and  $T_w$  is the wall temperature. For adiabatic walls, the

heat flux  $q_w = 0$ , and Equation 3.18 can be reduced to,

$$T = T_w - \frac{\gamma u^2}{2 c_p}, \quad (3.19)$$

where  $u$  is the cell velocity,  $c_p$  is the specific heat at constant pressure and  $\gamma$  is a constant equal to  $Pr^{1/3}$ . Hence, the boundary-layer profile is defined in terms of the shear stress  $\tau_w$  and the wall heat transfer  $q_w$ . Effectively this means that for a given velocity and temperature in the first cell the heat flux and shear stress can be defined and vice versa.

The implementation of this compressible wall function in Eilmer for adiabatic and constant temperature walls follows the process suggested by Nichols et al. [137]

1. Set the wall velocity to zero for non-moving body problems or to the grid velocity for moving wall cases.
2. (a) For adiabatic walls: use the velocity and temperature at the center of the first cell, to solve Equation 3.19 for the wall temperature  $T_w$  and extrapolate the pressure from the cell centre to the wall to obtain pressure at the wall. The wall density  $\rho_w$  is obtained using the equation of state.
  - (b) For constant temperature walls: extrapolate the pressure from the first cell centre to the wall and solve for the wall density using the equation of state with the given wall temperature  $T_w$ .
3. (a) For adiabatic walls: iteratively solve Equation 3.13 to obtain the wall shear stress  $\tau_w$  in the local coordinates using the distance of the first cell centre from the wall.
  - (b) For constant temperature walls: iteratively solve Equation 3.13 and 3.18 for the wall shear stress  $\tau_w$  and heat transfer  $q_w$  in the local coordinate using the distance of the cell centre from the wall.
4. Rotate the stress tensor into the Cartesian coordinates and update the viscous flux at the wall.

Once the wall shear stress and heat transfer (for constant temperature wall) have been calculated, the turbulence transport variables can be calculated at the centre of the first cell. The eddy viscosity  $\mu_t$  is given by,

$$\frac{\mu_t}{\mu_w} = 1 + \frac{\partial y_{white}^+}{\partial y^+} - \kappa e^{-\kappa B} \left( 1 + \kappa u^+ + \frac{(\kappa u^+)^2}{2} \right) - \frac{\mu_{w+1}}{\mu_w}, \quad (3.20)$$

where  $\mu_w$  and  $\mu_{w+1}$  are the molecular viscosity at the wall and first cell centre from the wall, respectively.  $\frac{\partial y_{white}^+}{\partial y^+}$  is given by,

$$\frac{\partial y_{white}^+}{\partial y^+} = 2 y_{white}^+ \frac{\kappa \sqrt{\Gamma}}{Q} \left[ 1 - \frac{(2 \Gamma u^+ - \beta)^2}{Q^2} \right]^{\frac{1}{2}} . \quad (3.21)$$

The values of the transport model turbulence variables in the first cell must also be defined. The turbulent kinetic energy  $k$  and specific turbulent dissipation  $\omega$  at the first cell from the wall for the  $k - \omega$  turbulence model are given by,

$$\omega_i = \frac{6 \mu_w}{0.075 \rho_w y^2} , \quad (3.22)$$

$$\omega_o = \frac{6 u_\tau}{\sqrt{C_\mu} \kappa y} , \quad (3.23)$$

$$\omega = \sqrt{\omega_i^2 + \omega_o^2} , \quad (3.24)$$

$$k = \frac{\omega \mu_t}{\rho} . \quad (3.25)$$

This two level model for  $\omega$  was suggested by Veiser [141] and implemented as part of the compressible wall function proposed by Nichols et al. [137], is implemented in Eilmer.

### Flow Over Flat Plate Using Wall-Modeled Turbulence Model

The wall function described previously was incorporated into the in-house computational fluid dynamics solver Eilmer. The intention of this implementation is to reduce the computational cost of turbulent simulations for foil bearings, hence representative test cases (flat plate, Couette and Poiseuille flows) are studied to validate the wall function.

The first validation case is air flow over a flat plate. The turbulent friction correlations by van Driest are used for comparison with numerical simulations [136]. Because of its simplicity, this test case is used as a fundamental case to validate the initial implementation of wall functions.

The schematic diagram of the simulation is shown in Figure 3.14. The left and north boundary surfaces are taken as inflow conditions, where static pressure, temperature and velocity of the air flow are prescribed. In this case, the inflow condition is set to 0.1 MPa, 300 K and 100.0 m/s. The right boundary surface is modeled as outflow with a zero gradient condition. The south is defined as a wall boundary. For this test case, two wall boundary conditions, adiabatic and constant temperature, are

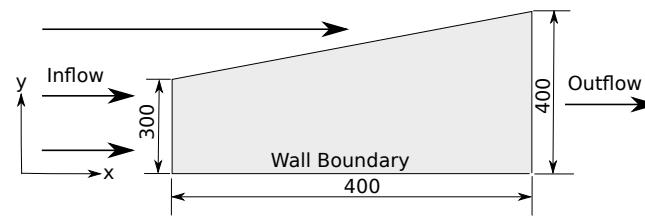


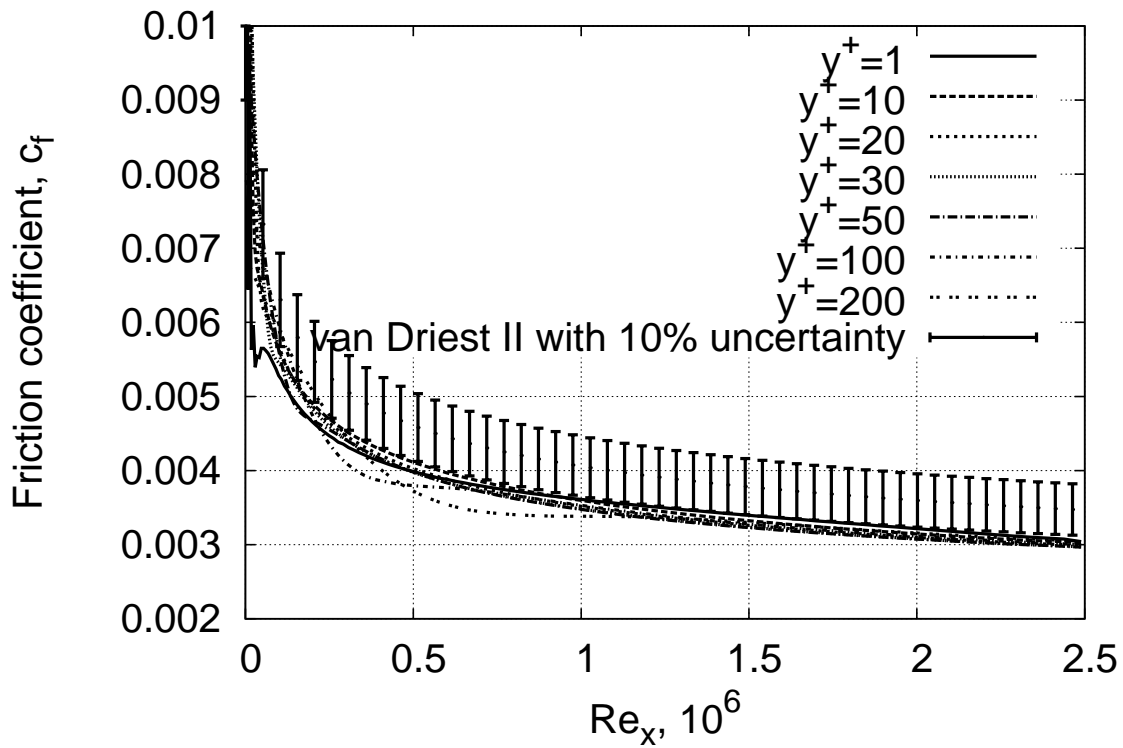
**Figure 3.14:** Schematic diagram of the simulation domain for flat plate, in mm.

used. The velocity boundary profiles (including the calculation of  $y^+$  value) extracted at a position 380 mm from the leading edge are shown in Figures. 3.15 and 3.16.

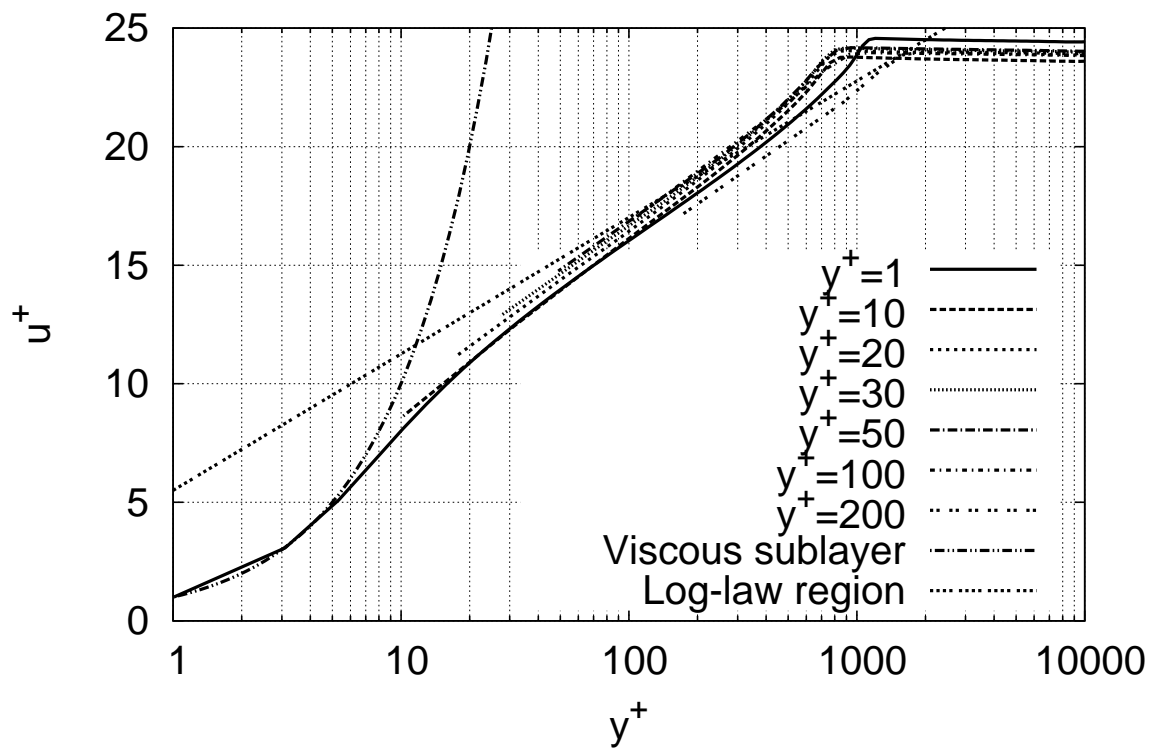
For the adiabatic wall case, the predicted values of the friction coefficient along the lower wall with varying initial grid wall spacing using the  $k - \omega$  turbulence model are shown in Figure 3.15(a). Also shown are theoretical values from van Driest [136, 142], with a 10 % uncertainty range. The  $y^+ = 1$  results were created without using a wall function and are included for reference. The wall function predictions using  $y^+ = 10, 20, 30$  and  $50$  are in close agreement with the fully resolved simulation ( $y^+ = 1$ ). Reasonable agreement also exists between the predictions and the van Driest correlation with the simulation consistently under predicting. For  $y^+ = 100$  and  $200$ , some deviation exists at Reynolds number below  $0.5 \times 10^6$ , but good agreement exists for higher Reynolds numbers. Velocity profiles and the law of the wall are shown in Figure 3.15(b). Again the  $y^+ = 1$  results obtained without using the wall functions are included for reference. Close agreement exists between the simulated profiles, far from the wall.

The corresponding results for a constant temperature wall (320 K) are shown in Figure 3.16. Again, the values from van Driest [136, 142] and the  $y^+ = 1$  results, created without using a wall-function are included. The wall function predictions using  $y^+ = 10, 20, 30$  and  $50$  are in close agreement with the fully resolved simulation ( $y^+ = 1$ ). Also reasonable agreement exists between the predictions and the van Driest correlation. For  $y^+ = 100$ , again a deviation of friction coefficient exists around Reynolds number of  $0.5 \times 10^6$  and good agreement is achieved at higher Reynolds numbers. The predicted heat transfer is shown in Figure 3.16(b). The differences between the different grid spacings are larger than for the friction coefficient predictions.

It is found that the absolute error between wall function and experimental results (van Driest) are 5.17 % for the adiabatic cases and 12.29 % for the constant wall temperature cases, similar to the values cited by Nichols et al. [137]. Velocity and temperature profiles at 380 mm from the leading



(a)



(b)

**Figure 3.15:** Performance comparison with different grid spacings for adiabatic walls, (a) friction coefficient; (b) law of the wall. 380 mm from leading edge,  $Re_x = 2.39 \times 10^6$ .

edge are shown in Figure 3.17. These are in reasonable agreement with each other and with theory for all of the wall spacings tested.

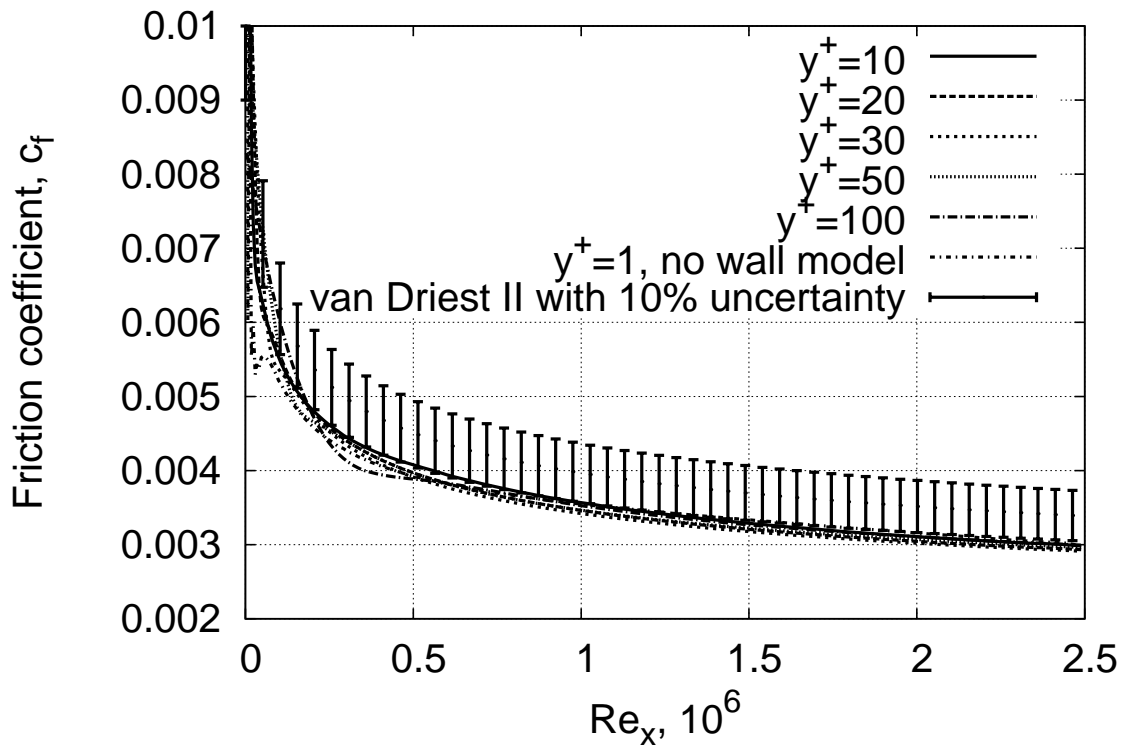
Based on the verification studies, it has been shown that a  $y^+$  value less than 100 is required to ensure the accurate prediction of the shear stress and heat transfer. With these test cases for adiabatic and constant temperature walls, the implementation of wall functions is validated for these simple cases.

### **Turbulent Couette and Poiseuille Flows Using Wall-Modeled Turbulence Model**

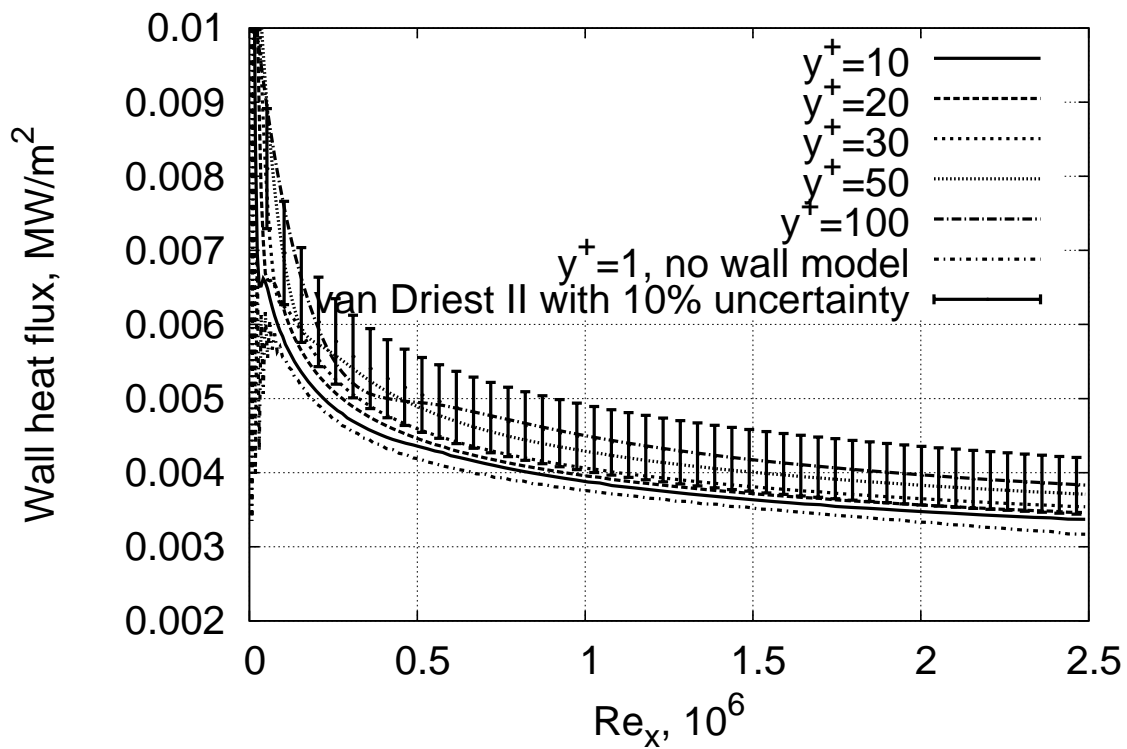
The next test cases (Couette and Poiseuille flows) are representative of flows in foil bearings. They can be used to validate the suitability of this wall function for the bearing flowfield. Five test cases from the experimental results given by El Telbany and Reynolds [134, 135] are considered. These include pure Couette flow, pure Poiseuille flow and hybrid Couette and Poiseuille flow, which are the typical flows within foil bearings. The test rig [134, 135] described in literature uses 2440 mm long parallel walls, with the main measurement station at the centre of the channel and 1980 mm from the blowing end. For test cases used in this section, the height between two parallel walls was 66 mm, and the belt forming the moving wall has a translational velocity of 12.84 m/s. The pressure difference between the inlet and outlet of the moving belt is attained by a blower. The exact value of pressure difference across the moving belt is not indicated in literature, but it can be obtained from the shear stress listed for the experiments [134, 135].

A two-dimensional computational domain is used as the measured region is located in the centre of the belt. The schematic diagram is shown in Figure 3.12. The left and right boundary patches are modeled as fixed pressure. By varying the pressure difference between inlet and outlet, different forms of hybrid Couette and Poiseuille flows are created. The north boundary is taken as a fixed temperature wall with a prescribed translational velocity, while the south is regarded as a stationary fixed temperature wall.

The experimental results used for comparison are listed in Table 3.6. The case index is in accordance with the literature [134, 135].  $u_{\tau 1}$  indicates the high stress wall, while  $u_{\tau 2}$  is for the low stress wall. Case 1 is the pure Couette flow, and there is no pressure difference across the moving belt, while case 15 is the pure Poiseuille flow, as indicated by a non-moving belt. With a certain amount of pressure difference across the moving belt, case 2, 3 and 5 are regarded as hybrid Couette and Poiseuille flows, but Couette flows are still dominant. For these hybrid flows, the belt velocity is set

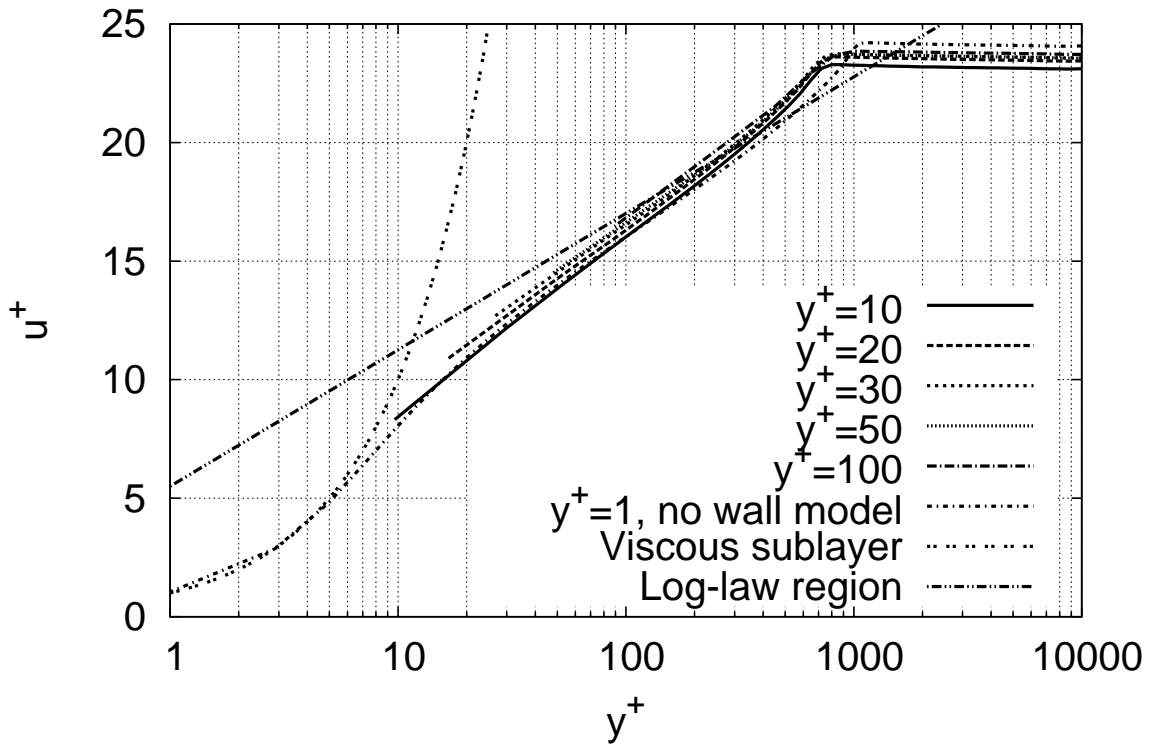


(a)

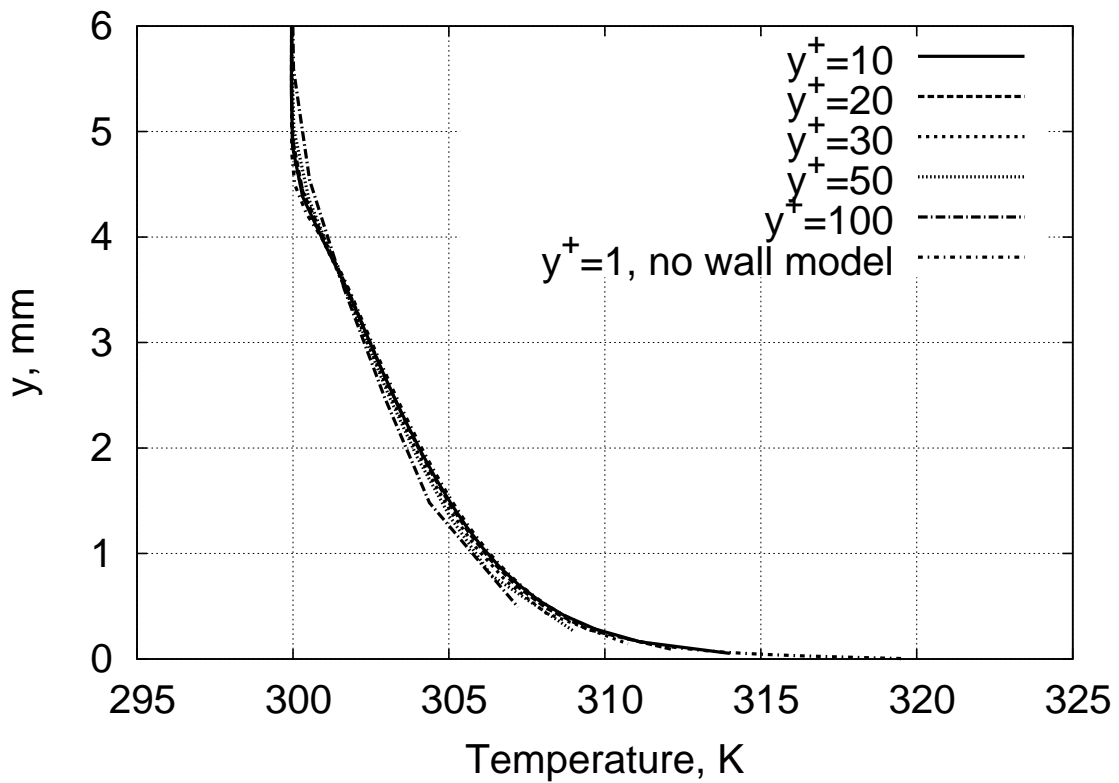


(b)

**Figure 3.16:** Performance comparison with different grid spacings for constant temperature walls, (a) friction coefficient; (b) heat flux.



(a)



(b)

Figure 3.17: Law of the wall and temperature, 380 mm from leading edge,  $Re_x = 2.39 \times 10^6$ .

**Table 3.6:** Details of El Telbany and Reynolds tests.

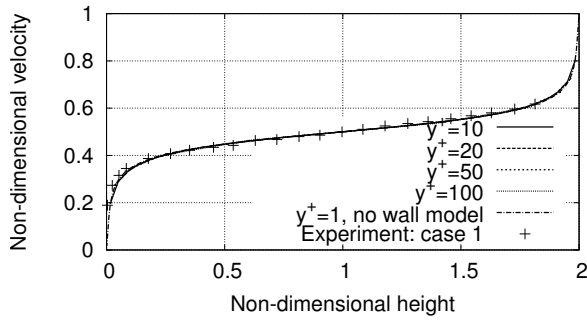
Case	$U_b$ , m/s	$u_{\tau 1}$ , m/s	$u_{\tau 2}$ , m/s	Pressure difference, Pa
1	12.84	0.282	0.282	0
2	12.84	0.328	0.233	2.3771
3	12.84	0.362	0.1809	4.3782
5	12.84	0.383	0.1305	5.7765
15	0	0.659	0.659	38.6913

as 12.84 m/s. All the cases were generated by running the belt in the same direction as the blown flow of air. The pressure differences in Table 3.6 are not provided in literature, but are calculated from the friction velocity of the high and low stress walls,

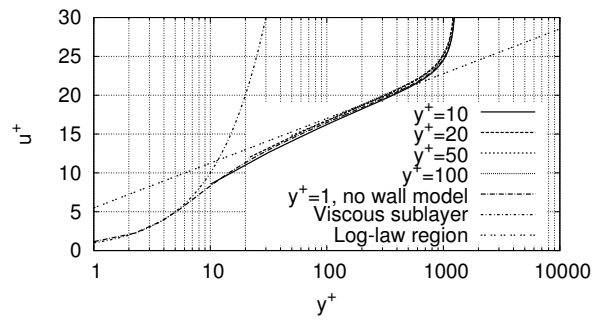
$$\text{Couette flow: case 2, 3 and 5} \quad \Delta p = \frac{(\rho u_{\tau 1}^2 - \rho u_{\tau 2}^2) L_b}{H_b}, \quad (3.26)$$

$$\text{Poiseuille flow: case 15} \quad \Delta p = \frac{(\rho u_{\tau 1}^2 + \rho u_{\tau 2}^2) L_b}{H_b}. \quad (3.27)$$

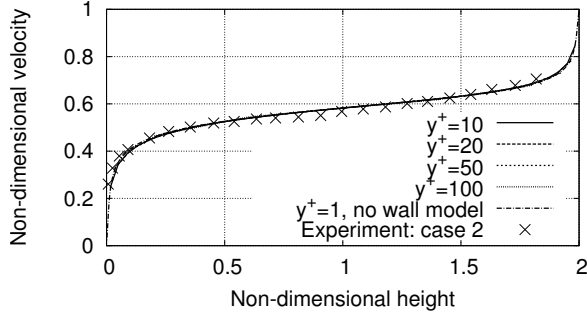
The resulting velocity profiles and the law of the wall for different test cases with various grid spacings are plotted in Figure 3.18. The boundary layer velocity profile is normalised with the belt moving velocity of 12.84 m/s and the  $y$  distance is normalised by the half height of the parallel channel, 33 mm. The results at  $y^+ = 1$  are created without a wall function and plotted as the reference. In all cases, good agreement is attained between the different numerical models. Good agreement is also achieved in comparison to the experimental data for case 2, 3 and 15, both at the high-stress and low-stress walls. The solution accuracy still maintains at different grid spacings is good for hybrid Couette and Poiseuille flow cases. The highest  $y^+$  values for the different test cases shown in Figure 3.18 are obtained by using 5 uniform cells across the channel. This is the coarsest grid, which still presents good agreement to the experimental data. Case 5 shows some differences between experimental data and numerical simulations, but the results from numerical simulations are self-consistent at different grid spacings. For the plot of the law of the wall in Figure 3.18(d), (f) and (h), even if the results from the wall function is self-consistent, a difference is spotted between wall-modelled and wall-resolved approaches, and the magnitude of this difference is gradually increasing from cases 2 to 5. This deviation is caused by the over-predicted wall shear stress from the wall function as reported in Table 3.7.



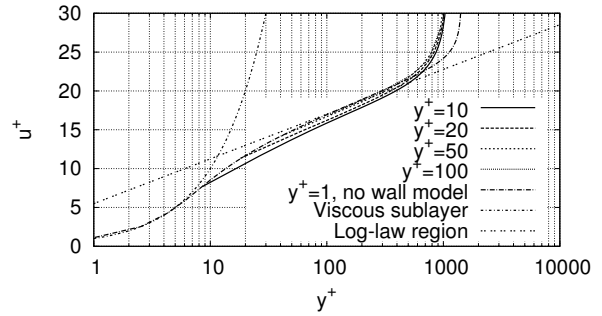
(a): Case 1, boundary layer.



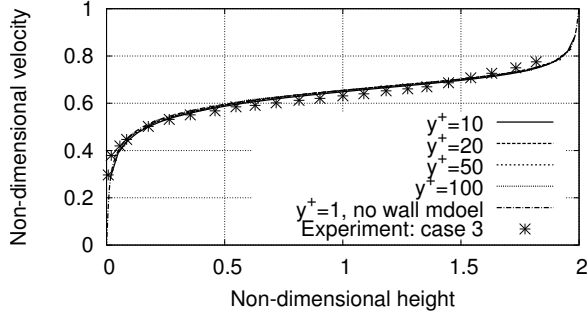
(b): Case 1, law of the wall.



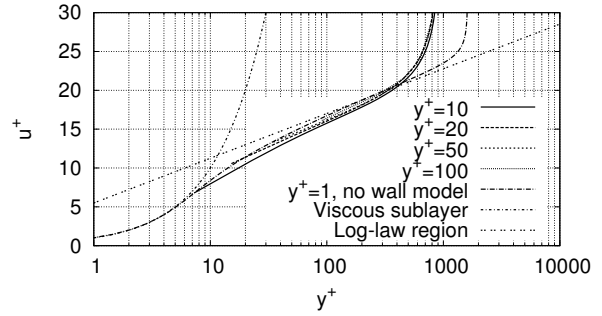
(a): Case 2, boundary layer.



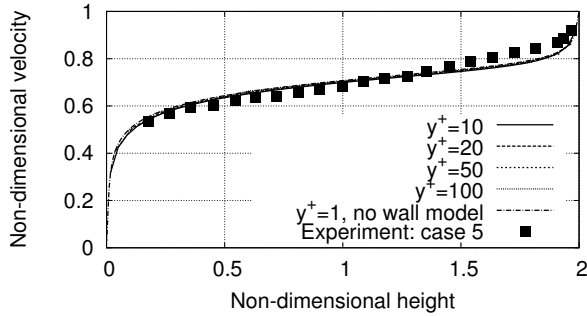
(b): Case 2, law of the wall.



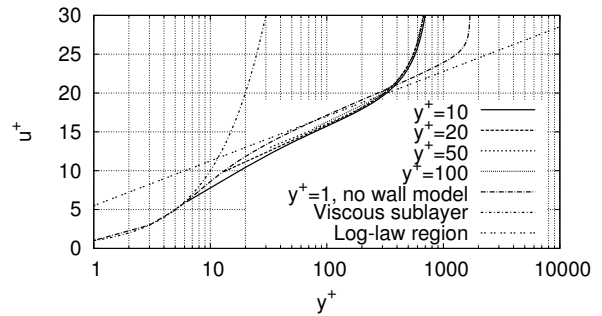
(a): Case 3, boundary layer.



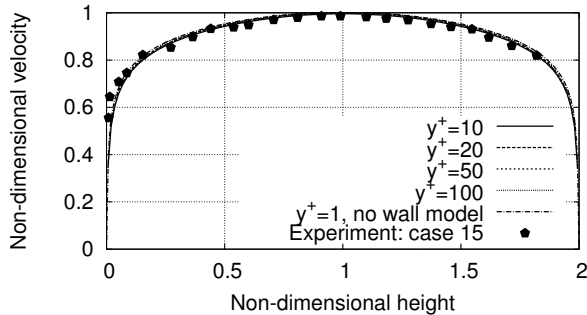
(b): Case 3, law of the wall.



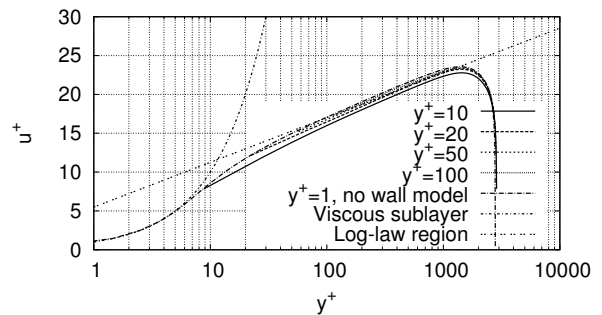
(a): Case 5, boundary layer.



(b): Case 5, law of the wall.



(a): Case 15, boundary layer.



(b): Case 15, law of the wall.

**Figure 3.18:** Performance comparison with different grid spacings for various cases.

**Table 3.7:** Comparison of frictional velocity (in m/s) at different grid spacings. The low stress wall is the moving wall in cases 1,2,3 and 5.

High stress wall				
Case index	Exp.	$y^+ = 1$	$y^+ = 10$	$y^+ = 20$
1	0.282	0.292	0.293	0.292
2	0.328	0.328	0.339	0.335
3	0.362	0.369	0.373	0.372
5	0.383	0.389	0.398	0.397
15	0.659	0.637	0.656	0.655
Low stress wall				
Case index	Exp.	$y^+ = 1$	$y^+ = 10$	$y^+ = 20$
1	0.282	0.292	0.293	0.292
2	0.233	0.245	0.251	0.247
3	0.1809	0.208	0.212	0.206
5	0.1305	0.179	0.182	0.178
15	0.659	0.637	0.656	0.655

To further validate the implemented wall functions, the friction velocities from experimental results and numerical simulations are listed in Table 3.7. Good agreement exists between experiment and simulations. Despite differences in velocity profile far from the wall (center of channel) the wall shear stress is predicted correctly. It is found that a  $y^+$  value less than 100 can achieve accurate result for turbulent Couette and Poiseuille flows and that at least 5 cells are required to correctly simulate the velocity profile. The wall function method for Couette and Poiseuille type flows has been thoroughly validated here. This indicates that the wall function can be applied for the bearing flowfield simulations.

### Suitability of Wilcox's 2006 $k - \omega$ Turbulence Model for Foil Bearings

To test the suitability of the implemented Wilcox's 2006  $k - \omega$  for the fluid flow within foil bearings the experimental results of case 5 from the previous section are used for a turbulence model comparison. Figure 3.19 depicts the results for different turbulence models. The result of Wilcox's 2006  $k - \omega$  model is from Eilmer, while the results for other turbulence models (SST  $k - \omega$ , Spalart Allmaras, standard  $k - \epsilon$  and Nonlinear  $k - \epsilon$  Shih) are all obtained using the simpleFoam solver [139]. It can be seen from Figure 3.19 that both standard  $k - \epsilon$  and Nonlinear  $k - \epsilon$  Shih show a large difference with experimental data, while good agreement between other turbulence models (Wilcox's 2006  $k - \omega$ , SST  $k - \omega$ , Spalart Allmaras) is attained. However a certain deviation to experimental data exists

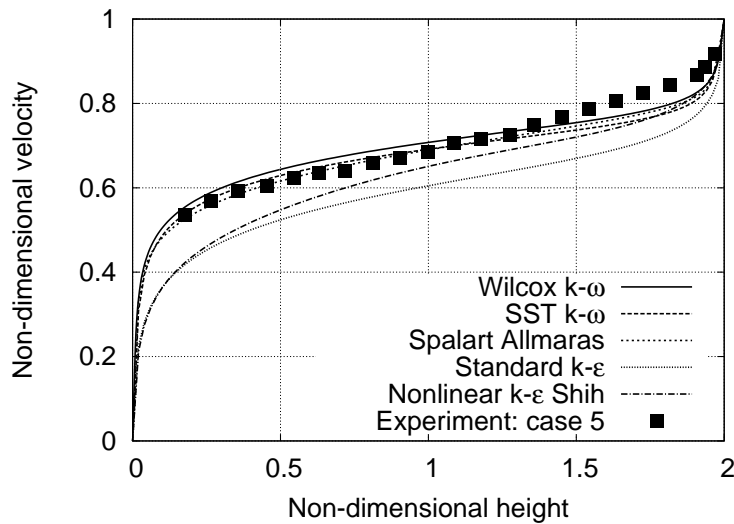


**Figure 3.19:** Comparison of different turbulence models for case 5.

for all turbulence models. The implemented Wilcox's 2006  $k - \omega$  is perhaps best for this test case. The reason for the remaining deviation could be that the current turbulence models cannot handle this flow or errors in the experimental data. Unfortunately uncertainty bands for experimental data are not given by Telbany et al. [134]. It is recommended that a more accurate simulations such as large eddy simulation or direct numerical simulation are conducted to further investigate this deviation.

### 3.4.3 Stabilisation Method for Turbulent Simulations

The film thickness within foil bearings is typically of the order of microns, where as the foil bearing dimensions are of the order 10s of mm. For example, the NASA foil thrust bearing has inner and outer radii of 25.4 mm and 50.8 mm [73], respectively. This particular geometry results in cells with a high aspect ratio (over 1000). The resulting ill-conditioned meshes can cause checker-boarding (numerical oscillation) during turbulent simulations with Eilmer. The checker-boarding phenomenon is not new to the CFD community. For the CFD code developed by Dawes [143], an adaptive artificial viscosity term is added to the governing equations to control odd-even point solution decoupling and to suppress oscillations in regions with strong pressure gradients. Using the diffusion and anti-diffusion equations as a filter numerical diffusion is also reduced [144]. To stabilise turbulent simulations in Eilmer, the artificial dissipation terms proposed by Jameson, Schmidt and Turkel [145] were selected to dampen the high-frequency oscillations. For this method, an artificial dissipative flux is added into governing

equations, written as,

$$d_{j+\frac{1}{2}} = d_{j+\frac{1}{2}}^{(2)} - d_{j+\frac{1}{2}}^{(4)} = \epsilon_{j+\frac{1}{2}}^{(2)} \Delta w_{j+\frac{1}{2}} - \epsilon_{j+\frac{1}{2}}^{(4)} (\Delta w_{j+\frac{3}{2}} - 2\Delta w_{j+\frac{1}{2}} + \Delta w_{j-\frac{1}{2}}) , \quad (3.28)$$

where,

$$\Delta w_{j+\frac{1}{2}}^{(2)} = \begin{bmatrix} \rho_{j+1} - \rho_j \\ (\rho u)_{j+1} - (\rho u)_j \\ (\rho u H)_{j+1} - (\rho u H)_j \end{bmatrix} . \quad (3.29)$$

The spectral radius of the Jacobian matrix in cell  $j$  is  $r_j = |u| + c$ , where  $c$  is the local speed of sound. The dissipative coefficient  $\epsilon_{j+\frac{1}{2}}^{(2)}$  and  $\epsilon_{j+\frac{1}{2}}^{(4)}$  are switched on and off by a pressure sensor,

$$s_j = \left| \frac{p_{j+1} - 2p_j + p_{j-1}}{p_{j+1} + 2p_j + p_{j-1}} \right| . \quad (3.30)$$

Interface values of the spectral radius and sensor are defined as,

$$r_{j+\frac{1}{2}} = \max(r_{j+1}, r_j) , \quad s_{j+\frac{1}{2}} = \max(s_{j+1}, s_j) . \quad (3.31)$$

Then,

$$\epsilon_{j+\frac{1}{2}}^{(2)} = k_2 s_{j+\frac{1}{2}} r_{j+\frac{1}{2}} , \quad \epsilon_{j+\frac{1}{2}}^{(4)} = \max(0, k_4 r_{j+\frac{1}{2}} - c_4 \epsilon_{j+\frac{1}{2}}^{(2)}) . \quad (3.32)$$

The typical values of the constants  $k_2$ ,  $k_4$  and  $c_4$  are,

$$k_2 = 0.2 \sim 1 , \quad k_4 = \frac{1}{256} \sim \frac{1}{16} , \quad c_4 = 2 . \quad (3.33)$$

In this method, the second-order dissipation term  $d_{j+\frac{1}{2}}^{(2)}$  is used to suppress overshooting caused by shocks and the fourth-order dissipation term  $d_{j+\frac{1}{2}}^{(4)}$  is used to damp the spurious oscillations in smooth regions [145]. Therefore, for the current simulations the second term can be neglected and only the fourth-order artificial dissipation term is added to the system. This term provides additional dissipation to suppress spurious numerical oscillations when the grid size is not small enough to render the physical viscosity and will not contaminate the physical solutions [146]. However, for cells close to wall boundary conditions, these artificial dissipation terms are turned off to eliminate over-dissipation as suggested by Goncalves et al. [147]. For the implementation within Eilmer, this

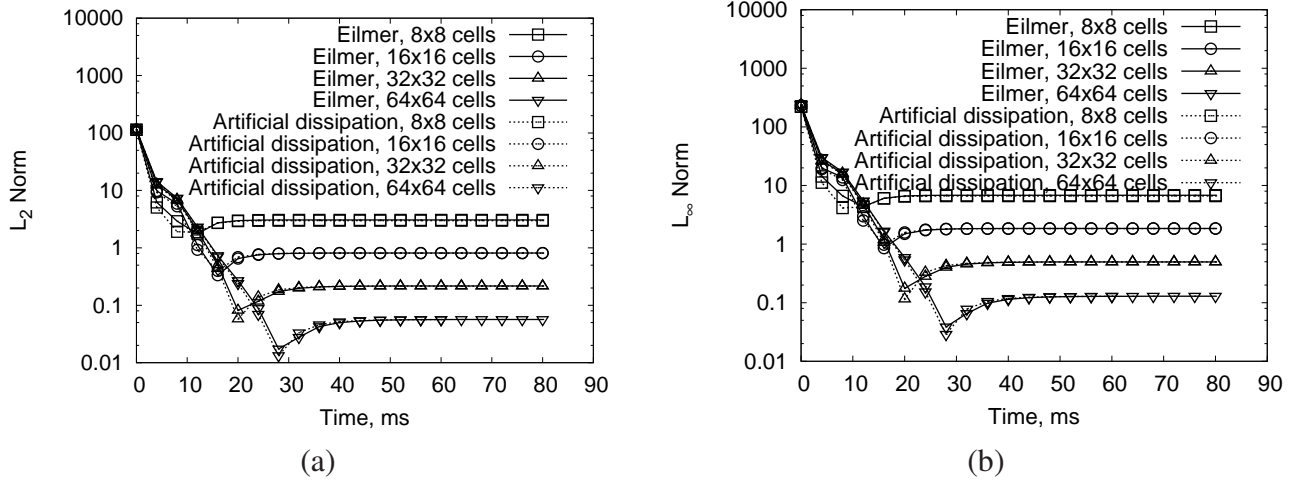


**Figure 3.20:** Convergence history of norms based on turbulent kinetic energy for different mesh sizes: a)  $L_2$  norms, b)  $L_\infty$  norms.

artificial dissipation is turned off in the first four cells from the wall.

### Verification of Eilmer with Artificial Dissipation Using the Method of Manufactured Solution

After the implementation of the fourth-order artificial dissipation in Eilmer, the verification is performed to test the influence of this addition on the fluid solver. Here the method of manufactured solutions is utilised. The detailed introduction of this verification method applied to Eilmer including inviscid, viscous and RANS solvers can be found in Ref. [117, 148]. In this section, the verification is applied to the RANS solver within Eilmer, and Wilcox's 2006  $k - \omega$  turbulence model is selected. The computational setup is the same as outlined in Ref. [148], where exact Dirichlet values obtained from the manufactured solution are prescribed at boundaries. A squared computational domain with a structured grids is investigated. Three different computational meshes ( $8 \times 8$ ,  $16 \times 16$ ,  $32 \times 32$  and  $64 \times 64$ ) are employed to investigate the order of accuracy. The discretisation error is evaluated by  $L_2$  and  $L_\infty$  norms, as defined in Ref. [117].

The time-dependent data of the  $L_2$  and  $L_\infty$  norms of the turbulent kinetic energy from different meshes are plotted in Figure 3.20. Other parameters, like density, dissipation rate can also be utilised in Figure 3.20. The results are obtained from Eilmer with and without artificial dissipation ( $k_4=0.02$ ), respectively. Good agreement is achieved between these two approaches in terms of the steady state and dynamic performances. Also, the difference between two approaches exists in the initial state, but reduces at the final steady state.

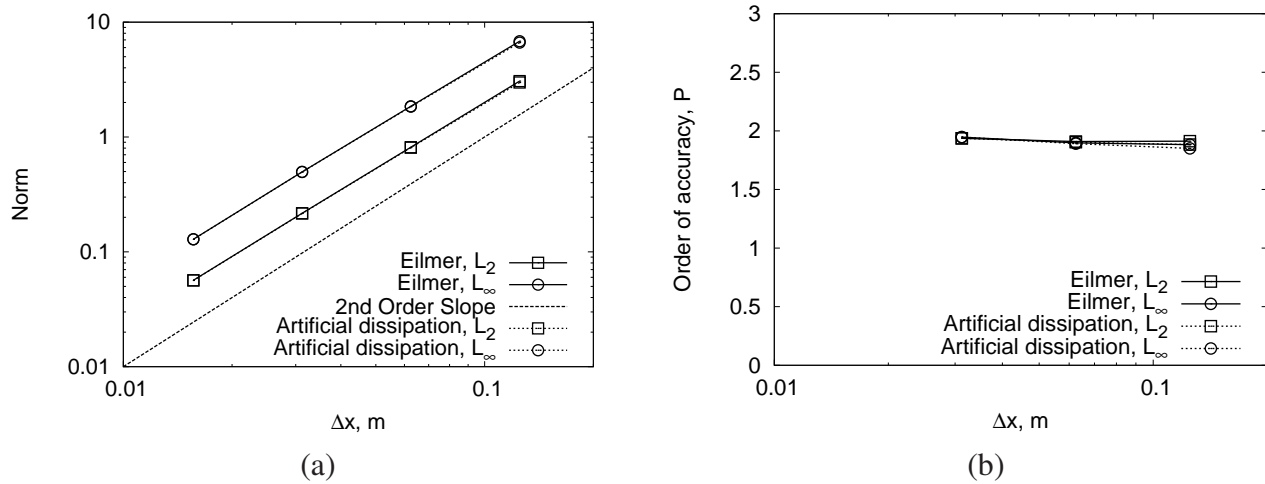


**Figure 3.21:** (a) Norms and (b) observed order of accuracy.

Figure 3.21(a) shows the steady state error norms in terms of cell sizes. The order of accuracy can be determined from the norm values [117] and the results are depicted in Figure 3.21(b). The results from Eilmer and Eilmer with artificial dissipation both indicate an order of two is achieved. The variation of order of accuracy between these two approaches is gradually reduced as the mesh density increases. It is noted that a second order of accuracy is also achieved by investigating  $L_2$  and  $L_\infty$  norms of the specific dissipation and density, which are not shown here. These results prove that the implemented fourth-order artificial dissipation has no influence on the accuracy of the RANS solver in Eilmer, and the second order accuracy is still ensured.

### Influence of Artificial Dissipation on Checker-Boarding

For turbulent simulations of foil thrust bearings, the time step determined from a CFL number of 0.5 in conjunction with the predictor-corrector time stepping method results in a large checker-boarding effect and divergence of the simulation. Alternatively, it is found that this checker-boarding effect can be minimized by selecting a smaller time step. However, the time step has to be extremely small to suppress the checker-boarding effect. Numerical experiments were carried out to test the suitability of the fourth-order artificial dissipation in providing solution stability without affecting the solution due to excessive dissipation. The test case is the fluid flow within a rigid foil thrust bearings with rotational speeds of 20 000 rpm, 30 000 rpm and 40 000 rpm (geometry is defined in Table 2.1). Ambient pressure and temperature are selected as 1.4 MPa and 300 K, respectively. The rotor to top foil separation is chosen as  $22 \mu\text{m}$ . The artificial dissipation constant  $k_4$  is set as 0.02 in this case. A

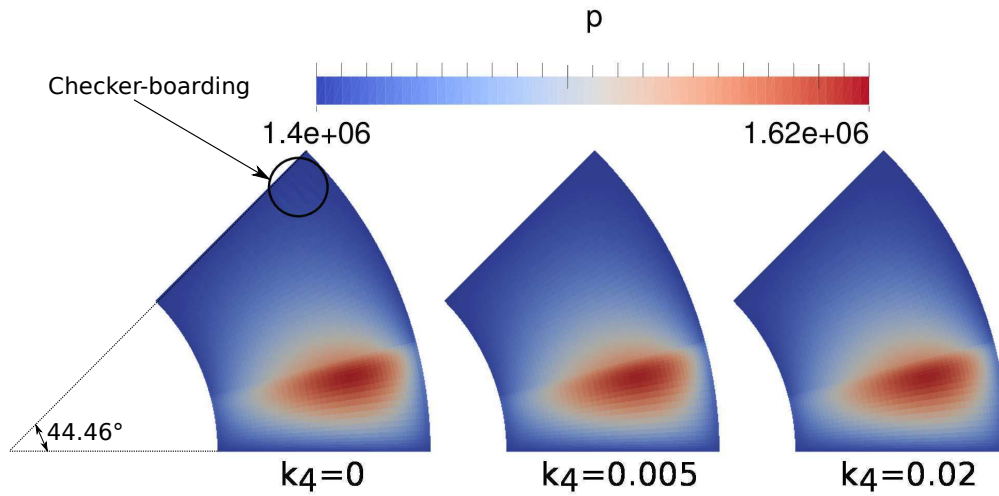


**Figure 3.22:** Pressure contour of the rigid foil thrust bearings, rotational speed: 30 000 rpm, rotor to top foil separation: 22  $\mu\text{m}$ .

mesh of  $48 \times 96 \times 15$  was selected. Grid independence was previously established.

**Table 3.8:** Comparison of time step used by different modeling approaches.

Rotational speed	Eilmer $\Delta t$	$k_4=0$ Wall clock	Eilmer $\Delta t$	$k_4=0.02$ Wall clock	Speed-up
20 000 rpm	$1.231 \times 10^{-9}$ s	20 912 s	$2.481 \times 10^{-9}$ s	10 741 s	1.95
30 000 rpm	$7.185 \times 10^{-10}$ s	35 479 s	$2.338 \times 10^{-9}$ s	11 343 s	3.13
40 000 rpm	$3.123 \times 10^{-10}$ s	81 313 s	$2.171 \times 10^{-9}$ s	12 383 s	6.57

The time steps used for simulations with and without artificial dissipation ( $k_4=0.02$ ) are compared in Table 3.8. It is noted that the time step used for Eilmer without dissipation in Table 3.8 cannot entirely remove the checker-boarding effect, but is able to provide a stable computation. It is found that high rotational speed presents a critical requirement for the time step in Eilmer. The additions of artificial dissipation ensure a comparatively large time step can be maintained. The simulations shown in Table 3.8 were performed on two 12 core Intel Xeon E5-2680V3 2.5 GHz CPU workstations, and the wall clock time was recorded for comparison. The speed-up capability with the artificial dissipation increases with the rotational speed, and the highest value is 6.57 times at the rotational speed of 40 000 rpm.

The pressure and velocity contours at the rotational speed of 30 000 rpm are shown in Figure 3.22

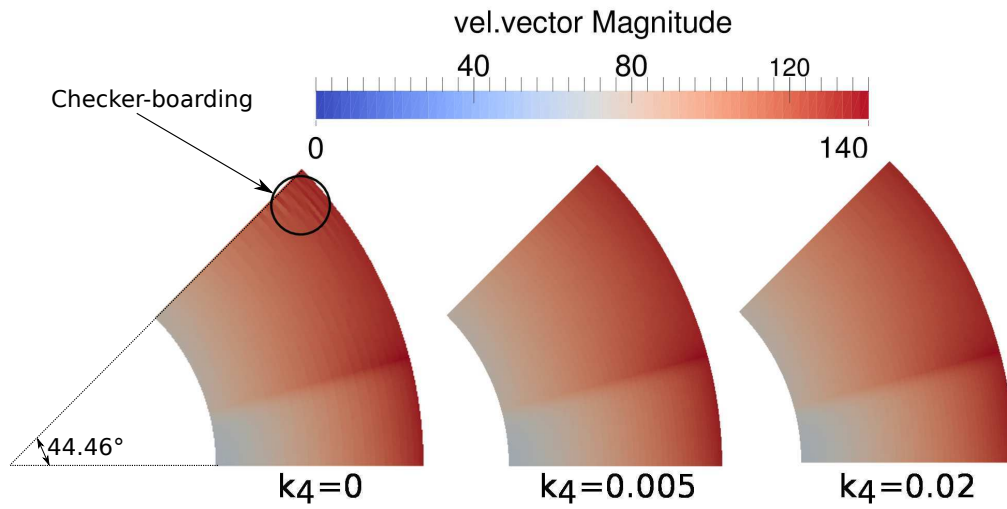


**Figure 3.23:** Velocity contour of the rigid foil thrust bearings, rotational speed: 30 000 rpm, rotor to top foil separation: 22 μm.

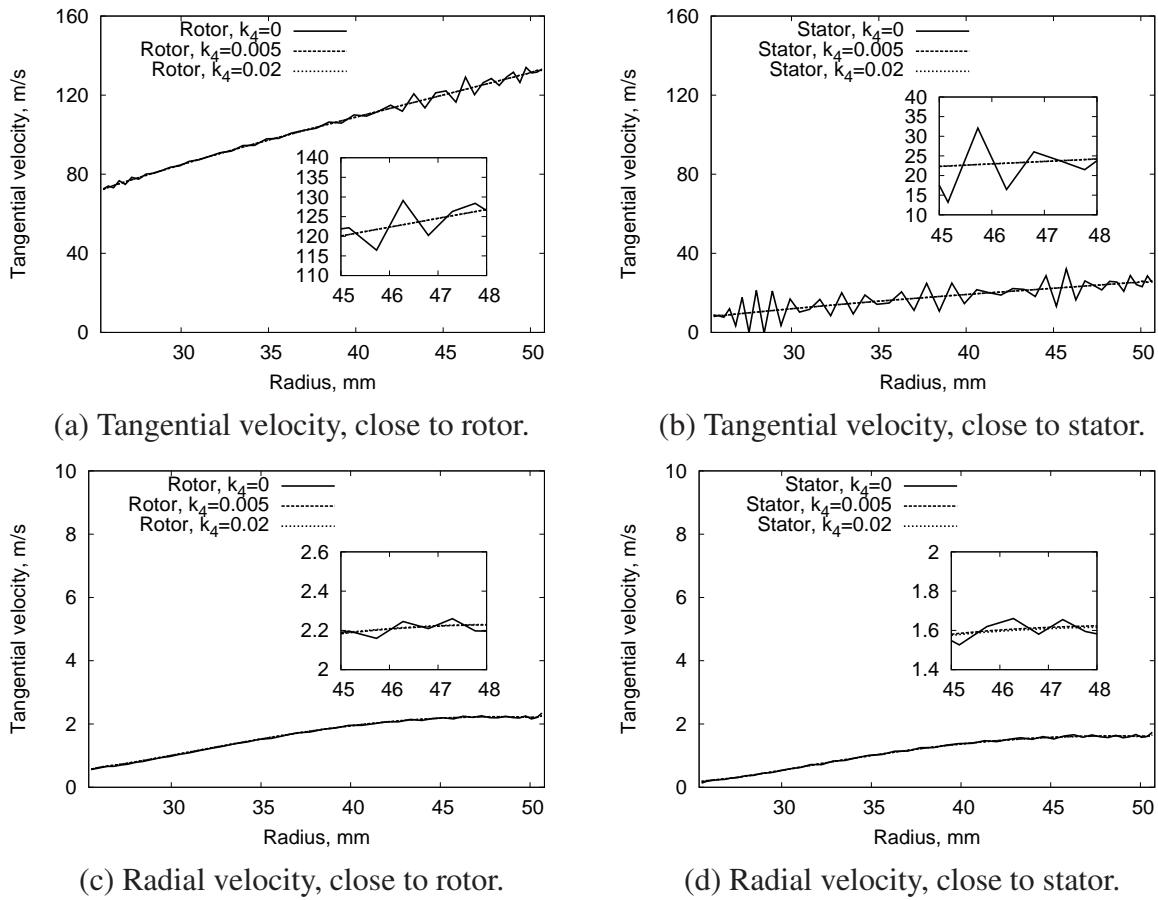


**Figure 3.24:** Comparison of tangential and radial velocities at a circumferential angle of 44.46°.

and 3.23. These results are obtained from simulations with and without artificial dissipation using the time steps listed in Table 3.8. The study of foil thrust bearings at this rotational speed was also performed with the  $k_4$  of 0.005. This additional case is used to investigate the impact of different  $k_4$  on the simulations. It is shown in Figure 3.22 that the pressure contour is similar for these two modeling approaches and selected  $k_4$ , even if there is a small checker-boarding at the top right corner for the case without artificial dissipation. The checker-boarding effect is more obvious for velocity contours as highlighted with by the circle in Figure 3.23. This effect can be fully eliminated by the addition of the fourth-order artificial dissipation. To further investigate the influence of the artificial dissipation, tangential and radial velocities at the first cell from the rotor and stator at an angle of  $44.46^\circ$  are compared in Figure 3.24. Due to the checker-boarding effect, the tangential and radial velocities exhibit a zigzag distribution in the radial direction. The fluctuation amplitude of the tangential and radial velocity are as high as 15 m/s and 0.2 m/s, respectively. This non-physical behaviour is successfully smoothed with the addition of the artificial dissipation, of either  $k_4=0.005$  or  $k_4=0.02$ . The relative difference between different  $k_4$  (0.005 and 0.02) is less than 0.3%. This shows that this artificial dissipation can be used to stabilise the simulations without creating new non-physical effects or affecting the solution accuracy.

### Selection of Appropriate Damping Coefficients

This section investigates the minimum  $k_4$  to stabilise the turbulent simulations for Couette type flow. It is noted that the checker-boarding effect is not observed in two dimensional simulations for the hybrid pressure and shear driven flows. The three dimensional turbulent simulations are performed for CO<sub>2</sub> foil thrust bearings, with the geometry in accordance to Table. 2.1. The pressure and temperature boundary conditions are set as 1.4 MPa and 300 K. The results are obtained by evaluating the turbulent simulations of foil thrust bearings at three rotational speeds (20 000 rpm, 30 000 rpm and 40 000 rpm) and three minimum rotor stator separation (14  $\mu\text{m}$ , 18  $\mu\text{m}$  and 22  $\mu\text{m}$ ). A computational mesh of  $48 \times 96 \times 15$  is set for all cases, resulting in different cell aspect ratios.

The minimum requirement for  $k_4$  to stabilise the turbulent simulations for foil thrust bearings are listed in Table 3.9. For the selected operating conditions,  $k_4$  less than 0.01 is typically sufficient. It is found that the minimum  $k_4$  varies with rotational speed and cell aspect ratio. For fixed rotational speeds, the higher cell aspect ratios require large  $k_4$  to stabilise simulations. A similar trend is found for increasing rotational speed at fixed cell aspect ratio, which requires a larger  $k_4$  to stabilise the

**Table 3.9:** Matrix of rotational speeds and minimum rotor to top foil separation to show trends in  $k_4$  required to stabilise simulations.

	14 $\mu\text{m}$	18 $\mu\text{m}$	22 $\mu\text{m}$
20 000 rpm	0.006	0.004	0.003
30 000 rpm	0.008	0.006	0.005
40 000 rpm	0.01	0.009	0.007

turbulent simulations of foil thrust bearings. As discussed previously,  $k_4$  between 0.005 and 0.02 have a negligible influence on the flow field. Therefore, it is recommended that a  $k_4$  larger than 0.01 is selected to ensure stable foil bearing simulations.

### 3.5 Conclusions

This chapter describes the development and validation of the CFD code Eilmer for foil bearing simulations. Three different test cases are simulated to verify the predictions from Eilmer. The moving wall and periodic boundary conditions are verified with Taylor Couette flow, while the suitability of Eilmer in simulating centrifugal and inertial effects is verified by simulations of high speed air thrust bearings. For wavy thrust bearings with more complex geometry, CFD results show good agreement compared to Reynolds equation for symmetric wavy as well as a high compression geometry. For turbulent simulations, two new features: wall functions and a fourth-order artificial dissipation, are added to Eilmer. The implemented compressible wall function from Nichols et al. [137] is able to correctly simulate hybrid pressure and shear driven flows, typical for foil bearings. A  $y^+$  value at the first cell from the wall of less than 20 is required to accurately calculate the wall shear stress for the studied geometries. Wilcox's 2006  $k - \omega$  model is found to be one of most accurate turbulence models for hybrid pressure and shear driven flows compared to other models including: SST  $k - \omega$ , Spalart Allmaras, standard  $k - \epsilon$  and Nonlinear  $k - \epsilon$  Shih. It is also demonstrated that the inclusion of a fourth-order artificial dissipation has no influence on the spatial accuracy of Eilmer, and that second order accuracy is still maintained. The fourth-order artificial dissipation can speed up turbulent simulations within foil thrust bearings, while ensuring a stable and accurate computation without contaminating the fluid flow. For the test case used in this Chapter, a speed-up of 6.57 times is achieved at a rotational speed of 40 000 rpm. The minimum  $k_4$  value for stabilising turbulent simulations increases in terms of the rotational speed and cell aspect ratio. It is recommended that a  $k_4$

dissipation constant between 0.01 and 0.02 is selected.

# Fluid-Structure Coupled Simulations

---

## 4.1 Introduction

To model the influence of structural deformation of the foil elements on the fluid flow, a moving grid capability is added to Eilmer. In this chapter, the fundamental theory of moving grids and structural deformation is addressed, and a small number of test cases are presented to test the suitability of the developed solvers, both Eilmer with moving grid and the structural deformation solver for foil bearings. Section 4.2 details the theory behind the moving grid. Section 4.3 investigates the suitability of Eilmer to simulate a range of test cases with moving grid. Section 4.4 documents the structural deformation model for the top and bump foils and the associated verification case. Finally, the coupling strategy between fluid and structural deformation solver is introduced and verified in Section 4.5.

## 4.2 Moving Grid

Due to the formulation of Eilmer, which uses boundary conforming grids, to effectively couple fluid and structure simulation, a moving grid has to be implemented. The governing equations for the compressible flow solver are still the same as Equation B.1, but the terms within the convective and viscous flux expressions need to be altered to account for grid movement.

### 4.2.1 Convective Flux Update with Moving Grid

For the convective flux with moving grid, the interface moving velocity  $\mathbf{w}_{if}$  is incorporated into the convective flux  $\mathbf{F}_i$  [149, 150],

$$\mathbf{F}_i = \begin{bmatrix} G \\ \mathbf{L} \\ H \end{bmatrix} = \begin{bmatrix} \rho(\mathbf{u} - \mathbf{w}_{if}) \cdot \hat{\mathbf{n}} \\ \rho(\mathbf{u} - \mathbf{w}_{if})\mathbf{u} \cdot \hat{\mathbf{n}} + p \hat{\mathbf{n}} \\ \rho E(\mathbf{u} - \mathbf{w}_{if}) \cdot \hat{\mathbf{n}} + p \mathbf{u} \cdot \hat{\mathbf{n}} \end{bmatrix}. \quad (4.1)$$

so that the convective flux  $\mathbf{F}'_i$  relative to the interface (mass flux  $G'$ , momentum flux  $\mathbf{L}'$  and energy flux  $H'$ ) can be determined from the left and right interface flow states as,

$$\mathbf{F}'_i = \begin{bmatrix} G' \\ \mathbf{L}' \\ H' \end{bmatrix} = \begin{bmatrix} \rho(\mathbf{u} - \mathbf{w}_{if}) \cdot \hat{\mathbf{n}} \\ \rho(\mathbf{u} - \mathbf{w}_{if})(\mathbf{u} - \mathbf{w}_{if}) \cdot \hat{\mathbf{n}} + p \hat{\mathbf{n}} \\ \rho E(\mathbf{u} - \mathbf{w}_{if}) \cdot \hat{\mathbf{n}} + p(\mathbf{u} - \mathbf{w}_{if}) \cdot \hat{\mathbf{n}} \end{bmatrix}. \quad (4.2)$$

These can be calculated with flux scheme like Liou and Steffen's AUSM scheme [151], Wada and Liou's AUSMDV scheme [152] and Macrossan's EFM scheme [153]. The convective flux relative to the interface can then be transformed to the global reference frame using the following transformation [153],

$$G = G', \quad (4.3)$$

$$\mathbf{L} = \mathbf{L}' + G' \mathbf{w}_{if}, \quad (4.4)$$

$$H = H' + \frac{1}{2}G' |\mathbf{w}_{if}| + \mathbf{L}' \cdot \mathbf{w}_{if}. \quad (4.5)$$

The key parameter is the effective interface moving velocity  $\mathbf{w}_{if}$  as reported by Petrie-Repar [149] and Johnston [150]. Correct selection ensures that the Geometric Conservation Law is satisfied, which implies that any extra volume accumulated by one cell is accounted for by loss of the same volume from other cells or movement of the domain boundaries. Thus, for a single cell, the effective swept volumes  $V_{if}$ , defined by two faces  $[ABCD]_n$  and  $[ABCD]_{if}$ , must be equal to volume change due to the discretised grid motion defined by the volume between ( $[ABCD]_n$  and  $[ABCD]_{n+1}$ ), as depicted

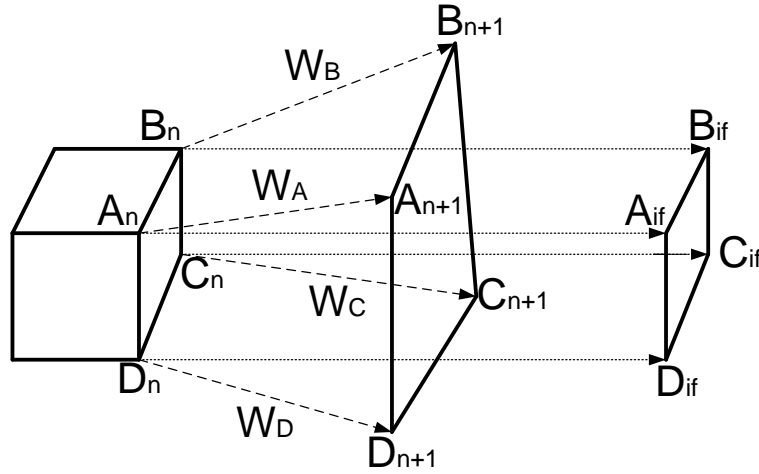


**Figure 4.1:** Schematic diagram for the moving interface.  $A_n, B_n, C_n, D_n$  are the vertices at time  $n$ ,  $A_{n+1}, B_{n+1}, C_{n+1}, D_{n+1}$  is the vertices at time  $n + 1$ .  $A_{if}, B_{if}, C_{if}, D_{if}$  are the effective vertices at time  $n + 1$ , used to calculate the swept volume  $V_{if}$ .  $W_A, W_B, W_C, W_D$  grid-velocities associated with the vertices.

in Figure 4.1. The effective interface moving velocity  $w_{if}$  can then be defined as,

$$w_{if} \cdot \hat{\mathbf{n}} = \frac{V_{if}}{A_{if} \Delta t} \tag{4.6}$$

Ambrosi et al. [154] stated a method to calculate the effective interface velocity for two-dimensional meshes. This can be found in Petrie-Repar’s PhD thesis [149]. The motion of boundary edges in two dimensions is composed of two triangles and the effective moving area in two dimensions is then calculated with the sum of these two triangles. For three-dimensional meshes, Grandy [155] presented a way to calculate the effective volume. The motion of the boundary interface is divided into six pyramids for three dimensional meshes and then the effective volume is the sum of these individual pyramid.

The time-evolution equation for the conserved quantities (Equation B.5) can now be integrated in time. The predictor-corrector scheme is selected to integrate the governing equation and the cell-averaged conserved quantities in Equation B.5 are advanced from time  $n$  to time  $n + 1$ , which is

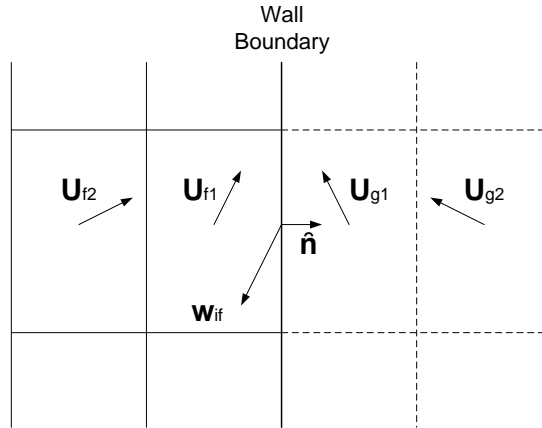


**Figure 4.2:** Ghost cell configuration for a slip wall condition.

shown as,

$$\Delta \mathbf{U}^1 = \sum (\mathbf{F}_i \cdot \mathbf{S})^n \Delta t , \quad (4.7)$$

$$\mathbf{U}^1 = \frac{V^n \mathbf{U}^n + \Delta \mathbf{U}^1}{V^{n+1}} , \quad (4.8)$$

$$\Delta \mathbf{U}^2 = \sum (\mathbf{F}_i \cdot \mathbf{S})^1 \Delta t , \quad (4.9)$$

$$\mathbf{U}^{n+1} = \mathbf{U}^1 + \frac{\Delta \mathbf{U}^2 - \Delta \mathbf{U}^1}{2V^{n+1}} . \quad (4.10)$$

The superscripts 1 and 2 indicate intermediate results used in the predictor-corrector time-step. The convective component of boundary conditions is implemented by filling in the ghost-cell data and then applying the normal reconstruction and flux calculation without further discrimination of the boundary cells. This approach works for solid walls, inflow, and outflow boundaries, as shown in Figure 4.2. For computing gas transport due to convective fluxes, the interface moving velocity at the wall boundary should be considered when reflecting the velocities in ghost cells to ensure a zero mass flux through wall boundaries [150]. This can be stated as,

$$(\mathbf{u}_{f1} - \mathbf{w}_{if}) \cdot \hat{\mathbf{n}} = -(\mathbf{u}_{g1} - \mathbf{w}_{if}) \cdot \hat{\mathbf{n}} , \quad (4.11)$$

$$(\mathbf{u}_{f2} - \mathbf{w}_{if}) \cdot \hat{\mathbf{n}} = -(\mathbf{u}_{g2} - \mathbf{w}_{if}) \cdot \hat{\mathbf{n}} . \quad (4.12)$$

### 4.2.2 Viscous Flux Update with Moving Grid

Viscous fluxes,  $F_v$  in Eilmer are evaluated separately to the convective fluxes,  $F_i$  and after the grid has moved. Internal to the mesh, the moving grid does not have to be included in the evaluation of viscous fluxes, as viscous fluxes are updated after the grid has moved. However, the moving grid must be considered for the wall boundary conditions. Viscous boundary conditions in Eilmer use data specified at cell faces that lie along the boundary surface. At those locations, the tangential component of the interface moving velocity must be included in the boundary velocity to correctly compute the spatial derivatives used in the evaluation of the viscous fluxes. In the current implementation, the tangential velocity at cell interfaces is approximated by averaging the vertex velocities,

$$\mathbf{w}_a = \frac{\mathbf{w}_A + \mathbf{w}_B + \mathbf{w}_C + \mathbf{w}_D}{4}, \quad (4.13)$$

$$\mathbf{w}_{if} = (\mathbf{w}_a \cdot \hat{\mathbf{t}}) \hat{\mathbf{t}}. \quad (4.14)$$

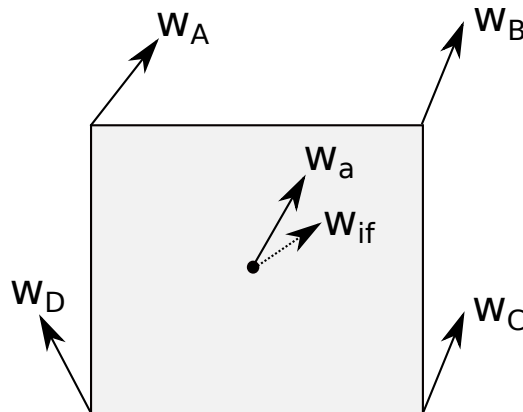


**Figure 4.3:** Schematic diagram for tangential moving velocity.

The schematic diagram of the tangential moving velocity  $w_{if}$  obtained from the vertices  $w_A$ ,  $w_B$ ,  $w_C$  and  $w_D$  are shown in Figure 4.3.

## 4.3 Fluid-Structure Simulation: Test Cases

A number of test cases were simulated to verify and validate the moving grid implementation in Eilmer. In this section, a randomly moving grid, a constant velocity piston in a tube, and an accelerating projectile in a tube, the inviscid flow about a pitching airfoil, the viscous flow over an oscillating

plate, and turbulent flow about a pitching airfoil are discussed. Together, these examples provide a thorough demonstration of the moving-grid capability that has been implemented in Eilmer.

### 4.3.1 Random Grid Motion

The first test case is random grid motion, an approach that has been used by several authors [149, 150, 156, 157] developing CFD code with moving grids. It verifies that mass, momentum, and energy are conserved in Eilmer.

The initial  $10 \times 10$  two-dimensional mesh for this test case is shown in Figure 4.4(a). The initial density, pressure and temperature in the simulation domain are  $1.168 \text{ kg/m}^3$ ,  $100 \text{ kPa}$  and  $300 \text{ K}$ , respectively, and the velocity is set to zero. The internal vertices of the mesh, are assigned random velocities with the  $x$  and  $y$  components varying between  $-0.4 \text{ m/s}$  and  $0.4 \text{ m/s}$ , and the velocity of the external vertices are set to zero. If the scheme is correct, density, pressure and temperature should remain constant and the flow velocity zero.

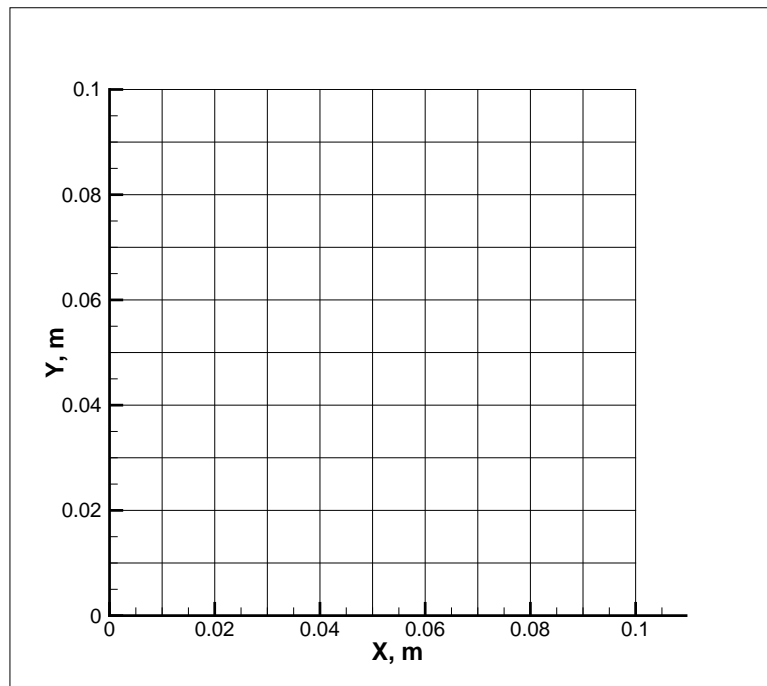
The simulation was run for 607 steps to a simulation time of  $5.0 \text{ ms}$ . The final mesh is shown in Figure 4.4(b). Density, pressure and temperature remained constant and the maximum change in velocity for all cells within the simulation domain is  $9.521 \times 10^{-14} \text{ m/s}$ . This is close to machine precision and verifies that the code satisfies the Geometric Conservation Law. A three-dimensional mesh with random grid motion was also simulated, the initial states were the same as used for the two-dimensional mesh, and the maximum change in velocity was less than  $1.0 \times 10^{-13} \text{ m/s}$ , while the other parameters remained the same. This confirms Geometric Conservation Law is also satisfied for 3D meshes.

These results verify the calculation of the effective interface moving velocity for 2D and 3D meshes. At the same time, the correct implementation of predictor-corrector time-stepping scheme in Eilmer is also tested.

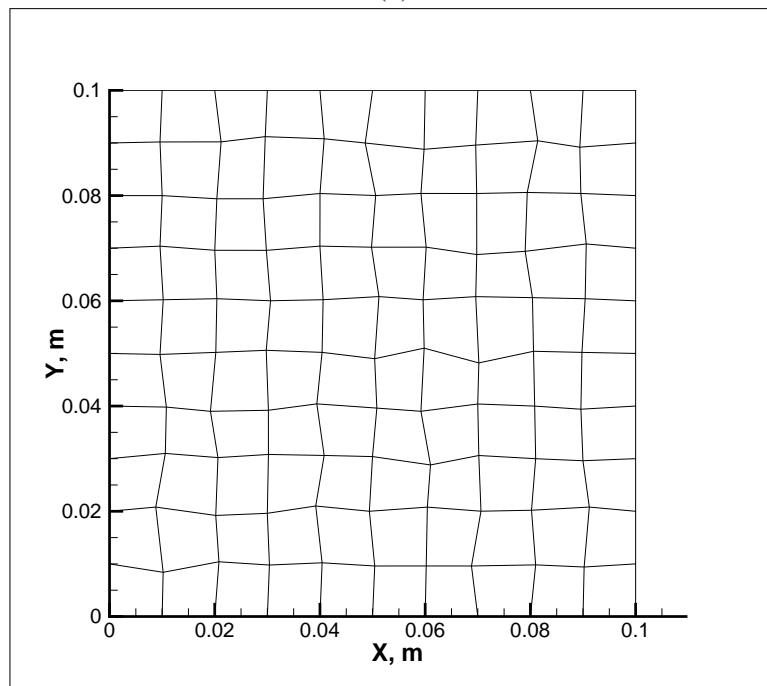
### 4.3.2 Constant Velocity Piston

The problem of a piston moving with a constant velocity in an inviscid shock tube has an analytical solution [158] and is used to verify that the code can solve the Euler equations accurately in a moving reference frame.

This test case is performed on a grid of  $320 \times 20$  cells. The 2D simulation domain is  $0.8 \text{ m}$  long and  $0.04 \text{ m}$  wide. It is filled initially with quiescent perfect air at  $\rho=1 \text{ kg/m}^3$  and  $p=100 \text{ kPa}$ . The



(a)



(b)

**Figure 4.4:** (a) Initial two-dimensional mesh for random grid motion, (b) final two-dimensional mesh.

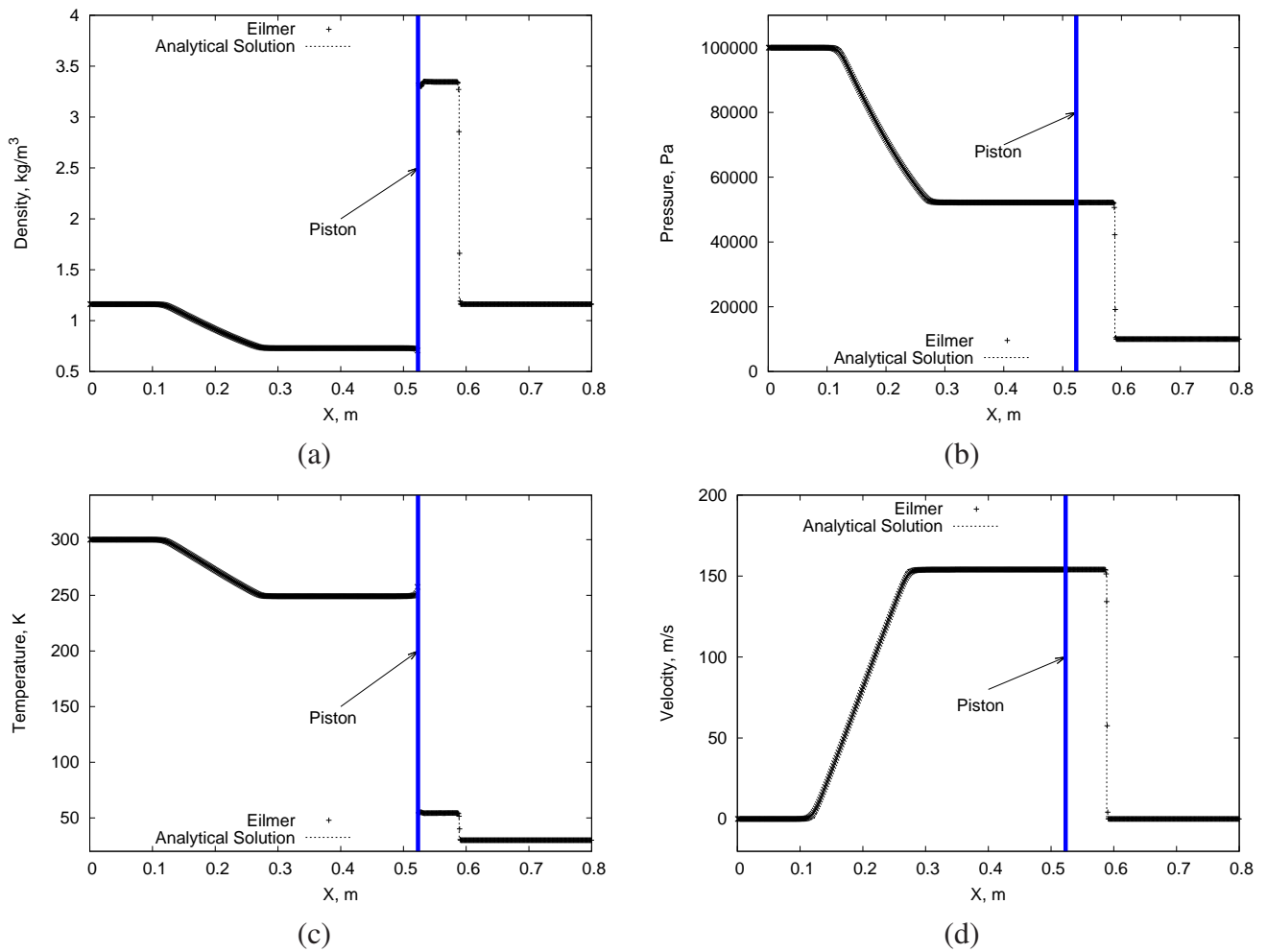


**Figure 4.5:** Comparison results of Eilmer and analytical solution, (a) density, (b) pressure, (c) temperature, (d) velocity.

piston moves at a constant velocity of  $u=154 \text{ m/s}$ ,  $v=0 \text{ m/s}$ . Profiles of pressure, temperature, density and  $x$ -velocity are extracted from the centerline after  $800 \mu\text{s}$  and compared with the analytical solution derived from wave theory. The numerical results are in excellent agreement with analytical values as shown in Figure 4.5. Note that there is a deviation in the density and temperature profile near the piston location. This is also presented by authors of [156, 157, 159]. This case demonstrates the correct implementation of wall boundaries that have a velocity component normal to the wall.

### 4.3.3 Projectile in Tube

The motion of a projectile in a tube is examined to verify the ability of the code to solve coupled fluid-structure interaction. This case has been analysed by L1D [160], a quasi-one-dimensional Lagrangian

code for modeling of free-piston-driven shock tunnels. Moreover, an analytical solution for this flow problem, is reported in by Jacobs [160].

The simulation geometry is a tube with a constant diameter of 10 mm. The reservoir gas extends from 0 to 4 m. There is no gas in front of the piston. The length of the piston is 0.01 m, with mass 0.001 kg. The schematic diagram is illustrated in Figure 4.6. The initial flow condition are the same as the test case in Ref. [160]. The density, pressure and temperature are  $1.0 \text{ kg/m}^3$ , 100 kPa and 348.4 K, respectively.

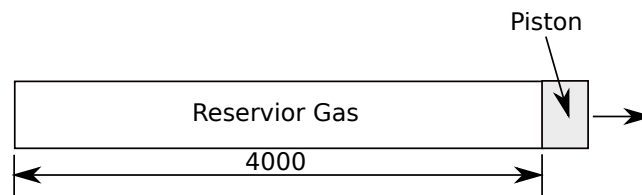


**Figure 4.6:** Schematic diagram of projectile in tube, dimensions in mm.

The simulation starts at  $t = 0$  with the release of the projectile. The projectile accelerates along the tube and allows the driver gas to expand behind it. A grid of  $96 \times 10$  cells is used to simulate the tube behind the projectile. The pressure at the end wall and piston face are recorded and compared with the result from L1D [160] in Figure 4.7. The change of pressure at end wall at  $t \approx 10$  ms is due to the expansion propagating to the left into the quiescent driver gas reflecting off the end of the tube. The decreases of pressure on piston face at  $t \approx 23$  ms is caused by the reflected expansion wave reaching the piston [160]. The position and velocity of the piston at each time step are also recorded. The comparison with L1D, and ideal solution, is shown in Figure 4.8. There is a deviation between piston position and velocity in results from Eilmer after  $x = 3$  and the ideal solution. The same was also noted in L1D. The ideal solution assumes an infinitely long driver and an vacuum in front of the projectile. The deviation is caused by the expansion that reaches the projectile. This test case indicates Eilmer is capable of simulating coupled inviscid fluid-structure problems.

#### 4.3.4 Pitching NACA0012 Airfoil

The pitching NACA0012 airfoil is to test moving grids used for inviscid simulations. Experimental results from AGARD report [161] document the unsteady transonic flow over a NACA0012 airfoil. The airfoil undergoes pitching oscillations around a point on the chord, one quarter chord length from

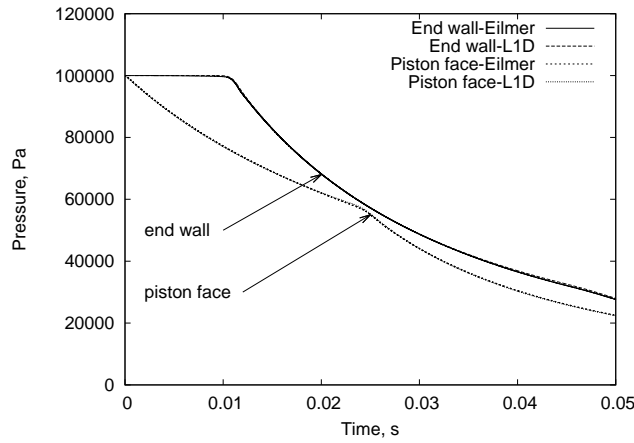
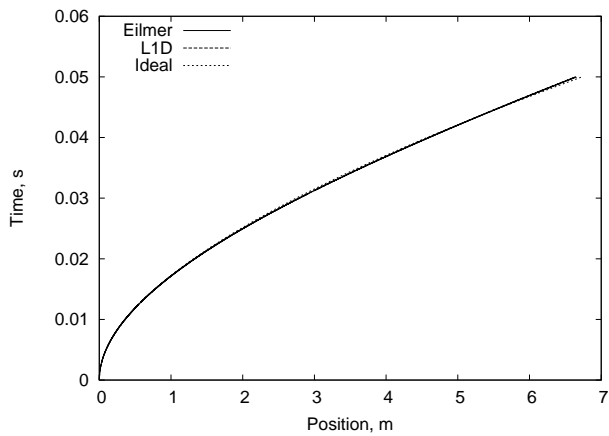
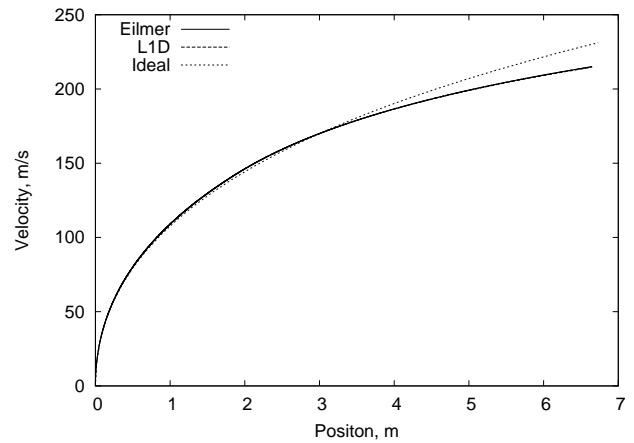


**Figure 4.7:** Comparison of pressure at end wall and piston face.



(a)



(b)

**Figure 4.8:** Comparison of results between Eilmer, L1D, and ideal solution, (a) simulation time and piston position, (b) piston velocity and piston position.

the leading edge. The selected case is AGARD test case CT5. The free stream velocity,  $U_\infty$ , is parallel to the  $x$  axis and the Mach number is set to  $M=0.755$ , corresponding to a Reynolds number of  $5.5 \times 10^6$ . The oscillation cycle is defined as,

$$\alpha = \alpha_m + \alpha_0 \sin(\omega t) , \quad (4.15)$$

where the mean angle of attack is  $\alpha_m=0.016^\circ$ , and the amplitude of the pitching oscillation is  $\alpha_0=2.51^\circ$ .  $\omega$  is defined as the circular pitch frequency, which is calculated from the reduced frequency,  $\kappa=0.0814$ , defined as,

$$\kappa = \frac{\omega c}{2U_\infty} . \quad (4.16)$$

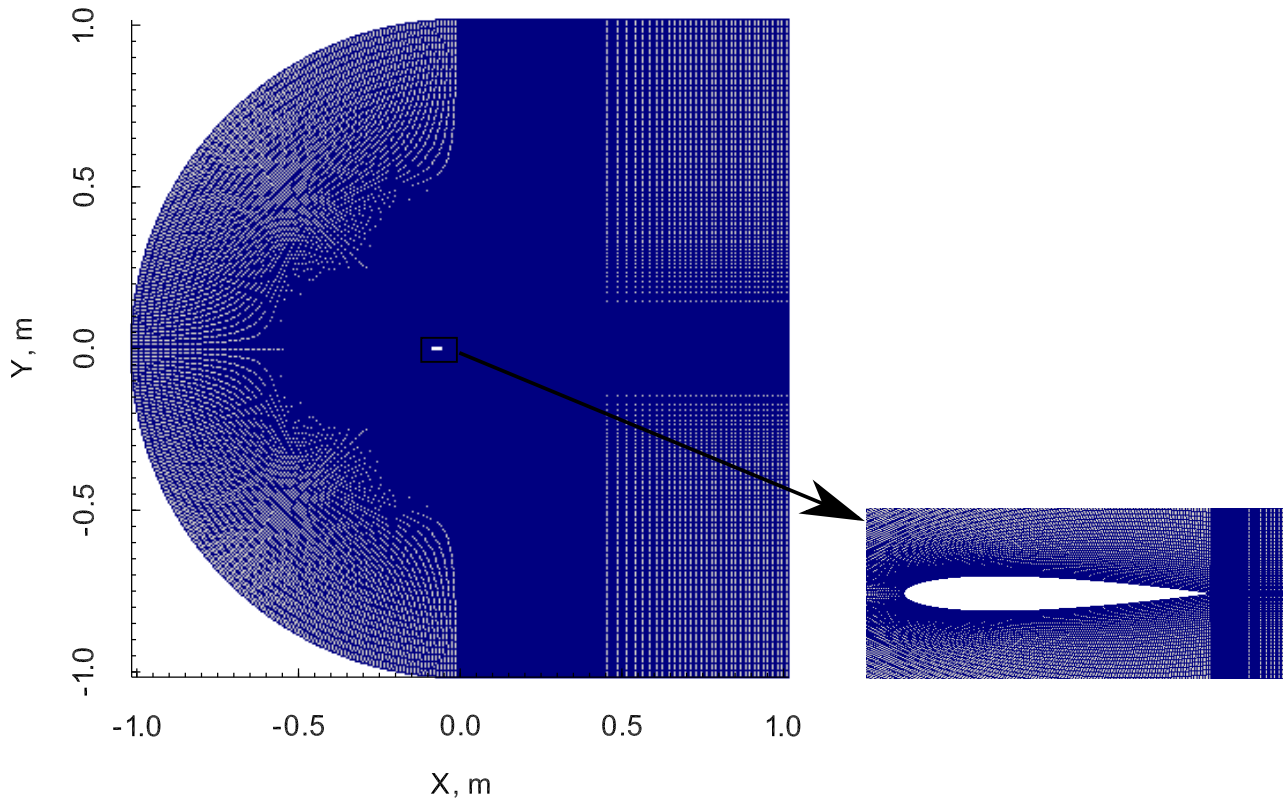
In many computations of this problem, the mesh is fixed and the free stream velocity  $U_\infty$  is rotated, however, the free-stream air velocity is set as constant and the entire mesh is rotated, including the airfoil. The grid velocity is calculated according to the angular velocity of the pitching airfoil and the distance between the grid point and the center of rotation.

Figure 4.9 shows the computational domain for the inviscid simulation of the pitching NACA0012 airfoil. The left boundary is regarded as a velocity inlet, the right is set to an extrapolation outflow boundary condition, and the airfoil surface is modeled as a fixed temperature wall. The outer boundaries are 10 chord lengths away from the airfoil. Three different sets of computational meshes are used for the grid independence study. These are a coarse mesh of  $500 \times 160$  cells, a medium mesh of  $750 \times 240$  cells and a fine mesh of  $1000 \times 320$  cells.

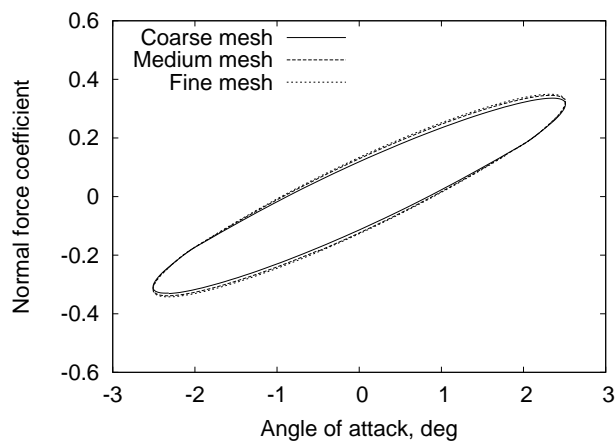
The comparison of normal force coefficient is shown in Figure 4.10. The maximum relative error between the fine and coarse mesh is 4.64 %, whereas it is 1.32 % between the fine and medium mesh. The medium computational mesh of  $750 \times 240$  cells is selected for examination of the pressure distribution and force coefficients.

Figure 4.11 compares instantaneous surface pressure between Eilmer and experiment [161]. The pressure distribution at different angles of attack is well captured by the simulation. Since the pressure is strongly influenced by the shock/boundary interaction, and the present simulation is inviscid, there is a difference in the indicated shock location.

The experiment also calculated the normal force and moment coefficients during one pitching loop. The experimental data, along with the corresponding results from the numerical simulation,



**Figure 4.9:** Computational domain for NACA0012 airfoil.



**Figure 4.10:** Grid convergence study for pitching NACA0012.

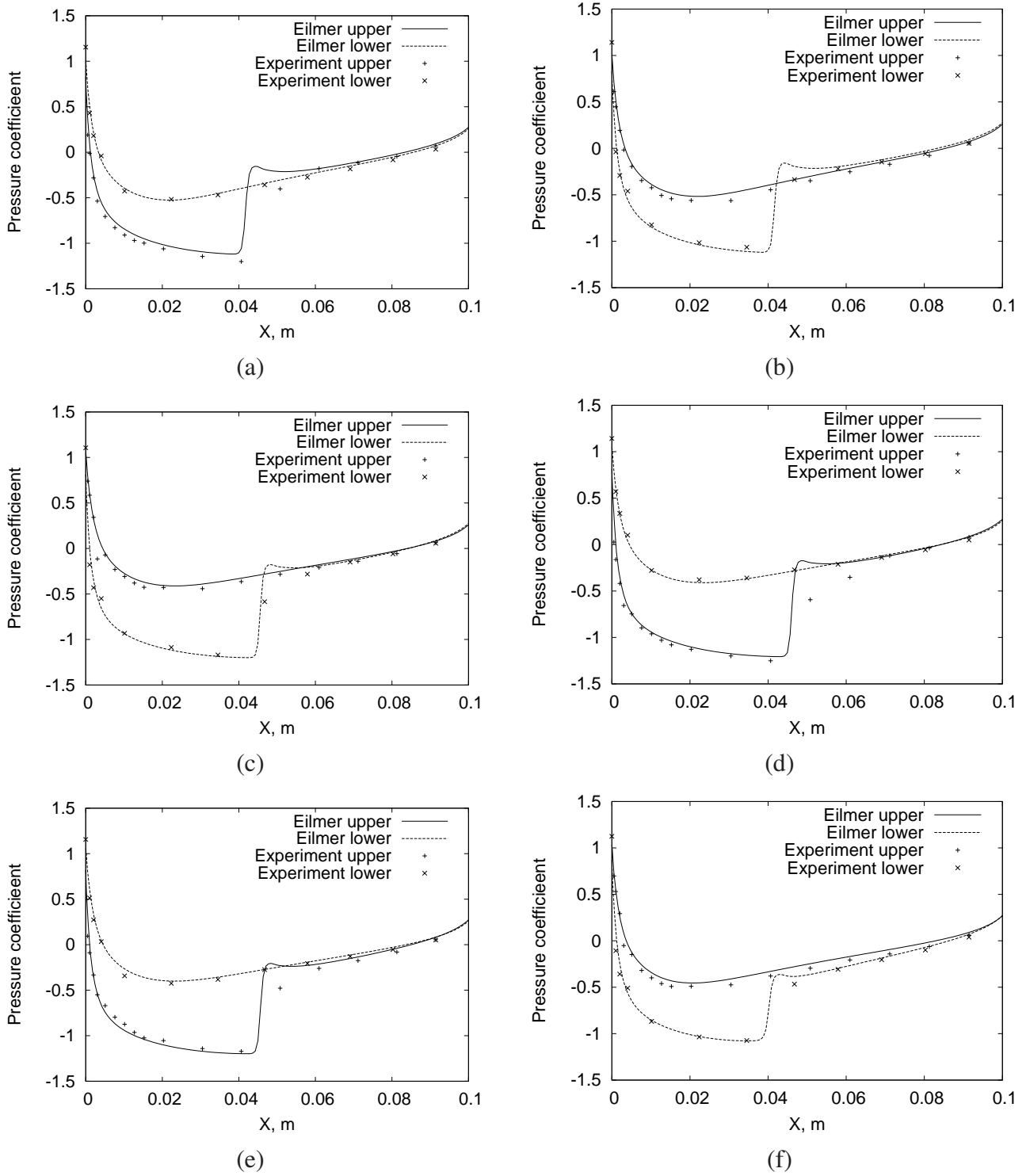


**Figure 4.11:** Instantaneous pressure coefficient, (a)  $0.52^\circ$ ,  $\downarrow$ , downward stroke, (b)  $-0.54^\circ$ ,  $\uparrow$ , upward stroke, (c)  $-2.00^\circ$ ,  $\uparrow$ , upward stroke, (d)  $2.01^\circ$ ,  $\downarrow$ , downward stroke, (e)  $2.34^\circ$ ,  $\downarrow$ , downward stroke, (f)  $-2.41^\circ$ ,  $\downarrow$ , downward stroke.

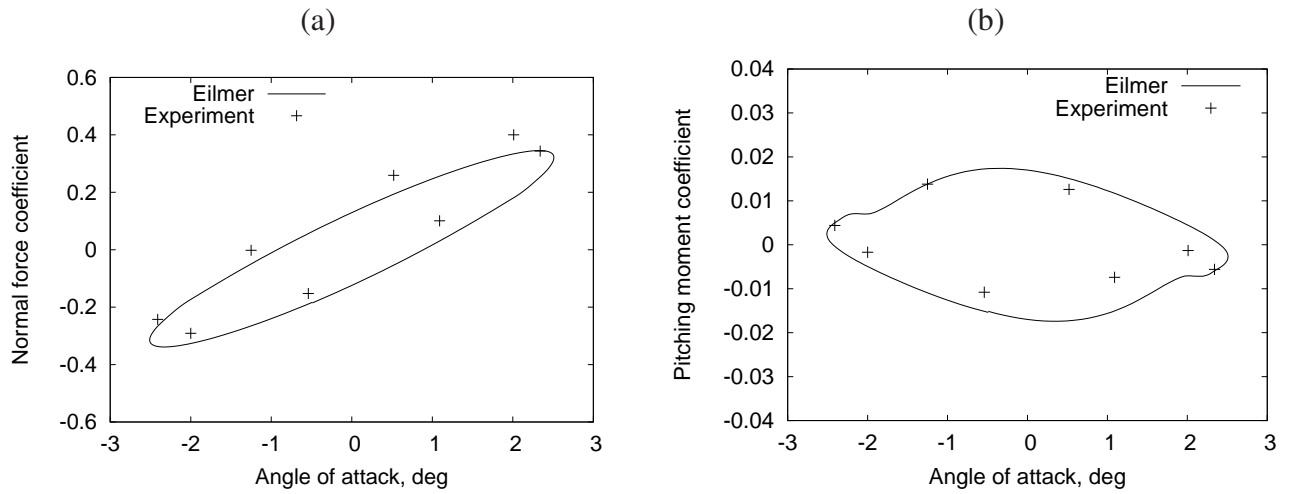


**Figure 4.12:** Comparison between Eilmer and experiment, (a) normal force coefficient, (b) moment coefficient.

are shown in Figure 4.12. The agreement is similar to what has been observed for other solvers, for example as shown in Ref. [162].

It is concluded that this test case validates the components of the code to simulate inviscid flow through a moving grid. Turbulent flow through the moving grid will be discussed separately, in Section 4.3.6.

### 4.3.5 Oscillating Plate

In order to verify the implementation of the viscous fluxes in the presence of a moving grid, the flow known as Stokes's second flow [123] is examined. This flow is the result of an infinite flat plate undergoing a time-periodic oscillatory translational motion with a stagnant fluid. The time-periodic plate velocity  $u(t)_{plate}$  is given by,

$$u(t)_{plate} = u_{max} \cos(\omega t) , \quad (4.17)$$

where  $u_{max}$  is the maximum plate velocity,  $\omega$  is the frequency of oscillation, and  $t$  is time. The resulting flow is time-periodic finally. Stokes derived an analytical solution for this flow [123], given by,

$$u(y, t) = u_{max} e^{-y\sqrt{\frac{\omega}{2\nu}}} \cos\left(\omega t - y\sqrt{\frac{\omega}{2\nu}}\right) , \quad (4.18)$$

where  $\nu$  is the kinematic viscosity of the working fluid. This equation can be solved to obtain the

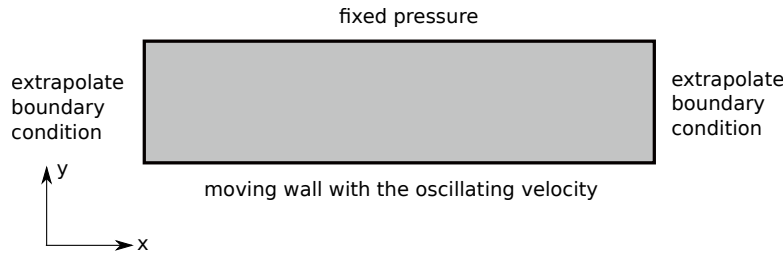


**Figure 4.13:** Computational domain for the oscillating plate.

instantaneous velocity profile. The wall shear stress  $\tau_{wall}$  can be derived from Equation 4.18 and is written as,

$$\tau_{wall} = \left. \frac{du(y, t)}{dy} \right|_{y=0} = \rho u_{wall} \sqrt{\frac{\omega \nu}{2}} (\sin(\omega t) - \cos(\omega t)) . \quad (4.19)$$

The corresponding skin friction coefficient  $C_f$  is,

$$C_f = \frac{\tau_{wall}}{0.5 \rho u_{max}^2} . \quad (4.20)$$

To simulate this flow, the computational domain of  $40 \text{ mm} \times 10 \text{ mm}$ , shown in Figure 4.13, was used. The bottom boundary was set as a wall with an oscillating translational velocity. The maximum velocity of the plate was  $u_{max} = 100 \text{ m/s}$ , and the frequency of oscillation was  $2000 \text{ rad/s}$ . The left and right boundaries were taken as an extrapolation boundary conditions, possible due to the infinite plate width, while the top was set to fixed pressure. The initial condition of the working fluid (air, in this case) was  $0.1 \text{ MPa}$  and  $300 \text{ K}$ . Three different computational meshes were used for a grid independence study. These were a coarse mesh of  $24 \times 30$  cells, a medium mesh of  $48 \times 60$  cells, and a fine mesh of  $96 \times 120$  cells. For each of these meshes, cells were clustered toward the oscillating wall to ensure the boundary layer is correctly captured. The boundary layer profile and the associated friction coefficient at a simulation time of  $1 \text{ ms}$  were extracted from these meshes and are shown in Figure 4.14. The relative differences in friction coefficient between fine and coarse meshes was less than  $1.19 \%$ , and it was  $0.09 \%$  between fine and medium meshes. It appears that the medium mesh has adequately captured the interesting features of this flow.

The instantaneous velocity profile at different phase angles is compared with Equation 4.18 in Figure 4.15. The simulation results show very good agreement with the analytical solution. The relative error is less than  $0.02 \%$ , as shown in Figure 4.15(a). Figure 4.15(b) shows the time history of

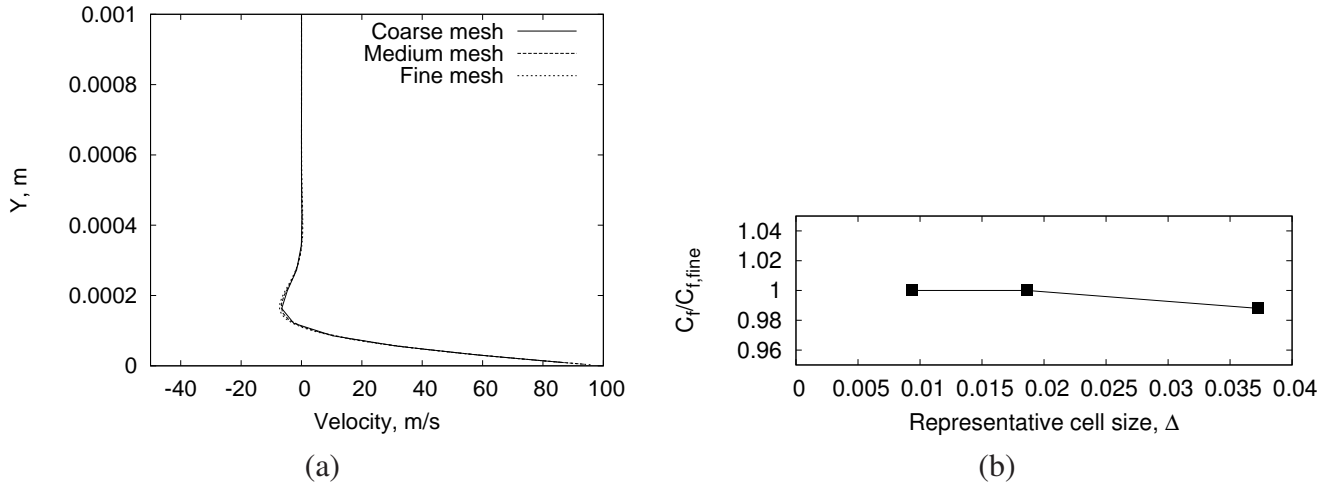


**Figure 4.14:** Grid convergence study of oscillating plate: (a) velocity distribution at 1 ms, (b) Friction coefficient over the fine mesh in terms of representative cell size at 1 ms.

the local skin friction coefficient compared with the analytic result computed by Equation 4.20. Again, very good agreement is evident. It is concluded that this test case verifies the correct implementation of the viscous fluxes for moving grid in Eilmer as well as the correct application of the tangential interface velocity at wall boundary interface when computing the spatial derivatives of flow quantities.

### 4.3.6 Pitching NACA64A010 Airfoil (Turbulent)

Finally, the simulation of viscous unsteady flow at transonic conditions is performed for the NACA 64A010 airfoil for which experimental data was reported by Davis [161]. For this test case, the flow is fully attached to the airfoil during pitching and allows us to use a two-dimensional simulation. The high Reynolds number associated with the flow provides an opportunity to test the code components for computing turbulent flow in the presence of a moving grid and pressure gradients. The pitching motion of the airfoil is defined as,

$$\alpha(t) = \alpha_m + \alpha_0 \sin(\omega t) , \quad (4.21)$$

where  $\alpha(t)$  is the instantaneous angle of attack,  $\alpha_0$  is the pitching range, and  $\alpha_m$  is the mean angle of attack. The angular frequency  $\omega$  is related to the reduced frequency  $\kappa$ , which is defined in Equation 4.16. The freestream Mach number is  $M_\infty=0.796$ ,  $\alpha_0=1.01^\circ$ ,  $\alpha_m=0^\circ$ , and  $\kappa=0.202$ . The Reynolds number based on chord length is  $1.3 \times 10^7$ , and the airfoil rotates about the quarter-chord point.

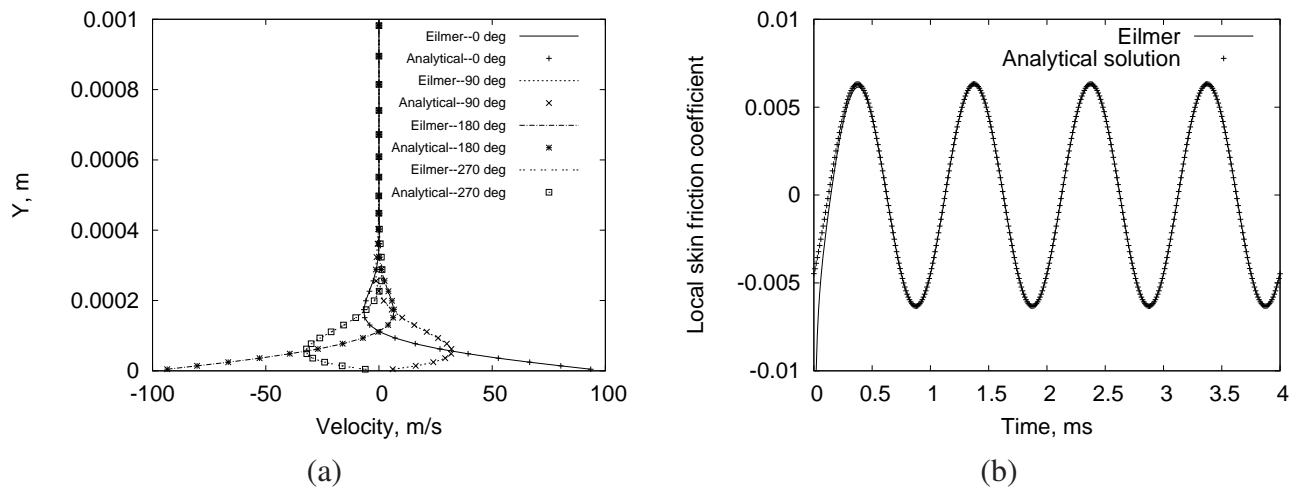


**Figure 4.15:** Comparison of results between Eilmer and analytical solution, (a) velocity profile at different phase angles, (b) local skin friction coefficient.

The computational domain for the turbulent simulation of the pitching of this airfoil was essentially the same as the pitching NACA 0012 airfoil, shown in Figure 4.9. The left boundary was regarded as velocity inlet, while the right was set as a extrapolation boundary condition. The airfoil surface was modeled as fixed temperature wall. These outer boundaries were again 10 chord lengths away from the airfoil. Three different computational meshes were used for a grid independence study. These were a coarse mesh of  $360 \times 120$  cells, a medium mesh of  $720 \times 240$  cells and a fine mesh of  $1080 \times 360$  cells. The cell spacing close to the wall is set to achieve  $y^+ < 1$  along the airfoil and there were at least 15 cells in the wall-normal direction within the boundary layer. The  $k-\omega$  two equation turbulence model was used in this simulation without a wall function.

The comparison of result for lift force is shown in Figure 4.16. The relative differences between coarse and medium mesh are less than 6.14 %, while they are only 1.7 % between medium and fine mesh. As the medium mesh calculation has a reasonable computational cost, it was selected for the following analysis.

The results for the lift and moment coefficients  $C_l$  and  $C_m$  for a pitching loop using Eilmer are shown in Figure 4.17. The lift force coefficient  $C_l$  in Figure 4.17(a) is close to experiment, however, the computation of the momentum coefficient  $C_m$  misses two pocket-like features in the experimental data between the maximum and minimum angles of attack. This difference was also evident in simulation results by Barakos and Drikakis [163]. Since aerodynamic moment is very sensitive to shock

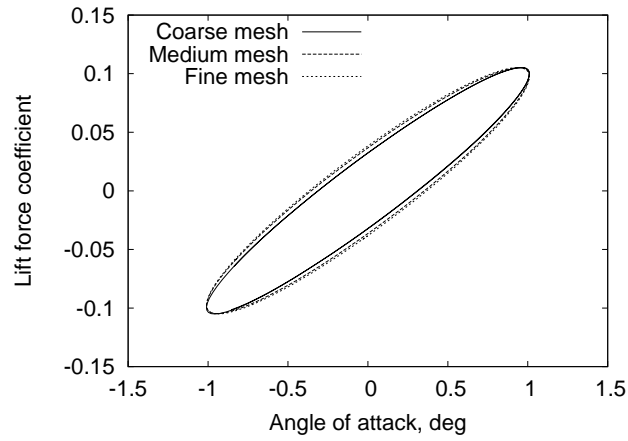


**Figure 4.16:** Grid convergence study for the pitching NACA64A010 airfoil.

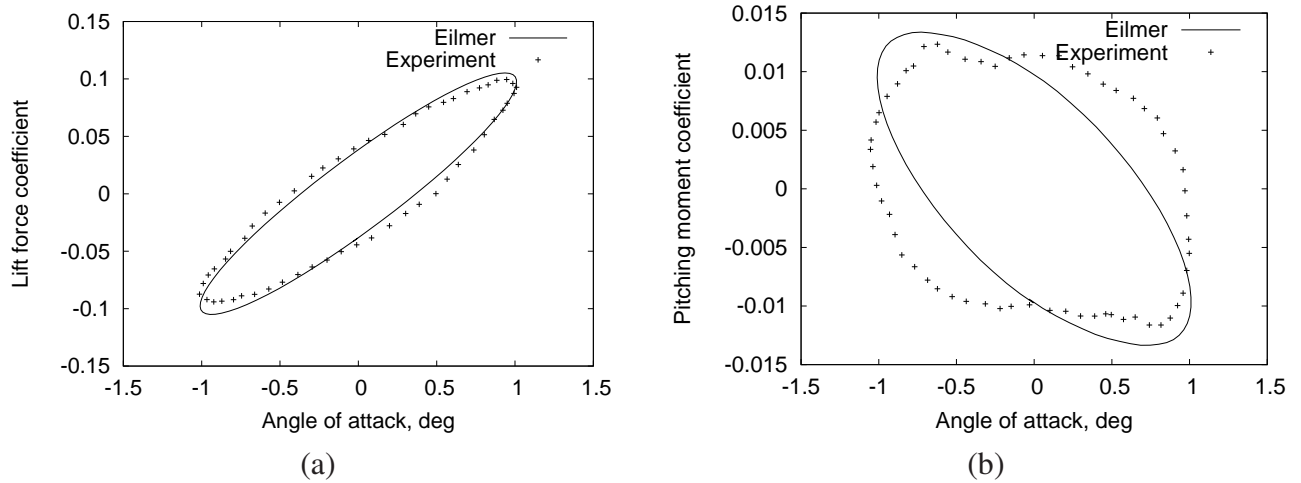


**Figure 4.17:** Comparison of results between Eilmer and experiment [161], (a) lift force coefficient  $C_l$  vs angle of attack  $\alpha$ , (b) moment coefficient  $C_m$  vs angle of attack  $\alpha$ .

locations, the details of shock/boundary-layer interaction may affect the moment significantly. Despite these small differences, it is concluded that Eilmer is capable of accurately simulating a turbulent flow through a moving grid.

## 4.4 Structural Deformation Solver

Foil bearings consist of top and bump foils as shown in Figure 2.9. The corrugated bump foil is utilised to support the plate-like top foil. During operation, the top and bump foils are deformed, due to the pressure force. The deformed parts have to be considered as the deflections are of similar size as the film thickness.

### 4.4.1 Top Foil Model

In the current study, the top foil is approximated as a circular thin plate structure. The polar coordinates  $r$  and  $\theta$  are used when solving the bending problems for the circular plate, and the governing equation, from Ref. [164] is,

$$\left(\frac{\partial^2}{\partial r^2} + \frac{1}{r} \frac{\partial}{\partial r} + \frac{1}{r^2} \frac{\partial^2}{\partial \theta^2}\right) \left(\frac{\partial^2 w}{\partial r^2} + \frac{1}{r} \frac{\partial w}{\partial r} + \frac{1}{r^2} \frac{\partial^2 w}{\partial \theta^2}\right) = \frac{q}{D} + \rho_t h_t \frac{\partial^2 w}{\partial t^2} , \quad (4.22)$$

where  $w$  is the local deflection,  $r$  is the local radius,  $\theta$  is the local angle,  $\rho_t$  and  $h_t$  are the density and thickness of the top foil,  $D$  is the stiffness of the thin pad (top foil) and  $q$  is the force acting on the top foil, defined as,

$$q = p - K_B w - C_B \dot{w} . \quad (4.23)$$

Here  $K_B$  and  $C_B$  are the stiffness and damping coefficients of the bump foils that provide support to the top foil. The stiffness of the thin plate  $D$  is defined as,

$$D = \frac{E h^3}{12(1 - \mu^3)} . \quad (4.24)$$

The above governing equation is a special case of the Kirchhoff plate equation. It is simplified considerably for isotropic and homogeneous plates for which the in-plane deformations can be neglected. The theory assumes that a mid-surface plane can be used to represent a three-dimensional plate in two-dimensional form. The assumptions are [165].

- Straight lines normal to the mid-surface remain straight after deformation;

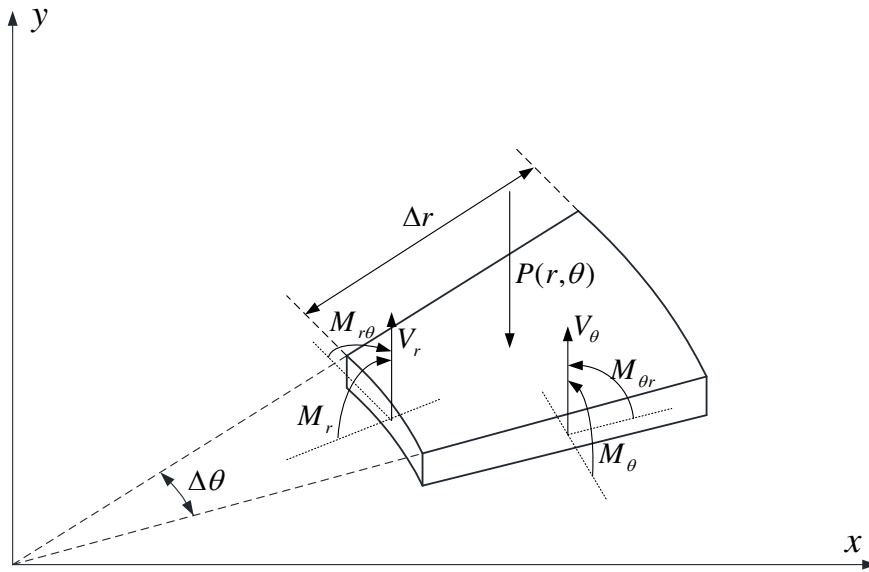


**Figure 4.18:** Schematic diagram for forces and moments.

- Straight lines normal to the mid-surface remain normal to the mid-surface after deformation;
- The thickness of the plate does not change during a deformation;
- This equation does not include in-plane tension and is only applicable for plates that carry load in bending.

This governing equation is only accurate for small deflections and for thin plates subjected to perpendicular forces and bending moments. This is applicable for the structural deformation of the top foil, as it has three free and one fixed edge and only carries load in bending.

The bending or twisting moment in the polar system are defined as  $M_r$ ,  $M_\theta$  and  $M_{r\theta}$ , and the shear forces are  $V_r$  and  $V_\theta$ , shown in Figure 4.18. The bending or twisting moments  $M_r$ ,  $M_\theta$ ,  $M_{r\theta}$  and  $M_{\theta r}$  in the polar system are defined as [164],

$$M_r = -D \left[ \frac{\partial^2 w}{\partial r^2} + \mu \left( \frac{1}{r} \frac{\partial w}{\partial r} + \frac{1}{r^2} \frac{\partial^2 w}{\partial \theta^2} \right) \right], \quad (4.25)$$

$$M_\theta = -D \left[ \frac{1}{r} \frac{\partial w}{\partial r} + \frac{1}{r^2} \frac{\partial^2 w}{\partial \theta^2} + \mu \frac{\partial^2 w}{\partial r^2} \right], \quad (4.26)$$

$$M_{r\theta} = M_{\theta r} = -D (1 - \mu) \left( \frac{1}{r} \frac{\partial^2 w}{\partial r \partial \theta} + \frac{1}{r^2} \frac{\partial w}{\partial \theta} \right). \quad (4.27)$$

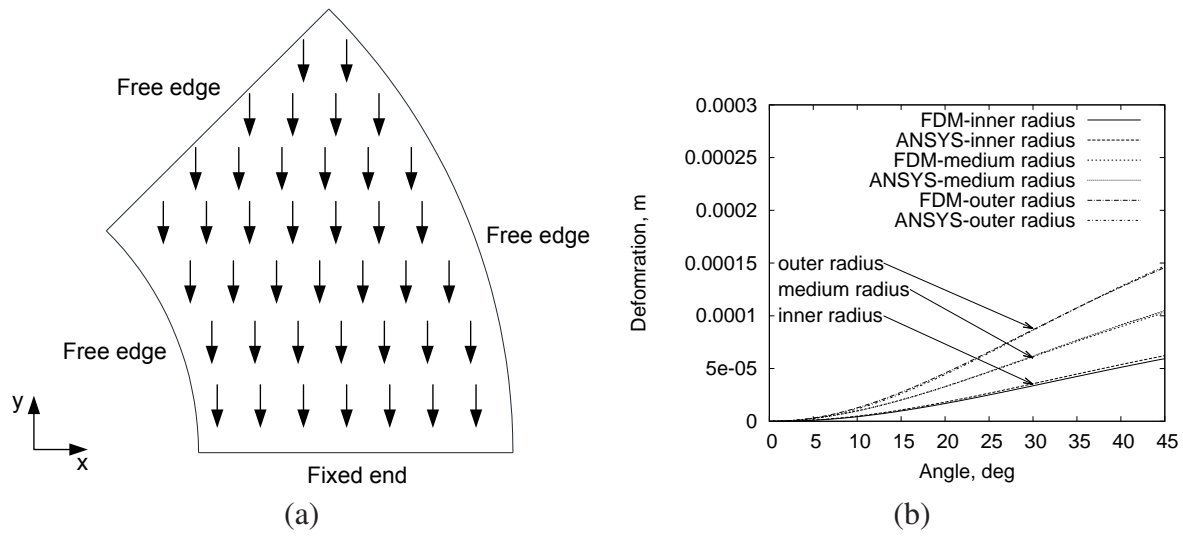


**Figure 4.19:** (a) Schematic diagram of top foil in foil bearings, (b) deformation comparison between ANSYS and the Kirchhoff plate structural deformation code at different radii.

The edge forces in radial direction  $V_r$  and in tangential direction  $V_\theta$  are defined as [164],

$$V_r = -D \left[ \frac{\partial}{\partial r} \left( \frac{\partial^2 w}{\partial r^2} + \frac{1}{r} \frac{\partial w}{\partial r} + \frac{1}{r^2} \frac{\partial^2 w}{\partial \theta^2} \right) + \frac{1-\mu}{r} \frac{\partial}{\partial \theta} \left( \frac{1}{r} \frac{\partial^2 w}{\partial r \partial \theta} - \frac{1}{r^2} \frac{\partial w}{\partial \theta} \right) \right], \quad (4.28)$$

$$V_\theta = -D \left[ \frac{1}{r} \frac{\partial}{\partial \theta} \left( \frac{\partial^2 w}{\partial r^2} + \frac{1}{r} \frac{\partial w}{\partial r} + \frac{1}{r^2} \frac{\partial^2 w}{\partial \theta^2} \right) + (1-\mu) \frac{\partial}{\partial r} \left( \frac{1}{r} \frac{\partial^2 w}{\partial r \partial \theta} - \frac{1}{r^2} \frac{\partial w}{\partial \theta} \right) \right]. \quad (4.29)$$

For the structural deformation of the top foil, the boundary conditions are shown in Figure 4.19(a): the attachment edge is a fixed end. The other boundaries are set as free edges, with constant  $r$  and  $\theta$ . In addition, a nonuniform pressure,  $p(r, \theta)$  defined by Equation 4.23, is prescribed on the top foil, as shown in Figure 4.18. The corresponding boundary conditions, constraints are:

- Fixed end at constant angle:  $\theta = 0$

$$w = 0|_{\theta=0} \quad \frac{\partial w}{\partial \theta} = 0|_{\theta=0}, \quad (4.30)$$

- Free edge at constant radius:  $r = r_0$

$$M_r = 0|_{r=r_0} \quad V_r = 0|_{r=r_0}, \quad (4.31)$$

**Table 4.1:** Operating condition of foil thrust bearings from SNL's test loop [8].

Parameters	Value
Working fluid	CO <sub>2</sub>
Ambient pressure	1.4 MPa
Ambient temperature	300 K
Inner diameter	0.0508 m
Outer diameter	0.1060 m
Designed rotational speed	75 000 rpm
Designed minimum film thickness	5 μm

- Free edge at constant angle:  $\theta = \alpha$

$$M_{\theta} = 0|_{\theta=\alpha} \quad V_{\theta} = 0|_{\theta=\alpha} \quad . \quad (4.32)$$

The finite difference method (FDM) is used to solve the bending Equation 4.22. The expanded form of Equation 4.22, neglecting the time term is,

$$\frac{\partial^4 w}{\partial r^4} + \frac{2}{r} \frac{\partial^3 w}{\partial r^3} - \frac{1}{r^2} \frac{\partial^2 w}{\partial r^2} + \frac{1}{r^3} \frac{\partial w}{\partial r} + \frac{2}{r^2} \frac{\partial^4 w}{\partial r^2 \partial \theta^2} - \frac{2}{r^3} \frac{\partial^3 w}{\partial \theta^2 \partial r} + \frac{4}{r^4} \frac{\partial^2 w}{\partial \theta^2} + \frac{1}{r^4} \frac{\partial^4 w}{\partial \theta^4} = \frac{q}{D} \quad . \quad (4.33)$$

To verify the implementation, a test case of a 45° segment of a circular thin plate is selected. The thickness of this plate is chosen as 150 μm, which is a typical thickness for the top foil [23], and a uniform pressure of 70 Pa is prescribed on the top. The inner and outer radii are the same as for the bearing used by SNL listed in Table 4.1. The material selected is stainless steel with a modulus of elasticity of 200 GPa and a Poisson's ratio of 0.3. The deflections are compared with the results from the static structural solver in ANSYS [166], which is a well-verified solver for this type of deformation problem.

A grid independence study was performed for both codes, and results are shown in Figure 4.20. The deflection at the inner, medium and outer radii of the circular thin plate from the developed structural deformation solver is compared between three different meshes: coarse mesh (100×120 cells), medium mesh (200×240 cells) and fine mesh (400×480 cells). The comparison between these different meshes is good, with the maximum relative error being less than 0.23%. The maximum deflection in terms of representative cell size,  $\Delta$ , is plotted in Figure 4.20(c) and (d). For these 2D

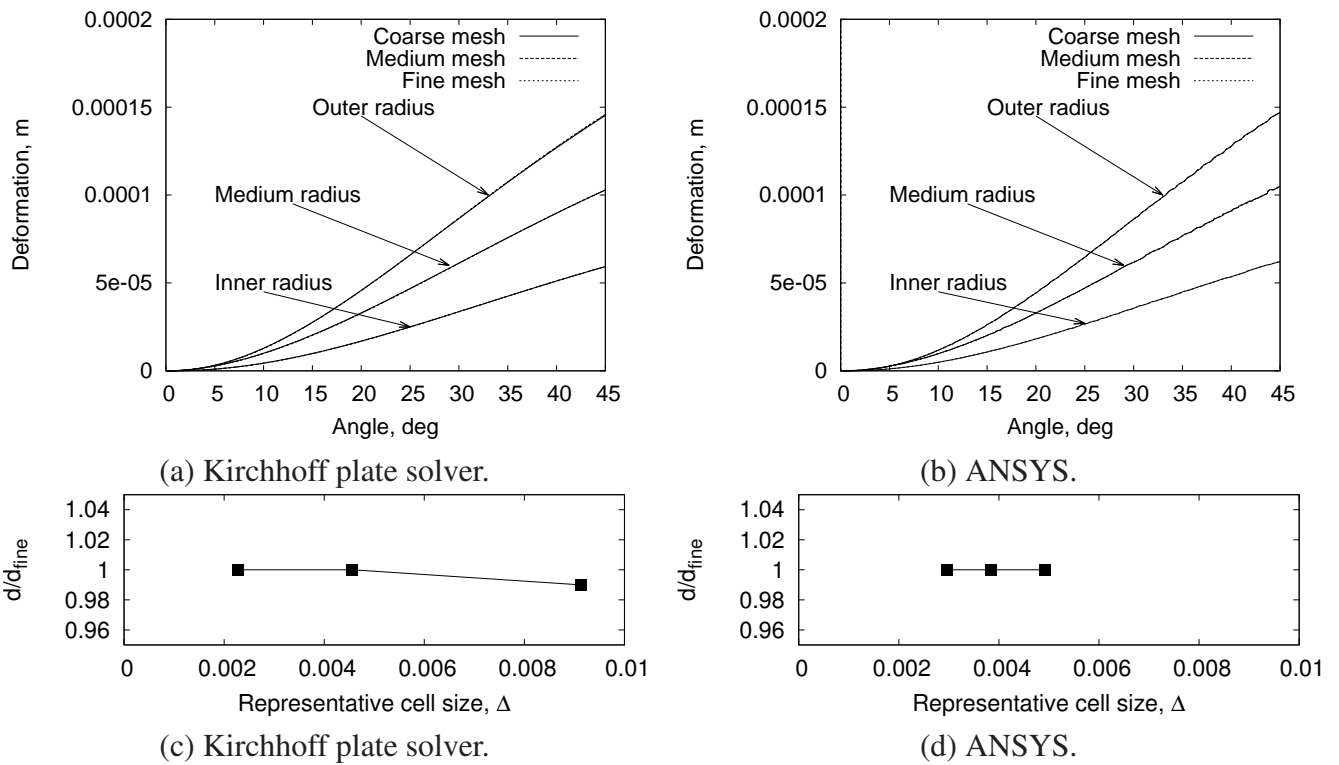


**Figure 4.20:** Grid convergence study: (a) & (b) local deflection, (c) & (d) maximum deflection.

calculations, the representative cell size,  $\Delta$ , is computed as  $\sqrt{1/N_{cells}}$ , where  $N_{cells}$  is the total number of cells for each mesh. The medium mesh shows the converged result for the maximum deflection and is selected for the structural deformation solver in the subsequent analysis. A grid independence study for the finite element solver in ANSYS was also undertaken for different meshes: coarse mesh (41 299 nodes), medium mesh (67 383 nodes) and fine mesh (113 851 nodes). The computed deformations are shown in Figure 4.20(b). The maximum relative error between different meshes is less than 0.047 %, so the coarse mesh is used in the following analysis.

The comparison result between these two codes is shown in Figure 4.19(b). The maximum relative error between the structural deformation code based on Kirchhoff plate equation and ANSYS is less than 3.5 %. It is concluded that this structural deformation solver is suitable for studying foil bearings.

### 4.4.2 Bump Foil Model

An advanced bump foil model introduced by Gad et al. [100] is selected as introduced in Section 2.5. This bump foil stiffness model considered the interaction between bumps and the friction between

bump foil and the surrounding structure, and is considered to be the most accurate bump foil model available in literature [100]. The assumptions of his model are:

- The bump foil displacement is from the fixed end to the free end;
- The deflection of the top foil follows the bump foil deflection and no relative deflection exists;
- The deflection is elastic;
- Bump ends are assumed to be a rigid support.

The calculation procedure is sequential. The calculation process is detailed in Figure 4.21.

Structural damping is required for dynamic analysis, however studies on the bump foil damping coefficient are limited. Balducchi et al. [75] experimentally determined the structural damping coefficients at various excitation frequency and load conditions. They found that the variation of structural damping with respect to frequency is small, allowing  $C_B$  to be treated as being a function of load only. Using the data from Balducchi et al. [75], a polynomial can be created, relating structural damping,  $C_B$  to load,  $F_Z$  (see Figure 4.22). This polynomial is used in the following analysis to obtain the structure damping coefficients.

## 4.5 Fluid-Structure Simulation: Coupling Strategy

Two coupling strategies are possible, weak and strong. Weak coupling between the gas-dynamic and structural-deformation solvers is when one of the solvers is held, while the other advances for a number of iterations. Weak coupling can provide a relatively fast way to reach steady-state or quasi-steady state solution, however the interface fluxes are only balanced in the final steady state. Conversely, strong coupling maintains the conservation laws at each step, and is therefore essential for time-evolving solutions. Strong coupling also means that the grid must be adapted at each flow time step and this was done for the transient validation cases discussed in this section. For the steady-state performance estimation of foil thrust bearings discussed later, the grid motion is executed at a comparatively larger but fixed time step  $\Delta t_s$  to save computational cost. The calculation update sequence is as follows:

1. The fixed-geometry foil thrust bearings are simulated with Eilmer;
2. The simulation with Eilmer is paused at  $t + \Delta t_s$ ;

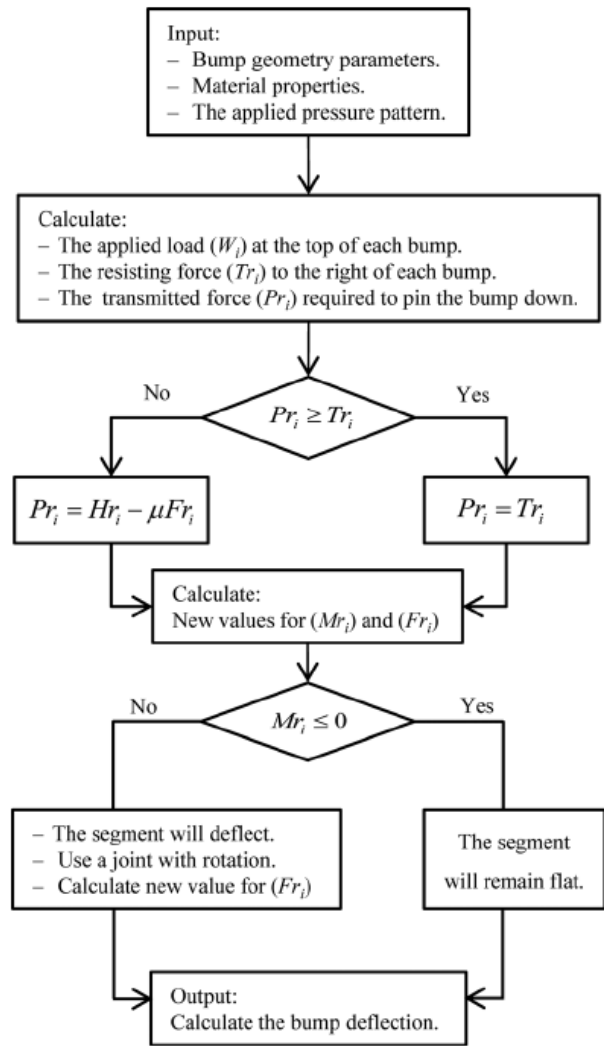
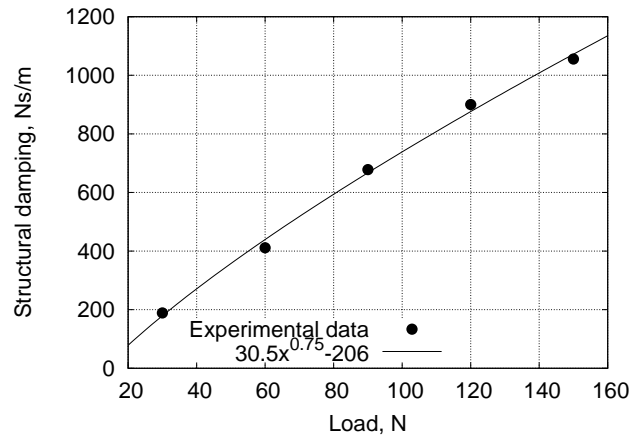


Figure 4.21: Flow chart of the bump foil model, taken from [100].



**Figure 4.22:** Structural damping coefficient,  $C_B$ .

3. Pressure load is passed from Eilmer to the structural deformation code;
4. The structural solution is updated;
5. Deflection is passed from the structural deformation code to Eilmer;
6. Grid in Eilmer is updated and fluid domain simulation continues;
7. Repeat steps 2-6 until the steady-state solution is achieved.

Since the fluid solver uses a cell-centred finite-volume method, and the structural deformation code used a node-based finite-difference formulation, and as the solvers require different meshes for grid independence, the data is stored in a different mesh for each solver. A mapping algorithm is used when passing pressure values from Eilmer to the structural deformation code and deflection from the structural deformation code back to Eilmer.

Figure 4.23 shows the stencils for mapping pressure and deflection at the fluid-structure interface. When passing pressure from Eilmer to the structure solver (pressure is stored at the cell centre in Eilmer and vertices for the structure solver), the mapping method firstly searches for neighbouring cell centre from Eilmer for each vertex in the structure solver. A bilinear interpolation method is then used to calculate pressure for the vertex of the structure solver as shown in Figure 4.23(a). This is only applied when four neighbouring cells are found; otherwise the mapping method will search for the nearest cell centre instead. The same mapping method is also applied when passing the deflection from the structure solver to Eilmer (from structure vertex to fluid mesh vertex), as shown in

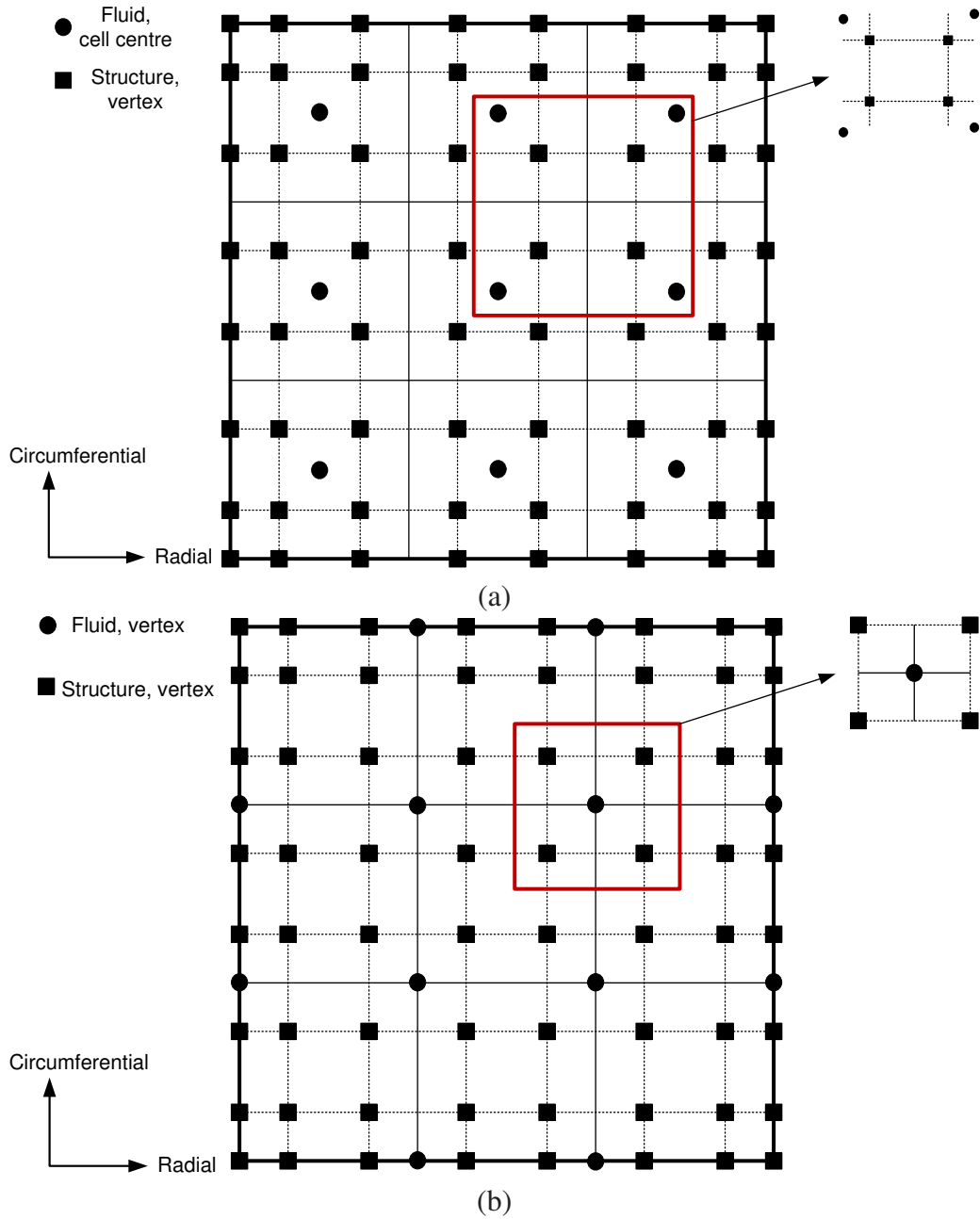


**Figure 4.23:** Stencil for mapping method at the fluid-structure interface, (a): from Eilmer to the structure solver, (b): from the structure solver to Eilmer.

**Table 4.2:** Comparison of pressure force between Eilmer and the structure solver.

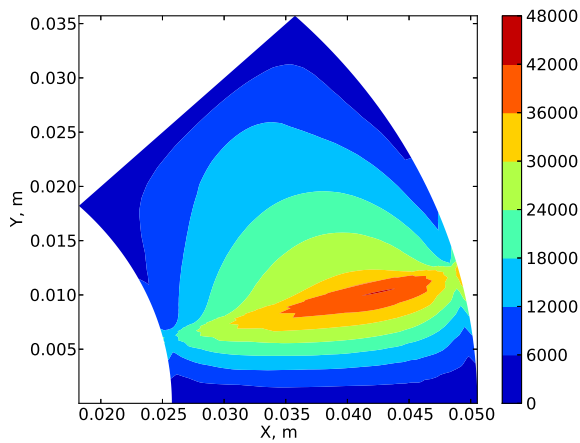
Radius range	Angle range	Force, structure	Force, Eilmer	Relative error
25.4 mm to 50.8 mm	0° to 45°	10.73 N	10.80 N	0.69 %
25.4 mm to 50.8 mm	11.48° to 12.85°	0.74 N	0.74 N	0 %
25.4 mm to 50.8 mm	15.63° to 15.93°	0.1259 N	0.1262 N	0.22 %
25.4 mm to 50.8 mm	18.29° to 19.31°	0.364 N	0.363 N	0.23 %
25.4 mm to 50.8 mm	25.71° to 27.81°	0.475 N	0.477 N	0.37 %
25.4 mm to 50.8 mm	36.24° to 37.96°	0.21 N	0.22 N	0.39 %

Figure 4.23(b). This coupling approach usually requires fine meshes at the fluid-structure interfaces to ensure physical conservation [167]. The following analysis has shown that the respective fluid and structural meshes at grid independence state from the two solvers are adequate. For example, a  $48 \times 96 \times 15$  mesh for Eilmer and a  $200 \times 240$  mesh for the structure solver.

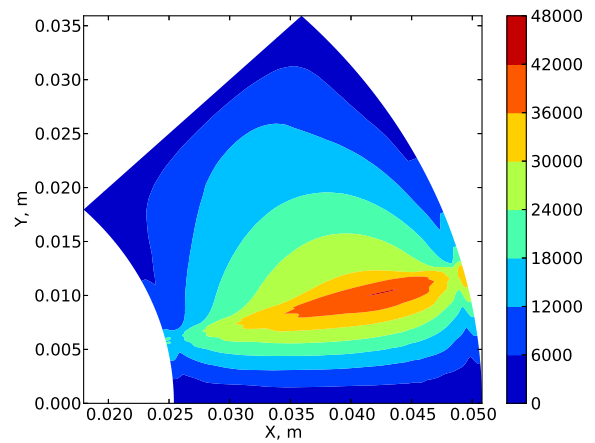
Figure 4.24 shows the pressure and deflection contours at the fluid-structure interface for these two solvers indicating the order of the mapping process ((a)→(b)→(c)→(d)). These contours indicate the same pattern (pressure and mapped pressure, deflection and mapped deflection), however, a more detailed comparison is undertaken to verify the accuracy. To verify the mapped pressure from Eilmer to the structure solver, the pressure forces acting on specific regions of the top foil for the two solvers are compared. As shown in Table 4.2, the relative error for pressure forces between these two solvers is less than 0.7 %. This is sufficiently accurate for mapping pressure at the fluid-structure interface. To verify the mapped deflection field, the deflection solved by the structure solver and the mapped deflection for Eilmer are shown in Figure 4.25. This indicates a relative error of 1 %, which is sufficiently accurate.

## 4.6 Conclusions

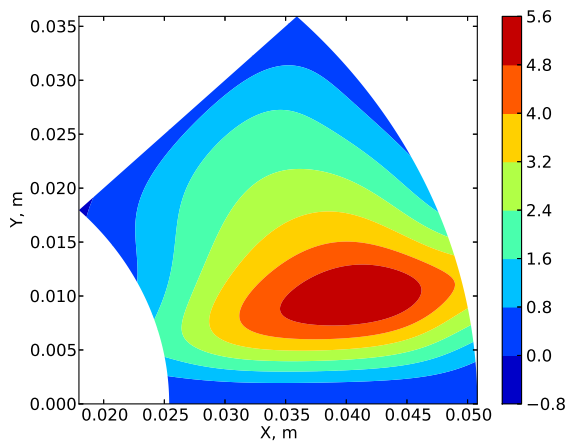
In this section, a computational tool to simulate the three-dimensional elasto-hydrodynamic operation of foil thrust bearings is developed. This computational problem consists of two parts, fluid simulation and structural deformation. The CFD code Eilmer was modified to include a moving grid capability. Different cases were provided to test the suitability of Eilmer to simulate inviscid, viscous and turbulent flows. Additionally, a new finite difference solver was developed for the structural deformation within the foil bearing. This is verified with the commercial software ANSYS, and the relative differ-



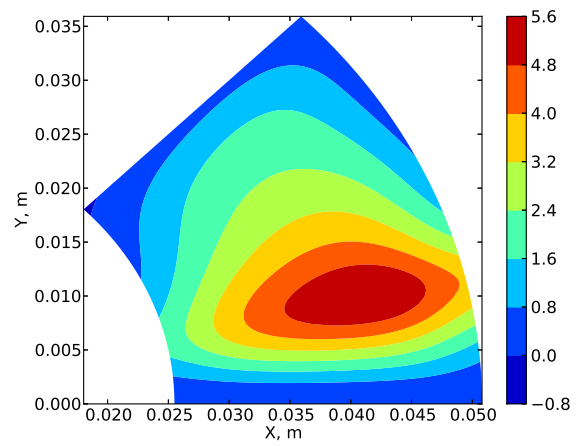
(a) Eilmer, pressure in Pa.



(b) Structure solver, mapped pressure in Pa.



(c) Structure solver, deflection in  $\mu\text{m}$ .



(d) Eilmer, mapped deflection in  $\mu\text{m}$ .

**Figure 4.24:** Pressure and deflection contours at the fluid-structure interface, the mapping process is (a) $\rightarrow$ (b) $\rightarrow$ (c) $\rightarrow$ (d).

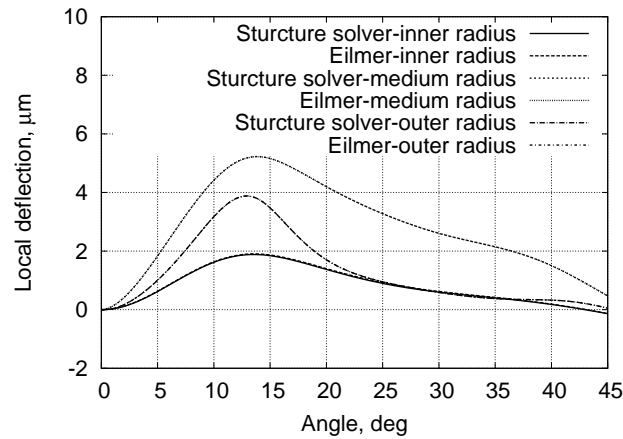


**Figure 4.25:** Comparison of deflection by the structure solver and mapped deflection for Eilmer.

ence is less than 3.5%. A coupling strategies between fluid and structural deformation solvers was developed to obtain the steady state and dynamic performances of foil thrust bearings. Within the coupling strategy, a mapping algorithm is used to exchange pressure and deflection between the two solvers. A difference of less than 1% is found. So far, the work has been verified through comparison to numerical results from literature and good agreement has been observed.

# Foil Bearing Steady State Performance

## 5.1 Introduction

Steady state performance of foil thrust bearings, using the fluid-structure simulation tool developed in Chapter 4 is studied in this Chapter. First, Section 5.2 outlines the parameters used to evaluate bearing performance. Section 5.3 then briefly details the validation of the developed fluid-structure simulation tool by comparing to experimental data of air foil thrust bearings. Section 5.4 selects the gas model for real gas properties of CO<sub>2</sub>. Section 5.5 compares results from Reynolds equation and Eilmer to highlight the new flow physics introduced by high density CO<sub>2</sub>. Section 5.6 compares the steady state performance at different operating conditions. Section 5.7 revisits the selection of the computational domain for foil thrust bearings by comparing the steady state performances. Finally, Section 5.8 presents the steady state performance at different rotational speeds and rotor-to-stator separations.

## 5.2 Steady State Performance Evaluation

The fluid-structure simulation starts with a stationary flow and a initial rotor to top foil separation between the rotor and stator defined by the *relaxed* bump foil height and top foil as shown in Figure 5.1. Once the steady state pressure distribution is obtained, the load  $F_z$  and power loss  $P_w$  are the two key parameters used to evaluate steady state performances. They are defined as,

$$F_z = \int (p - p_a) dA , \quad (5.1)$$

$$P_w = w_r \int r \mu \left. \frac{dU_\theta}{dz} \right|_{z=z_{rotor}} dA , \quad (5.2)$$

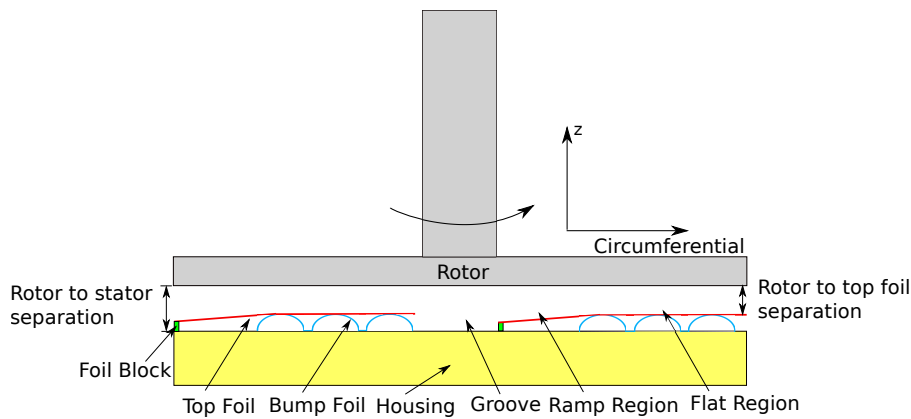


**Figure 5.1:** Side view of foil thrust bearings, not to scale.

where  $p$  is the pressure in the film,  $p_a$  is the ambient pressure,  $A$  is area,  $w_r$  is the rotational speed,  $\mu$  denotes the viscosity, and  $\frac{dU_\theta}{dz}$  is the gradient of the tangential velocity close to the rotor surface.

### 5.3 Validation for Steady State Performance

Dickman [73] presented experimental results for three identical thrust foil bearings operating with shaft speeds as high as 40 000 rpm under increasing loads. Since air was used as operating fluid in these experiments, viscous heating effects will be low, and the results can be used as a test case for fluid-structure coupled simulation of foil thrust bearings. Table 2.1 lists the geometry and material properties of the tested thrust foil bearing. The bearing configuration, materials, and the experimental results, are regarded as a benchmarking test model for foil thrust bearings [26]. Dickman [73] did not release all information about the tested foil thrust bearings so some geometric items in Table 2.1 have been obtained from San Andrés et al. [26].

The corresponding computational domain of the foil thrust bearings is shown in Figure 5.2. It consists of two parts, namely, the ramp and the flat region. The top surface of the computational domain is the rotor while the bottom surface is the top foil. The rotational direction is shown in Figure 5.2. Boundary conditions at the surrounding surfaces are modeled as fixed pressure and temperature, the top wall is regarded as a moving wall with fixed temperature, and the bottom wall (top foil) is set as a fixed temperature wall and coupled with the structural deformation solver. Three different computational meshes are considered for the grid independence study. These are a coarse mesh of  $24 \times 48 \times 10$  cells, a medium mesh of  $48 \times 96 \times 15$  cells and fine mesh of  $72 \times 144 \times 20$  cells.

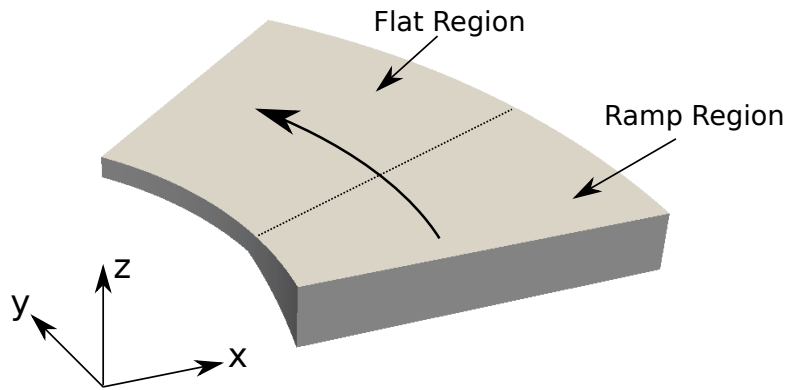


**Figure 5.2:** Computational domain for foil thrust bearings, not to scale.

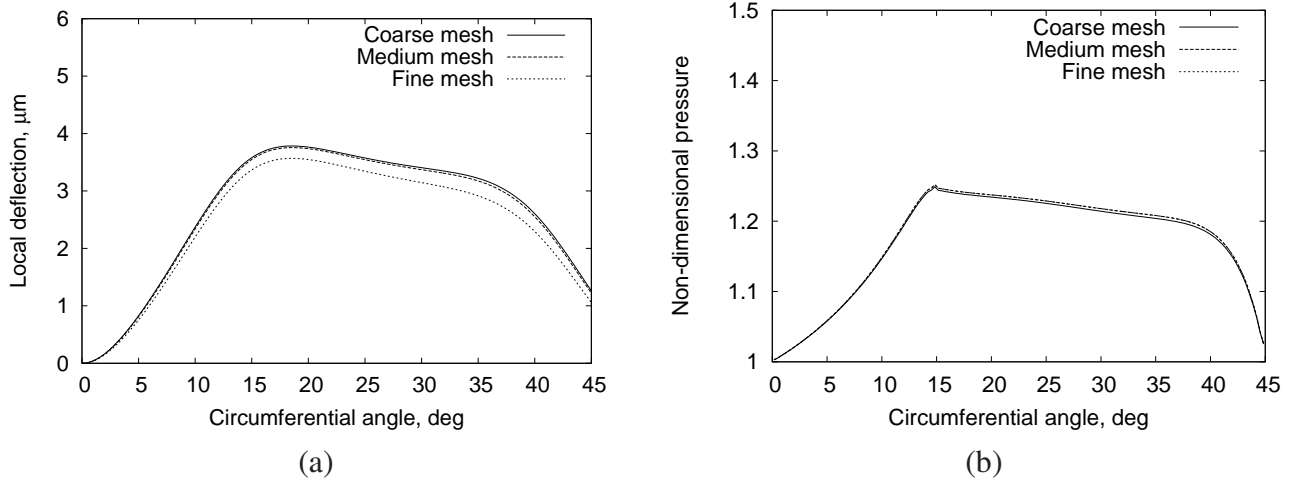
**Table 5.1:** Performance comparison of foil thrust bearings with different computational meshes.

Parameters	Coarse mesh	Medium mesh	Fine mesh
Lift force	59.89 N	60.82 N	61.03 N
Friction torque	0.0161 Nm	0.0161 Nm	0.0162 Nm

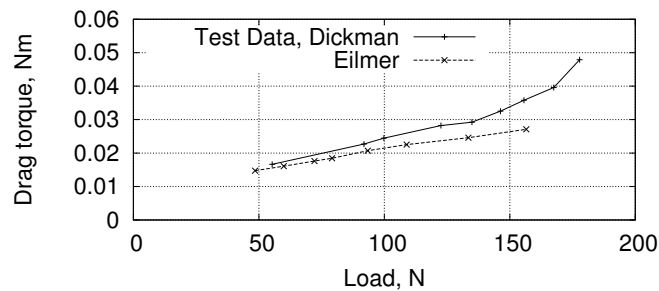
During operation, the fluid is drawn from the ramp to the flat region. The non-dimensional pressure and local deflection at the medium radius of the computational domain of the foil thrust bearings are extracted and compared, as shown in Figure 5.3 and summarised in Table 5.1. For the pressure field, the relative difference between the coarse and medium meshes is 0.24 %, and between the medium and fine meshes it is less than 0.1 %. For the local deflection, the relative difference between coarse and medium mesh is 0.87 % and 0.27 % between the medium and fine mesh. The medium mesh is considered in the subsequent discussion.

Figure 5.4 compares measurement from Dickman [73] and numerical simulation at a rotational speed of 21 000 rpm. There is good agreement between predicted and measured data for small to moderate loads. This is also reported by San Andrés et al. [26] where it is also noted that the rapid increase in drag at the highest applied load in the tests is caused by rubbing contact between the top foil and the shaft collar. Simulations for these highest load values are not performed.

Figure 5.5 shows the numerical result of the maximum deformation of the top foil under the same minimum film thickness. There is a small difference between Eilmer results and the results from San Andrés et al. [26] this is attributed to the use of different fluid and structural models. Ref. [26]



**Figure 5.3:** Grid convergence study for foil thrust bearings: (a) local deflection at the medium radius, (b) pressure at the medium radius.



**Figure 5.4:** Comparison of measurements and numerical simulation at fixed rotational speed of 21 000 rpm.

used the Reynolds equation for the flow modelling and a finite element plate model to determine the elastic deformation of a top foil and its supporting bump strip layers. Despite these differences, the overall numerical performance of the present simulations is acceptable, and the suitability of this fluid-structure simulation tool for foil bearings is demonstrated.

## 5.4 Selection of Gas Models

Conboy [8] reported an operating condition of 1.4 MPa and 300 K for the foil thrust bearings used during the preliminary tests at SNL. The position of this operating condition on the Pressure-Enthalpy diagram for  $\text{CO}_2$  is shown in Figure 5.6.

In this section, the simulation results obtained using an ideal gas model (perfect equation of state

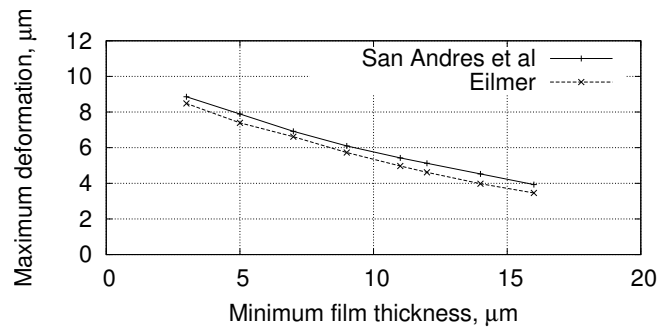


**Figure 5.5:** Comparison of maximum deformation between Eilmer and numerical results from Ref. [26].

and Sutherland's law for transport properties) and results obtained using a look-up table generated by REFPROP [120] are compared. The different thermodynamic and transport properties. Pressure, compressibility factor, density, temperature, dynamic viscosity and thermal conductivity at the medium radius of the foil thrust bearings are plotted in Figure 5.7. The difference in results obtained using the ideal gas model and look-up table are between 1% and 10%. The largest deviation is in density. This is due to difference in equation of state, ideal gas (perfect-gas equation of state, Sutherland law for viscosity and conductivity) and REFPROP (Span and Wagner [168] for equation of state). The compressibility factor from the look-up table is around 0.93 as shown in Figure 5.7(b), which indicates slight non-ideal gas behaviour at this operating point. In addition, the transport properties of CO<sub>2</sub> do not follow the conventional relationship that is described by Sutherland's law, as indicated in Figures 5.7(e) and (f). Finally, it is noted that the optimum operating condition of foil thrust bearings for sCO<sub>2</sub> cycles is unknown, and may be close to the critical point. To ensure the foil thrust bearings operation at any operating point can be evaluated reliably, the look-up table approach is used for the subsequent analysis in this thesis.

## 5.5 Comparison Between Reynolds Equation and Eilmer

This section compares foil bearing predictions attained from using Reynolds equation and the CFD method (Eilmer). For laminar flow between a rotating and stationary disc, the simplified Reynolds equation is given as (see Section 2.1),

$$\frac{1}{r} \frac{\partial}{\partial r} \left( r \rho h^3 \frac{1}{\mu} \frac{\partial p}{\partial r} \right) + \frac{1}{r^2} \frac{\partial}{\partial \theta} \left( \rho h^3 \frac{1}{\mu} \frac{\partial p}{\partial \theta} \right) = \Lambda \frac{\partial(\rho h)}{\partial \theta} . \quad (5.3)$$

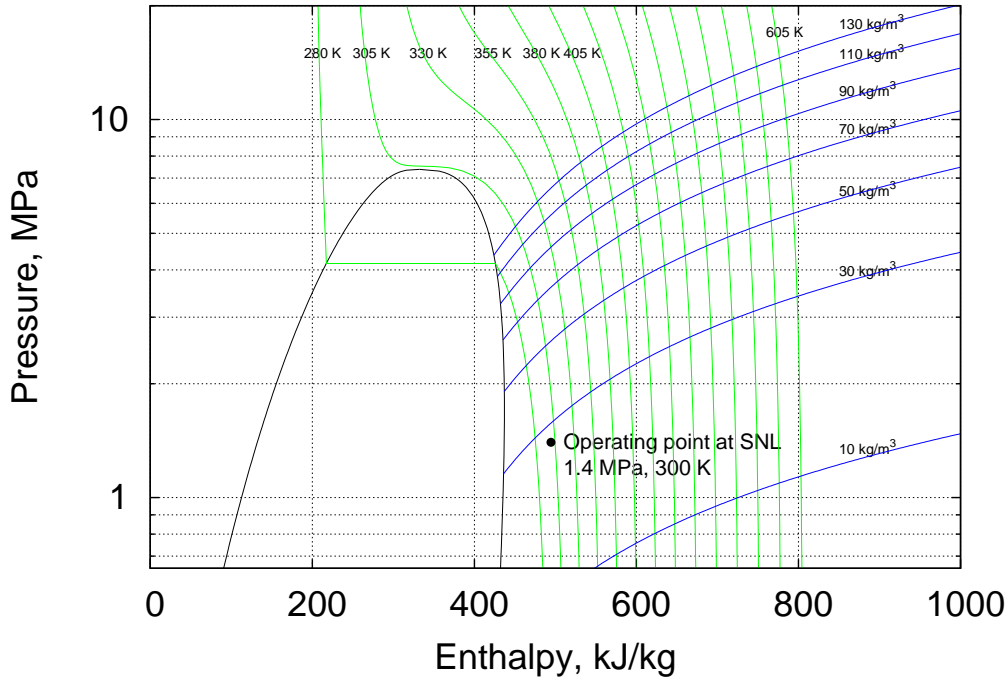


Figure 5.6: Pressure-Enthalpy diagram for CO<sub>2</sub>.

When required, additional correction factors can be included to account for turbulent effects [8]. However, the current comparison is restricted to laminar formulation shown in Equation 2.4, and the laminar simulation for Eilmer. The load capacity  $F$  and friction torque  $T$  for the Reynolds equation solution are calculated as [84, 85],

$$F = \int_r \int_\theta (p - p_a) dr d\theta, \quad (5.4)$$

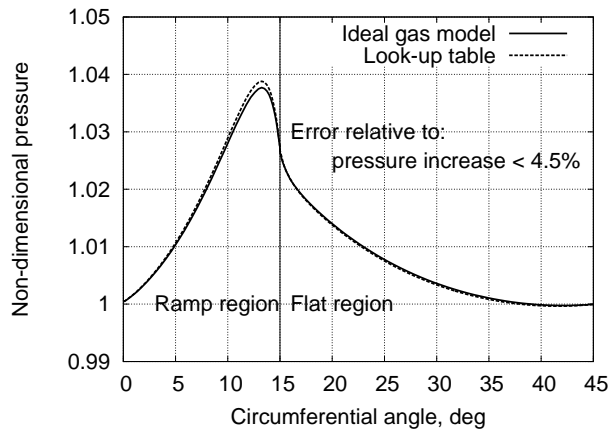
$$T = \int_r \int_\theta \left[ \frac{h}{2} \frac{\partial p}{\partial \theta} + \frac{\mu \omega r^2}{h} \right] r dr d\theta. \quad (5.5)$$

The accuracy of Reynolds equation to model air foil thrust bearings is well established [26, 76, 84]. This section explores the differences that exist between the two modelling approaches for two operating conditions:

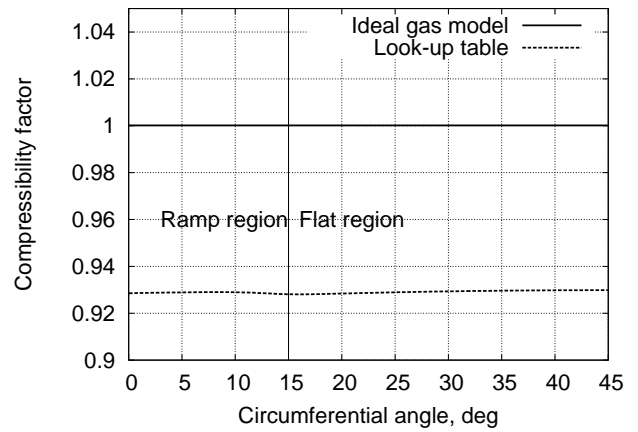
**Low density:** working fluid, CO<sub>2</sub>, pressure, 0.1 MPa, temperature, 300 K, density, 1.77 kg/m<sup>3</sup>;

**High density:** working fluid, CO<sub>2</sub>, pressure, 1.4 MPa, temperature, 300 K, density, 26.61 kg/m<sup>3</sup>.

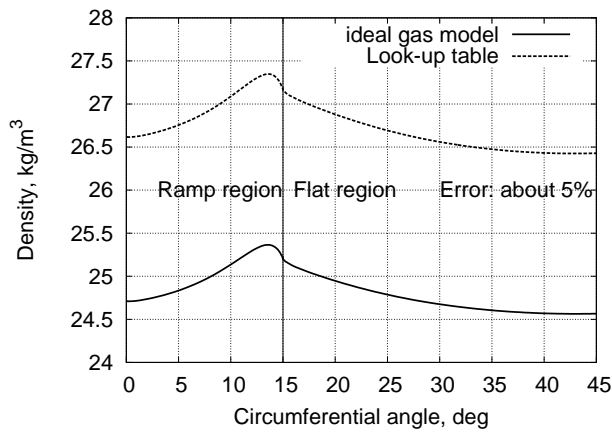
The studied bearing geometry is based on Table. 2.1, however as the aim is to compare fluid



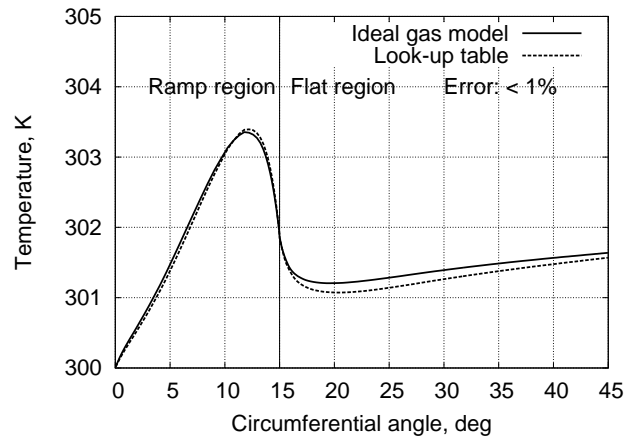
(a)



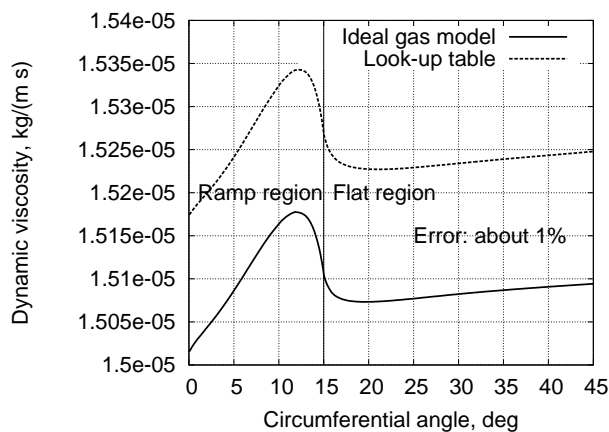
(b)



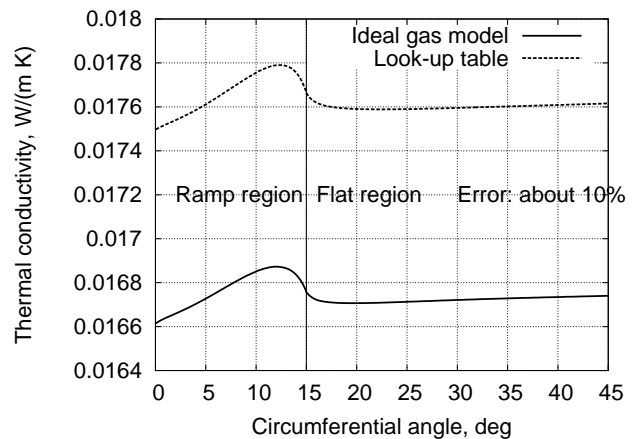
(c)



(d)



(e)



(f)

**Figure 5.7:** Comparison of thermodynamic properties at the medium radius with the rotational speed of 30000 rpm: (a) Pressure, (b) Compressibility factor, (c) Density, (d) Temperature, (e) Dynamic viscosity, (f) Thermal conductivity.

**Table 5.2:** Performance comparison of the fixed geometry thrust bearings between Eilmer-laminar and Reynolds equation.

Operating conditions	Methodology	Load capacity N	Torque Nmm
0.1 MPa, 300 K	Reynolds equation	621.38	93
0.1 MPa, 300 K	Eilmer-laminar	629.56	96
1.4 MPa, 300 K	Reynolds equation	624.46	96
1.4 MPa, 300 K	Eilmer-laminar	1137.46	97

solvers, structural deformations are not considered. The rotational speed is set to 50 000 rpm and the initial rotor-to-stator separation is set to 5  $\mu\text{m}$ . The illustration is depicted in Figure 5.1, which is the clearance between rotor and top foil.

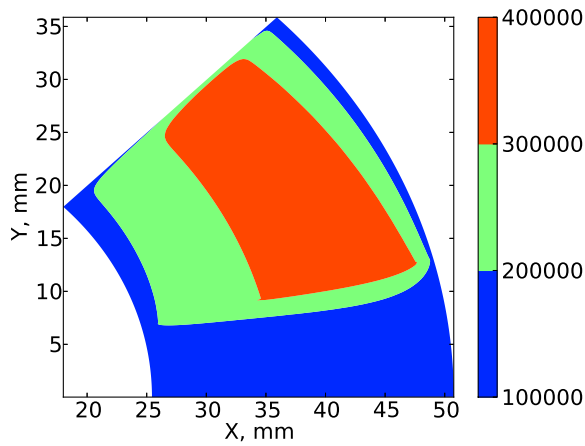
The results from Eilmer and Reynolds equation are shown in Figure 5.8. At the low density condition (0.1 MPa, 300 K), the solutions from Reynolds equation and Eilmer are almost identical. On the contrary, at the high density condition (1.4 MPa, 300 K), a higher peak pressure is predicted in the ramp region by Eilmer. This difference in predicted pressure distribution manifests as a notable performance difference as summarised in Table. 5.2. For the low density conditions close agreement exists, however for the high density condition the variation in load capacity is 45 %. The cause of this difference is one of the foci of this Chapter.

For high pressure CO<sub>2</sub> (dense gas) new physical effects not included in the Reynolds equation influence performance. As CFD methods perform a more comprehensive analysis of the flow behaviour, Eilmer is used to create new insight how dense gas operation affects foil bearing performance.

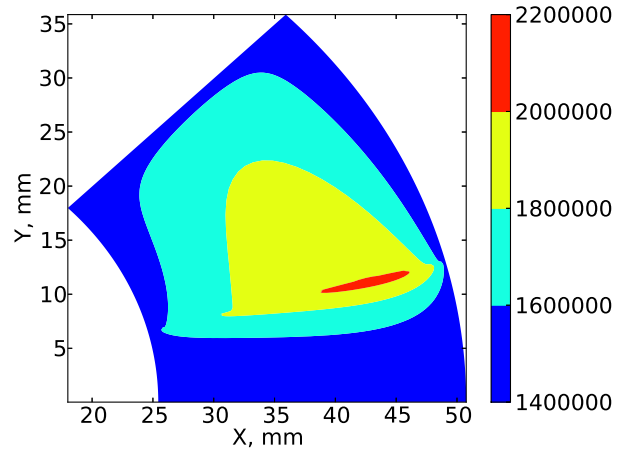
This following parts are devoted to explain the cause of different load coupling between Reynolds equation and Eilmer. The geometry of the foil thrust bearing is the same as listed in Table 2.1 and the minimum film thickness (rotor to top foil separation) is set to 16  $\mu\text{m}$ . A rigid bearing is used, as this allows a more direct comparison between the cases.

The difference is revealed by comparing the simulation to Reynolds equation. To compare the operation with a low and high density gas, the same bearing was simulated, operating with air and CO<sub>2</sub> and with the operating conditions listed in Table 5.3.

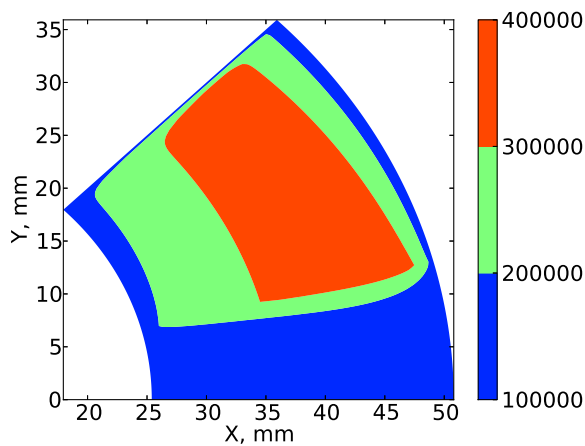
Maps of pressure increase relative to the operating pressure are shown in Figure 5.9. The flow inside the foil thrust bearings is a typical shear driven flow and the pressure increase is mainly created



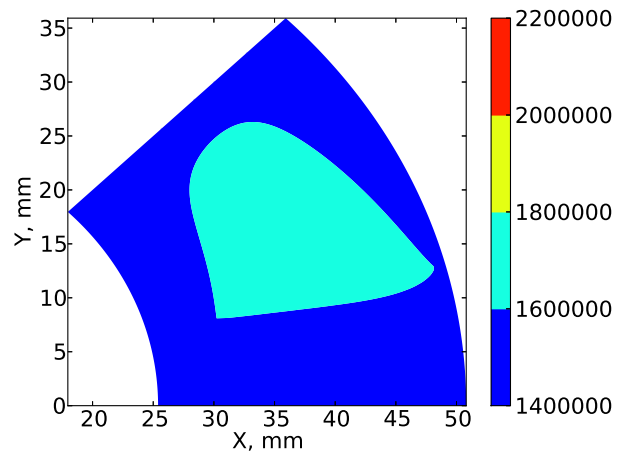
(a) Eilmer-laminar.



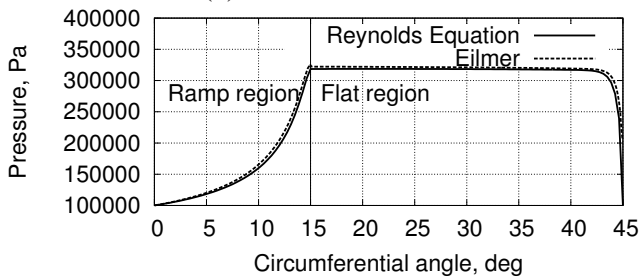
(b) Reynolds equation.



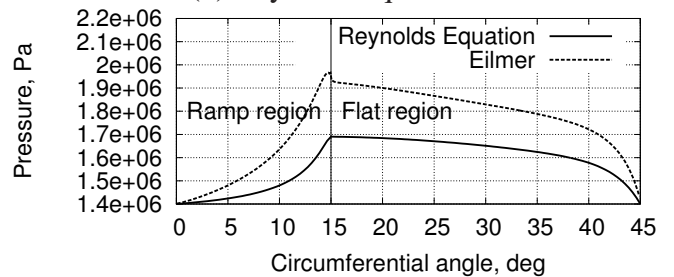
(c) Eilmer-laminar.



(d) Reynolds equation.



(e) Low density condition.

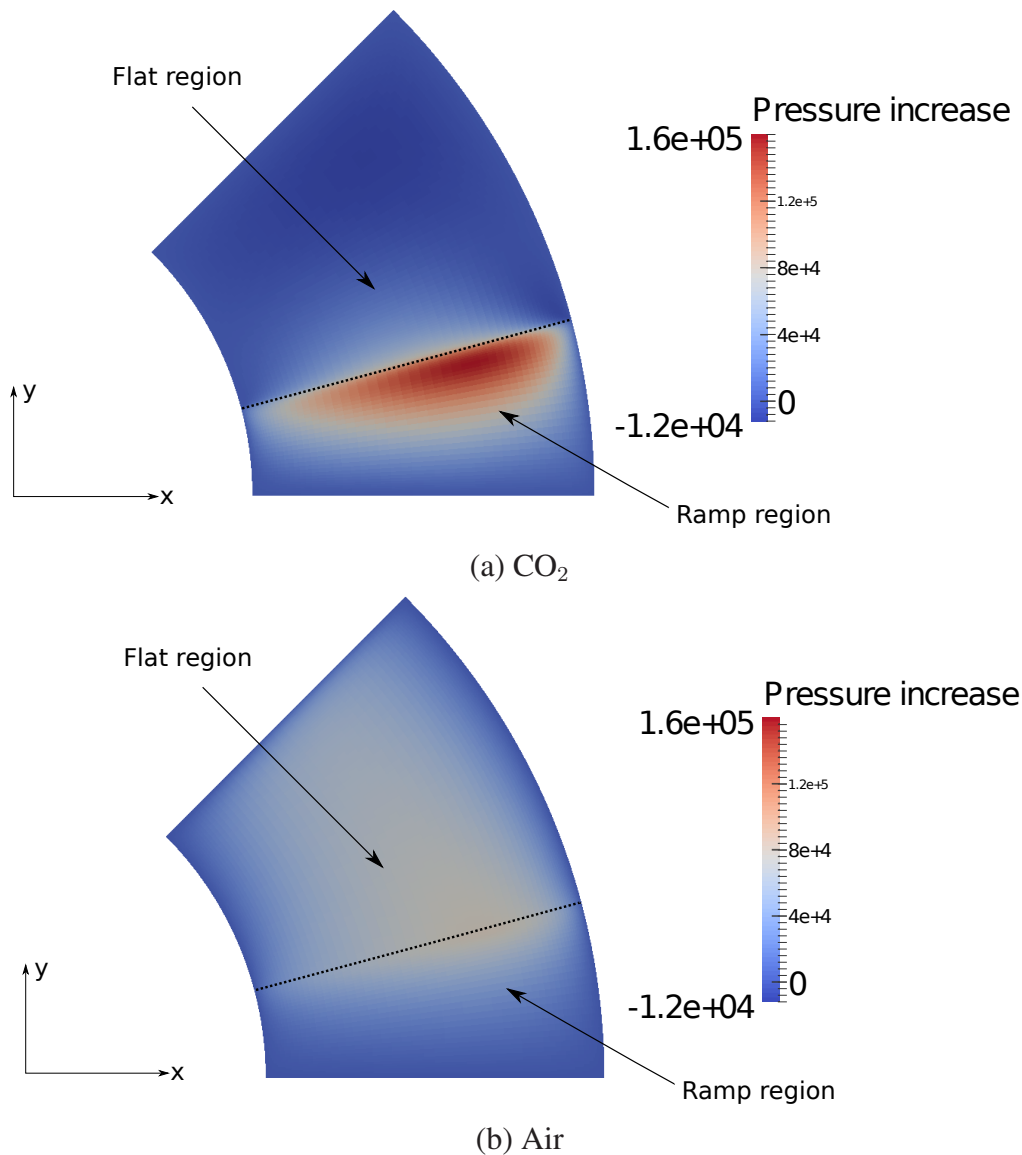


(f) High density condition.

**Figure 5.8:** Comparison between Eilmer-laminar and Reynolds equation, (a) Pressure (in Pa) contour for low density condition, (b) Pressure (in Pa) contour for high density condition, (c) Pressure (in Pa) contour for low density condition, (d) Pressure (in Pa) contour for high density condition, (e) & (f) Comparison of pressure at the medium radius.

**Table 5.3:** Operating conditions for CO<sub>2</sub> and air.

Parameters	CO <sub>2</sub>	Air
Pressure	1.4 MPa	0.1 MPa
Temperature	300 K	300 K
Density	26.93 kg/m <sup>3</sup>	1.16 kg/m <sup>3</sup>
Viscosity	$15.17 \times 10^{-6}$ kg/ms	$18.57 \times 10^{-6}$ kg/ms

**Figure 5.9:** Pressure increase contour for foil thrust bearings, (a) CO<sub>2</sub>, rotational speed: 60 000 rpm, (b) Air, rotational speed: 60 000 rpm.

by viscous forces and the convergent geometry. At both conditions, the maximum pressure is at the end of the ramp and at the start of the flat region. The two conditions (Air and CO<sub>2</sub>) display quite different pressure distributions with CO<sub>2</sub> showing a much increased peak magnitude. To compare the results, the non-dimensional pressure parameter [8] is used,

$$\Lambda = \frac{6 \omega \mu_o}{p_o} \left( \frac{R_2}{h_2} \right)^2, \quad (5.6)$$

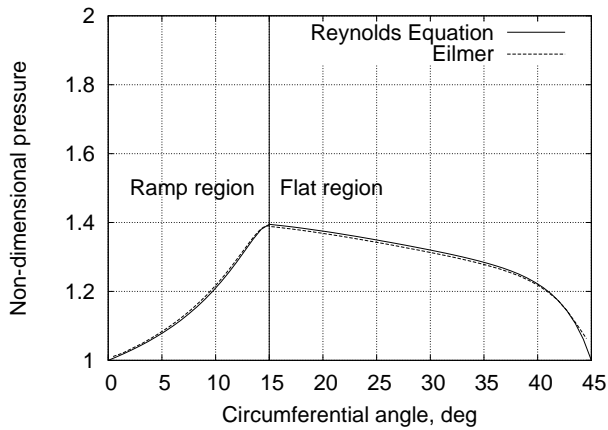
where subscript *o* indicates the operating condition,  $h_2$  is the minimum film thickness and  $R_2$  is the outer radius of the foil thrust bearing. Hence, the pressure increase relative to the operating pressure is proportional to,

$$\Delta p \propto p_a (\Lambda - 1). \quad (5.7)$$

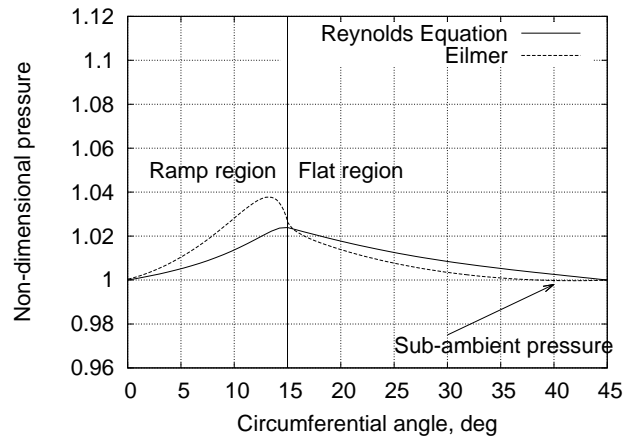
where  $p_a$  is the ambient pressure. The non-dimensional pressure distribution at two different rotational speeds (30 000 rpm and 60 000 rpm) is compared between Eilmer and Reynolds equation (Equation 5.8) in Figure 5.10. As this version of Reynolds equation doesn't include inertia forces, the comparison highlights effects of the fluid inertia. As indicated in Figures 5.10(a) and (c), the pressure distribution between Eilmer and Reynolds equation are in good agreement if air is the operating fluid, however, different results are shown for CO<sub>2</sub>. The results from Eilmer show a higher pressure in the ramp region compared to Reynolds equation, and a lower pressure in the flat region (Figures 5.10(b) and (d)).

To further explore this difference, Figure 5.11 and Figure 5.12 show flow properties (pressure increase, radial and tangential velocity) for a number of radial slices on the ramp and the flat region obtained using Eilmer. These figures highlight how fluid is transported by the combination of shear, pressure and inertia effects. Figure 5.13 shows sketches of streamlines close to the rotor and stator (at 90% and 10% film thickness) created to highlight the flow pattern. These figures show a significant difference in gas flow, internal to the bearing.

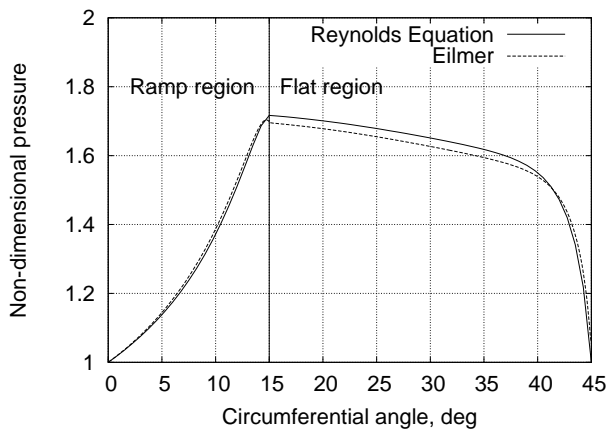
In the air case, fluid is drawn into the bearing from the ramp start, and pressurised as the viscous forces push the fluid up the ramp into a convergent gap. The highest pressure is generated along the bearing centre line ( $r_{center} \approx \frac{1}{2}(r_{inner} + r_{outer})$ ) and fluid flows radially inwards and radially outwards towards the fixed pressure boundary conditions. The same process continues after the ramp, where fluid continues to flow from the centre line towards the inner and outer edge. Effectively a



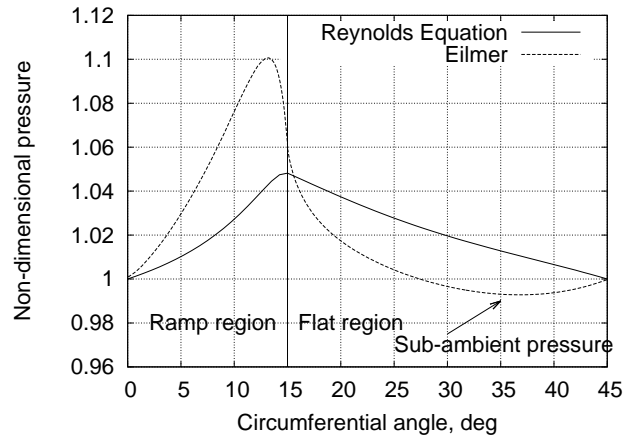
(a) Air, 30 000 rpm



(b) CO<sub>2</sub>, 30 000 rpm



(c) Air, 60 000 rpm



(d) CO<sub>2</sub>, 60 000 rpm

**Figure 5.10:** Comparison of non-dimensional pressure distribution at the medium radius between Eilmer and Reynolds equation.

fixed amount of air is drawn up the ramp into the bearing and this depletes as air leaks to the inner and outer edges, as illustrated by the streamline sketches in Figures 5.13(a) and (b). This resembles a fluid flow that is dominated by the pressure and viscous forces.

The flow field for CO<sub>2</sub> is very different. Again, fluid is drawn into the bearing from the ramp start, however, the fluid close to the rotor now experiences a significant radial force due to inertial effects. Hence, while the flow field close to the stator is similar to the flow experienced with air, predominantly outwards flow exists close to the rotor. See Figure 5.11(a) and (b) for radial velocity profiles, where the bold line corresponds to the location of  $v_{radial} = 0$ . Only towards the end of the ramp ( $\theta > 12.21 \text{ deg}$ ), when the pressure inside the bearing is much higher than the surrounding pressure (large  $\frac{dP}{dr}$ ) does the flow direction at the bearing inner radius reverse, as shown in Figure 5.11(c). This illustrates that for CO<sub>2</sub> bearings, inertia effects have a significant impact on the flow field. The overall effects are illustrated in the streamline sketches shown in Figures 5.13(c) and (d). In addition to changing the flow, the strong inertia effects also create a mechanism that locally enhances pressure increase and lift generation on the ramp. The strong inertia force acting on the fluid close to the bearing inner edge balances the pressure gradient. This manifests as a radial velocity,  $v_{radial} \approx 0$  in the third of the film closest to the rotor and inner edge. Consequently, the amount of gas that is drawn into the bearing from the start of the ramp depletes less quickly and also receives some additional in-flow close to the rotor.

After the ramp, the CO<sub>2</sub> flow continues to be different to that of air. Here, the inertial effects continue to dominate and the flow has a strong outwards component. This is especially clear at high speeds and shown in Figure 5.12. The result is a more rapid mass loss through the outer edge of the bearing. As a consequence, a region with sub-ambient pressure can be generated in the flat region. This is because the available flow area in the radial direction increases with radius, thus creating a restriction (location of smallest flow area) at the bearing inner edge. The same effect has also been identified by Garratt et al. [127] and Pinkus et al. [169], who studied inertial effects in film riding bearings. Consequently, rather than enhancing the lift generation, the flat region can now be detrimental to total bearing lift. Furthermore, in an actual bearing, this subambient pressure may lead to separation of the top foil from bump foil, which will cause further issues.

Looking back at Figure 5.10, which compares the Eilmer results with the solution to Reynolds equation, the large differences seen for CO<sub>2</sub> confirm the importance of using a full 3D CFD in order

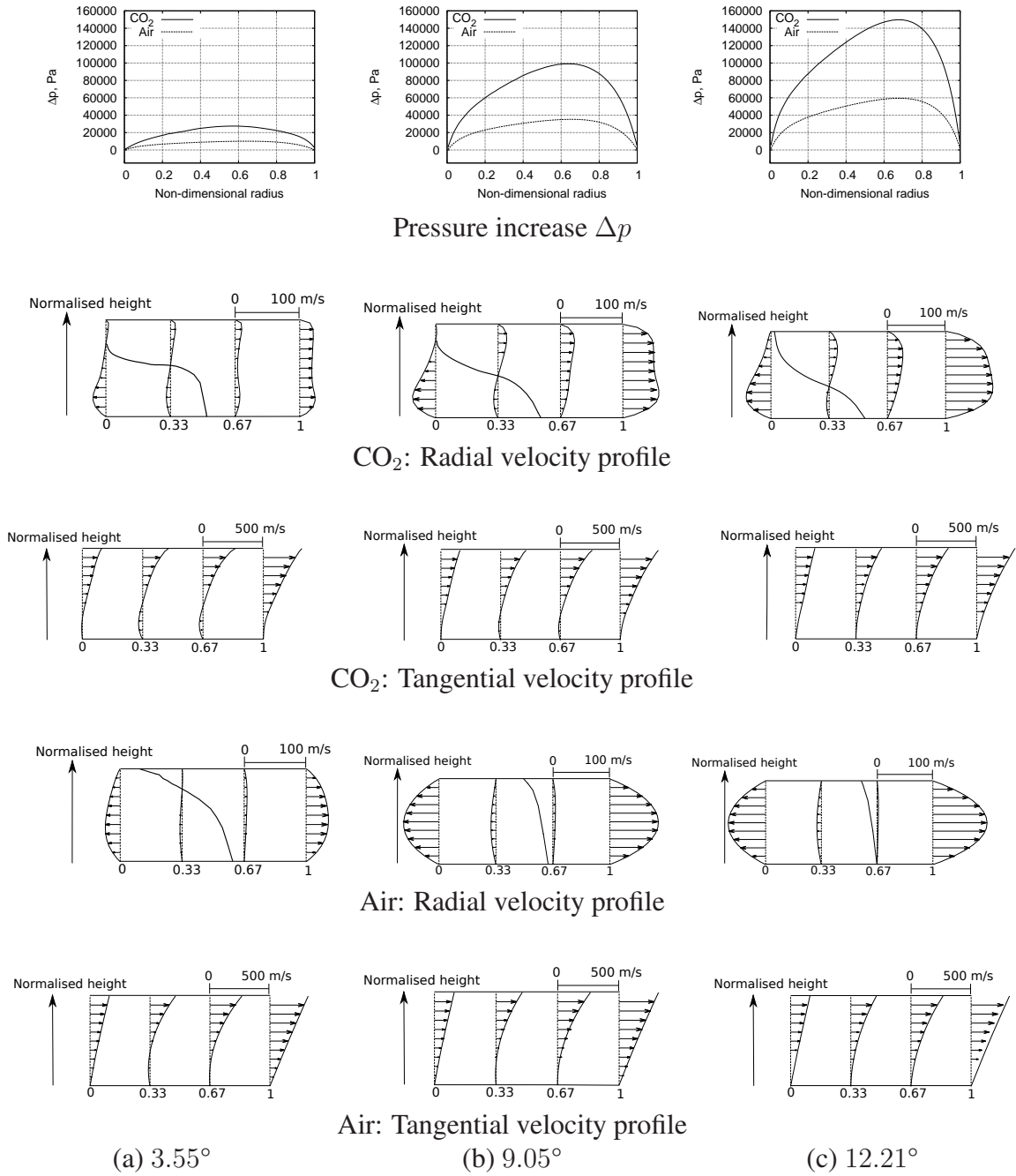


**Figure 5.11:** Ramp region: pressure increase, radial and tangential velocity at different circumferential angles. Rotational speed: 60 000 rpm, ramp ends at 15°, (Rotor at top, stator at bottom).

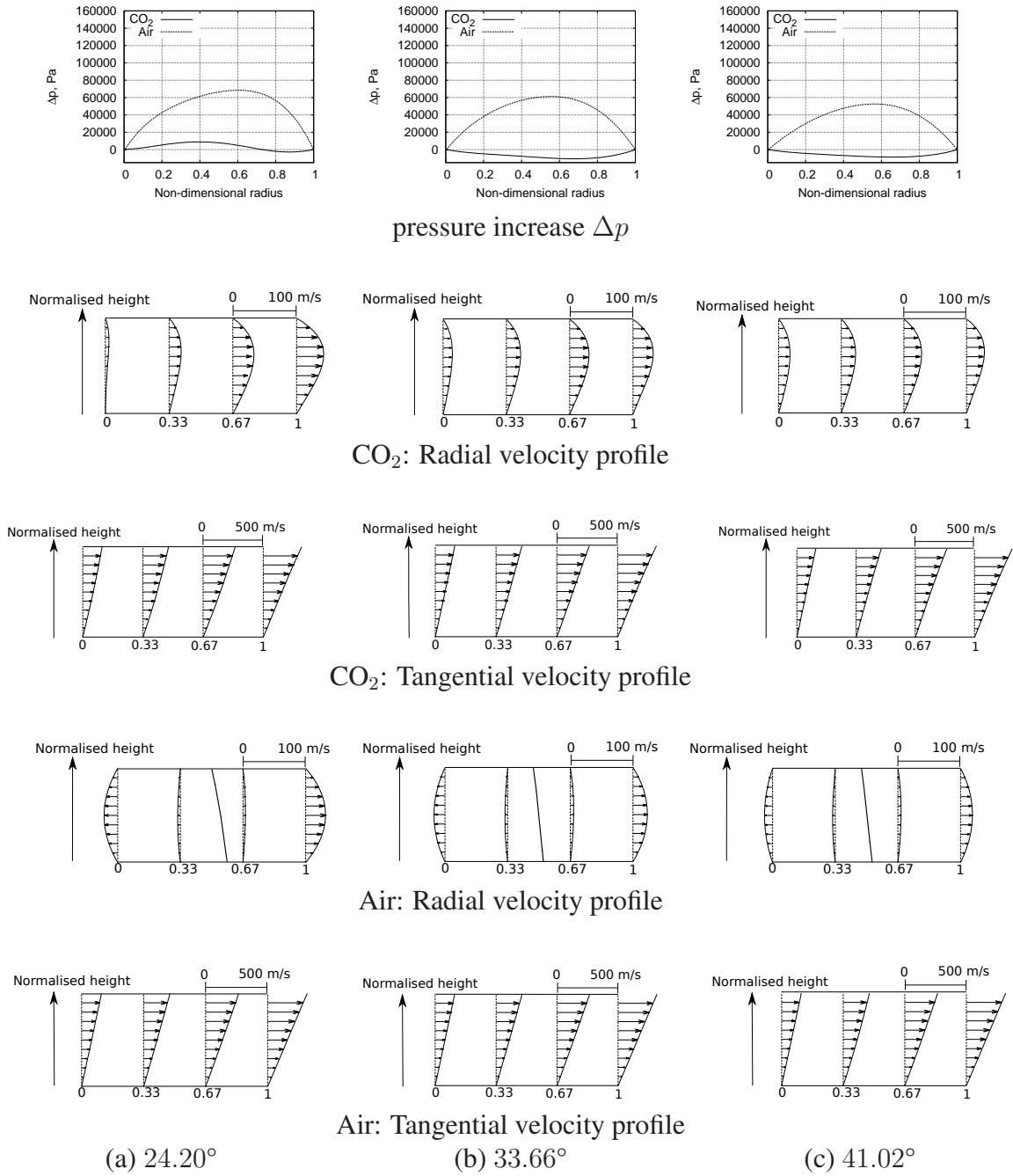


**Figure 5.12:** Flat region: pressure increase, radial and tangential velocity at different circumferential angles. Rotational speed: 60 000 rpm, flat starts at 15°, (Rotor at top, stator at bottom).

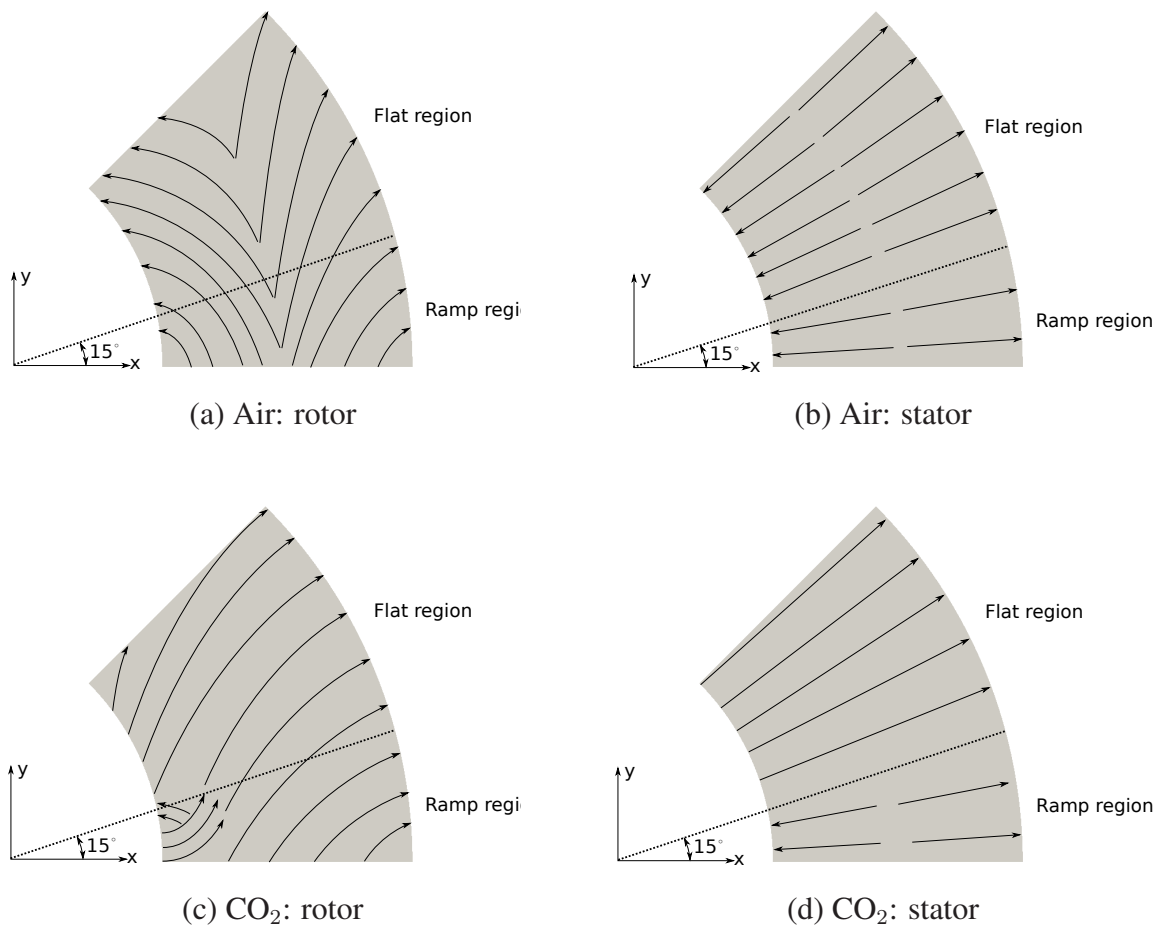


**Figure 5.13:** Approximate streamlines at 90% (rotor) and 10% (stator) film thickness (radial component is exaggerated).

to correctly analyse film-riding bearings when operating with dense gases. When using light gases (air), the solutions agree to within 4%. However for dense gas cases, significant differences exist, which are caused by the fact that Reynolds equation cannot account for the irregular radial velocity profiles that are created by the strong inertial effects.

## 5.6 Effect of Operating Conditions

For the small sCO<sub>2</sub> test rig at SNL, leakage flow passes around the compressor and turbine and through labyrinth shaft seals to provide lubrication to the foil bearings [5] as shown in Figure 5.14. The leakage flow is continuously pumped out of this region using a scavenging pump to maintain a reduced pressures, which is around 1.4 MPa and 300 K. This is taken as the operating condition for the foil thrust bearings in SNL's tests [8]. This turbomachinery architecture incorporating foil bearings can eliminate system contamination from oil and enable high speed operation. Therefore, the architecture of the turbomachinery system is simplified by using foil bearings.

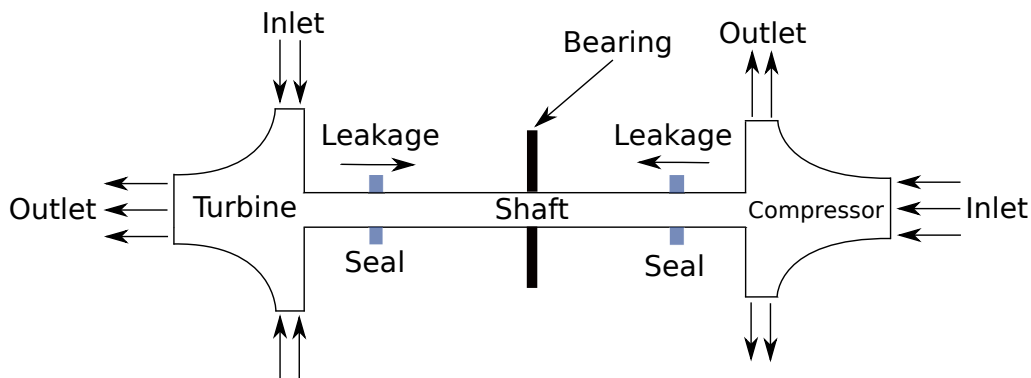


**Figure 5.14:** The architecture of a supercritical CO<sub>2</sub> turbomachinery system.

### 5.6.1 Selection of Operating Conditions

The effect of operating conditions on the performance of foil thrust bearings for sCO<sub>2</sub> power cycles is unknown. With different CO<sub>2</sub> ambient pressure and temperature, the fluid exhibits changing properties as shown in Figure 5.15 (dynamic viscosity and density). Dynamic viscosity simply varies as a function of temperature, allowing the investigation to be de-coupled from viscosity by maintaining a fixed temperature. More importantly, as shown in Figure 5.15, CO<sub>2</sub> exhibits a wide range of densities (1 to 90 kg/m<sup>3</sup>), which results in very different fluid dynamics and centrifugal inertia effects.

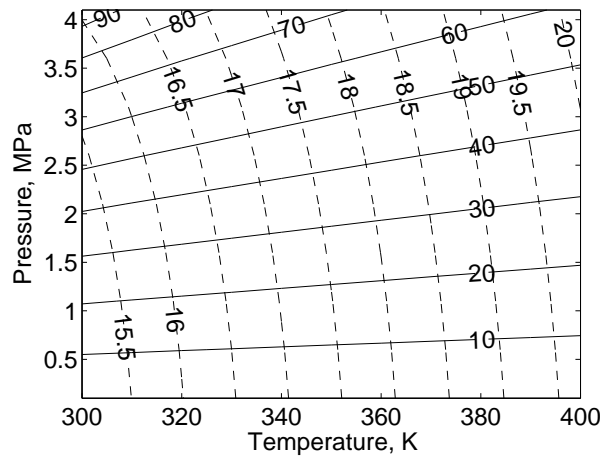


**Figure 5.15:** Density (solid line, in  $kg/m^3$ ) and dynamic viscosity (dashed line, in  $\times 10^6 kg/ms$ ) at different operating conditions.

As indicated in Section 5.5 (rigid bearing simulation) the highly dense  $CO_2$  generates a higher peak pressure in the ramp region and a higher pressure drop in the flat region compared to what is expected at more traditional operating conditions.

Due to the high density, the flow can also be in the turbulent regime [8]. The transition from laminar to turbulent flow can be determined by the rotational Reynolds number  $Re_r$ , defined as,

$$Re_r = \frac{\rho \omega r h_2}{\mu} . \quad (5.8)$$

No experimental study has been undertaken to determine the critical Reynolds number  $Re_c$  for  $CO_2$ , however, Souchet [131] recommended 900 to 1600 as the critical Reynolds number for fluid flow in bearings. Below 900 the flow is purely laminar, above 1600 the flow is fully turbulent and the flow is regarded as transitional between these Reynolds numbers. The turbulent flow can increase load capacity and friction torque for foil thrust bearings, due to the effects of eddy viscosity in the turbulent regime [132].

The bearing studied in this Chapter has the geometry from Dickman [73], summarised in Table 2.1. However, the inner and outer radii of the foil thrust bearing have been adapted to suit a 100 kW radial inflow turbine currently being designed at the authors institution, which are 8 mm and 32 mm, respectively. A uniform distribution of bump foil stiffness is prescribed over the entire pad (ramp and flat regions) and the magnitude of bump stiffness per unit area is set to  $6.44 N/mm^3$ . The bump

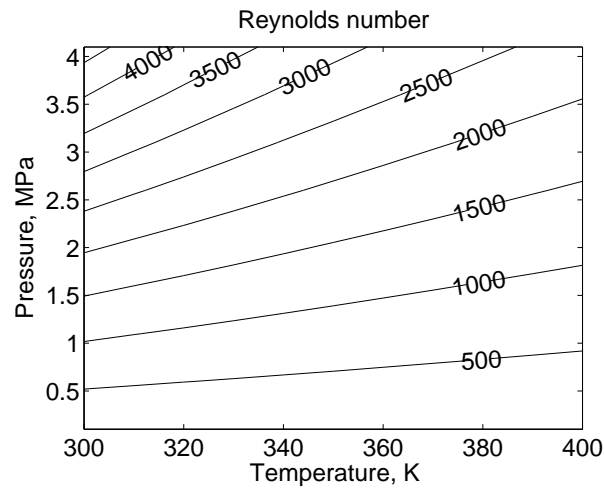


**Figure 5.16:** Rotational Reynolds number at different operating conditions (based on  $5\ \mu\text{m}$  initial gap and 50 000 rpm).

foil distribution and stiffness should be studied to maximise the bearing performance in future. The rotational speed is set to 50 000 rpm and the initial rotor and top foil separation is set to  $5\ \mu\text{m}$ .

In the SNL experiment, foil thrust bearings are placed downstream of the seals [5]. To match these conditions, the operating pressure range was selected as 0.1 to 4.0 MPa and the operating temperature range was selected as 300 to 400 K. As shown in Figure 5.16, the rotational Reynolds number for these operating conditions ranges from 200 to 4000, resulting in different flow regimes across the range of operating conditions.

### 5.6.2 Centrifugal Effects

Using the laminar flow solvers, the foil thrust bearing exhibits largely varying performance characteristics across the operating range as shown by the contours of load capacity and torque in Figure 5.17. The results are obtained by evaluating the foil thrust bearing performance at multiple points across the operating pressure (0.1 MPa, 0.4 MPa, 0.7 MPa, 1.0 MPa, 1.2 MPa and 1.4 MPa) and the operating temperature (300 K, 320 K, 340 K, 360 K, 380 K and 400 K) range. For some cases, localised transition to turbulence might take place close to the outer radius. As no transition model is implemented in Eilmer at the moment and, as this transition is localised, all cases have been simulated as fully laminar.

For laminar simulations with a fixed operating pressure, both the load capacity and friction torque increase with increasing operating temperature, this can be easily explained by the conventional the-

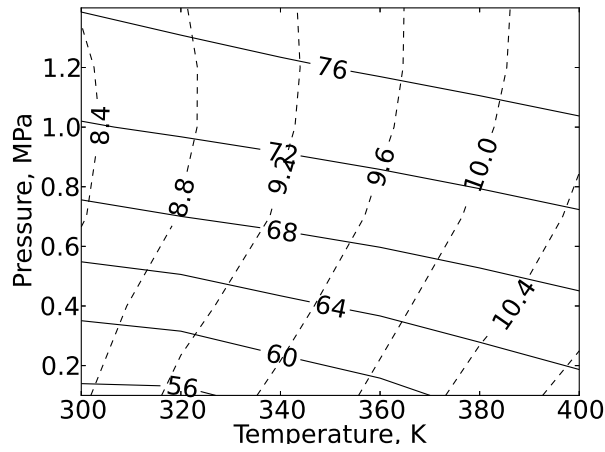


**Figure 5.17:** Performance comparison at different operating conditions from laminar fluid solver, solid line: load capacity in N, dashed line: torque in Nmm, Eilmer-laminar. Rotational speed: 50 000 rpm.

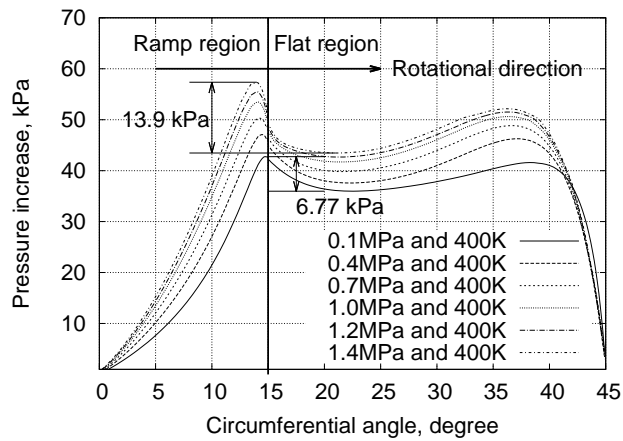


**Figure 5.18:** Pressure increase ( $p - p_a$ ) at the different operating pressures. Operating temperature fixed at 400 K, Eilmer-laminar. Rotational speed: 50 000 rpm.

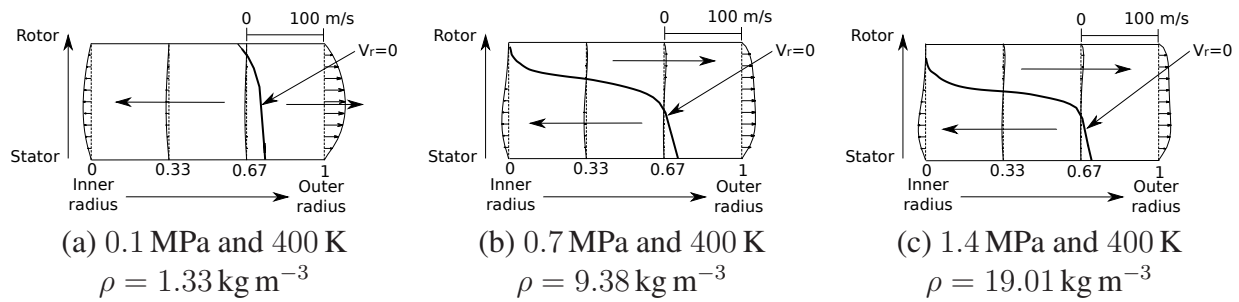


**Figure 5.19:** Radial velocity profile in the ramp region (circumferential angle:  $5^\circ$ ) for different operating conditions, bold line:  $V_r = 0$ , Eilmer-laminar.

ory for predicting the bearing performance, where viscous forces are dominant. The increased operating temperature and resulting high dynamic viscosity results in larger viscous forces. Hence, both the load capacity and friction torque increase as operating temperature increases. On the other hand, for the simulations with the fixed operating temperature, the friction torque is almost constant for the different operating pressure as shown in Figure 5.17. However as operating pressure increases the load capacity of the foil thrust bearing increases also. Variation can be as high as 40 %.

To provide more insight to this increase in load capacity, the pressure increase relative to the operating pressure at the medium radius for the different operating pressure is shown in Figure 5.18. For these operating conditions, the ambient temperature is fixed at 400 K, implying constant viscous forces under the same rotational speed and bearing geometry. Figure 5.18 shows that there is a higher peak pressure in the ramp region for the high operating pressures. In the flat region, the pressure then decreases, but there is a comparatively larger pressure drop for the highest operating pressure (1.4 MPa) as shown in Figure 5.18. The pressure drop is approximately 13.9 kPa, roughly twice the amount observed for the lowest operating pressure (0.1 MPa).

To explain this difference, Figures 5.19 and 5.20 show the radial velocity profile for three radial slices (ramp and flat region). The arrowed contours in these figures indicate the local radial velocity component at the different position. For the current bearing geometry and rotational speed the maximum radial velocity is approximately 30 m/s at the outer radius, while the maximum tangential velocity varies between 42 m/s and 168 m/s. The bold line corresponds to the location of zero radial velocity. On the left of the zero radial velocity line,  $\text{CO}_2$  flows towards the inner radius, while to right  $\text{CO}_2$  flows towards the outer radius.

In the ramp region, as shown in Figure 5.19 close to the rotor the zero radial velocity line

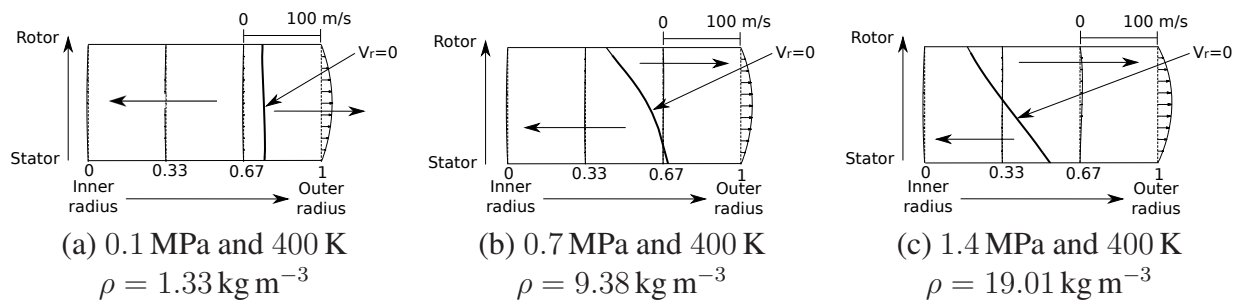


**Figure 5.20:** Radial velocity profile in the ramp region (circumferential angle:  $25^\circ$ ) for the different operating conditions, bold line:  $V_r = 0$ . Note, the inner radius velocity profile are so small that they are difficult to see, Eilmer-laminar.

moves towards the inner edges as operating pressure increases. At a pressure of 1.4 MPa the region closest to the rotor actually experiences flow with a radially outward direction entering the bearing. The location of the zero radial velocity close to the stator remains almost fixed at approximately  $0.3 r_{inner} + 0.7 r_{outer}$ . In the flat region, the same trend exists as shown in Figure 5.20. The zero radial velocity line close to the rotor also moves towards the inner edge. So does the zero radial velocity line close to the stator, but at a lower rate. To aid the understanding of the flow pattern, streamlines close to the rotor and stator (at 90 % and 10 % film thickness) for the two operating conditions (0.1 MPa, 400 K and 1.4 MPa, 400 K) are plotted in Figures 5.21 and 5.22. Close to the rotor very similar streamlines are shown, as tangential velocities are substantially larger than the radial velocities. However, a zoomed-in view at the inner radius, close to the rotor highlights the different flow pattern. The streamlines are parallel to the tangential direction for the high density condition, while the flow moves towards the inner radius at the low density condition. This shows that for the high density case centrifugal effects have altered the flow pattern. The contours of radial velocity close to the rotor, Figures 5.21(a) and 5.22 (d), further highlight the difference in flow pattern and how increased outwards flow exists for the dense gas. For the streamlines at the stator, a backward flow is shown in the ramp region, which is due to the pressure forces being higher than the shear stress. The corresponding top foil deflection for these two operating pressures is illustrated in Figure 5.23. Both operating conditions show the highest deflection in the bearing centre, while the minimum deflection is indicated at the surrounding edges.

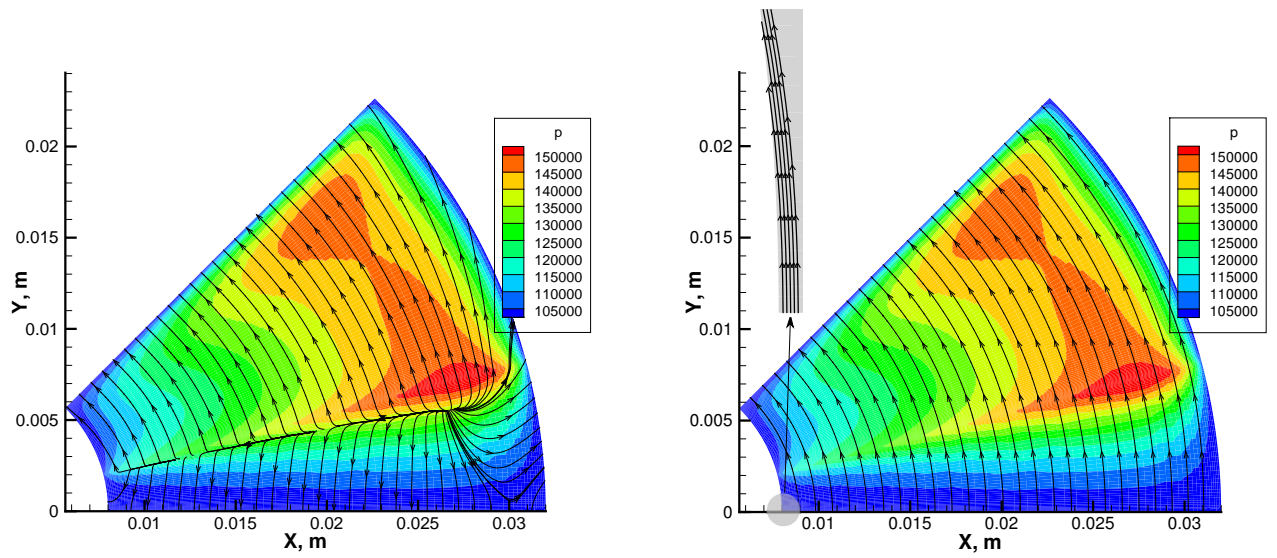
At the low operating pressure (0.1 MPa, 400 K,  $\rho = 1.33 \text{ kg m}^{-3}$ ), fluid is drawn into the bearing from the ramp start, and pressurised as the viscous forces drag the fluid up the ramp into a convergent gap. The highest pressure is generated along a constant radius line (approximately at  $0.3 r_{inner} +$

$0.7 r_{outer}$ ) and fluid flows radially inwards and radially outwards towards the bearing edges (fixed pressure boundary conditions). The same process continues after the ramp, where fluid continues to flow from this line towards the inner and outer edge. Effectively a fixed amount of  $\text{CO}_2$  is drawn into the bearing and this depletes as  $\text{CO}_2$  leaks to the inner and outer edge as illustrated by the streamline in Figure 5.21. This resembles a fluid flow that is dominated by the pressure and viscous forces.

The flow-field for the high operating pressure (1.4 MPa, 400 K,  $\rho = 19.01 \text{ kg m}^{-3}$ ) is different. Again  $\text{CO}_2$  is drawn into the bearing from the ramp start. However the fluid close to the rotor now experiences a significant radial force due to centrifugal inertia effects. Hence while the flow-field close to the stator is similar to the flow experienced with the low operating pressure, predominantly outwards flow exists close to the rotor, see Figure 5.19(c). Only towards the end of the ramp, when the pressure inside the bearing is much higher than the surrounding pressure (large  $\frac{dP}{dr}$ ) does the flow direction at the bearing inner radius reverse. This illustrates that for bearings operating with highly dense  $\text{CO}_2$ , inertia effects have a significant impact on the flow-field. In addition to changing the flow, the inertial effect also creates a mechanism, which enhances pressure increase and lift generation. The overall effects are illustrated by the streamlines shown in Figure 5.22. The strong inertia force acting on the fluid close to the bearing inner edge balances the pressure gradient, which manifests a radial velocity,  $V_r \approx 0$  in the top sixth of the film close to the inner edge as shown in Figure 5.19(c). This means, contrary to the low density case, where fluid spills out of the inner edge over the entire film height, now fluid is actually pumped into the bearing close to the rotor (approximately a sixth of the film height). Consequently the amount of gas that is drawn into the bearing from the ramp start depletes less quickly.

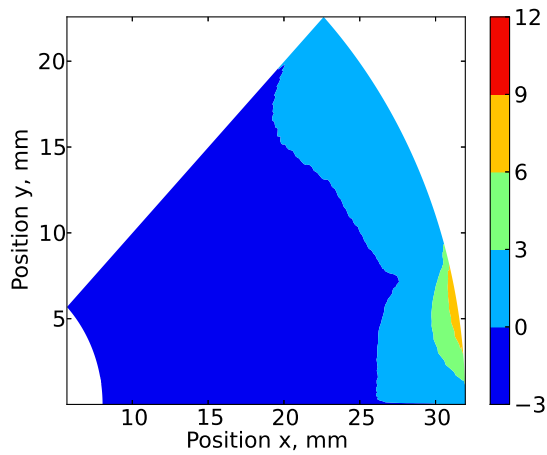
After the ramp, the high operating pressure flow continues to be different. Here the centrifugal effects continue to influence the flow direction as shown in Figures 5.20 and 5.22. The bearing now experiences increased leakage at the outer edge and most of the flow is drawn outwards. This is particularly the case close to the rotor. Effectively for most of the flat region the centrifugal force dominates the pressure gradient, leading to a mainly outwards flow. The result is a mass loss through the bearing outer edge. The same effect has also been identified in Ref. [127, 169], which studied inertia effects in film riding bearings. Consequently, rather than keeping the higher pressure created in the ramp region, the flat region now experiences an increased pressure drop as shown in Figure 5.18.

The effects described above, and particularly the ability to create a high peak pressure at the end

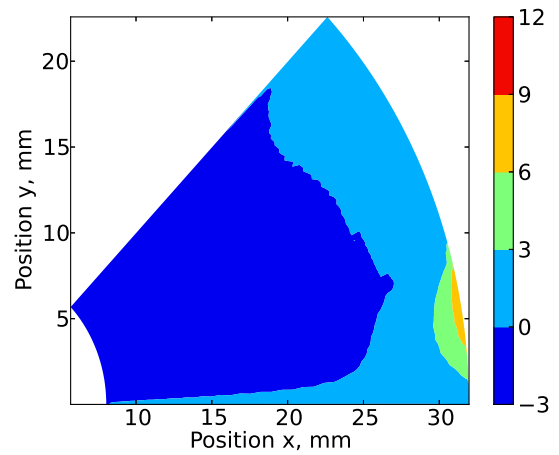


(a) stator, pressure (in Pa) contour and streamline

(b) rotor, pressure (in Pa) contour and streamline

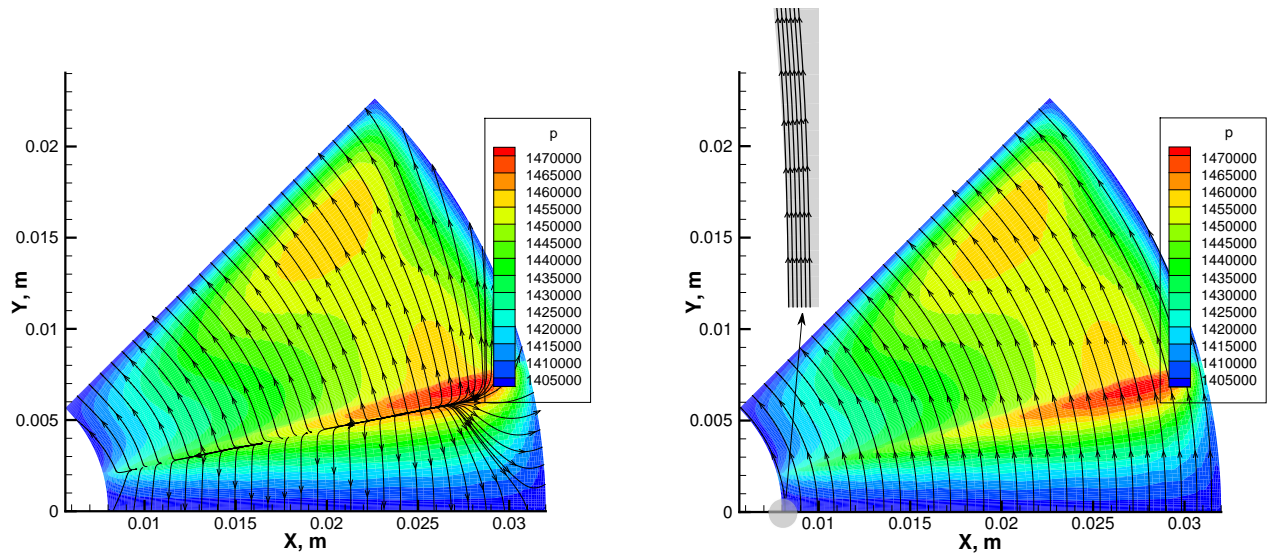


(c) stator, radial velocity (in m/s)



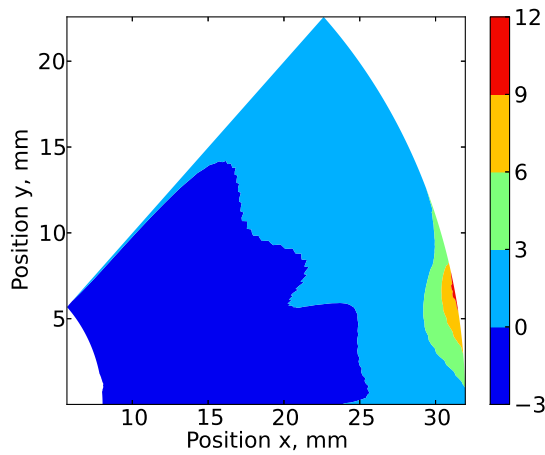
(d) rotor, radial velocity (in m/s)

**Figure 5.21:** Streamlines and radial velocity close to stator and rotor. Operating condition: 0.1 MPa and 400 K,  $\rho=1.33 \text{ kg m}^{-3}$ . the rotational direction is anti-clockwise, Eilmer-laminar.

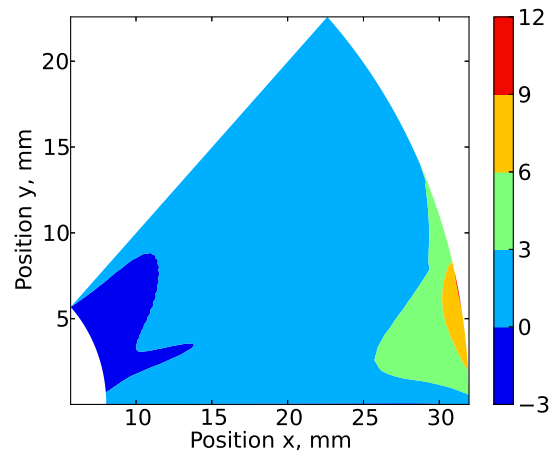


(a) stator, pressure (in Pa) contour and streamline

(b) rotor, pressure (in Pa) contour and streamline



(c) stator, radial velocity (in m/s)



(d) rotor, radial velocity (in m/s)

**Figure 5.22:** Streamlines and radial velocity close to stator and rotor. Operating condition: 1.4 MPa and 400 K,  $\rho=19.01 \text{ kg m}^{-3}$ , the rotational direction is anti-clockwise, Eilmer-laminar.

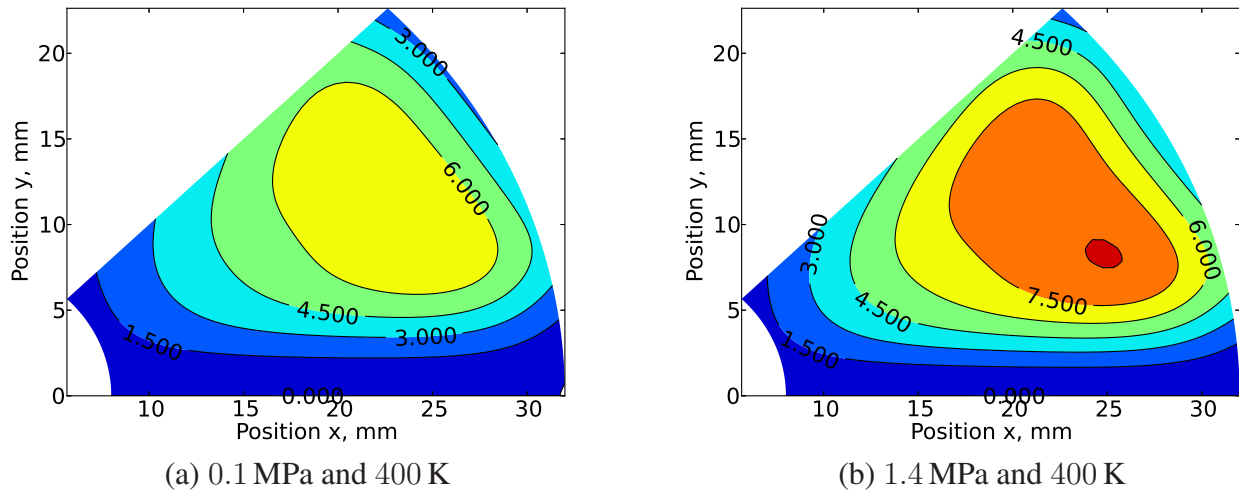


**Figure 5.23:** Local deflection (in  $\mu\text{m}$ ) for two operating conditions, rotational direction: anti-clockwise, Eilmer-laminar.

of the ramp is also counteracted by the motion of the foils. Effectively in the high pressure regions, the top foil is deflected most, which results in a large gap and diminishing viscous effects. The corresponding top foil shape for the two simulations is shown in Figure 5.23. The general shape is similar, however the deflection for the high pressure operating point (higher density) are increased by almost 50%. The largest increases in deflection exist at the location of peak pressure (approximately at  $0.3 r_{inner} + 0.7 r_{outer}$ ) and close to the end of the ramp. While a convergent shape from the peak pressure region towards the bearing edge is preferable to maximise pressures within the gap, the ability to retain mass is governed by the final restriction. Consequently the increased gap height at the outer radius of the bearing in combination with centrifugal forces that generate and increased outwards flow leads to substantial mass loss from the bearing and simultaneous decrease in pressure as observed in Figures 5.21 and 5.22. Therefore, the observed pressure drop at the high operating pressure is a combined effect of the centrifugal force and the top-foil shape.

These results highlight the mechanism by which centrifugal inertia forces influence the performance of the foil thrust bearing. For high density, high pressure applications the centrifugal inertia effect can cause additional fluid to be entrained into the bearing in the ramp region close to the inner edge of the rotor. This can augment the peak pressure magnitude. However in the flat region the inertial effect leads to increased fluid leakage through the bearing outer edge, which reduces pressure

and total load capacity. Contrary to rigid bearings, the deflected top foil can prevent the mass loss through the radial direction. It is recommended that the use of stiffer bump foils close to outer radius can further prevent mass loss.

### 5.6.3 Turbulence Effects

Due to the high density of  $\text{CO}_2$ , the flow regime transitions to turbulence at some operating conditions as shown in Figure 5.16. The addition of eddy viscosity in the turbulent flow has a significant impact on the performance of the foil thrust bearings. To investigate this influence the results from different operating pressures in the range 0.1 MPa to 4.0 MPa are compared. The operating temperature and the rotational speed are fixed at 400 K and 50 000 rpm and the initial minimum film thickness is set to 5  $\mu\text{m}$ . In the absence of a transition model in Eilmer, the simulations are divided into laminar and turbulent cases. For operating pressure less than 1.64 MPa ( $Re=900$ ), the flow is modelled as laminar, while the turbulence model is used for operating pressures larger than 2.89 MPa ( $Re=1600$ ).

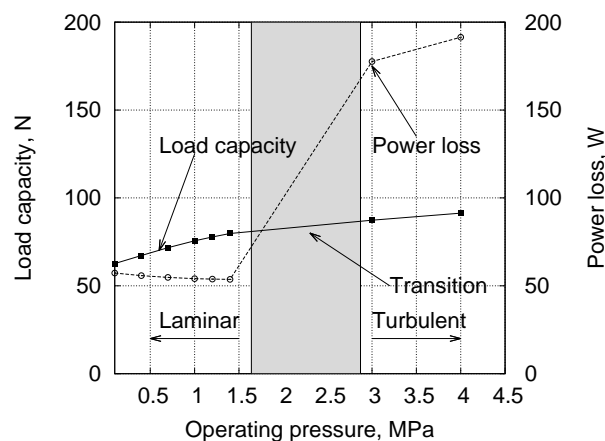


**Figure 5.24:** Performance comparison for different flow regimes, the operating temperature is fixed as 400 K.

The results of power loss and load capacity at the different operating pressures are compared in Figure 5.24. For the laminar case power loss is almost constant with at approximately 55 W for the current bearing geometry and operating conditions. This is due to the linear velocity distribution between rotor and stator in the laminar flow regime and the fact that viscosity is largely independent of pressure. The small reduction with pressure can be attributed to increasing bump foil deflections caused by the increasing load being supported. However, in the turbulent regime the power loss increases to 190 W. As a consequence of turbulence the velocity profile in the boundary layer close to

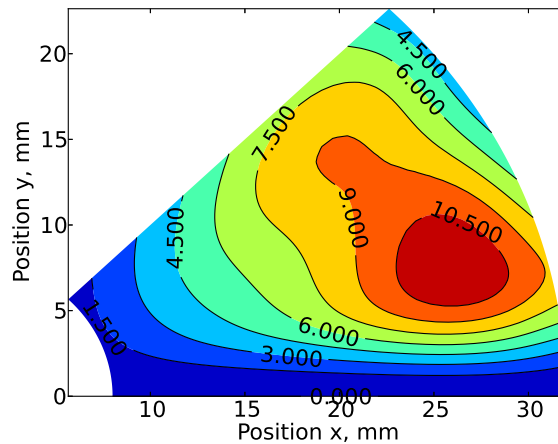


**Figure 5.25:** Local deflection (in  $\mu\text{m}$ ) at an operating pressure of 1.4 MPa and operating temperature of 400 K.

rotor and stator becomes steeper. This results in increased wall shear stress and subsequently a larger power loss as shown in Figure 5.24.

Load capacity shows a near linear relationship in terms of operating pressure as shown in Figure 5.24. Figure 5.27 shows the pressure and streamline, at the operating condition of 4.0 MPa and 400 K, with a Reynolds number 2260. The streamlines close to the rotor are very similar to an equivalent laminar case (e.g. Figure 5.22(b)). However, close to the stator substantial differences exist compared to the laminar cases shown in Figure 5.21(a) and Figure 5.22(a). In the turbulent flow regime, only the fluid closest to the wall within the laminar sub-layer is strongly affected by viscous effects. This is confirmed by the steep velocity gradient as shown in Figure 5.26 compared to laminar flows. The fluid further away, in the transition layer is much more susceptible to pressure gradients and other effects. Consequently a larger portion of the flow is now affected by the pressure gradients, resulting in the substantial reversed flow on the ramp and increased flow towards the foil edges. The deflected shape shown in Figure 5.25 is still similar to the laminar simulation (see Figure 5.23), but the maximum deflection has doubled to  $12.0\ \mu\text{m}$ . It is expected that the load capacity and rotor torque can be improved through optimisation of the bump foil stiffness and top foil thickness.

## 5.7 Revisit of Computational Domain: Steady State Performance

In literature, typically only the ramp and flat regions of foil thrust bearings are considered as the computational domain [8, 26, 76, 84, 85], and a fixed static pressure boundary condition is set at the

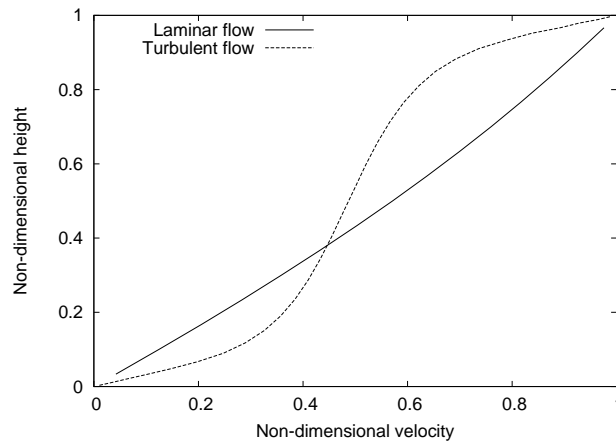


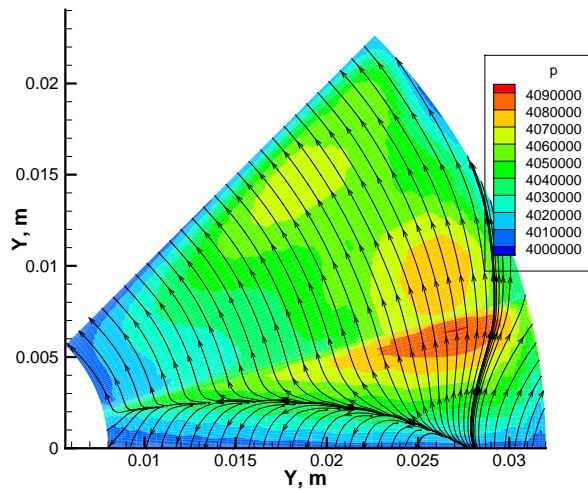
**Figure 5.26:** Comparison of tangential velocity profile at laminar and turbulent flow at the medium radius with the circumferential angle of  $24.20^\circ$ .

leading and trailing edges (see Figure 5.28(a)). Thus, the groove region between two adjacent bearing pads is neglected, and the pressure in this region is commonly assumed as ambient. However, this groove region or the trailing edge shape can play a significant effect on bearing performance. For example, the chevron shaped trailing edge proposed by Bruckner [170] provides enhanced mixing and a substantial passive cooling mechanism. This allows a twofold increase in bearing load capacity and enhances the damping as confirmed by experimental results.

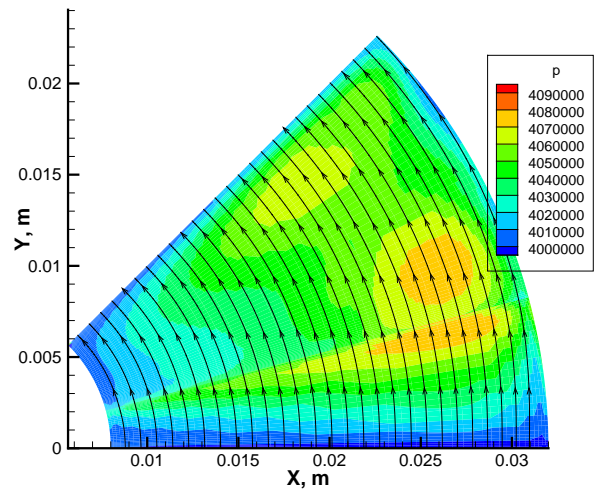
This section is devoted to the selection of the computational domain for rotordynamic analysis of foil thrust bearings operating with  $\text{CO}_2$ . The selection is performed by comparing the steady state and dynamic performances of foil thrust bearings. The bearing geometry is defined in Table 2.1. The data of this prototype was released by the National Aeronautics and Space Administration (NASA) [23]. The ambient static pressure and temperature are 1.4 MPa and 300 K, respectively. Two different computational domains are selected,

- Domain 1: ramp and flat regions as shown in Figure 5.28(a);
- Domain 2: ramp, flat and groove regions as shown in Figure 5.28(b).

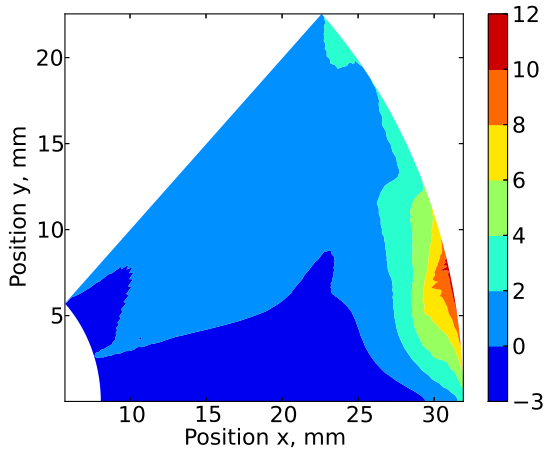
For domain 1, the ambient pressure and temperature are set at the leading and trailing edges. For domain 2, the leading edge is connected with the groove region by a cyclic boundary condition. The top surface is regarded as the rotor, where a rotational speed is prescribed. The bottom is modelled as a fixed temperature wall and connected to the structural deformation solver. The boundaries at



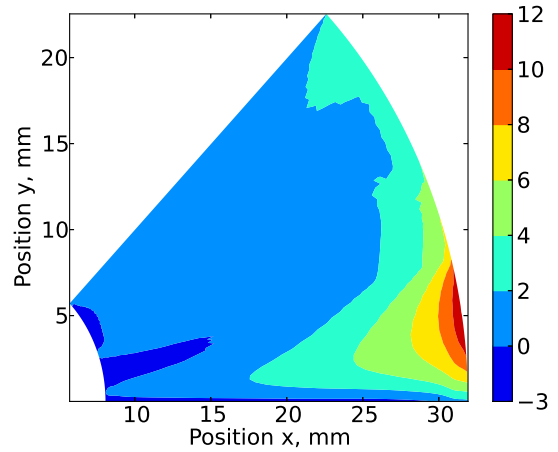
(a) stator, pressure contour and streamline



(b) rotor, pressure contour and streamline



(c) stator, radial velocity (in m/s)



(d) rotor, radial velocity (in m/s)

**Figure 5.27:** Pressure and radial velocity close to stator and rotor. Operating condition: 4.0 MPa and 400 K, the rotational direction in anti-clockwise, Eilmer-turbulent.

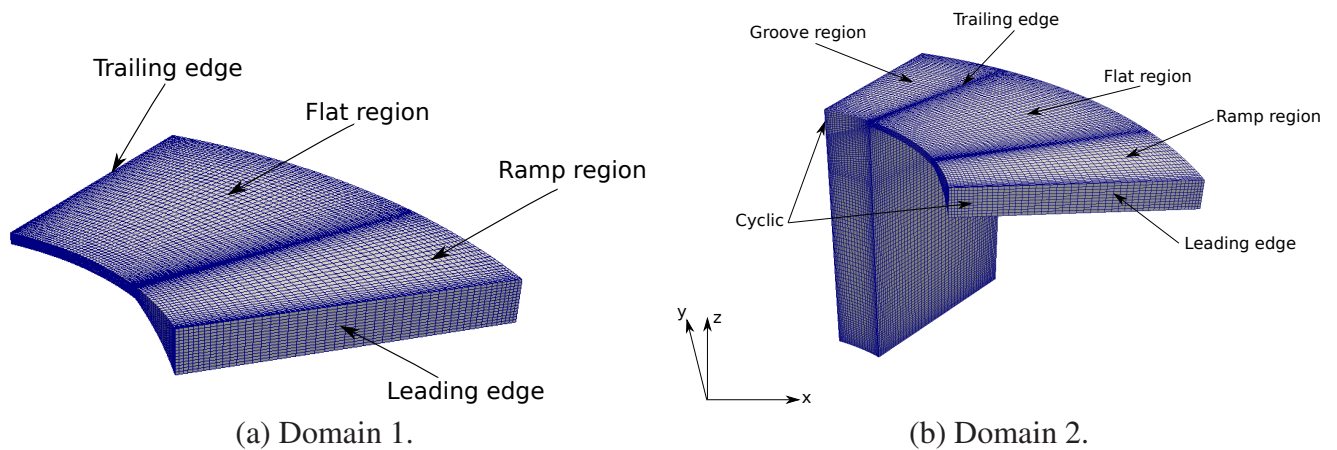


**Figure 5.28:** Schematic diagram of different computational domains for foil thrust bearings.

the inner and outer radii are modelled as the fixed static pressure and temperature. Both cases are investigated for operation with a fixed rotational speed of 40 000 rpm and for three load cases (200 N, 300 N and 400 N). To rule out the effects of the deformed shape and structural parameters, e.g. structural stiffness and damping, a rigid computational domain is used for the comparison.

The steady state gauge pressure contours at a load of 200 N, and gauge pressure along the medium radius are depicted in Figure 5.29. Here, the gauge pressure is the static pressure with respect to the ambient pressure (1.4 MPa in this paper).

As observed in Figure 5.29, the gauge pressure contours are similar for the two domains, but a difference in magnitude is observed close to the leading and trailing edges. The computational domain 2 now predicts a pressure above ambient at the leading edge (circumferential angle equals to  $0^\circ$ ), and a sub-ambient pressure at the trailing edge (circumferential angle equals to  $45^\circ$ ) as shown in Figure 5.29(c). The pressure increases when the flow enters from the groove into the ramp region and decreases when exiting from the trailing edge. This highlights the importance of simulating the groove to ensure accurate pressure distributions.

## 5.8 Steady State Performance

Using the full computational domain, the steady state performance (load capacity and power loss) is investigated. Results are obtained by evaluating performances of the foil thrust bearing operating with  $\text{CO}_2$  at multiple rotational speeds (30 000 rpm, 40 000 rpm and 50 000 rpm) and at different rotor to top foil separations (from  $10\ \mu\text{m}$  to  $26\ \mu\text{m}$ , intervals of  $2\ \mu\text{m}$ ). A mesh with  $48 \times 72 \times 15$  cells is used

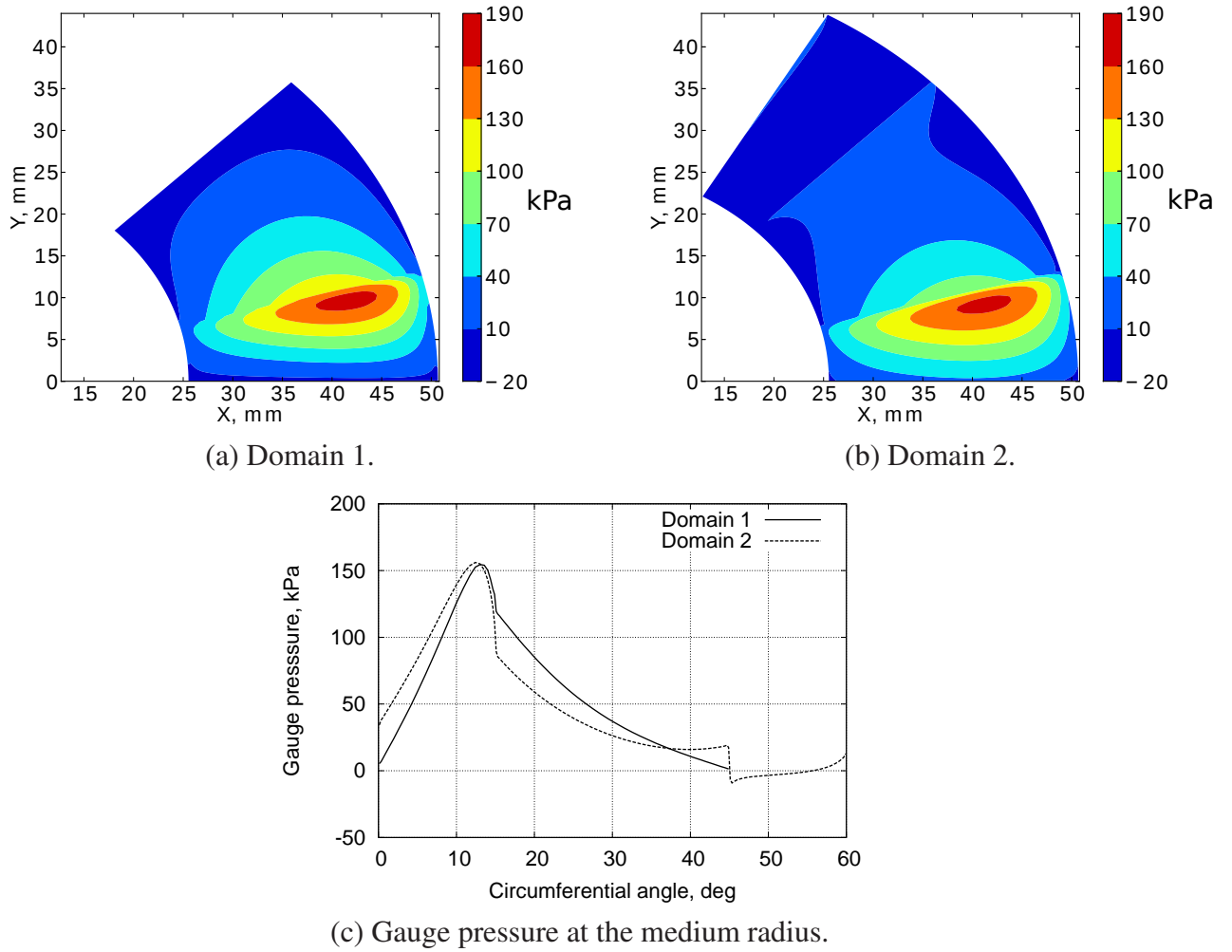


**Figure 5.29:** Comparison of pressure distribution at different computational domains, rotational speed is 40 000 rpm and load is 200 N, notable differences in pressure at start of ramp and end of flat regions.

for the fluid film and  $48 \times 24 \times 105$  cells is used for the groove. The meshes have been shown to give grid independent.

The film pressures and deflection contours at different rotor to top foil separations ( $10 \mu\text{m}$ ,  $18 \mu\text{m}$  and  $26 \mu\text{m}$ ) are shown in Figure 5.30, for a rotational speed of 30 000 rpm. The slices of gauge pressure and local deflection at the medium radius are plotted in Figure 5.30(g) and (h). The maximum deflection (approximately  $70 \mu\text{m}$ ) is in the ramp region close to the outer radius. The reason is that there are no bump foils underneath the top foil within the ramp. Thus no structural support is provided for the top foil. The deflection is between 0 to  $10 \mu\text{m}$  in the flat region. The peak pressure is observed at the end of the ramp region, which is attributed to the convergent shape. The pressure then reduces in the flat region due to leakage through the sides and the centrifugal inertia effects as highlighted in Refs. [171, 172]. However, pressure increases again close to the trailing edge (circumferential angle equals to  $45^\circ$ ) for the high load case (initial rotor to top foil separation of  $10 \mu\text{m}$ ), shown in Figure 5.30(g). Since the bump foils exhibit a hardening effect [173], especially at high load conditions, the change of the local deflection is not proportional to the load. This is confirmed in Figure 5.30(h), showing that the deflection at the trailing edge is almost the same for the cases with the initial rotor to top foil separations of  $18 \mu\text{m}$  and  $26 \mu\text{m}$ , despite the different pressure (see Figure 5.30(g)). For the high load, a second convergent shape is generated close to the trailing edge and provides a mechanism to increase the pressure here.

The results of load capacity and power loss at different rotor to top foil separations and rotational speeds are depicted in Figure 5.31. The maximum load of 516 N is obtained with a power loss of 1648 W (rotational speed of 50 000 rpm). The magnitudes of load and power loss are consistent with work by Conboy [8] using turbulent Reynolds equation to solve film pressure. As shown in Figure 5.31(a), the load capacity of foil thrust bearings exhibits a roughly linear relationship in terms of rotor to top foil separations. This is attributed to the increased compression of fluid film when the rotor to top foil separation decreases.

The power loss shown in Figure 5.31(b) also increases linearly as a function of the rotor to top foil separation, but at a slower rate compared to load capacity. The power loss is mainly attributed to the turbulent Couette flow and is inversely proportional to the gas film thickness. It is noted that the power loss is less sensitive to the rotor to top foil separation. This can be explained by the increase in the top foil deflection, which increase as load increases as shown in Figure 5.30. Only a 20 % change

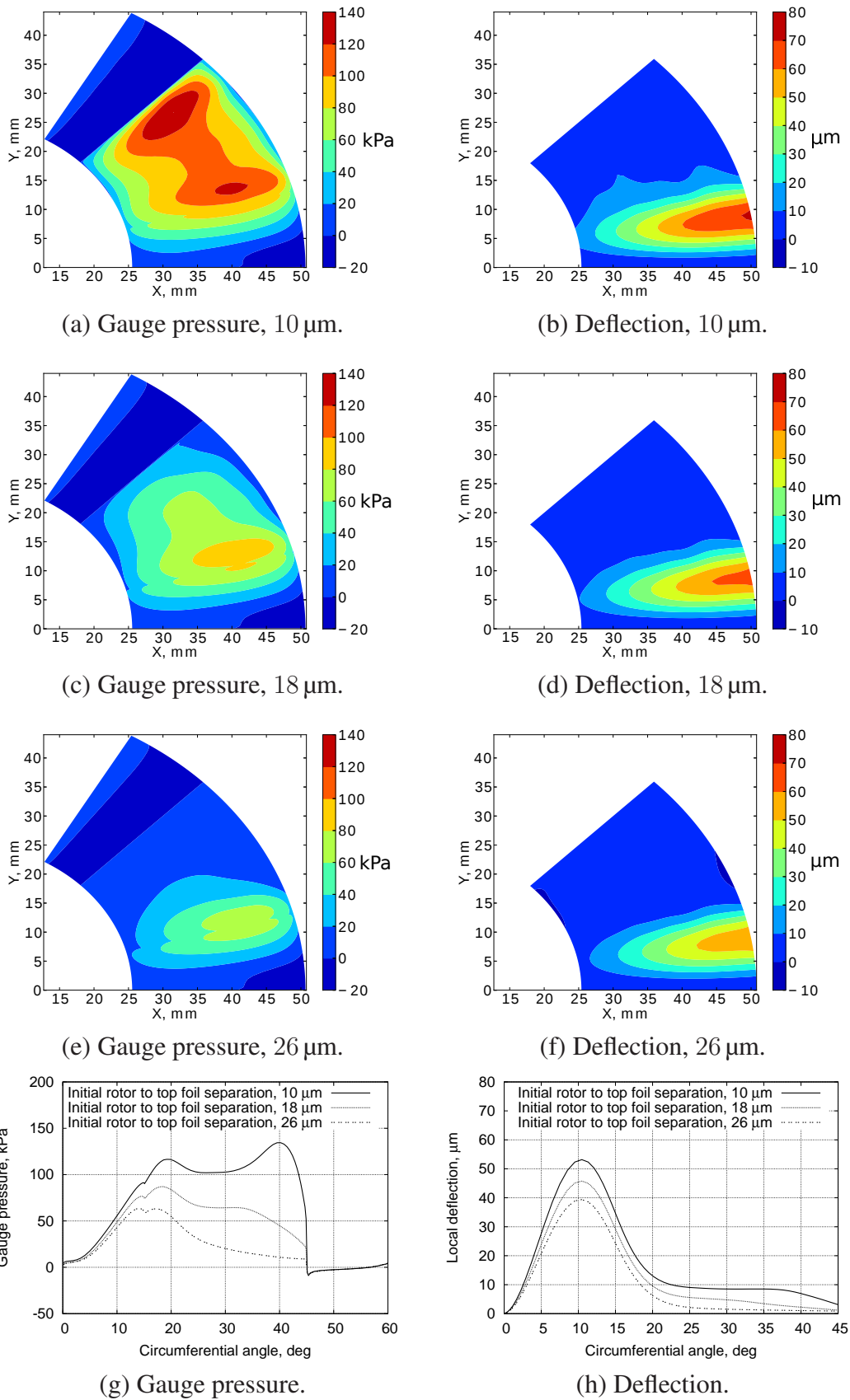


**Figure 5.30:** Gauge Pressure (unit in kPa) and deflection (unit in  $\mu\text{m}$ ) contours at different rotor to top foil separation, rotational speed of 30 000 rpm.

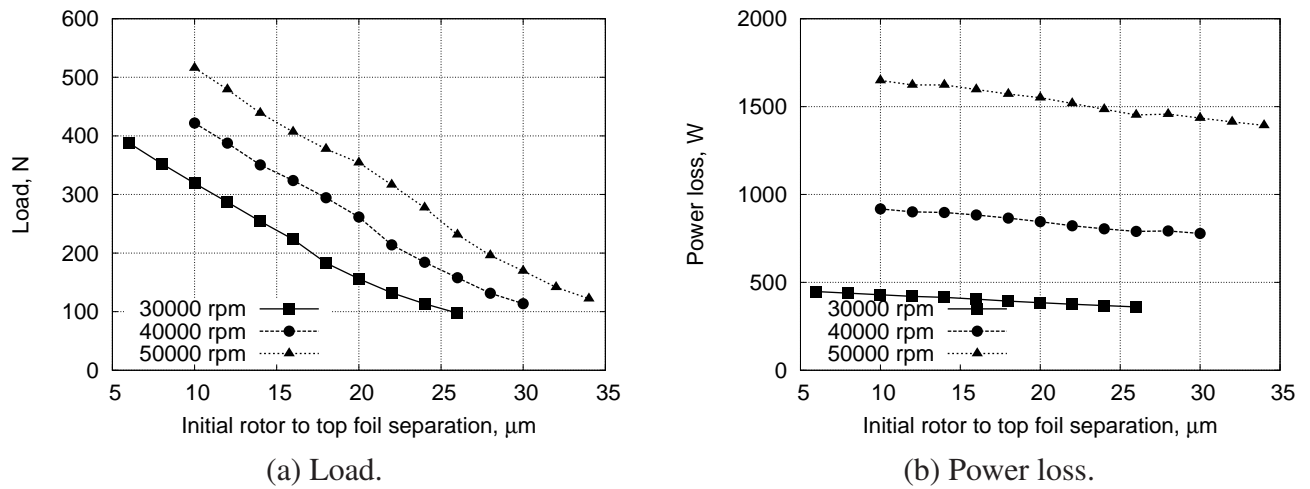


**Figure 5.31:** Steady state performance of foil thrust bearings under different rotational speed and initial film thickness.

is observed across the range of rotor to top foil separations at each speed. However, the power loss increases by almost 100% when the rotational speed increases from 30 000 rpm to 40 000 rpm. This confirms that rotational speed is the main driver behind power loss and heat generation, much more than load.

## 5.9 Conclusions

The modified fluid-structure simulation tool is used to identify the challenges of operating foil thrust bearings with high pressure CO<sub>2</sub>. It is found that at SNL’s operating point for foil thrust bearings (1.4 MPa and 300 K), there is the noticeable deviation of properties between the ideal gas model and look-up table and a slightly non-ideal gas behaviour was also indicated. It is recommended that the look-up table approach is used in the subsequent analysis. With dense CO<sub>2</sub> as the operating fluid, there is a different pressure distribution resulting from CFD and Reynolds equation analyses. The Reynolds equation analysis cannot account for the irregular radial velocity profiles that are driven by strong inertial effects.

The effect of operating conditions on the performance of foil thrust bearings were investigated. It is found that a ten-fold increase of CO<sub>2</sub> pressure and thus density can significantly alter foil bearings performance. The density change can alter load capacity by up to 40 %. This is due to the additional mass flow at the inner edge of the ramp region created by centrifugal inertia effects. But centrifugal inertia effects also cause an increased leakage towards the outer edges in the flat region which is

detrimental to lift generation.

Due to the high densities foil thrust bearings can also operate in the turbulent flow regime. As a consequence of the additional eddy viscosity, the foil thrust bearings now experience different velocity profiles across the film height, which result in increased power consumption. In contrast, load capacity only shows a slight increase for turbulent flows. Due to the compliance of the bump foils, which deflect almost twice as much under turbulent conditions, the potential to increase lift is decreased. Load capacity and power loss of the foil thrust bearings for operation with CO<sub>2</sub> can be enhanced through optimisation of bump foil and top foil stiffness in future.

For the selected rotor to top foil separations and rotational speeds, the maximum load can be up to 516 N, whilst a maximum power loss of 1648 W is also generated. Both load and power loss increase linearly as the rotor to top foil separations decrease at different rotational speeds, but a slower rate is obtained for power loss compared to load. The rotational speed has a larger effect on the power loss compared to the rotor to top foil separations.

---

# Foil Bearing Dynamic Performance

---

## 6.1 Introduction

Dynamic performance is also a key parameter to consider selecting appropriate bearings. These parameters influence the vibration of the shaft. Typically, bearings with high stiffness and damping coefficients are desirable. These features are favourable to reduce the shaft vibration amplitude. In this Chapter, the procedure to obtain stiffness and damping coefficients from fluid-structure simulations is introduced in Section 6.2. Section 6.3 details the suitability of the method to calculate stiffness and damping by comparing to a verification case. Section 6.4 revisits the computational domain including the groove by highlighting dynamic performances.

## 6.2 Dynamic Performance Evaluation

Once the steady state solution for foil thrust bearings using fluid-structure simulation tool is obtained, a sinusoidal rotor excitation is applied, as shown in Figure 6.1 to obtain the dynamic stiffness and damping. The conventional rotordynamic model to quantify reaction forces, for small axial rotor motions is presented in Equation 6.1 [174]. Here all coefficients are assumed frequency dependent and added mass effects are neglected,

$$-f_z(t) = K(\Omega) \Delta z(t) + C(\Omega) \Delta \dot{z}(t) . \quad (6.1)$$

$K$  is the stiffness coefficient,  $C$  is the damping coefficient,  $\Omega$  is the excitation frequency,  $f_z$  is the reaction force and  $\Delta z$  is the perturbed rotor position. The reaction forces  $f_z$  acting on the rotor are

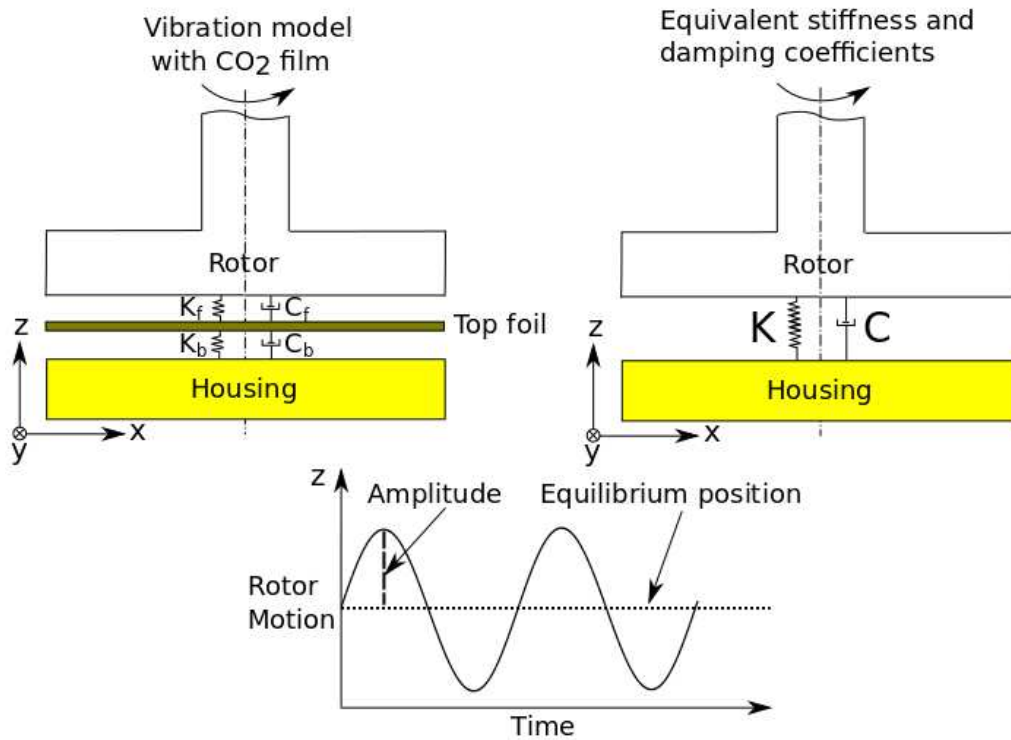


**Figure 6.1:** Schematic diagram of rotor perturbation motion.

obtained by integrating the instantaneous pressure,

$$f_z(t) = \int (p(t) - p_a) dA , \quad (6.2)$$

where  $p$  is the pressure acting on the rotor surface, while  $p_a$  is the ambient pressure, and  $A$  is the rotor area. The reaction forces have the same frequency as the prescribed rotor movement but are shifted in phase. The rotor position is perturbed using a uni-directional harmonic function,

$$\Delta z(t) = \delta \sin(\Omega t) , \quad (6.3)$$

where the amplitude  $\delta$  is defined as a fraction of the clearance between rotor and bearing and the excitation frequency  $\Omega$  is chosen as a fraction of the rotational speed of the rotor.

The rotordynamic coefficients can be determined by analysing the reaction forces due to the prescribed rotor motion. To solve the frequency-dependent rotordynamic coefficients in Equation. 6.1,

the Laplace transform is performed over the interval  $[0, T]$ , written as,

$$F(s) = D(s) Z(s) . \quad (6.4)$$

The time-dependent component are,

$$F(s) = \int_0^T f(t) e^{st+\phi} dt , \quad (6.5)$$

$$D(s) = K(\Omega) + s C(\Omega) , \quad (6.6)$$

$$Z(s) = \int_0^T \Delta z(t) e^{st} dt , \quad (6.7)$$

where  $s = i\Omega$ ,  $i = \sqrt{-1}$  and  $\phi$  is the phase lag between the rotor motion and the reaction forces. The phase lag  $\phi$  between the rotor position and the reaction force is obtained by measuring the peak-to-peak time delay  $\Delta T$  between the harmonic motion and force data from the unsteady CFD simulations. This is turned into a phase lag using  $\phi = 2\pi\Omega\Delta T$ . As all the component are complex variables,  $F(s)$  and  $Z(s)$  can be written as,

$$F(s) = F_r(\Omega) + i F_i(\Omega) , \quad (6.8)$$

$$Z(s) = Z_r(\Omega) + i Z_i(\Omega) . \quad (6.9)$$

The real and imaginary parts of reaction force and rotor motion are computed as [175],

$$Z_r(\Omega) = \frac{1}{2} \sum_{i=1}^n \Delta t [\Delta z(t_i) \cos(\Omega t_i) + \Delta z(t_{i-1}) \cos(\Omega t_{i-1})] , \quad (6.10)$$

$$Z_i(\Omega) = \frac{1}{2} \sum_{i=1}^n \Delta t [\Delta z(t_i) \sin(\Omega t_i) + \Delta z(t_{i-1}) \sin(\Omega t_{i-1})] , \quad (6.11)$$

$$F_r(\Omega) = \frac{1}{2} \sum_{i=1}^n \Delta t [f(t_i) \cos(\Omega t_i) + f(t_{i-1}) \cos(\Omega t_{i-1})] , \quad (6.12)$$

$$F_i(\Omega) = \frac{1}{2} \sum_{i=1}^n \Delta t [f(t_i) \sin(\Omega t_i) + f(t_{i-1}) \sin(\Omega t_{i-1})] . \quad (6.13)$$

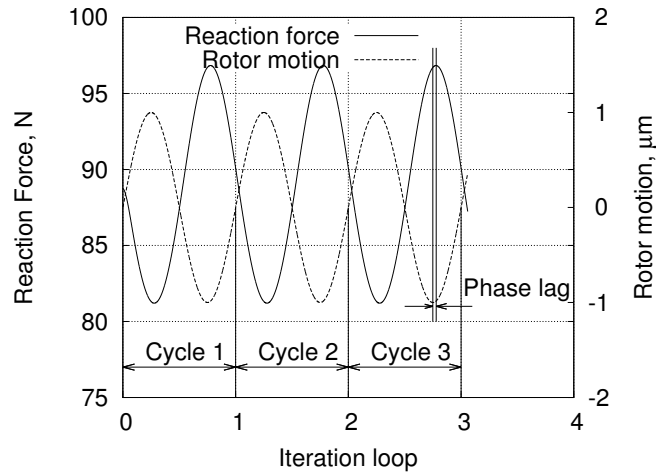


**Figure 6.2:** History plot of reaction force and rotor motion.

By substituting the above equations into Equation 6.4, the following equations are obtained,

$$F_r = K(\Omega) Z_r - \Omega C(\Omega) Z_i, \quad (6.14)$$

$$F_i = K(\Omega) Z_i + \Omega C(\Omega) Z_r. \quad (6.15)$$

Hence, it is now straightforward to calculate the stiffness and damping coefficients as,

$$K(\Omega) = -\frac{F_r Z_r + F_i Z_i}{Z_r^2 + Z_i^2}, \quad (6.16)$$

$$C(\Omega) = \frac{F_r Z_i - F_i Z_r}{\Omega (Z_r^2 + Z_i^2)}. \quad (6.17)$$

### 6.3 Verification of Dynamic Analysis Capability

The structural deformation solver is executed with a comparatively large time step  $\Delta t_s$  during fluid-structure simulations to obtain the steady state bearing performance. To accurately predict the dynamic performance of foil thrust bearings,  $\Delta t_s$  has to be selected appropriately. To investigate this, the rotational speed of the foil thrust bearing is set to 21 000 rpm, matching the operating conditions from the experiment presented by Dickman [73]. The rotordynamic performance of this foil thrust bearing was investigated by San Andrés [26], and his results are used for verification.

The optimal mesh ( $48 \times 96 \times 15$ ) for foil thrust bearings, as attained in Chapter 5 is used. In order to

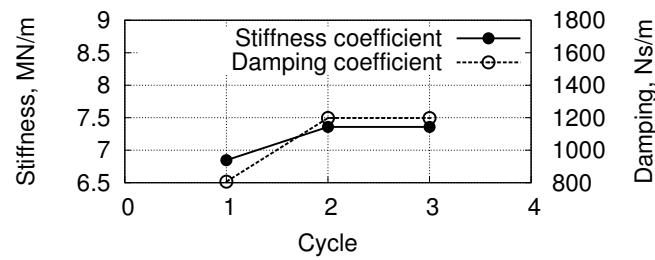


**Figure 6.3:** Comparison of the calculated stiffness and damping coefficient at different cycles.

establish time-step independence, first the number of oscillations required to reach a steady response has to be determined. The time history of the reaction force and rotor motion for a time step  $\Delta t_s = 2 \mu\text{s}$  for the structural deformation solver is depicted in Figure 6.2. The phase lag is approximately  $10^\circ$  ( $80 \mu\text{s}$ ). The rotordynamic coefficients are compared in Figure 6.3. It is found that the results converge after two periods. This matches the observations from Ref. [175].

Three different time steps,  $\Delta t_s$  ( $2 \mu\text{s}$ ,  $1 \mu\text{s}$  and  $0.5 \mu\text{s}$ ) are used for a sensitivity study to select a suitable time step for fluid-structure simulations. The results are shown in Figure 6.4(a) and are all calculated during the second harmonic motion of the rotor. Insensitivity to the size of the time step is observed for all cases and  $1 \mu\text{s}$  is selected for the subsequent analysis. The effect of perturbation amplitude (5 %, 10 % and 15 % of the clearance) is compared in Figure 6.4(b). This indicates the insensitivity of results to excitation amplitude. A 10 % perturbation amplitude is used for the following studies.

San Andrés et al. [26] predicted the synchronous rotordynamic performance of air foil thrust bearings at a rotational speed of 21 000 rpm. His results are based on small perturbations of Reynolds equation. These results can be used as a the verification case. The results obtained using the current code are compared to results for San Andrés [26] in Figure 6.5. Good agreement is achieved for damping coefficients at the various load conditions. A slight difference is found for stiffness coefficients. This can be attributed to the use of different top & bump foil models. However, the trend in terms of load capacity is the same.

## 6.4 Revisit of Computational Domain: Dynamic Performance

This section is a follow-up of Section 5.7. The synchronous stiffness and damping coefficients at different loads are shown in Figure 6.6. The computational domain 1 overpredicts rotordynamic coef-

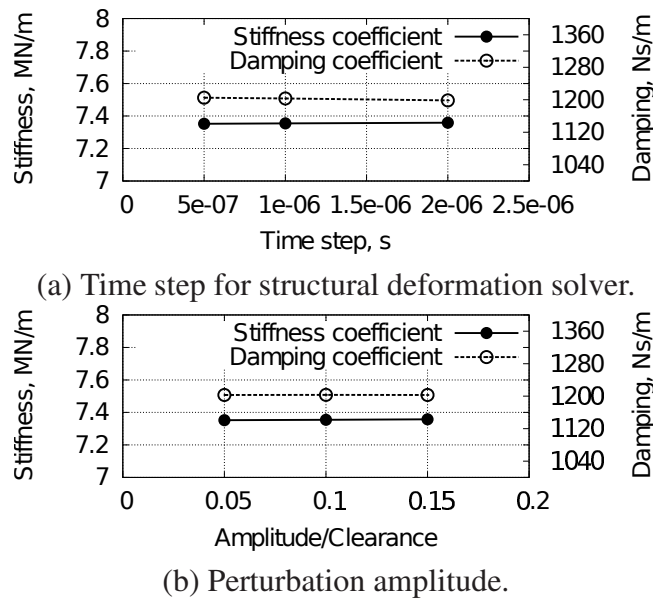


Figure 6.4: Comparison of the calculated stiffness and damping coefficient at different parameters.

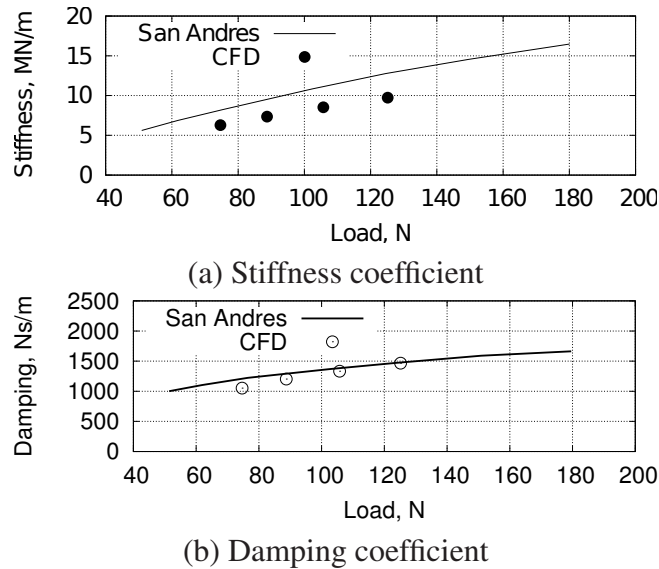
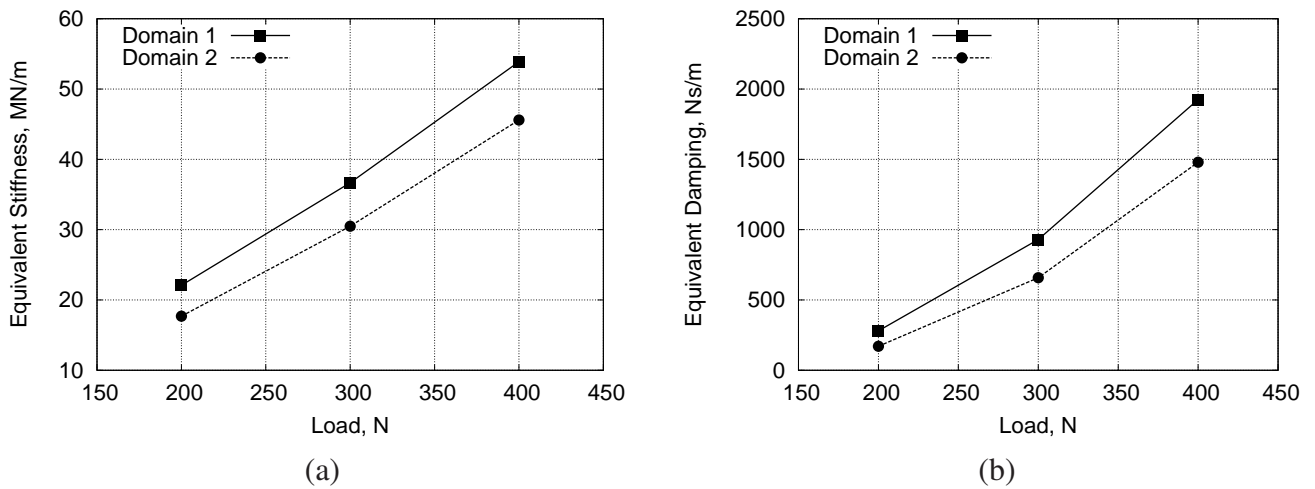


Figure 6.5: Comparison of CFD and numerical results from San Andrés [26], rotational speed: 21 000 rpm.



**Figure 6.6:** Comparison of foil thrust bearings performance at different computational domain, (a): synchronous stiffness; (b): synchronous damping.

ficients. At a load of 200 N, the synchronous stiffness decreases by approximately 20 % compared to that of computational domain 1, while a reduction of 39 % is observed for synchronous damping. Moreover, these differences increase with increasing load. The reason is that the fixed static pressure condition at the leading and trailing edges cannot provide accurate transient performance, as pressure is truncated at these boundaries. Therefore, pressure waves do not propagate to the next thrust pad correctly. The groove may act as a destabilising force to the rotor as revealed by results from computational domain 2. Since a notable difference is found between these two computational domains in terms of the steady state and dynamic performances, domain 2 shown in Figure 5.28, is utilised for further analysis.

## 6.5 Conclusions

In this Chapter, the dynamic performances of foil thrust bearings are investigated. The computational domain including the groove should be utilised, since rotordynamic coefficients are different compared to those obtained from a computational domain consisting of only ramp and flat regions. Dynamic performances of foil thrust bearings operating with CO<sub>2</sub> in terms of load and rotational speeds will be investigated in future.



---

# Fluid-Structure-Thermal Simulations

---

## 7.1 Introduction

The necessity to predict of thermal behaviour of foil bearings has been discussed in Chapter 2. This chapter presents a computational framework for a three-dimensional fluid-structure-thermal simulation of foil thrust bearings. First, the basic computational framework for fluid-structure-thermal simulations is provided including a description of the fluid, structural deformation, and heat conduction solvers in Section 7.2. Next, the coupling strategies between these solvers are introduced, followed by two test cases. Section 7.3 details the heat transfer model applied to foil thrust bearings. Finally, the fluid-structure-thermal simulation results for air and CO<sub>2</sub> foil thrust bearings are presented and discussed in Section 7.4.

## 7.2 Computational Framework

The computational model includes three aspects: fluid, structural deformation, and heat conduction solvers. The corresponding fluid and structural deformation solvers are discussed in Chapter 4. Only the heat conduction solver is explained in this Chapter.

### 7.2.1 Heat Conduction Solver

As the fluid solver Eilmer currently is not capable of three-dimensional heat conduction analysis, the solver LaplacianFoam from the open source CFD toolbox FOAM-Extend-3.0 [139] is used to model heat conduction through the solid parts of the foil bearing. The governing equation for conduction in LaplacianFoam is,

$$\frac{\partial T}{\partial t} - \nabla^2(D_T \cdot T) = 0 \quad . \quad (7.1)$$

Since LaplacianFoam is already a mature solver for solving the transient Laplace's equation, verification or validation cases are not provided here.

## 7.2.2 Coupling Method: Fluid-Thermal

For fluid-thermal interactions, only the steady-state performance of the foil thrust bearings is of interest due to the large time constant  $\tau_{heat}$  for the heat conduction problem. Effectively the time it takes for foil bearing components to adjust temperature is much longer than the time it takes for the foils to change shape or for fluid properties to adjust. Thus the temperature will affect steady state performance and not be directly linked to dynamic performance. In the final, steady state, heat flux between domains (fluid and solid) and temperature at the fluid-structure interface has to agree. The condition at the interface,  $i$  can be mathematically expressed as,

$$\mathbf{q}_{i,f} = \mathbf{q}_{i,s} \quad , \quad (7.2)$$

$$T_{i,f} = T_{i,s} \quad . \quad (7.3)$$

where  $\mathbf{q}$  is the heat flux,  $T$  is the temperature and subscripts  $f$  and  $s$  indicate the interface of fluid and solid domain, respectively. Considering only conduction at the interfaces, the flux condition can be expanded as,

$$\mathbf{q}_{i,f} = -\lambda_{i,f} \left. \frac{\partial T}{\partial \mathbf{n}} \right|_{i,f} \cdot \mathbf{n}_i = \mathbf{q}_{i,s} = -\lambda_{i,s} \left. \frac{\partial T}{\partial \mathbf{n}} \right|_{i,s} \cdot \mathbf{n}_i \quad (7.4)$$

where  $\lambda$  is thermal conductivity. The spatial derivative  $\left. \frac{\partial T}{\partial \mathbf{n}} \right|_{i,f}$  for the fluid domain is approximated using a one-sided difference between the wall-adjacent cell centre temperature and the interface temperature. For turbulent simulations with wall functions, the heat flux  $\mathbf{q}_{i,f}$  is extracted from the wall function. The temperature gradient at the solid domain  $\left. \frac{\partial T}{\partial \mathbf{n}} \right|_{i,s}$ , is defined as

$$\left. \frac{\partial T}{\partial \mathbf{n}} \right|_{i,s} = \frac{\mathbf{q}_{i,f}}{\lambda_{i,s}} \quad , \quad (7.5)$$

Since only the steady state of the foil thrust bearings is of interest, a weak coupling strategy is proposed for the fluid-thermal simulations. Relaxation at each iteration is necessary to increase the stability of the numerical scheme. A simple relaxation strategy is given by,

$$\mathbf{T}_{i,f}^{k+1} = \mathbf{T}_{i,f}^k + \beta \mathbf{f}_{i,s}^k \quad , \quad (7.6)$$

where  $\beta$  is the under-relaxation factor and  $k$  is the index of the iteration loop. During the iteration loop  $k$ , a nonlinear operation is applied to an input vector  $\mathbf{T}_{i,f}^k$  generating an output vector  $\mathbf{T}_{i,s}^k$  of the same size. The residual vector is defined as  $\mathbf{f}_{i,s}^k = \mathbf{T}_{i,s}^k - \mathbf{T}_{i,f}^k$ . Typically  $\beta$  is set to a constant between 0 and 1. This relaxation factor is consistent for each cell but can be different for each fluid-thermal iteration loop.

Alternatively, an optimal value of the relaxation factor can be selected for each iteration. Different dynamic relaxation techniques are reported in literature. In this study, we use the variant of vector Aitken  $\Delta^2$  method formulated in Ref. [176], because it is easy to be implemented and does not require too much memory during computations. This algorithm starts with a known sequence of two input/output pairs of vectors and calculates an optimum relaxation parameter as,

$$\beta_k = \beta_{k-1} + \beta_{k-1} \frac{\Delta \mathbf{f}^{kT} \mathbf{f}^k}{\|\mathbf{f}^k\|_2^2}, \quad (7.7)$$

where the residual difference vector is  $\Delta \mathbf{f}^k = \mathbf{f}^{k-1} - \mathbf{f}^k$ . The first iteration is carried out using a pre-selected relaxation constant  $\beta_0$ . This method is straightforward to implement, needs minimum processor and storage resources, and only takes a single residual evaluation per iteration. The entire procedure is as follows

1. The fluid domain is solved by Eilmer with an imposed initial temperature  $\mathbf{T}_{i,f}^k$  until an equilibrium fluid state is achieved;
2. Heat flux  $\mathbf{q}$  at the fluid-solid interfaces in Eilmer is evaluated. The temperature gradient at the solid side is calculated based on the continuity of heat flux across the fluid-structure boundary (Equation 7.4 and 7.5);
3. The temperature gradient is taken as the boundary condition for the heat conduction analysis. The simulation is conducted with LaplacianFoam until the temperature solution in the solid is converged;
4. The surface temperature  $\mathbf{T}_{i,s}^k$  at the interfaces from LaplacianFoam is extracted. The new  $\mathbf{T}_{i,f}^k$  is set as the boundary condition for Eilmer. In the first iteration loop, a pre-defined under-relaxation factor is used in Equation 7.6, thereafter  $\beta$  is calculated with Equation 7.7;
5. Repeat steps 1-4 using the new  $\mathbf{T}_{i,f}^k$  until convergence.

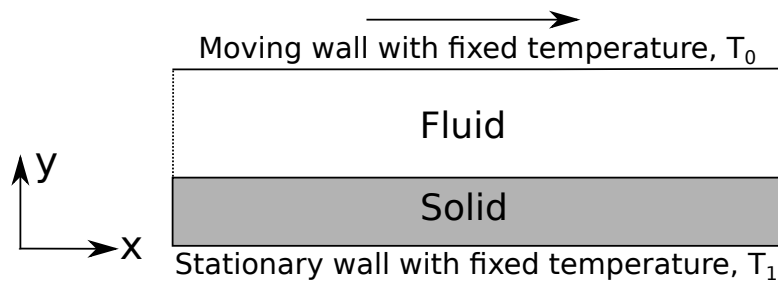


**Figure 7.1:** Schematic diagram for conjugate Couette flow.

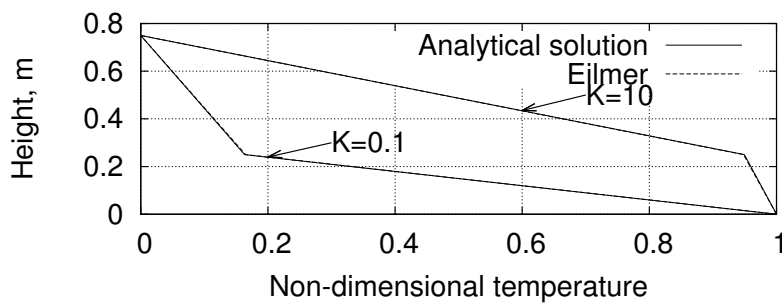


**Figure 7.2:** Comparison of temperature distribution between fluid-thermal simulation and analytical solution.

For air foil thrust bearings, it typically takes 60 iteration loops to obtain a converged solution. 30 loops are usually sufficient for CO<sub>2</sub> foil thrust bearings. Two validation cases for the proposed fluid-thermal coupling method are discussed next.

### 7.2.3 Conjugate Couette Flow

The first validation case is the problem of conjugate Couette flow in a parallel plate channel, a typical shear driven flow for conjugate heat transfer analysis. The schematic diagram is depicted in Figure 7.1 with a fluid between a hot upper wall with temperature  $T_0$  that moves at a constant velocity and a stationary conducting solid at the bottom. The side of the conducting solid away from the fluid is maintained at a constant temperature  $T_1$ . The solid part has a height of 0.25 m, while the height of the fluid domain is 0.5 m.

The computed solutions are compared with the analytical solutions [177] in Figure 7.2. This shows excellent agreement with the analytical solutions for two conducting ratios,  $K = \lambda_s/\lambda_f$ . The relative error between numerical results and analytical solution is less than 0.04 %.

## 7.2.4 Conjugate Nozzle Flow

This test case is used to validate turbulent conjugate heat transfer. The supersonic flow inside a cooled axisymmetric convergent divergent nozzle is investigated. The analysis is based on the experimental data reported by Back et al. [178]. The test nozzle is axisymmetric, has a throat diameter of 0.0458 m, and contraction area ratio of 7.75:1, an expansion area ratio of 2.68:1, a convergent half-angle of 30 deg, and a divergent half-angle of 15° deg as shown in Figure 7.3. The detailed geometry and operating condition are available in Ref. [179, 180].

The temperature distribution for the outer wall of the nozzle from the experiment is shown in Figure 7.4(a). This is used as the nonuniform temperature boundary for the outer wall in the numerical simulation. The uncertainty on the temperature measurements is approximately 2 % [178]. The inflow condition for this axisymmetric nozzle is,  $T_0=843.3$  K and  $p_0=517.1$  kPa.

This case of conjugate nozzle flow has previously been simulated by Marineau et al. [180] and Liu et al. [181]. The wall material was not specified by Back et al. [178], however the thermal conductivity of the material,  $\lambda_s$ , can be determined from the temperature gradient and the heat flux provided by Back et al. [178]. Marineau et al. [180] concluded that the thermal conductivity of the nozzle wall material is approximately 27 W/mK. The conjugate nozzle heat transfer problem is solved by imposing the temperature profile shown Figure 7.4(a) along the outside wall. The temperatures at the solid sides that correspond to the nozzle inlet and outlet are specified as 299 and 283 K, respectively, as suggested by the experimental data. The problem was simulated using the fluid thermal coupling strategy discussed in Section 7.2.2. The grid was refined until a grid independent solution was obtained. Turbulence was modelled using the  $k-\omega$  model without wall functions. The schematic diagram is shown in Figure 7.3.

Figure 7.4(b) shows the comparison between predicted inner wall temperatures and experimental data. The predicted wall temperatures are close to the experimental values. Due to unknown parameters from the experiment, there are some deviations between numerical results and experiment data, especially inaccuracies close to the nozzle inlet and exit. This is also reported in Ref. [180, 181] and most likely due to the solid thermal boundary condition applied to the axial faces. The suitability of the proposed coupling strategy for fluid-thermal simulation has been tested. This coupling strategy is further refined to include couple structural deformation solver in Section 7.2.5.

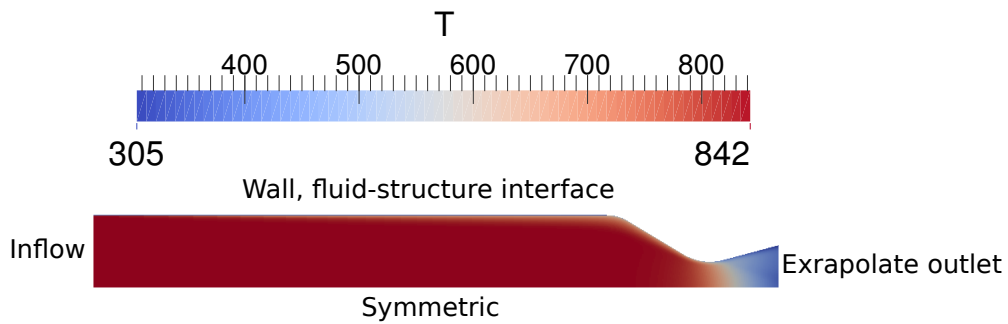


**Figure 7.3:** Boundary conditions for conjugate nozzle flow, coloured by temperature.

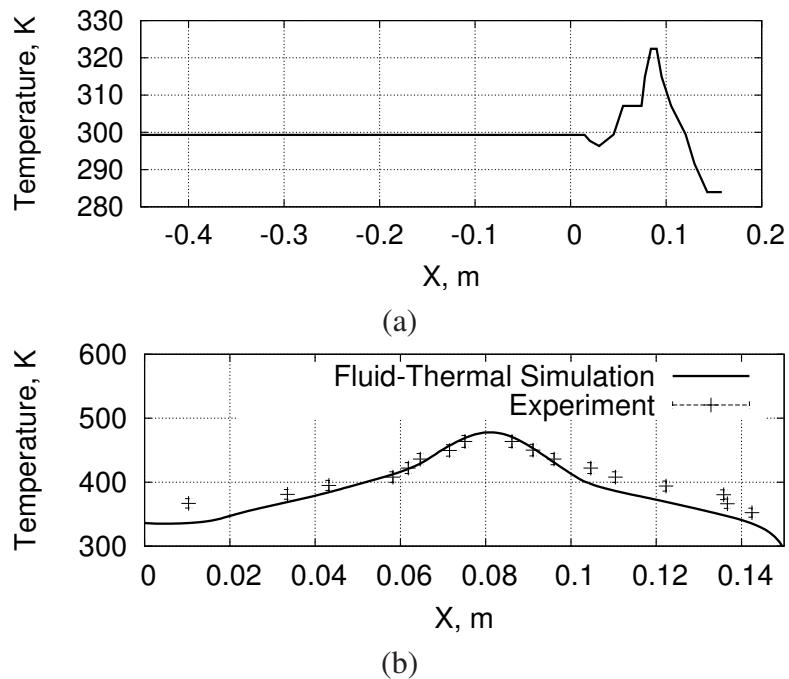


**Figure 7.4:** (a) Temperature distribution along outer wall of nozzle [178], used as the nonuniform temperature boundary condition for numerical simulation, (b) comparison of temperature distribution along inner wall of nozzle between numerical simulation and experiment [178].

### 7.2.5 Coupling Method: Fluid-Structure-Thermal

The three individual solvers for the current problem (transient fluid flow, structural deformation and heat conduction) within foil thrust bearings have been described as well as the individual coupling methods for fluid-structure and fluid-thermal simulations. However, these solvers have to be coupled for a full fluid-structure-thermal simulation. The magnitude of the structural deflection is typically in microns, thus the effect of the deflection is minimal when solving the heat diffusion problem in the solid. Therefore, the effect of the deformation is not considered when solving the thermal equations. However the effect of temperature is considered by the structural solver.

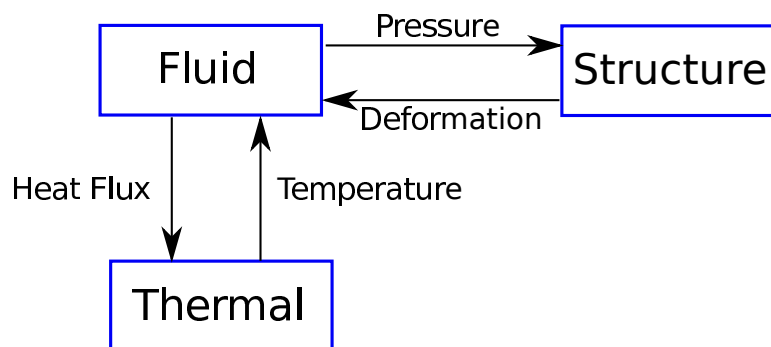


**Figure 7.5:** Schematic diagram for fluid-structure-thermal simulations.

The schematic diagram showing information exchange between the solvers for the fluid-structure-thermal simulations is shown in Figure 7.5. A tight coupling is implemented between the fluid and structure solvers, as the structural deformation reacts to the pressure increase in the fluid domain quickly and to allow rotordynamic analysis. Transient simulations of the coupled fluid-structure system, starting from stationary fluid case, have shown that the dynamically coupled fluid structure system can reach a steady operating point in less than 1 ms. However, as noted prior, the time constants in the heat conduction solver system are large, usually of the order of minutes. Hence, the temperature field takes a long time to achieve an equilibrium state. As shown in Ref. [112], it usually takes 3000 s for a three-pad journal bearings to reach the thermal equilibrium state. Hence, a weak coupling between the fluid and heat conduction solvers is selected.

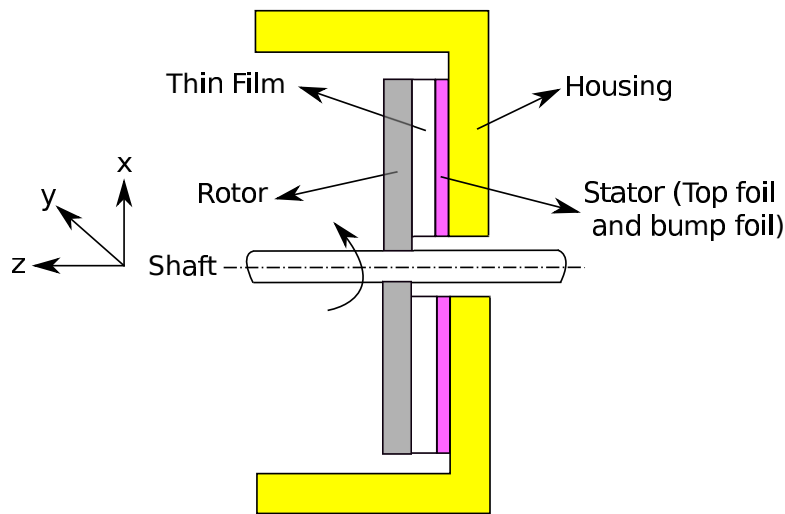


**Figure 7.6:** Schematic diagram for layout of foil thrust bearings.

## 7.3 Application to Foil Thrust Bearings

In this section, the detailed thermal analysis of a foil thrust bearing is described. The layout of a foil thrust bearing in a typical turbomachinery system is shown in Figure 7.6. It consists of shaft, rotor, stator (bump and top foils) and bearing housing. For the thermal analysis, the simulation domain is extended to include the rotor, stator and housing to allow a fluid-structure-thermal simulation of the foil thrust bearings while taking account of the surroundings. This provides an accurate temperature distribution within the foil thrust bearing components.

### 7.3.1 Heat Transfer Model for Rotor

The computational domain for the rotor is depicted in Figure 7.7. It uses a computational mesh of  $64 \times 120 \times 40$  cells. Although foil thrust bearings consist of several sectors (usually 6), only one sector is simulated with a periodic boundary condition to reduce computational cost. The computational domain for the rotor is different from that of the thin film. The inner radius is extended to the shaft as shown in Figure 7.6 and the outer radius is the same as the fluid domain.

For boundary conditions, the north and south boundaries (shaded surfaces) are connected with periodic boundary conditions. The bottom boundary ( $z = z_{min}$ ) is modelled as the fluid-solid interface, and the coupling method for fluid-thermal simulation is used here. As the rotor is spinning, a mixing-plane or tangentially strip averaged boundary conditions is applied when mapping the heat

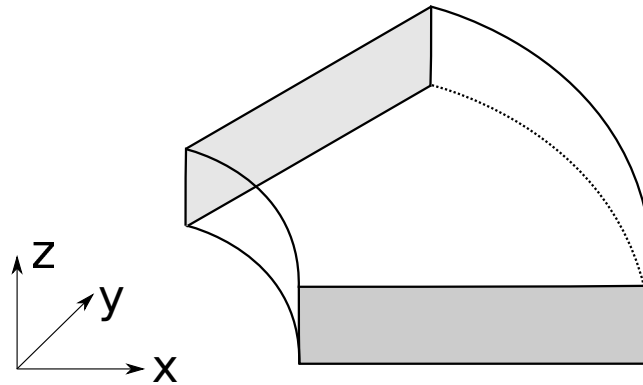


**Figure 7.7:** Computational domain for the rotor.

flux from fluid domain to the rotor. In this way, heat flux at the fluid domain is averaged in the tangential direction when passed to the solid interface. Since the west boundary (the inner radius) is connected with the shaft, a fixed operating temperature is imposed by considering the large heat transfer area between the shaft and the operating fluid. At the east (the outer radius) and top ( $z = z_{max}$ ) surfaces, convective heat transfer is assumed. For this purpose the rotor is modelled as a simple rotating disk exposed to an infinite quiescent medium. The following empirical correlations for heat transfer on rotating discs [182] are used.

$$\begin{aligned}
 Nu &= 0.33 Re^{0.5} Pr^{1/3} & Re < 1.95 \times 10^5 , \\
 Nu &= 10 \times 10^{-20} Re^4 Pr^{1/3} & 1.95 \times 10^5 < Re < 2.5 \times 10^4 , \\
 Nu &= 0.0188 Re^{0.8} Pr^{1/3} & Re > 2.5 \times 10^5 .
 \end{aligned} \tag{7.8}$$

### 7.3.2 Heat Transfer Model for Stator

The computational domain of the stator is shown in Figure 7.8. The stator geometry is much more complex than the rotor, and consists of top foil, bump foils and housing.

The upper surface of the top foil is the fluid-thermal interface, and the coupling method for fluid-thermal simulation is implemented at this boundary. Since the stator is a non-rotating part, and as there is a slight pressure difference in the radial direction, a natural convective boundary condition is applied at the inner and outer radius, within the bump foil channels and on the backside of the top foil. This approach was also employed by Lee and Kim [116]. In typical foil bearing applications

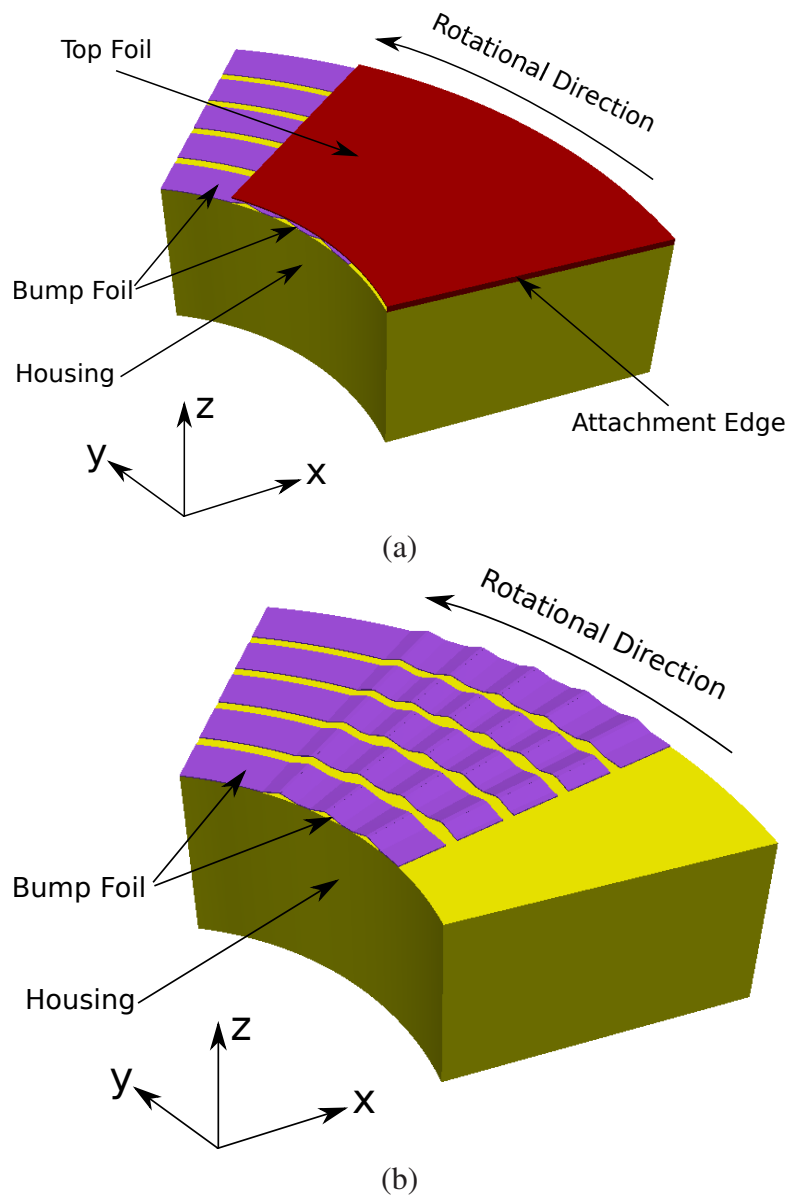


**Figure 7.8:** Computational domain for the stator, (a): Stator in three dimensional, (b): Stator with top foil removed in three dimensional.

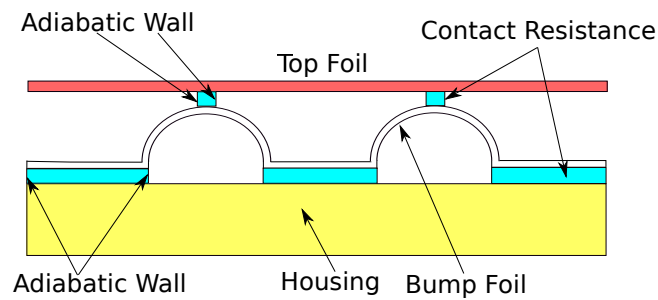


**Figure 7.9:** Schematic diagram of heat transfer from top foil to thrust plate.

forced convective cooling, achieved by applying a pressure gradient between the bearing inner and outer edge, is employed to cool the rear of the top foil and bump foil structure by enhanced heat transfer. The pressure gradient is set to suit the application (rotational speed and load). To remove the additional dependency on pressure gradient, the current study employs natural convection within the bump channel, rear of top foils, and inner and outer surfaces of the housing. The heat transfer coefficient is calculated by the method described in [183],

$$Nu = 0.36 + \frac{0.518(Fr Pr)^{1/4}}{(1 + (0.559/Pr)^{9/16})^{4/9}} \quad Gr Pr < 10^9, \quad (7.9)$$

where  $Gr$  is the Grashof number,  $Pr$  is the Prandtl number, and  $Nu$  is the Nusselt number. However, the presented modelling framework has the flexibility to incorporate a forced convection model, as required.

In addition, the back surface of the top foil and the stator housing experience thermal and mechanical contact with the bump foil. Figure 7.9 illustrates the thermal resistances at the bump contacts with the top foil and bearing housing. The bump foils link the top foils, which are heated by the viscous shear in the thin film, to the bearing housing via these thermal contact resistances. Thermal contacts are complicated in nature due to the thermal constriction and spreading of heat flux lines as well as the random distribution and the unknown boundary condition of micro-contacts [109]. For nominally flat and rough surfaces, the thermal contact resistance ( $m^2K/W$ ) obtained from experimental results

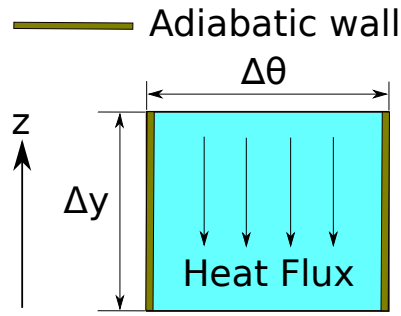


**Figure 7.10:** Schematic diagram of the additional geometry to account for the contact resistance.

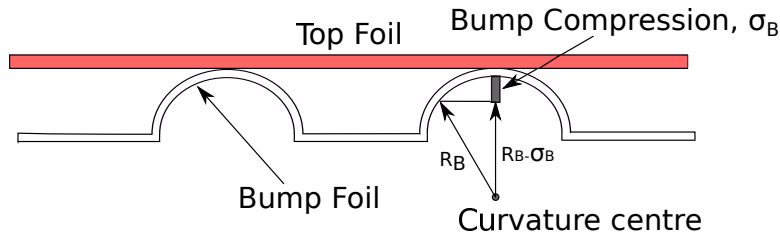


**Figure 7.11:** Schematic diagram of the deflection of the bump foil.

in [113, 116] is expressed as,

$$\text{if } P_{bump} \leq 0.9$$

$$R_{cont} = (7.115P_{bump}^4 - 16.159P_{bump}^3 + 13.08P_{bump}^2 - 4.503P_{bump} + 1.207) \times 10^{-3} ,$$

$$\text{if } P_{bump} > 0.9$$

$$R_{cont} = 0.633 \times 10^{-3} , \quad (7.10)$$

where  $P_{bump}$  is the local gauge pressure expressed in bar. In the present study, these contact resistances are modelled as additional structures within the foil thrust bearings as shown in Figure 7.10 that are inserted into computational model. For these additions, boundaries that are not connected with the top foil or bump foil or housing are modelled as adiabatic walls as shown in Figure 7.9. The height of the additional structure  $\Delta y$  is calculated as,

$$\Delta y = \lambda_s R_{cont} . \quad (7.11)$$

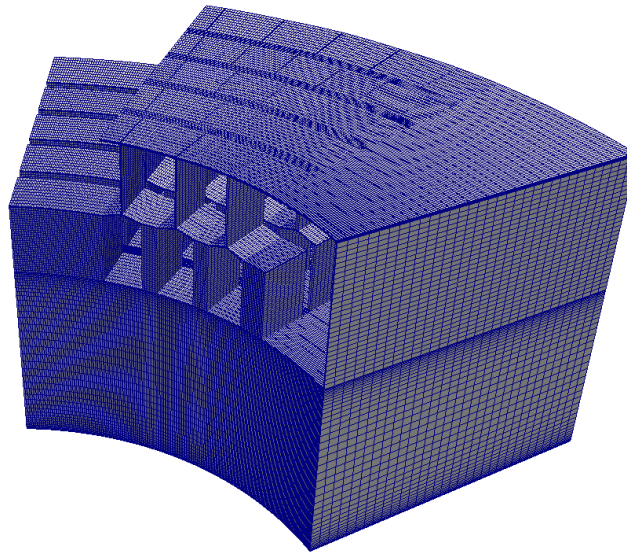


**Figure 7.12:** Schematic diagram of computational mesh of stator.

The bump contact area ( $A_{cont}$ ) between the bump and top foil varies depending on the applied pressure and is accompanied by beam-like deformation of the bump foils, as illustrated in Figure 7.11. For simplicity, the bump contact area is approximated using the model shown in Figure 7.11. The bump foil deflection  $\sigma_B$  is obtained from the fluid-structure simulation. The trigonometric relation shown in Figure 7.11 determines the contact distance using the bump arc radius of curvature ( $R_B$ ) and the calculated bump foil deflection, resulting in a contact width, given by,

$$\Delta\theta = 2\sqrt{R_B^2 - (R_B^2 - \sigma_B)^2} . \quad (7.12)$$

The resulting computational domain of stator incorporating the contact resistances is shown in Figure 7.12.

## 7.4 Comparison Between Air and CO<sub>2</sub> Foil Thrust Bearings

To assess the relative performance and effects of heat generation of the bearing operating with air and CO<sub>2</sub>, the bearing is simulated with an axial load of 110 N applied to the rotor. The remaining operating conditions are summarised in Table 7.1. The fluid domain is replotted and shown in Figure 7.13. The computational mesh of  $48 \times 96 \times 15$  was shown to be grid independent in Chapter 5. It is recommended by Bruckner [170, 184] that the groove between adjacent thrust pads is used for passive thermal

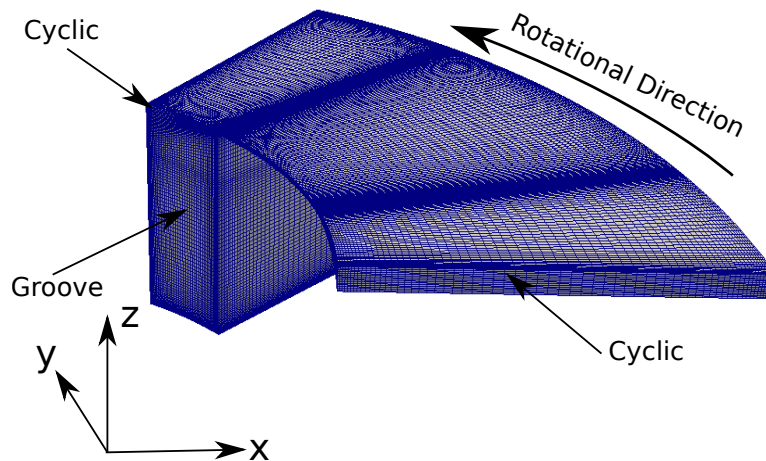


**Figure 7.13:** Computational domain of a foil thrust bearing.

control, hence this part is also modelled. The leading and trailing edges of a thrust pad are connected with cyclic boundary conditions. The stator geometry shown in Figure 7.8 is meshed with an in-house tool and converted into an OpenFOAM format mesh [185]. The studied bearing geometry is in accordance with the bearing presented by NASA [23], summarised in Table 7.1. Not all data for this geometry is released by NASA. The parameters labelled with "a" are estimated based on the authors' experience.

At these operating conditions, the power loss is 47.94 W and 146.51 W for air and CO<sub>2</sub> respectively. The higher loss for CO<sub>2</sub> is attributed to this bearing operating in a turbulent flow regime as confirmed by Reynolds number is Table 7.1. The temperature distributions within the fluid, close to the fluid-structure interface are depicted in Figures 7.14 and 7.15. The rotor temperatures are smeared circumferentially due to the rotor motion. At the same time there is an increase in temperature in the radial direction, due to increase in relative velocity and outward convection of the fluid. Contrary to this on the stator, a non-uniform temperature develops, exhibiting cold regions immediately above the bump foil contacts. This is due to better heat transfer from the rear of the top foil to the bump foils, compared to natural convection that is applied to the remainder of the top foil rear surface.

Experimental data for thrust bearing foil temperature distributions are limited. Furthermore, the thermal boundary condition and structural parameters of the rotor and stator are generally not provided. These parameters are essential for the thermal analysis and to thermally anchored simulations [115, 116]. Also, data in literature relates to journal style bearings (for example [79]), these

**Table 7.1:** Geometry and parameters for the foil thrust bearing.

Geometry	Value	Operating Condition	Value
Number of pads	6	Working fluid	air and CO <sub>2</sub>
Outer diameter	101.6 mm	air	0.1 MPa and 300 K
Inner diameter	50.8 mm	CO <sub>2</sub>	1.4 MPa and 300 K
Shaft diameter <sup>a</sup>	46 mm	Rotor-to-stator sep.	10.12 μm (air) and 17.82 μm (CO <sub>2</sub> )
Pad arc extend	45 deg	Reynolds number	73 (air) and 3533 (CO <sub>2</sub> )
Pad taper extend	15 deg	Load	110 N
Groove extend	60 deg	Load per unit area	18.1 kPa
Top foil thickness	0.15 mm	Power loss	47.94 W (air) and 146.51 W (CO <sub>2</sub> )
Rotor thickness <sup>a</sup>	16 mm		
Stator thickness <sup>a</sup>	20 mm		
Groove depth <sup>a</sup>	0.6 mm		
Rotational speed	21 000 rpm		
Pad area	6080.5 mm <sup>2</sup>		

have only limited value in regards to thrust bearings, which have substantially different rotor and stator shapes and boundary conditions. Therefore, verification and analysis relies on the investigation of energy conservation and flows.

Heat is generated within the thin gas film due to a combination of viscous effects and compression work on the fluid. This heat, which equals the power loss, can be removed by the following processes:

1. Advection by the gas being pumped through the film in the radial and tangential directions, this includes the exchange and replacement of the fluid in the grooves between discrete pads;
2. Convection into the rotor. Heat conducts through the rotor, either to the shaft (a fixed temperature boundary) or to the rear and outside surface, where forced convection takes place to an infinite fluid reservoir at 300 K;
3. Convection into the top foil. From here heat is removed either by natural convection within the bump foil structure (from top foil, bump foils and bearing housing) or conduction into the bearing housing through the bump foils. Natural convection boundary conditions are set using a bulk fluid temperature of 300 K.

The net heat flowcharts for air and CO<sub>2</sub> are shown in Figures. 7.14(c) and 7.15(c). In both cases the majority of the heat is convected to the rotor (90 % and 67 % for air and CO<sub>2</sub>). This is due to good

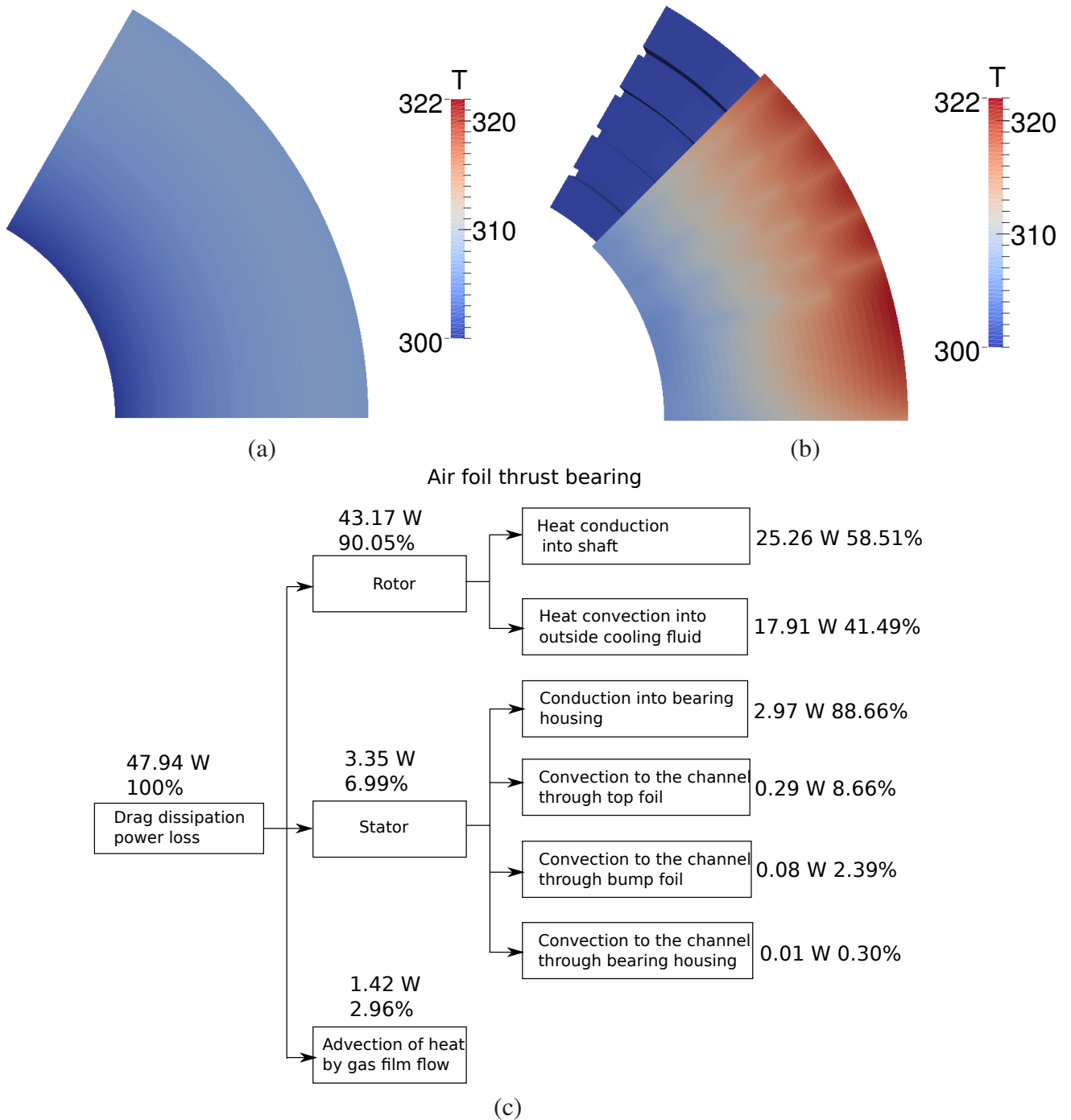


**Figure 7.14:** Air foil thrust bearings interface temperatures, (a): rotor; (b): stator; (c): heat flow chart for complete bearing.

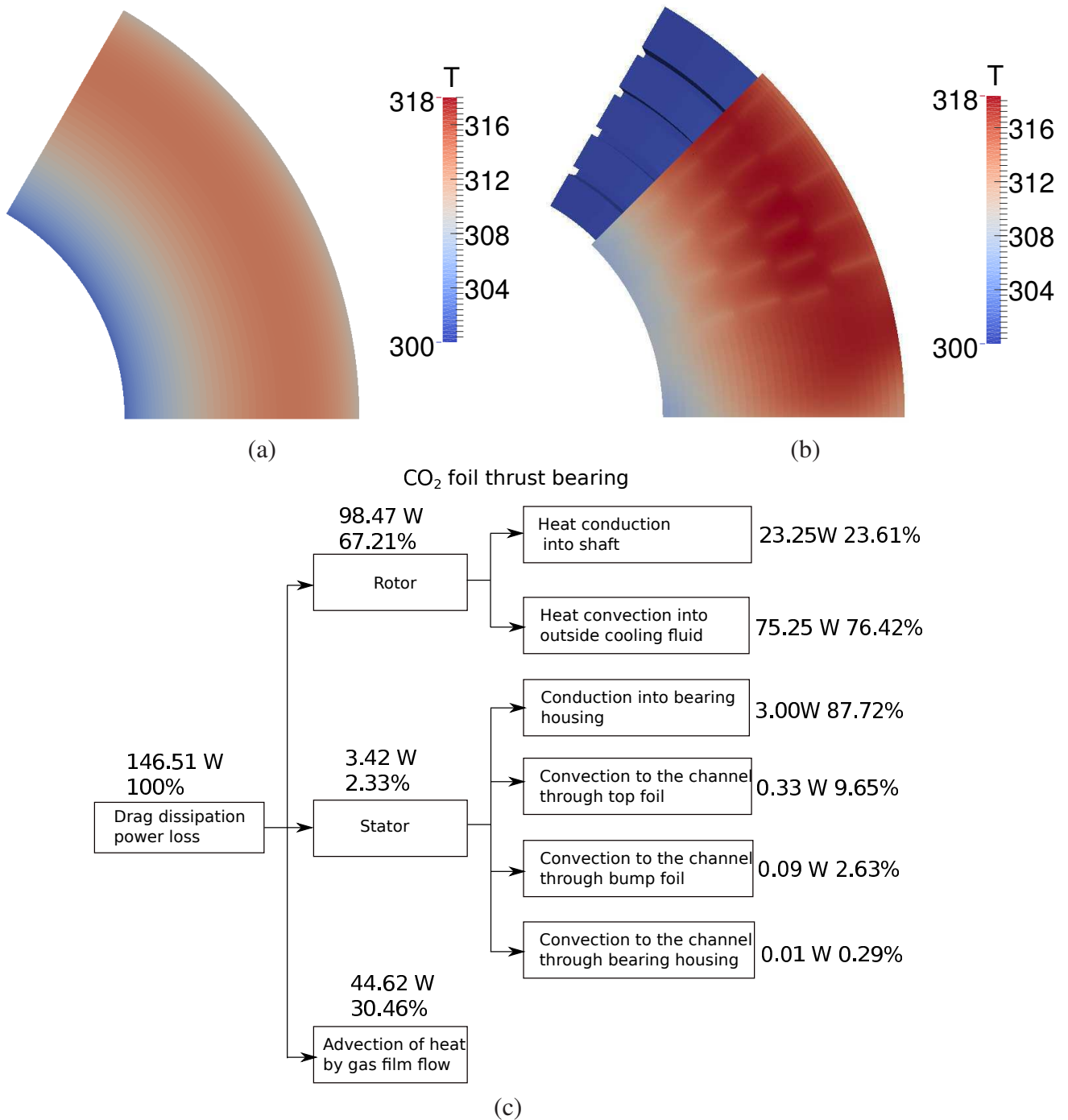


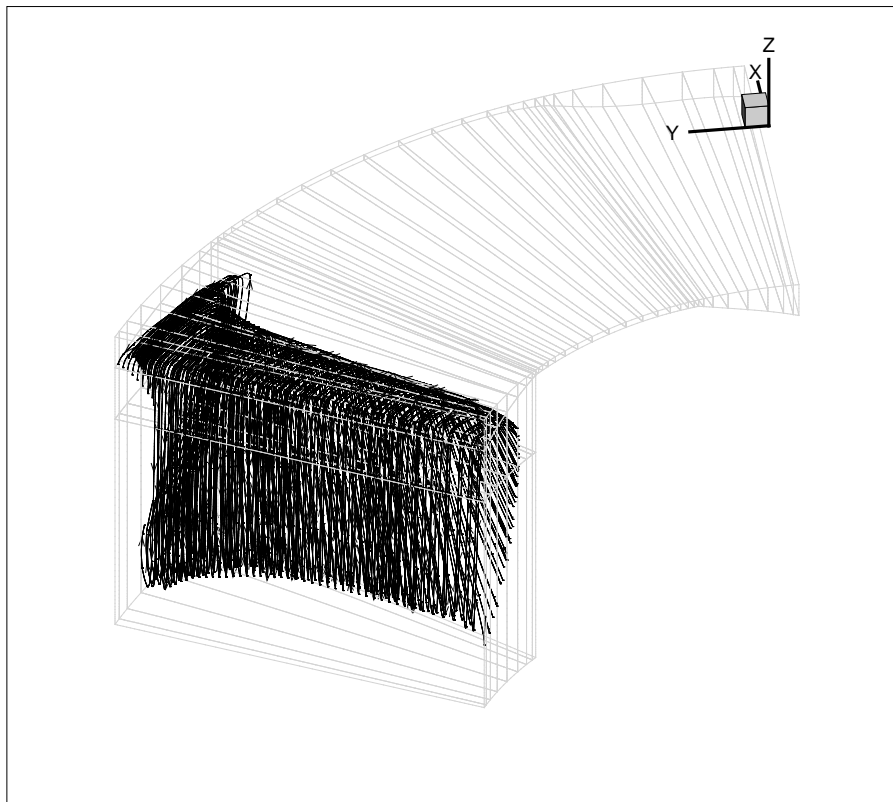
**Figure 7.15:** CO<sub>2</sub> foil thrust bearings interface temperatures, (a): rotor; (b): stator; (c): heat flow chart for complete bearing.

thermal conductivity of the rotor, which is able to maintain a surface temperature substantially below the stator. Once heat enters the rotor, the split between conduction to shaft and convection on the rear surface is substantially different (see relative heat fluxes in Figures 7.14 and 7.15). In the case of CO<sub>2</sub>, the turbulent flow regime, provides a much higher heat transfer coefficient (2314 W/m<sup>2</sup>K) on the rotor outside surface, approximately 10 times bigger than the corresponding coefficient for air (238 W/m<sup>2</sup>K). This high heat transfer coefficient, and corresponding lower surface temperature highlight the ability of CO<sub>2</sub> to provide effective coupling if the rotor operates in a CO<sub>2</sub> environment.

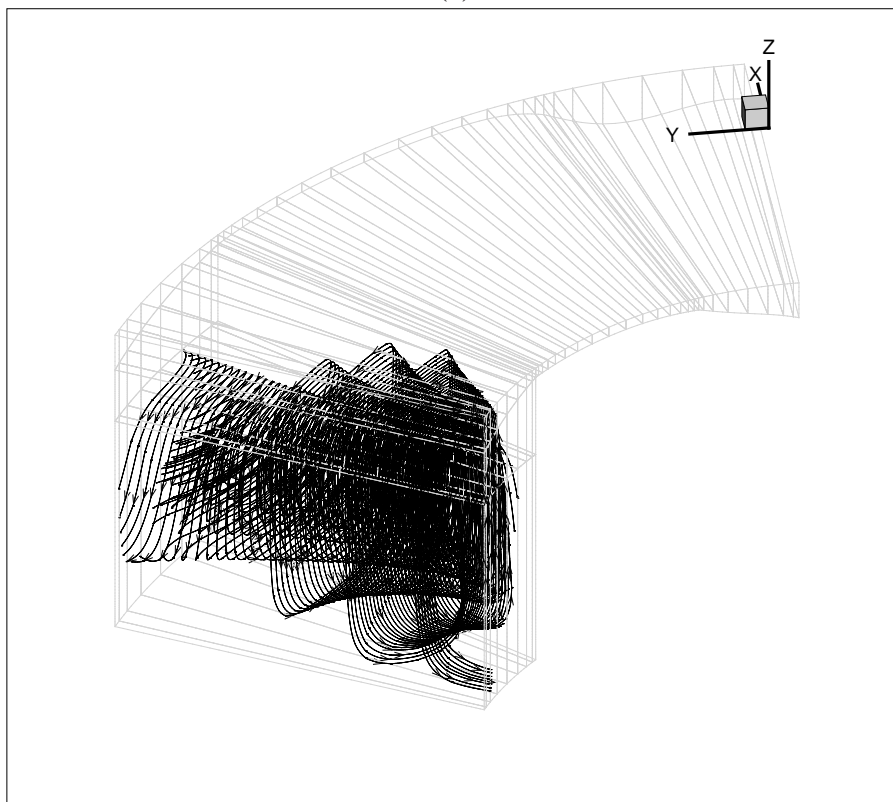
In contrast, the top foil surface reaches a significantly higher temperature and only a much smaller portion of the heat is convected in this direction. This is caused by the much higher thermal resistance of the bump foil structure. This is due to the contact resistance and also small conduction areas within the bump foils. Considering the split of heat flux downstream of the top foil, it can be seen that this is similar for air and CO<sub>2</sub>. The majority of heat ( 88 %) is conducted into the bearing housing structure. The remainder is convected to the fluid present within the bump channels. Most convection takes place from the top foil rear surface ( 9 %), followed by the bump foils ( 2.5 %), and a bit from the bearing housing surface ( 0.3 %). However, the total amount of removed energy is low because heat transfer relies on natural convection. These power splits within the bump channel are consistent with the results from Ref. [116].

A further aspect to consider is advection of heat by the gas in the film and grooves which is driven by the radial pumping of the bearing within the film and fluid exchange in the grooves as shown in Figure 7.16. The pumping mass flow rates are 0.004 g/s and 0.155 g/s for air and CO<sub>2</sub>, respectively. The higher flow rate for CO<sub>2</sub> is caused by increased density and centrifugal effects as discussed in Chapter 5. With the increased radial mass flow, the CO<sub>2</sub> bearing is able to advect a substantially larger portion of the generated heat. Through this process, the CO<sub>2</sub> bearing is able to remove approximately 30 % of the generated heat, whereas the air bearing is only capable of removing 3 %. This illustrates the favourable impact of radial pumping on bearing cooling. The improved fluid exchange in the groove is shown in Figure 7.16. The radial transportation is significant in Figure 7.16(b).

In future CO<sub>2</sub> applications, it is expected that foil thrust bearings will be required to operate with substantially higher loads due to the substantially higher operating pressures. While the comparison to air bearings has shown a favourable cooling performance, in particular due to the advection within in the film, more substantial cooling improvements will be required to maintain low, uniform top foil



(a)



(b)

**Figure 7.16:** Comparison of streamline between air and CO<sub>2</sub> thrust bearings in the groove, (a) air; (b) CO<sub>2</sub>.

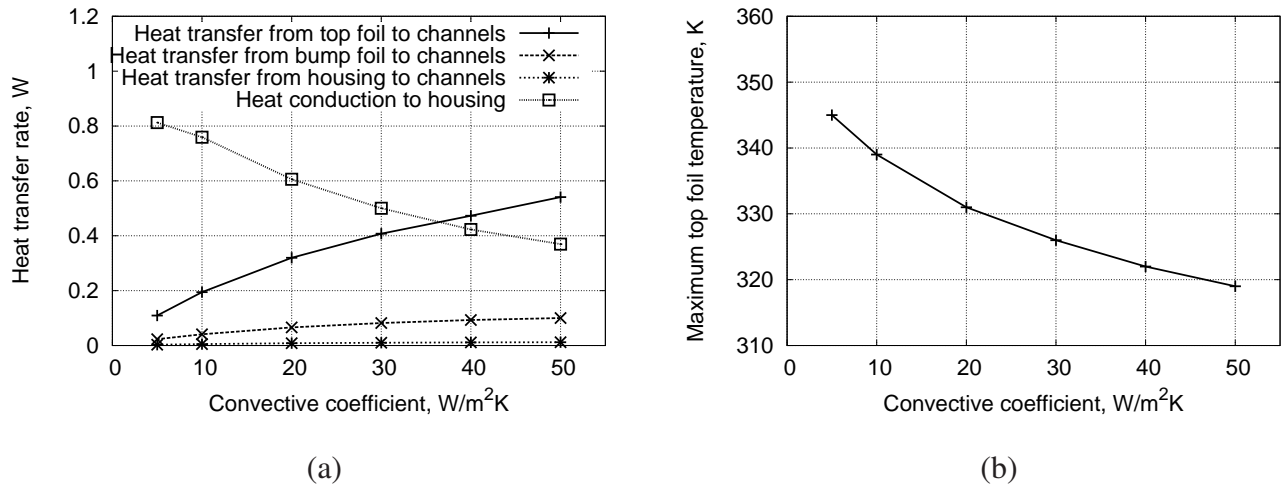


**Figure 7.17:** Comparison of (a) heat flow and maximum top foil temperature (b) for different convection coefficients within the bump channels.

temperatures. A mechanism to achieve this is to force fluid through the bump channels, for example, by applying a pressure difference in the radial direction. To provide insight towards this approach, a thermal investigation was conducted to analyse the effect of increasing heat transfer coefficient within the bump channels. Effectively this is the same as adding a convective cooling flow. For this analysis, only the stator side is considered. A uniform heat flux, corresponding to 1 W per pad (164 W/m<sup>2</sup>), is applied to the fluid side of the top foil. The resulting distributions of heat flow and maximum top foil temperature for different convective coefficients are shown in Figure 7.17. The lowest heat transfer coefficient of 5 W/m<sup>2</sup>K corresponds to the natural convection coefficient used previously. These data show that increasing heat transfer in the bump channels is an effective way to extract a larger portion of the supplied heat directly from the rear of the top foil. The heat transferred to the fluid in the channel increases almost 5-fold. This corresponds to a 39% reduction of the maximum top foil temperature as shown in Figure 7.17(b). At the same time, the requirement to conduct heat to the bearing housing through the bump foils diminishes.

## 7.5 Preliminary Performance Investigation

Radil and Zeszotek [79] performed an experimental investigation into the temperature profile of a foil journal bearings. Both journal rotational speed and radial load were key factors determining the heat generation. But rotational speed played a more significant role in heat generation and resulting

high peak temperature. This experimental data are typically used as the validation data for developed models [115, 116]. The deflection due to thermal stresses is found to be significant, and results in the operation failure [186] because of mechanical contact between rotor and top foil. Linear thermal expansion theory is usually employed to model thermal growth induced by the increased temperature [113, 115, 116].

In this section, the solver DisplacementFoam from the open source CFD toolbox FOAM-Extend-3.0 [139] is used to model heat conduction and deflections due to thermal stresses. Since DisplacementFoam is already a mature solver for solving thermal stresses, verification or validation cases are not provided here. The coupling is still the same as mentioned in Section 7.2.5. The difference in the modelling approach is that the deflection due to thermal stresses is calculated. For numerical simulations, CO<sub>2</sub> is used as the working fluid, a convective heat transfer coefficient of 50 W/m<sup>2</sup> K is prescribed on the bump foils. The bearing geometry is defined in Table 7.1.

First, the temperature and deflection contours at different rotor to top foil separations are compared in Figure 7.18 to 7.22. The rotational speed is set to 30 000 rpm. Figures 7.18 and 7.21 show the temperature increase relative to 295 K, which is the reference temperature when calculating the deflection due to thermal stresses. For the rotor, the higher power loss generated at lower separations creates a comparatively high temperature as shown in Figure 7.18 and subsequently higher deflection as shown in Figure 7.19. The deflection and temperature profiles along the radial direction at the rotor are depicted in Figure 7.20. The temperature and deflection does not indicate a relationship that can be modelled with the linear thermal expansion theory for thrust bearings. This implies that the more accurate modelling approach is needed for thermal deflections. For the stator, temperature and deflection contours are also plotted in Figures 7.21 and 7.22. Again, the highly loaded cases and associated high power loss and rotor to top foil separations generates the largest temperatures and thermal deflections.

The effect of rotational speed is compared in Figures 7.23 to 7.26. The performance is compared at two different rotational speeds: 40 000 rpm and 50 000 rpm. It has been confirmed that rotational speed has more impact on the power loss compared to rotor to top foil separations. For thermal behaviour, the differences in peak temperature and thermal deflection are almost 100 %. This is applied to both the rotor and stator.

To assess the need for fluid-structure-thermal prediction, comparison between two modelling ap-

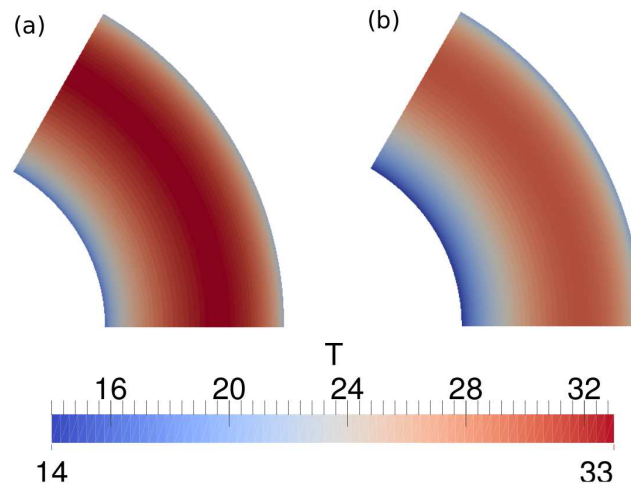


**Figure 7.18:** Comparison of rotor temperature (in K) at power loss, (a) 318 N and 417 W, (b) 100 N and 352 W, rotational speed is 30 000 rpm.

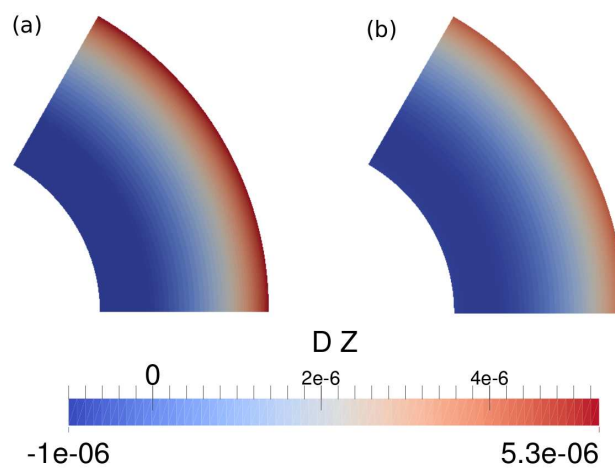


**Figure 7.19:** Comparison of rotor deflection (in m) at different power loss, (a) 318 N and 417 W, (b) 100 N and 352 W, rotational speed is 30 000 rpm.

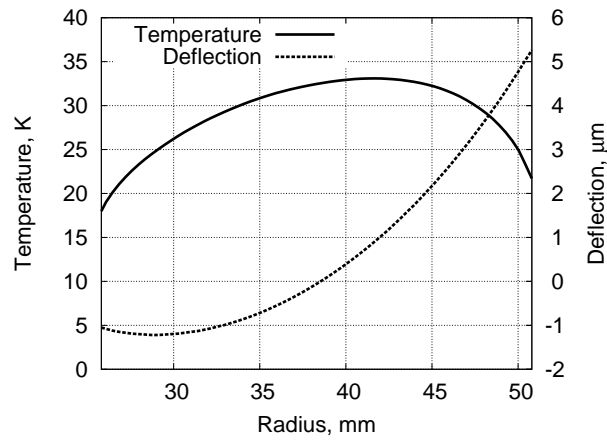


**Figure 7.20:** Temperature and deflection at the rotor, load of 318 N, power loss of 417 W, rotational speed is 30 000 rpm.

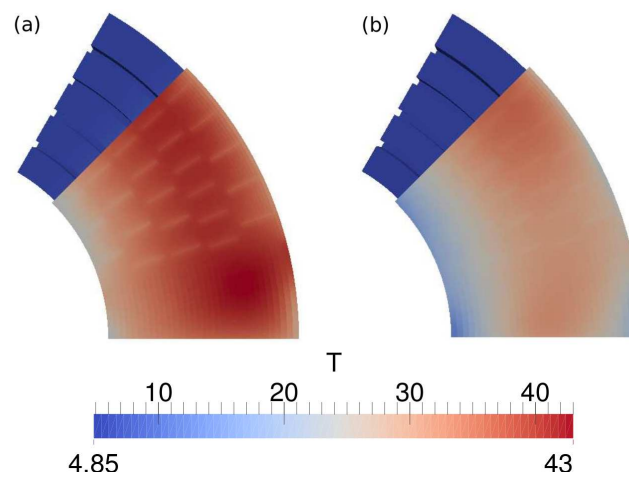


**Figure 7.21:** Comparison of stator temperature (in K) at different load and power loss, (a) 318 N and 417 W, (b) 100 N and 352 W, rotational speed is 30 000 rpm.

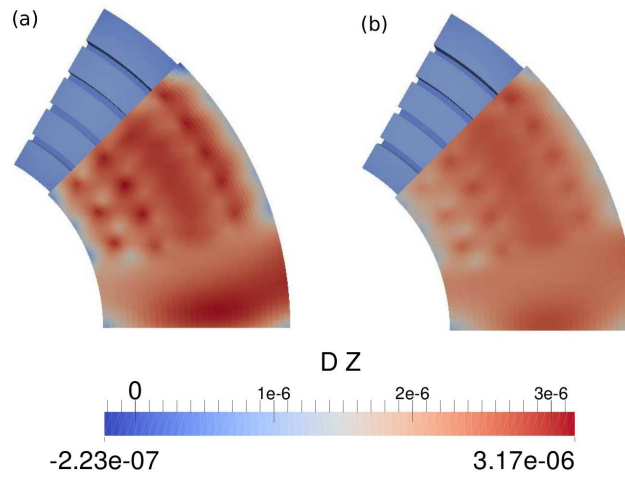


**Figure 7.22:** Comparison of stator deflection (in m) at different power loss, (a) 318 N and 417 W, (b) 100 N and 352 W, rotational speed is 30 000 rpm.

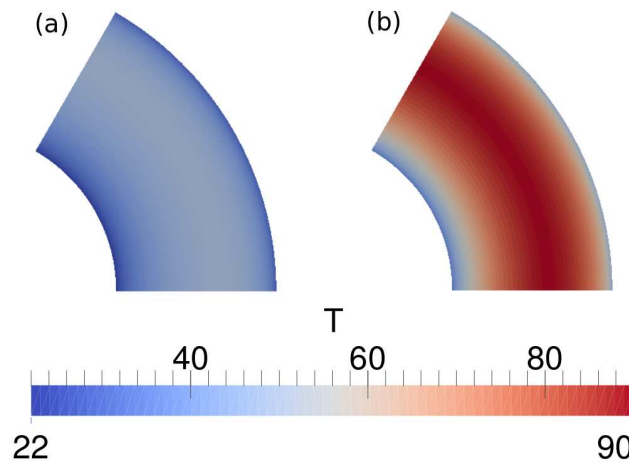


**Figure 7.23:** Comparison of rotor temperature (in K) at different rotational speed, (a) 40 000 rpm, load is 275 N, power loss is 815 W, (b) 50 000 rpm, load is 318 N, power loss is 1273 W.

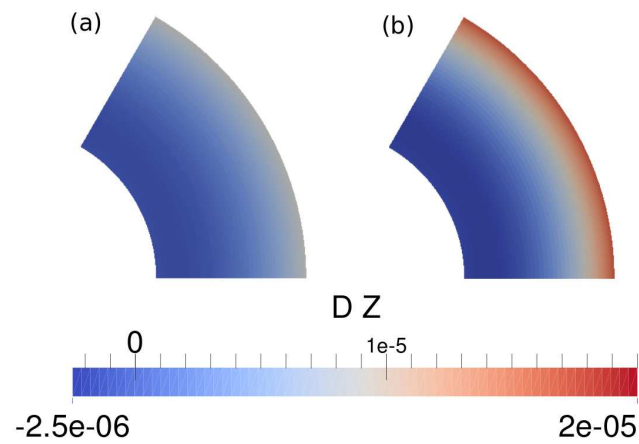


**Figure 7.24:** Comparison of rotor deflection (in m) due to thermal stress at different rotational speed, (a) 40 000 rpm, load is 275 N, power loss is 815 W, (b) 50 000 rpm, load is 318 N, power loss is 1273 W.

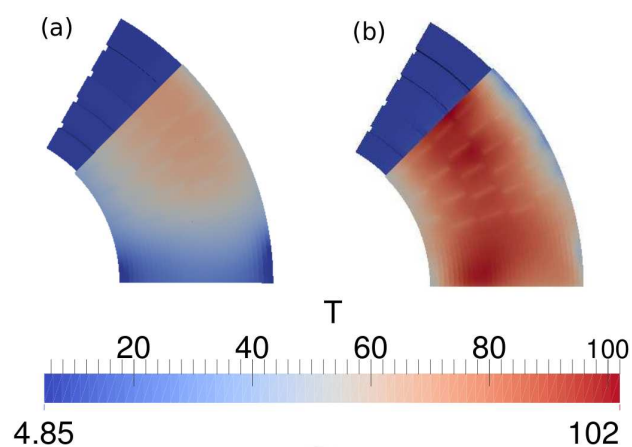


**Figure 7.25:** Comparison of rotor temperature (in K) at different rotational speed, (a) 40 000 rpm, load is 275 N, power loss is 815 W, (b) 50 000 rpm, load is 318 N, power loss is 1273 W.

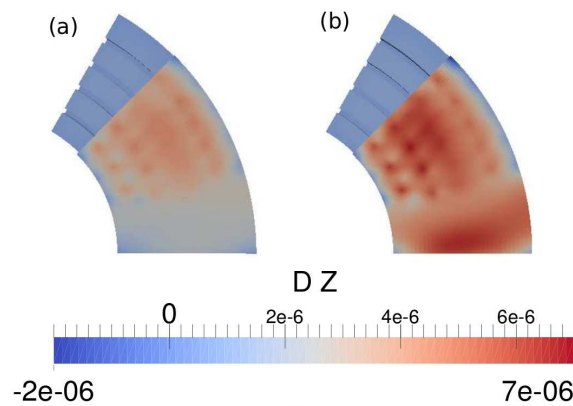


**Figure 7.26:** Comparison of stator deflection (in m) due to thermal stress at different rotational speed, (a) 40 000 rpm, load is 275 N, power loss is 815 W, (b) 50 000 rpm, load is 318 N, power loss is 1273 W.

proaches (fluid-structure and fluid-structure-thermal) is depicted in Figure 7.27. Load capacity and power loss are comparable from these approaches at the rotational speed of 30 000 rpm. Therefore, the inclusion of thermal modelling is not necessary in the prediction of bearing performance at the low rotational speed. At the rotational speed of 40 000 rpm, the deviation is found between load and power loss. This deviation becomes apparent at the rotational speed of 50 000 rpm. A reduction of 70 N in load is observed, while a reduction in power loss is also spotted. This is due to the large deflection at the rotor as shown in Figure 7.24. Thus, thermal solver has to be included at the rotational speed larger than 40 000 rpm for foil bearings operating with  $\text{CO}_2$ , since the predicted performance differs between two modelling approaches. When operating at high rotational speeds, the negative deflection (towards top foil) shown in Figure 7.24 might cause the mechanical contact between the rotor and top foil. This is also reported in Ref. [186] as the failure of foil bearings operating in high temperature.

## 7.6 Conclusions

In this chapter, a computational framework for the fluid-structure-thermal simulations of foil thrust bearings is developed. Individual solvers and their coupling strategies are detailed together with validation cases. A detailed description of the implemented foil bearing heat transfer models is provided. The numerical tool is used to conduct a comparison study between a foil thrust bearing of the same geometry operating with air and  $\text{CO}_2$ . This comparison highlights a number of differences in bearing operation, in particular the heat fluxes and cooling requirements. Power loss and heat generation

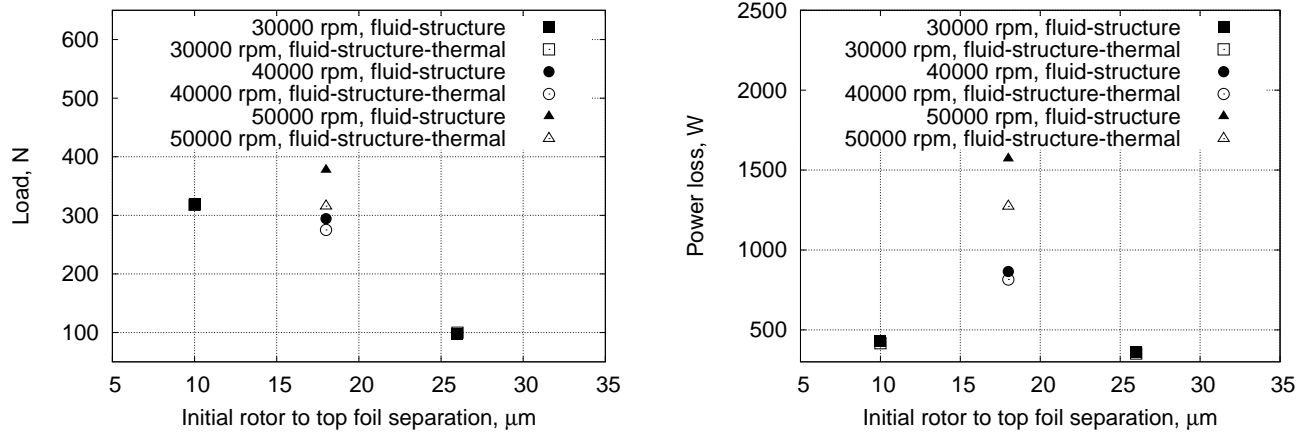


**Figure 7.27:** Comparison of bearing performance for different modelling approaches.

increases three-fold for the CO<sub>2</sub> bearing at the same load. However, due to improved cooling, peak temperatures are maintained below the air case. The CO<sub>2</sub> bearing significantly benefits from increased convective cooling on the rear surface of the rotor, if the rotor operates in a high pressure CO<sub>2</sub> environment. This allows substantially more energy to be extracted through the rotor. In addition, almost a third of the generated heat is advected with the fluid in the CO<sub>2</sub> case, compared to only 3% in the air case. This effect, is caused by the centrifugal pumping that naturally occurs in CO<sub>2</sub> bearings due to the high fluid density [187], the higher heat capacity of the working fluid and better fluid exchange in the groove. This is a highly advantageous mechanism for foil bearing cooling. Heat transfer to the stator is similar in both cases. Here heat flow is limited due to the high thermal resistance imposed by the bump structure. Only a comparatively small portion of the heat flux entering the top foil is extracted via convection to fluid in the bump channels when natural convection is assumed. A separate numerical investigation showed that applying force convection in the bump channels is an effective approach to enhance cooling, which will be essential for bearings operating at high loads. This chapter has provided some new insights to the heat flux distribution in foil bearings, how this is affected by the working fluid, and was identified mechanisms to enhance this heat transfer. At the rotational speed less than 30 000 rpm, the predicted bearing performance between fluid-structure and fluid-structure-thermal modelling approaches is comparable. However, at higher rotational speeds, the predicted performance differs due to large deflections due to thermal stresses. Therefore, thermal solver has to be included for foil thrust bearings operating at rotational speeds larger than 40 000 rpm.



---

# Conclusions and Future Work

---

## 8.1 Conclusions

The inspiration for this work was to investigate the possibility of using foil bearings for turbomachinery in the supercritical CO<sub>2</sub> cycle. The work presented in this thesis provides new insight into foil thrust bearings operated with high rotational speed and using highly dense CO<sub>2</sub> as the working fluid. The performance of CO<sub>2</sub> foil thrust bearings was investigated by systematically increasing the complexity of the foil bearing flow physics in each chapter, beginning with a rigid bearing, and progressing to fluid-structure interactions, fluid-structure-thermal modelling and finally rotordynamic analysis. In each chapter we improve our physical insight and understanding, as new layers of complexity are added. This approach has allowed a rigorous contribution to the knowledge to be constructed. The use of CFD for foil thrust bearings allowed the flow field to be probed in high detail to provide new significant insights into the operation of foil thrust bearings with CO<sub>2</sub>. The intention is that these new insights can be used in future CO<sub>2</sub> foil bearing designs to provide a greater degree of freedom to enable high speed turbomachinery system for supercritical CO<sub>2</sub> cycles. A brief summary of each chapter with major findings is given here:

- In Chapter 3, the in-house CFD code Eilmer is first modified for foil bearing simulations by adding new boundary conditions and reconstruction method. Next, to allow fast and stable turbulent simulations in thin film bearings, two new features are added: compressible wall function and fourth-order artificial dissipation. These new additions are verified and validated with different test cases representative of foil bearing flows. The compressible wall function from Nichols et al. [137] is able to be applied for the hybrid pressure and shear driven flow within foil bearings. A  $y^+$  value in the first cell from the wall of less than 20 is required to

accurately calculate the wall shear stress for the studied geometry. A comparison of turbulence models show that the Wilcox's 2006  $k - \omega$  model is most accurate for the hybrid pressure and shear driven flow compared to other models including: SST  $k - \omega$ , Spalart Allmaras, standard  $k - \epsilon$  and Nonlinear  $k - \epsilon$  Shih. Incorporating the fourth-order artificial dissipation allows a speed up of the the turbulent simulations for foil thrust bearings, while ensuring a stable and accurate computation without contaminating the fluid flow. For the test case used in this thesis, a speed-up of 6.57 times is achieved at a rotational speed of 40 000 rpm. The minimum  $k_4$  value for stabilising turbulent simulations increases in terms of the rotational speed and cell aspect ratio. It is recommended that  $k_4$  larger than 0.01 is selected.

- In Chapter 4, the moving grid capability is added to Eilmer to allow the multiphysics simulations. This capacity is validated with the different test cases including inviscid, viscous and turbulent simulations. In addition, a bespoke solver based on Kirchhoff plate theory was developed for the structural deformation of the top foil within foil bearings, and verified with the commercial software ANSYS. The coupling strategy is proposed to provide the steady state and time-accurate transient simulations. A mapping algorithm is used when exchanging pressure and deflection between two solvers, the difference is less than 1 %.
- In Chapter 5, the developed fluid-structure simulation tool for the steady state performance of foil thrust bearings was validated with the experimental data from literature. Using the developed fluid-structure solver, the steady state performance of foil bearings operating at different conditions is also investigated. It is found that a ten-fold increase of CO<sub>2</sub> pressure and thus density can significantly alter foil bearings performance. The density change can alter load capacity by up to 40 %. This is due to additional mass flow at the inner edge of the ramp region, caused by increased centrifugal inertia forces acting on the more dense CO<sub>2</sub>. But centrifugal inertia effects also cause an increased leakage towards the outer edges in the flat region which is detrimental to load generation. This work has highlighted the significance of the centrifugal inertia forces on the bearing performance and provided new insight to the underlying effects that influence bearing performance. Due to the high densities of CO<sub>2</sub>, the foil thrust bearings can experience turbulent flow within the film. As a consequence of the additional eddy viscosity, the foil thrust bearings now experience different velocity profiles across the film height, which result in increased power consumption. In contrast, load capacity only shows a slight increase

- as turbulence levels increase. This is due to the compliance of the bump foils, which deflect almost twice as much under turbulent conditions, thereby decreasing the potential to increase load.
- In Chapter 6, the procedure to obtain the dynamic performance of foil thrust bearings using the fluid-structure simulation tool is discussed and validated. The computational domain including the groove has to be utilised, since the steady state and rotordynamic coefficients are different by the presence of the groove.
  - In Chapter 7, a computational framework for the fluid-structure-thermal simulations of foil thrust bearings is developed by adding LaplacianFoam to the fluid-structure simulation tool. The numerical tool is used to conduct a comparative study between a foil thrust bearing of the same geometry operating with air and CO<sub>2</sub>. It was found that power loss and heat generation increases three-fold for the CO<sub>2</sub> bearing. However, due to improved cooling, peak temperatures are maintained below the air case. The CO<sub>2</sub> bearing significantly benefits from increased convective cooling on the rear surface of the rotor. This allows substantially more energy to be extracted through the rotor. In addition, almost a third of the generated heat is advected with the fluid in the CO<sub>2</sub> case, compared to only 3 % in the air case. This effect, caused by the centrifugal pumping and improved fluid exchange in the groove that naturally occurs in CO<sub>2</sub> bearings due to the high fluid density. This provides a new and effective cooling mechanism for CO<sub>2</sub> bearing. Heat transfer to the stator is similar for both cases. Here heat flow is limited due to the high thermal resistance imposed by the bump structure. Only a comparatively small portion of the heat flux entering the top foil is extracted via convection to fluid in the bump channels when natural convection is assumed. A separate numerical investigation showed that applying force convection in the bump channels is an effective approach to enhance cooling, which will be essential for bearings operating at high loads. At the rotational speed less than 30 000 rpm, the predicted bearing performance between fluid-structure and fluid-structure-thermal modelling approaches is comparable. The fluid-structure simulation tool can then be used. However, at higher rotational speeds, the predicted performance differs due to large deflections due to thermal stresses. Therefore, thermal solver has to be included for foil thrust bearings operating at rotational speeds larger than 40 000 rpm.

## 8.2 Recommendations for Foil Bearing Designs

Based on the results from this thesis, recommendations for foil bearing design for CO<sub>2</sub> operation include:

- Add bump foils underneath the ramp, this results in a more pad area to support the pressure.
- Cooling through the bump foil channels: The forced cooling in the bump foil channels can reduce the temperature increase by 39 %, and enable the bearing to operate at higher rotational speed or with increased load.
- Adding radially varying bump foil stiffness to minimise fluid loss from flat region.
- Optimise radial and tangential bump foil stiffness.
- Use groove to increase fluid exchange.

## 8.3 Future Research

Recommendations for future work include:

- **Dynamic Performance:** Dynamic performances of foil thrust bearings operating with CO<sub>2</sub> in terms of load and rotational speed will be investigated.
- **Further Improvement of Conjugate Heat Transfer:** The Neumann and Dirichlet conditions between fluid and solid interface require a long time to converge. Suitable acceleration methods have to be implemented.
- **Experimental Validation:** There is a lack of experimental data of foil thrust bearings operating with the high dense gas. Experimental validation should be conducted to provide relevant validation. This includes steady state performance at different rotational speeds and rotor to top foil separations. Temperature data is required to provide validation of the fluid-structure-thermal modelling approach. Dynamic stiffness and damping are also of interest, especially at high load condition, where the negative equivalent damping is predicted.
- **Parametric Study:** The geometry of foil thrust bearings investigated in this thesis is based on a geometry from NASA. However this is only a preliminary design. It was experimentally

confirmed that changing the trailing edge can increase the load capacity two-fold. At the same time, damping is also largely increased. Parametric studies have to be conducted to investigate the key parameter influencing bearing performance. Key parameters might include groove shape and depth, ramp height, top foil thickness and bump stiffness distribution.

- **Heat Transfer:** In this thesis, the heat transfer coefficient at the rear surface of the rotor is calculated from empirical correlations. A large heat transfer coefficient is obtained compared to air, if the rotor is submerged in CO<sub>2</sub> environment. The experimental validation has to be conducted to test the suitability of the high dense CO<sub>2</sub> as the efficient heat transfer fluid. Such work is currently underway at the University of Queensland.
- **Cooling Methods:** The deflection of the rotor due to thermal stresses is significant, leading to a substantial reduction in load capacity at high rotational speeds. Similarly, heat transfer to the stator is minimal due to the thermal resistance of the bump structure. To reduce the thermal deflection, the new cooling methods that minimise temperature non-uniformities within the foil thrust bearings should be investigated. This will decrease the thermal deflection and recover the load capacity.



---

## References

---

- [1] Feher, E. G., “The Supercritical Thermodynamic Power Cycle,” *Energy Conversion*, Vol. 8, 1968, pp. 85–90.
- [2] Angelino, G., “Perspectives for the Liquid Phase Compression Gas Turbine,” *ASME Journal of Engineering for Power*, Vol. 89, 1967, pp. 229–236.
- [3] Angelino, G., “Carbon Dioxide Condensation Cycles for Power Production,” *ASME Journal of Engineering for Power*, Vol. 90, 1968, pp. 287–295.
- [4] Dostal, V., *A Supercritical Carbon Dioxide Cycle for Next Generation Nuclear Reactors*, PhD Thesis, Massachusetts Institute of Technology, Cambridge, MA, 2004.
- [5] Conboy, T., Wright, S., Pasch, J., Fleming, D., Rochau, G., and Fuller, R., “Performance Characteristics of an Operating Supercritical CO<sub>2</sub> Brayton Cycle,” *ASME Journal of Engineering for Gas Turbines and Power*, Vol. 134, 2012, pp. 111703.
- [6] Qi, J., Reddell, T., Qin, K., Hooman, K., and Jahn, I. H., “Supercritical CO<sub>2</sub> Radial Turbine Design Performance as a Function of Turbine Size Parameters,” *ASME Journal of Turbomachinery*, Vol. 139, No. 8, 2017, pp. 081008.
- [7] Wright, S., Radel, R., Vernon, M., Rochau, G., and Pichard, P., “Operation and Analysis of a Supercritical CO<sub>2</sub> Brayton Cycle,” Technical report SAN2010-0171, Sandia National Laboratories, September 2010.
- [8] Conboy, T., “Real-Gas Effects in Foil Thrust Bearings Operating in the Turbulent Regime,” *ASME Journal of Tribology*, Vol. 135, No. 3, March 2013, pp. 031703.
- [9] Harnoy, A., *Bearing Design in Machinery: Engineering Tribology and Lubrication*, CRC press, 1st ed., 2002.

- [10] Preuss, J. L., “Application of Hydrostatic Bearings in Supercritical CO<sub>2</sub> Turbomachinery,” *The 5th International Supercritical CO<sub>2</sub> Power Cycles Symposium*, San Antonio, Texas, 2016, pp. 1–15.
- [11] Heshmat, H., Walowit, J., and Pinkus, O., “Analysis of Gas Lubricated Compliant Thrust Bearings,” *ASME Journal of Tribology*, Vol. 105, No. 4, October 1983, pp. 638–646.
- [12] Song, Y., Ren, X., Gu, C.-w., and Li, X.-s., “Experimental and Numerical Studies of Cavitation Effects in a Tapered Land Thrust Bearing,” *ASME Journal of Tribology*, Vol. 137, No. 1, 2015, pp. 011701.1–011701.9.
- [13] Missana, A., Booser, E., and Ryan, F., “Performance of Tapered Land Thrust Bearings for Large Steam Turbines,” *ASLE TRANSACTIONS*, Vol. 14, No. 4, 1971, pp. 301–306.
- [14] Khonsari, M. M. and Booser, E. R., *Applied Tribology: Bearing Design and Lubrication*, John Wiley & Sons, New Jersey, 2nd ed., 2008.
- [15] Dimond, T., Younan, A., and Allaire, P., “A Review of Tilting Pad Bearing Theory,” *International Journal of Rotating Machinery*, Vol. 2011, 2011, pp. 1–23.
- [16] Shalash, K. and Schiffmann, J., “On the Manufacturing of Compliant Foil Bearings,” *Journal of Manufacturing Processes*, Vol. 25, 2017, pp. 357–368.
- [17] San Andrés, L. and Chirathadam, T. A., “Performance Characteristics of Metal Mesh Foil Bearings: Predictions Versus Measurements,” *ASME Journal of Engineering for Gas Turbines and Power*, Vol. 135, No. 12, 2013, pp. 122503.
- [18] Feng, K., Liu, W., Yu, R., and Zhang, Z., “Analysis and Experimental Study on A Novel Gas Foil Bearing with Nested Compression Springs,” *Tribology International*, Vol. 107, 2017, pp. 65–76.
- [19] Ao, H., Jiang, H., Wei, W., and Ulanov, A., “Study on the Damping Characteristics of MR Damper in Flexible Supporting of Turbo-pump Rotor for Engine,” *Systems and Control in Aerospace and Astronautics, 2006. ISSCAA 2006. 1st International Symposium on*, IEEE, Harbin, China, 2006, pp. 1–5.

- 
- [20] San Andrés, L. and Chirathadam, T. A., “A Metal Mesh Foil Bearing and a Bump-type Foil Bearing: Comparison of Performance for Two Similar Size Gas Bearings,” *ASME Journal of Engineering for Gas Turbines and Power*, Vol. 134, No. 10, 2012, pp. 102501.
- [21] San Andrés, L., Chirathadam, T. A., and Kim, T.-H., “Measurement of Structural Stiffness and Damping Coefficients in a Metal Mesh Foil Bearing,” *ASME Journal of Engineering for Gas Turbines and Power*, Vol. 132, No. 3, 2010, pp. 032503.
- [22] San Andrés, L. and Chirathadam, T. A., “Metal Mesh Foil Bearing: Effect of Motion Amplitude, Rotor Speed, Static Load, and Excitation Frequency on Force Coefficients,” *Journal of Engineering for Gas Turbines and Power*, Vol. 133, No. 12, 2011, pp. 122503.
- [23] Dykas, B., Bruckner, R., DellaCorte, C., Edmonds, B., and Prah, J., “Design, Fabrication, and Performance of Foil Gas Thrust Bearings for Microturbomachinery Applications,” *ASME Journal of Engineering for Gas Turbines and Power*, Vol. 131, No. 1, October 2008, pp. 012301.
- [24] Hannon, W. M., *The Generalized Universal Reynolds Equation for Variable Property Fluid-Film Lubrication and Variable Geometry*, Phd thesis, University of Akron, Akron, Ohio, 2006.
- [25] Aksoy, S. and Aksit, M., “A Fully Coupled 3D Thermo-elastohydrodynamics Model for a Bump-type Compliant Foil Journal Bearing,” *Tribology International*, Vol. 82, 2015, pp. 110–122.
- [26] San Andres, L. and Diemer, P., “Prediction of Gas Thrust Foil Bearing Performance for Oil-Free Automotive Turbochargers,” *ASME Journal of Engineering for Gas Turbines and Power*, Vol. 137, No. 3, September 2014, pp. 032502.
- [27] Thatte, A., Loghin, A., Shin, Y., and Ananthasayanam, B., “Performance and Life Characteristics of Hybrid Gas Bearing in a 10 MW Supercritical CO<sub>2</sub> Turbine,” *ASME Turbo Expo 2016: Turbomachinery Technical Conference and Exposition*, American Society of Mechanical Engineers, Seoul, South Korea, 2016, pp. V009T36A018–V009T36A018.
- [28] Kim, D., “Design Space of Foil Bearings for Closed-Loop Supercritical CO<sub>2</sub> Power Cycles Based on Three-Dimensional Thermohydrodynamic Analyses,” *ASME Journal of Engineering for Gas Turbines and Power*, Vol. 138, No. 3, 2016, pp. 032504.

- [29] Moullec, Y. L., “Conceptual Study of a High Efficiency Coal-fired Power Plant with CO<sub>2</sub> Capture using a Supercritical CO<sub>2</sub> Brayton Cycle,” *Energy*, Vol. 49, 2013, pp. 32 – 46.
- [30] Turchi, C., Ma, Z., and Wagner, M., “Thermodynamic Study of Advanced Supercritical Carbon Dioxide Power Cycles for Concentrating Solar Power Systems,” *ASME Journal of Solar Energy Engineering*, Vol. 135, No. 4, June 2013, pp. 041007.
- [31] Gurgenci, H., “Challenges for Electrical Power Generation from EGS,” *Proceedings World Geothermal Congress 2010*, Bali, Indonesia, 2010.
- [32] Besarati, S. M. and Goswami, D. Y., “Analysis of Advanced Supercritical Carbon Dioxide Power Cycles with a Bottoming Cycle for Concentrating Solar Power Applications,” *ASME Journal of Solar Energy Engineering*, Vol. 137, 2014, pp. 011020.
- [33] Kim, Y. M., Sohn, J. L., and Yoon, E. S., “Supercritical CO<sub>2</sub> Rankine cycles for waste heat recovery from gas turbine,” *Energy*, Vol. 118, 2016, pp. 893–905.
- [34] Kim, Y., Kim, C., and Favrat, D., “Transcritical or Supercritical CO<sub>2</sub> Cycles using Both Low- and High-Temperature Heat Sources,” *Energy*, Vol. 43, No. 1, 2012, pp. 402 – 415, 2nd International Meeting on Cleaner Combustion (CM0901-Detailed Chemical Models for Cleaner Combustion).
- [35] “Direct normal irradiation in Australia,” <http://solargis.com/assets/graphic/free-map/DNI/Solargis-Australia-DNI-solar-resource-map-en.png>, Accessed: 2016-10-18.
- [36] Singh, R., Miller, S. A., Rowlands, A. S., and Jacobs, P. A., “Dynamic Characteristics of a Direct-heated Supercritical Carbon-dioxide Brayton Cycle in a Solar Thermal Power Plant,” *Energy*, Vol. 50, 2013, pp. 194–204.
- [37] Singh, R., Rowlands, A. S., and Miller, S. A., “Effects of Relative Volume-ratios on Dynamic Performance of a Directe-heated Supercritical Carbon-dioxide Closed Brayton Cycle in a Solar-thermal Power Plant,” *Energy*, Vol. 55, 2013, pp. 1025–1032.
- [38] Singh, R., Kearney, M. P., and Manzie, C., “Extremum-seeking Control of a Supercritical Carbon-dioxide Closed Brayton Cycle in a Direct-heated Solar Thermal Power Plant,” *Energy*, Vol. 60, 2013, pp. 380–387.

- 
- [39] Singh, R., *Dynamics and Control of a Closed Carbon-Dioxide Brayton Cycle*, Phd thesis, University of Queensland, Brisbane, Australia, 2013.
- [40] Twomey, B., Nagy, A., Russell, H., Rowlands, A., Czapla, J., Singh, R., de M Ventura, C. A., and Jahn, I., “The University of Queensland Refrigerant and Supercritical CO<sub>2</sub> Test Loop,” *ASME Turbo Expo 2016: Turbomachinery Technical Conference and Exposition*, American Society of Mechanical Engineers, Seoul, South Korea, 2016, pp. V003T25A013–V003T25A013.
- [41] Inverson, B. D., Conboy, T. M., Pasch, J. J., and Kruiuzenga, A. M., “Supercritical CO<sub>2</sub> Brayton Cycles for Solar-thermal Energy,” *Applied Energy*, Vol. 111, 2013, pp. 957–970.
- [42] T., C., Pasch, J., and Fleming, D., “Control of a Supercritical CO<sub>2</sub> Recompression Brayton Cycle Demonstration Loop,” *ASME Journal of Engineering for Gas Turbines and Power*, Vol. 135, 2013, pp. 111701.
- [43] Kang, Y.-S., Huh, J.-S., Cho, J., Shin, H., and Baik, Y.-J., “Design and Performance Assessments of a Partial Admission Axial Turbine Using Supercritical Carbon Dioxide,” *ASME 2016 Fluids Engineering Division Summer Meeting collocated with the ASME 2016 Heat Transfer Summer Conference and the ASME 2016 14th International Conference on Nanochannels, Microchannels, and Minichannels*, American Society of Mechanical Engineers, Seoul, South Korea, 2016, pp. V01AT09A010–V01AT09A010.
- [44] Zhang, H., Zhao, H., Deng, Q., and Feng, Z., “Aerothermodynamic Design and Numerical Investigation of Supercritical Carbon Dioxide Turbine,” *ASME Turbo Expo 2015: Turbine Technical Conference and Exposition*, American Society of Mechanical Engineers, Montreal, Quebec, Canada, 2015, pp. V009T36A007–V009T36A007.
- [45] Ventura, C. A., Jacobs, P. A., Rowlands, A. S., Petrie-Repar, P., and Sauret, E., “Preliminary Design and Performance Estimation of Radial Inflow Turbines: An Automated Approach,” *ASME Journal of Fluids Engineering*, Vol. 134, No. 3, 2012, pp. 031102.
- [46] Shanechi, M. M., Veidt, M., and Hooman, K., “Forced Response Analysis of Supercritical CO<sub>2</sub> Radial Inflow Turbine Designed for Concentrating Solar Power,” *ASME Turbo Expo 2016:*

*Turbomachinery Technical Conference and Exposition*, American Society of Mechanical Engineers, Seoul, South Korea, 2016, pp. V009T36A021–V009T36A021.

- [47] Kus, B. and Neksa, P., “Development of One-dimensional Model for Initial Design and Evaluation of Oil-free CO<sub>2</sub> Turbo-compressor,” *International Journal of Refrigeration*, Vol. 36, No. 8, 2013, pp. 2079–2090.
- [48] Lee, J., Lee, J. I., Yoon, H. J., and Cha, J. E., “Supercritical Carbon Dioxide Turbomachinery Design for Water-cooled Small Modular Reactor Application,” *Nuclear Engineering and Design*, Vol. 270, 2014, pp. 76–89.
- [49] Chu, X. and Laurien, E., “Direct Numerical Simulation of Heated Turbulent Pipe Flow at Supercritical Pressure,” *ASME Journal of Nuclear Engineering and Radiation Science*, Vol. 2, No. 3, June 2016, pp. 031019.
- [50] Baltadjiev, N. D., Lettieri, C., and Spakovszky, Z. S., “An Investigation of Real Gas Effects in Supercritical CO<sub>2</sub> Centrifugal Compressors,” *ASME Journal of Turbomachinery*, Vol. 137, No. 9, 2015, pp. 091003.
- [51] Monje, B., Sánchez, D., Savill, M., Pilidis, P., and Sánchez, T., “1D and 3D Tools to Design Supercritical CO<sub>2</sub> Radial Compressors: A Comparison,” *Proceedings of the 2nd International Seminar on ORC Power Systems*, Rotterdam, Netherlands, 2013.
- [52] Furusawa, T., Miyazawa, H., and Yamamoto, S., “Numerical Method for Simulating Flows of Supercritical CO<sub>2</sub> Compressor With Nonequilibrium Condensation,” *ASME Turbo Expo 2016: Turbomachinery Technical Conference and Exposition*, American Society of Mechanical Engineers, Seoul, South Korea, 2016, pp. V009T36A003–V009T36A003.
- [53] Pecnik, R., Rinaldi, E., and Colonna, P., “Computational Fluid Dynamics of a Radial Compressor Operating with Supercritical CO<sub>2</sub>,” *ASME Journal of Engineering for Gas Turbines and Power*, Vol. 134, No. 12, October 2012, pp. 122301.
- [54] Rinaldi, E., Pecnik, R., and Colonna, P., “Computational Fluid Dynamic Simulation of a Supercritical CO<sub>2</sub> Compressor Performance Map,” *ASME Journal of Engineering for Gas Turbines and Power*, Vol. 137, No. 7, July 2015, pp. 072602.

- 
- [55] Kim, S. G., Lee, J., Ahn, Y., Lee, J. I., Addad, Y., and Ko, B., “CFD Investigation of a Centrifugal Compressor Derived from Pump Technology for Supercritical Carbon Dioxide as a Working Fluid,” *Journal of Supercritical FLuid*, Vol. 86, 2014, pp. 160–171.
- [56] Behafarid, F. and Podowski, M. Z., “Modeling and Computer Simulation of Centrifugal CO<sub>2</sub> Compressors at Supercritical Pressures,” *ASME Journal of Fluids Engineering*, Vol. 138, No. 6, 2016, pp. 061106.
- [57] Guo, J., “Design Analysis of Supercritical Carbon Dioxide Recuperator,” *Applied Energy*, Vol. 164, 2016, pp. 21–27.
- [58] Sarkar, J., “Performance of a Flat-plate Solar Thermal Collector using Supercritical Carbon Dioxide as Heat Transfer Fluid,” *International Journal of Sustainable Energy*, Vol. 32, No. 6, 2013, pp. 531–543.
- [59] Kim, T. H., Kwon, J. G., Yoon, S. H., Park, H. S., Kim, M. H., and Cha, J. E., “Numerical Analysis of Air-foil Shaped Fin Performance in Printed Circuit Heat Exchanger in a Supercritical Carbon Dioxide Power Cycle,” *Nuclear Engineering and Design*, Vol. 288, 2015, pp. 110–118.
- [60] Dang, C. and Hihara, E., “In-tube Cooling Heat Transfer of Supercritical Carbon Dioxide. Part 2. Comparison of Numerical Calculation with Different Turbulence Models,” *International Journal of Refrigeration*, Vol. 27, No. 7, 2004, pp. 748–760.
- [61] He, S., Kim, W., and Bae, J., “Assessment of Performance of Turbulence Models in Predicting Supercritical Pressure Heat Transfer in a Vertical Tube,” *International Journal of Heat and Mass Transfer*, Vol. 51, No. 19, 2008, pp. 4659–4675.
- [62] Liao, S. and Zhao, T., “Measurements of Heat Transfer Coefficients from Supercritical Carbon Dioxide Flowing in Horizontal Mini/Micro Channels,” *ASME Journal of Heat Transfer*, Vol. 124, No. 3, 2002, pp. 413–420.
- [63] Dang, C. and Hihara, E., “In-tube Cooling Heat Transfer of Supercritical Carbon Dioxide. Part 1. Experimental Measurement,” *International Journal of Refrigeration*, Vol. 27, No. 7, 2004, pp. 736–747.

- [64] Oh, H.-K. and Son, C.-H., “New Correlation to Predict the Heat Transfer Coefficient in-tube Cooling of Supercritical CO<sub>2</sub> in Horizontal Macro-tubes,” *Experimental Thermal and Fluid Science*, Vol. 34, No. 8, 2010, pp. 1230–1241.
- [65] Kruiuzenga, A., Anderson, M., Fatima, R., Corradini, M., Towne, A., and Ranjan, D., “Heat Transfer of Supercritical Carbon Dioxide in Printed Circuit Heat Exchanger Geometries,” *ASME Journal of Thermal Science and Engineering Applications*, Vol. 3, No. 3, 2011, pp. 031002.
- [66] Peeters, J. W., Pecnik, R., Rohde, M., van der Hagen, T., and Boersma, B., “Turbulence Attenuation in Simultaneously Heated and Cooled Annular Flows at Supercritical Pressure,” *Journal of Fluid Mechanics*, Vol. 799, 2016, pp. 505–540.
- [67] Fairuz, Z. and Jahn, I., “The Influence of Real Gas Effects on the Performance of Supercritical CO<sub>2</sub> Dry Gas Seals,” *Tribology International*, Vol. 102, 2016, pp. 333–347.
- [68] Zakariya, M. F. and Jahn, I. H., “Performance of Supercritical CO<sub>2</sub> Dry Gas Seals Near the Critical Point,” *ASME Turbo Expo 2016: Turbomachinery Technical Conference and Exposition*, American Society of Mechanical Engineers, Seoul, South Korea, 2016, pp. V009T36A007–V009T36A007.
- [69] Thatte, A. and Dheeradhada, V., “Coupled Physics Performance Predictions and Risk Assessment for Dry Gas Seal Operating in MW-Scale Supercritical CO<sub>2</sub> Turbine,” *ASME Turbo Expo 2016: Turbomachinery Technical Conference and Exposition*, American Society of Mechanical Engineers, Seoul, South Korea, 2016, pp. V009T36A017–V009T36A017.
- [70] Bidkar, R. A., Sevincer, E., Wang, J., Thatte, A. M., Mann, A., Peter, M., Musgrove, G., Allison, T., and Moore, J., “Low-Leakage Shaft-End Seals for Utility-Scale Supercritical CO<sub>2</sub> Turboexpanders,” *ASME Journal of Engineering for Gas Turbines and Power*, Vol. 139, No. 2, 2017, pp. 022503.
- [71] Xu, F. and Kim, D., “Three-Dimensional Turbulent Thermo-Elastohydrodynamic Analyses of Hybrid Thrust Foil Bearings Using Real Gas Model,” *ASME Turbo Expo 2016: Turbomachinery Technical Conference and Exposition*, American Society of Mechanical Engineers, Seoul, South Korea, 2016, pp. V07BT31A030–V07BT31A030.

- [72] Kim, D., “Design Space of Foil Bearings for Closed-Loop Supercritical CO<sub>2</sub> Power Cycles Based on Three-Dimensional Thermohydrodynamic Analyses,” *ASME Journal of Engineering for Gas Turbines and Power*, Vol. 138, No. 3, October 2015, pp. 032504.
- [73] Dickman, J., *An Investigation of Gas Foil Thrust Bearing Performance and Its Influence Factors*, MS Thesis, Case Western Reserve University, Cleveland, OH, May 2010.
- [74] Balducchi, F., Arghir, M., Gauthier, R., and Renard, E., “Experimental Analysis of the Start-up Torque of a Mildly Loaded Foil Thrust Bearing,” *ASME Journal of Tribology*, Vol. 135, No. 3, 2013, pp. 031702.
- [75] Balducchi, F., Arghir, M., and Gauthier, R., “Experimental Analysis of the Dynamic Characteristics of a Foil Thrust Bearing,” *ASME Journal of Tribology*, Vol. 137, No. 2, 2015, pp. 021703.
- [76] Feng, K., Liu, L.-J., Guo, Z.-Y., and Zhao, X.-Y., “Parametric Study on Static and Dynamic Characteristics of Bump-type Gas Foil Thrust Bearing for Oil-free Turbomachinery,” *Proceedings of the Institution of Mechanical Engineers, Part J: Journal of Engineering Tribology*, Vol. 229, No. 10, 2015, pp. 1247–1263.
- [77] Dykas, B. and Radil, K., “Experimental Measurement of Thrust Foil Bearing Temperature Profiles,” *World Tribology Congress III*, American Society of Mechanical Engineers, Washington, D.C., USA, 2005, pp. 93–94.
- [78] Dykas, B. D., *Factors Influencing the Performance of Foil Gas Thrust Bearings for Oil-free Turbomachinery Applications*, Ph.D. thesis, Case Western Reserve University, 2006.
- [79] Radil, K. and Zeszotek, M., “An Experimental Investigation into the Temperature Profile of a Compliant Foil Air Bearing,” *Tribology Transactions*, Vol. 47, No. 4, 2004, pp. 470–479.
- [80] Kim, T. H., Park, M. S., Lee, J., Kim, Y. M., Ha, K.-K., Park, J., Lee, C., and Kim, C., “Identification of Dynamic Characteristics of Gas Foil Thrust Bearings Using Base Excitation,” *ASME Turbo Expo 2016: Turbomachinery Technical Conference and Exposition*, American Society of Mechanical Engineers, Seoul, South Korea, 2016, pp. V07BT31A006–V07BT31A006.

- [81] Reynolds, O., “On the Theory of Lubrication and Its Application to Mr. Beauchamp Tower’s Experiments, Including an Experimental Determination of the Viscosity of Olive Oil,” *Philosophical Transactions of the Royal Society of London*, Vol. 177, January 1886, pp. 157–234.
- [82] Bruckner, R., *Simulation and Modeling of the Hydrodynamic, Thermal, and Structural Behavior of Foil Thrust Bearings*, PhD Thesis, Case Western Reserve University, Cleveland, OH, 2004.
- [83] Wang, N., Chang, S., and Huang, H., “Comparison of Iterative Methods for the Solution of Compressible Fluid Reynolds Equation,” *ASME Journal of Tribology*, Vol. 133, 2011, pp. 021702.
- [84] Gad, A. M. and Kaneko, S., “Performance Characteristics of Gas-lubricated Bump-type Foil Thrust Bearing,” *Proceedings of the Institution of Mechanical Engineers, Part J: Journal of Engineering Tribology*, Vol. 229, No. 6, 2015, pp. 746–762.
- [85] Gad, A. M. and Kaneko, S., “Tailoring of the Bearing Stiffness to Enhance the Performance of Gas-lubricated Bump-type Foil Thrust Bearing,” *Proceedings of the Institution of Mechanical Engineers Part J Journal of Engineering Tribology*, Vol. 230, 2015.
- [86] Lee, D. and Kim, D., “Design and Performance Prediction of Hybrid Air Foil Thrust Bearings,” *ASME Journal of Engineering for Gas Turbines and Power*, Vol. 133, No. 4, 2011, pp. 042501.
- [87] Ng, C. W. and Pan, C. H. T., “A Linearized Turbulent Lubrication Theory,” *ASME Journal of Fluids Engineering*, Vol. 87, 1964, pp. 675–682.
- [88] Constantinescu, V., “Basic Relationships in Turbulent Lubrication and Their Extension to Include Thermal Effects,” *ASME Journal of Tribology*, Vol. 95, No. 2, April 1973, pp. 147–154.
- [89] Hirs, G., “A Bulk-Flow Theory for Turbulence in Lubricant Films,” *ASME Journal of Tribology*, Vol. 95, No. 2, April 1973, pp. 137–145.
- [90] Patanka, S., *Numerical Heat Transfer and Fluid Flow*, Hemisphere Publishing Co., New York, 1st ed., 1980.

- 
- [91] Chen, P. Y. K. and Hahn, E. J., “Use of Computational Fluid Dynamics in Hydrodynamic Lubrication,” *Proceedings of the Institution of Mechanical Engineers, Part J: Journal of Engineering Tribology*, Vol. 212, 1998, pp. 427–436.
- [92] Brajdic-Mitidieri, P., *Advanced Modelling of Elastohydrodynamic Lubrication*, Ph.D. thesis, Imperial College London, London, UK, 2005.
- [93] Guo, Z., Hirano, T., and Kirk, R. G., “Application of CFD Analysis for Rotating Machinery—Part I: Hydrodynamic, Hydrostatic Bearings and Squeeze Film Damper,” *ASME Journal of Engineering for Gas Turbines and Power*, Vol. 127, No. 2, 2005, pp. 445–451.
- [94] Papadopoulos, C. I., Kaiktsis, L., and Fillon, M., “Computational Fluid Dynamics Thermo-hydrodynamic Analysis of Three-Dimensional Sector-Pad Thrust Bearings With Rectangular Dimples,” *ASME Journal of Tribology*, Vol. 136, 2013, pp. 011702.
- [95] Zhang, X., Yin, Z., Jiang, D., and Gao, G., “The Design of Hydrodynamic Water-lubricated Step Thrust Bearings Using CFD Method,” *Mechanics & Industry*, Vol. 15, 2014, pp. 197–206.
- [96] Iordanoff, I., “Analysis of an Aerodynamic Compliant Foil Thrust Bearing: Method for a Rapid Design,” *ASME Journal of Tribology*, Vol. 121, No. 4, October 1999, pp. 816–822.
- [97] Lez, S. L., Arghir, M., and Frene, J., “A New Bump-Type Foil Bearing Structure Analytical Model,” *ASME Journal of Engineering for Gas Turbines and Power*, Vol. 129, No. 4, 2007, pp. 747–757.
- [98] Hryniewicz, P., Wodtke, M., Olszewski, A., and Rzadkowski, R., “Structural Properties of Foil Bearings: A Closed-form Solution Validated with Finite Element Analysis,” *Tribology Transactions*, Vol. 52, No. 4, 2009, pp. 435–446.
- [99] Feng, K. and Kaneko, S., “Analytical Model of Bump-Type Foil Bearings Using a Link-Spring Structure and a Finite Element Shell Model,” *ASME Journal of Tribology*, Vol. 132, No. 2, April 2010, pp. 021706.
- [100] Gad, A. and Kaneko, S., “A New Structural Stiffness Model for Bump-Type Foil Bearings: Application to Generation II Gas Lubricated Foil Thrust Bearing,” *ASME Journal of Tribology*, Vol. 136, No. 4, May 2014, pp. 041701.

- [101] Rubio, D. and San Andres, L., “Structural Stiffness, Dry Friction Coefficient, and Equivalent Viscous Damping in a Bump-type Foil Gas Bearing,” *ASME Journal of engineering for gas turbines and power*, Vol. 129, No. 2, 2007, pp. 494–502.
- [102] Agrawal, G. L., “Foil Air/gas Bearing Technology—an Overview,” *International Gas Turbine and Aeroengine Congress and Exhibition*, American Society of Mechanical Engineers, Orlando, Florida, June 1997.
- [103] Ku, C.-P. R. and Heshmat, H., “Structural Stiffness and Coulomb Damping in Compliant Foil Journal Bearings: Theoretical Considerations,” *Tribology transactions*, Vol. 37, No. 3, 1994, pp. 525–533.
- [104] Le Lez, S., Arghir, M., and Frene, J., “Static and Dynamic Characterization of a Bump-type Foil Bearing Structure,” *ASME Journal of Tribology*, Vol. 129, No. 1, 2007, pp. 75–83.
- [105] Andres, L. S. and Kim, T., “Analysis of Gas Foil Bearings Integrating FE Top Foil Models,” *Tribology International*, Vol. 42, 2009, pp. 111–120.
- [106] Lee, D. and Kim, D., “Three-Dimensional Thermohydrodynamic Analyses of Rayleigh Step Air Foil Thrust Bearing with Radially Arranged Bump Foils,” *Tribology Transactions*, Vol. 54, No. 3, March 2011, pp. 432–448.
- [107] Heshmat, C., Xu, D., and Heshmat, H., “Analysis of Gas Lubricated Foil Thrust Bearings Using Coupled Finite Element and Finite Difference Methods,” *ASME Journal of Tribology*, Vol. 122, No. 1, June 1999, pp. 199–204.
- [108] Lehn, A., Mahner, M., and Schweizer, B., “Elasto-gasdynamic Modeling of Air Foil Thrust Bearings with a Two-dimensional Shell Model for Top and Bump Foil,” *Tribology International*, Vol. 100, 2016, pp. 48–59.
- [109] Sim, K. and Kim, T. H., “Thermohydrodynamic Analysis of Bump-type Gas Foil Bearings using Bump Thermal Contact and Inlet Flow Mixing Models,” *Tribology International*, Vol. 48, 2012, pp. 137–148.
- [110] Salehi, M., Swanson, E., and Heshmat, H., “Thermal Features of Compliant Foil Bearings—Theory and Experiments,” *ASME Journal of Tribology*, Vol. 123, No. 3, 2001, pp. 566–571.

- 
- [111] Kim, D., Ki, J., Kim, Y., and Ahn, K., “Extended Three-Dimensional Thermo-Hydrodynamic Model of Radial Foil Bearing: Case Studies on Thermal Behaviors and Dynamic Characteristics in Gas Turbine Simulator,” *ASME Journal of Engineering for Gas Turbines and Power*, Vol. 134, No. 5, May 2012, pp. 052501.
- [112] Shrestha, S. K., Kim, D., and Kim, Y. C., “Experimental Feasibility Study of Radial Injection Cooling of Three-Pad Air Foil Bearings,” *ASME Journal of Tribology*, Vol. 135, No. 4, 2013, pp. 041703.
- [113] Lee, D. and Kim, D., “Three-dimensional Thermohydrodynamic Analyses of Rayleigh Step Air Foil Thrust Bearing with Radially Arranged Bump Foils,” *Tribology Transactions*, Vol. 54, No. 3, 2011, pp. 432–448.
- [114] DellaCorte, C., Lukaszewicz, V., Valco, M., Radil, K., and Heshmat, H., “Performance and durability of high temperature foil air bearings for oil-free turbomachinery,” *Tribology transactions*, Vol. 43, No. 4, 2000, pp. 774–780.
- [115] San Andrés, L. and Kim, T. H., “Thermohydrodynamic Analysis of Bump-type Gas Foil Bearings: a Model Anchored to Test Data,” *ASME Journal of Engineering for Gas Turbines and Power*, Vol. 132, No. 4, 2010, pp. 042504.
- [116] Lee, D. and Kim, D., “Thermohydrodynamic Analyses of Bump Air Foil Bearings with Detailed Thermal Model of Foil Structures and Rotor,” *ASME Journal of Tribology*, Vol. 132, No. 2, 2010, pp. 021704.
- [117] Gollan, R. and Jacobs, P., “About The Formulation, Verification and Validation of The Hypersonic Flow Solver Eilmer,” *International Journal for Numerical Methods in Fluids*, Vol. 73, No. 1, September 2013, pp. 19–57.
- [118] Jacobs, P., Gollan, R., Jahn, I., and Potter, D., “The Eilmer3 code: user guide and example book 2015 edition,” Technical report 2015/07, The University of Queensland, Brisbane, Australia, August 2015.
- [119] Ventura, C., Sauret, E., Jacobs, P., Petrie-Repar, P., and der Laan, P. V., “Adaption and Use of a Compressible Flow Code for Turbomachinery Design,” *5th European Conference on Com-*

*putational Fluid Dynamics ECCOMAS CFD 2010*, European Community on Computational Methods in Applied Sciences, Lisbon, Portugal, 2010.

- [120] Lemmon, E., Huber, M., and McLinden, M., “NIST Standard Reference Database 23: Reference Fluid Thermodynamic and Transport Properties-REFPROP, Version 9.1,” May 2013.
- [121] Jacobs, P., Gollan, R., Denman, A., O’Flaherty, B., Potter, D., Petrie-Repar, P., and Johnston, I., “Eilmer’s Theory Book: Basic Models for Gas Dynamics and Thermochemistry,” Tech. Rep. 2010/09, The University of Queensland, 2012.
- [122] Larignon, B. D., Marr, K., and Goldstein, D. B., “Monte Carlo and Navier-Stokes Simulations of Compressible Taylor-Couette Flow,” *Journal of thermophysics and heat transfer*, Vol. 20, No. 3, 2006, pp. 544–551.
- [123] Schlichting, H., *Boundary-layer Theory*, McGraw-Hill, New York, seventh ed., 1979.
- [124] DiPrima, R., Eagles, P., and Ng, B., “The Effect of Radius Ratio on the Stability of Couette Flow and Taylor Vortex Flow,” *Physics of Fluids (1958-1988)*, Vol. 27, No. 10, 1984, pp. 2403–2411.
- [125] Jones, C., “The Transition to Wavy Taylor Vortices,” *Journal of Fluid Mechanics*, Vol. 157, 1985, pp. 135–162.
- [126] Wereley, S. and Lueptow, R., “Azimuthal Velocity in Supercritical Circular Couette Flow,” *Experiments in fluids*, Vol. 18, No. 1-2, 1994, pp. 1–9.
- [127] Garratt, J. E., Hibberd, S., Cliffe, K. A., and Power, H., “Centrifugal Inertia Effects in High-speed Hydrostatic Air Thrust Bearings,” *Journal of Engineering Mathematics*, Vol. 76, No. 1, October 2012, pp. 59–80.
- [128] Zhao, H., Choy, F., and Braun, M., “Modeling and Analysis of a Wavy Thrust Bearing,” *Tribology Transactions*, Vol. 45, No. 1, 2002, pp. 85–93.
- [129] Peng, Z.-C. and Khonsari, M., “Hydrodynamic Analysis of Compliant Foil Bearings with Compressible Air Flow,” *ASME Journal of Tribology*, Vol. 126, No. 3, 2004, pp. 542–546.

- 
- [130] Brunetiere, N., Tournerie, B., and Frene, J., “Influence of Fluid Flow Regime on Performances of Non-Contacting Liquid Face Seals,” *ASME Journal of Tribology*, Vol. 124, No. 3, May 2002, pp. 515–523.
- [131] Souchet, D., *Comportement Thermohydrodynamique des butées á Patins Oscillants en régime Laminaire et Turbulent*, PhD Thesis, University of Poitiers, Poitiers, France, 1991.
- [132] Wilcox, D., *Turbulence Modeling for CFD*, DCW Industries, CA, 2nd ed., 2006.
- [133] Chan, W., Jacobs, P., and Mee, D., “Suitability of the  $k - w$  turbulence model for scramjet flowfiled simulations,” *International Journal for Numerical Methods in Fluids*, Vol. 70, No. 4, October 2011, pp. 493–514.
- [134] EL Telbany, M. and Reynolds, A., “Velocity Distribution in Plane Turbulent Channel Flows,” *Journal of Fluid Mechanics*, Vol. 100, 1980, pp. 1–29.
- [135] EL Telbany, M. and Reynolds, A., “Turbulence in Plane Channel Flows,” *Journal of Fluid Mechanics*, Vol. 111, 1981, pp. 283–318.
- [136] White, F., *Viscous Fluid Flow*, McGraw-Hill, New York, 3rd ed., 2006.
- [137] Nichols, R. H. and Nelson, C., “Wall Function Boundary Conditions Including Heat Transfer and Compressibility,” *AIAA Journal*, Vol. 42, No. 6, 2004, pp. 1107–1114.
- [138] Davidson, L. and Farhanieh, B., “CALC-BFC: A Finite Volume Code Employing Collocated Variable Arrangement and Cartesian Velocity Components for Computation of Fluid Flow and Heat Transfer in Complex Three-dimensional Geometries,” Technical report 91/14, Chalmers University of Technology, Sweden, 1991.
- [139] Weller, H., Tabor, G., Jasak, H., and Fureby, C., “A Tensorial Approach to Computational Continuum Mechanics using Object-oriented Techniques,” *Computers in Physics*, Vol. 12, No. 6, November 1998, pp. 620–631.
- [140] Gao, Z., Jiang, C., and Lee, C., “Improvement and Application of Wall Function Boundary Condition for High-speed Compressible Flows,” *Science China Technological Sciences*, Vol. 56, No. 10, 2013, pp. 2501–2515.

- [141] Veiser, W., Esch, T., and Menter, F., “Heat Transfer Predictions Using Advanced Two-Equation Turbulence Models,” Technical report CFX-VAL10/0602, CFX Technical Memorandum, ON, Canada, November 2002.
- [142] Van Driest, E. R., “On Turbulent Flow Near a Wall,” *Journal of the Aeronautical Sciences*, Vol. 23, No. 11, 1956, pp. 1007–1011.
- [143] Dawes, W., “A Computer Program for the Analysis of Three Dimensional Viscous Compressible Flow in Turbomachinery Blade Rows,” Technical report, Whittle Laboratory, University of Cambridge, UK, 1988.
- [144] Macrossan, M. N., “FCT Filter: Using The Diffusion And Anti-Diffusion Equations As A Filter,” Technical report 12/00, The University of Queensland, December 2000.
- [145] Jameson, A., Schmidt, W., and Turkel, E., “Numerical Solutions of the Euler Equations by Finite Volume Methods using Runge-Kutta Time-stepping Schemes,” *14th Fluid and Plasma Dynamics Conference*, American Institute of Aeronautics and Astronautics, Palo Alto, CA, June 1981.
- [146] Zhang, S., Yu, A., and Zulli, P., “Preconditioned Multigrid Method for Fluid Flow in Porous Media,” *Second International Conference on CFD in the Minerals & Process Industries*, CSIRO, Melbourne, Australia, June 1999.
- [147] Goncalves, E. and Houdeville, R., “Reassessment of the Wall Functions Approach for RANS Computations,” *Aerospace Science and Technology*, Vol. 5, No. 1, 2001, pp. 1–14.
- [148] Wang, J., Gollan, R., and Veeraragavan, A., “Verification of RANS Turbulence Model in Eilmer using the Method of Manufactured Solutions,” *Proceedings of the 20th Australasian Fluid Mechanics Conference*, Australasian Fluid Mechanics Society, Perth, WA, Australia, December 2016, pp. 1–4.
- [149] Petrie-Repar, P., *Numerical Simulation of Diaphragm Rupture*, PhD Thesis, University of Queensland, Brisbane, QLD, December 1997.
- [150] Johnston, I., *Simulation of Flow Around Hypersonic Blunt-Nosed Vehicles for the Calibration of Air Data System*, PhD Thesis, University of Queensland, Brisbane, QLD, January 1999.

- 
- [151] Liou, M. and Steffen, C., “A New Flux Splitting Scheme,” *Journal of Computational Physics*, Vol. 107, No. 1, July 1993, pp. 23–39.
- [152] Wada, Y. and Liou, M., “An Accurate and Robust Flux Splitting Scheme for Shock and Contact Discontinuities,” *Journal of Scientific Computing*, Vol. 18, No. 3, May 1997, pp. 633–657.
- [153] Macrossan, M., “The Equilibrium Flux Method for The Calculation of Flows with Non-equilibrium Chemical Reactions,” *Journal of Computational Physics*, Vol. 80, No. 1, January 1989, pp. 204–231.
- [154] Ambrosi, D., “Full Potential and Euler Solutions for Transonic Unsteady Flow,” *Aeronautical Journal*, Vol. 98, No. 1, pp. 340–348.
- [155] Grandy, J., “Efficient Computation of Volume of Hexahedral Cells,” Technical report UCRL-ID-128886, Lawrence Livermore National Laboratory, October 1997.
- [156] Trepanier, J., Reggio, M., Paraschivoiu, M., and Camarero, R., “Unsteady Euler Solutions for Arbitrarily Moving Bodies and Boundaries,” *AIAA Journal*, Vol. 31, No. 10, October 1993, pp. 1869–1876.
- [157] Trepanier, J., Reggio, M., Zhang, H., and Camarero, R., “A Finite-Volume Method for The Euler Equation on Arbitrary Lagrangian-Eulerian Grids,” *Computers and Fluids*, Vol. 20, No. 4, 1991, pp. 399–409.
- [158] Sod, G. A., “A Survey of Several Finite Difference Methods for Systems of Nonlinear Hyperbolic Conservation Laws,” *Journal of Computational Physics*, Vol. 27, No. 1, 1978, pp. 1–31.
- [159] Gollan, R., Johnston, I., O’Flaherty, B., and Jacobs, P., “Development of Casbar: a Two-phase Flow Code for the Interior Ballistics Problem,” *Proceedings of the 16th Australasian Fluid Mechanics Conference*, edited by P. Jacobs, T. McIntyre, M. Cleary, D. Buttsworth, D. Mee, R. Clements, R. Morgan, and C. Lemckert, The University of Queensland, Gold Coast, Queensland, Australia, December 2007, pp. 295–302.
- [160] Jacobs, P., “L1d: A Computer Program for the Simulation of Transient-Flow Facilities,” Technical report 1/99, The University of Queensland, January 1999.

- [161] AGARD, “Compendium of Unsteady Aerodynamic Measurements,” Technical report AGARD-R-702, 1982.
- [162] Jahangirian, A. and Hadidoolabi, M., “Unstructured Moving Grids for Implicit Calculation of Unsteady Compressible Viscous Flows,” *International Journal for Numerical Methods in Fluids*, Vol. 47, No. 10, 2005, pp. 1107–1113.
- [163] Barakos, G. and Drikakis, D., “An Implicit Unfactored Method for Unsteady Turbulent Compressible Flows with Moving Boundaries,” *Computers & Fluids*, Vol. 28, No. 8, November 1999, pp. 899–922.
- [164] Timoshenko, S. and Woinowsky-Krieger, S., *Theory of Plates and Shells*, McGraw-Hill, New York, 5th ed., 1959.
- [165] Reddy, J., *Theory and Analysis of Elastic Plates and Shells*, Taylor and Francis, Philadelphia, PA, 1st ed., 2007.
- [166] ANSYS, Inc, *ANSYS Mechanical User’s Guide*, 15th ed., 2014.
- [167] Joshi, O. and Leyland, P., “Stability Analysis of a Partitioned Fluid–Structure Thermal Coupling Algorithm,” *AIAA Journal of Thermophysics and Heat Transfer*, Vol. 28, No. 1, January 2014, pp. 59–67.
- [168] Span, R. and Wagner, W., “A New Equation of State for Carbon Dioxide Covering the Fluid Region from the Triple Point Temperature to 1100 K at Pressures up to 800 MPa,” *Journal of Physical and Chemical Reference Data*, Vol. 25, No. 6, 1996, pp. 1509–1596.
- [169] Pinkus, O. and Lund, J., “Centrifugal Effects in Thrust Bearings and Seals under Laminar Conditions,” *ASME Journal of Lubrication Technology*, Vol. 103, No. 1, January 1981, pp. 126–136.
- [170] Bruckner, R. J., “Passive Thermal Management of Foil Bearings,” June 2015, US Patent 9,062,712.
- [171] Qin, K., Jahn, I., and Jacobs, P., “Effect of Operating Conditions on the Elastohydrodynamic Performance of Foil Thrust Bearings for Supercritical CO<sub>2</sub> Cycles,” *ASME Journal of Engineering for Gas Turbines and Power*, Vol. 139, No. 4, November 2017, pp. 042505.

- [172] Qin, K., Jahn, I., Gollan, R., and Jacobs, P., “Development of a Computational Tool to Simulate Foil Bearings for Supercritical CO<sub>2</sub> Cycles,” *ASME Journal of Engineering for Gas Turbines and Power*, Vol. 138, No. 9, March 2016, pp. 092503.
- [173] Rubio, D. and San Andrés, L., “Bump-type Foil Bearing Structural Stiffness: Experiments and Predictions,” *Journal of engineering for gas turbines and power*, Vol. 128, No. 3, 2006, pp. 653–660.
- [174] Childs, D. W., *Turbomachinery Rotordynamics: Phenomena, Modeling, and Analysis*, John Wiley & Sons, New Jersey, 1st ed., 1993.
- [175] Yan, X., He, K., Li, J., and Feng, Z., “A Generalized Prediction Method for Rotordynamic Coefficients of Annular Gas Seals,” *ASME Journal of Engineering for Gas Turbines and Power*, Vol. 137, No. 9, 2015, pp. 092506.
- [176] Küttler, U. and Wall, W. A., “Fixed-point Fluid-structure Interaction Solvers with Dynamic Relaxation,” *Computational Mechanics*, Vol. 43, No. 1, 2008, pp. 61–72.
- [177] Malatip, A., Wansophark, N., and Dechaumphai, P., “Combined Streamline Upwind Petro Galerkin Method and Segregated Finite Element Algorithm for Conjugate Heat Transfer Problems,” *Journal of Mechanical Science and Technology*, Vol. 20, No. 10, 2006, pp. 1741–1752.
- [178] Back, L., Massier, P., and Gier, H., “Convective Heat Transfer in a Convergent-Divergent Nozzle,” *International Journal of Heat and Mass Transfer*, Vol. 7, 1964, pp. 549–568.
- [179] DeLise, J. and Naraghi, M., “Comparative Studies of Convective Heat Transfer Models for Rocket Engines,” *31st AIAA/ASME/SAE/ASEE Joint Propulsion Conference and Exhibit*, American Institute of Aeronautics and Astronautics, San Deigo, CA, July 1995.
- [180] Marineau, E., Schetz, J., and Neel, R., “Turbulent Navier-Stokes Simulations of Heat Transfer with Complex Wall Temperature Variations,” *9th AIAA/ASME Joint Thermophysics and Heat Transfer Conference*, American Institute of Aeronautics and Astronautics, San Francisco, California, June 2006.

- [181] Liu, Q., Luke, E., and Cinnella, P., “Coupling Heat Transfer and Fluid Flow Solvers for Multidisciplinary Simulations,” *AIAA Journal of Thermophysics and Heat Transfer*, Vol. 19, No. 4, October-December 2005, pp. 417–427.
- [182] aus der Wiesche, S. and Helcig, C., *Convective Heat Transfer From Rotating Disks Subjected To Streams Of Air*, Springer, 1st ed., 2016.
- [183] Holman, J., *Heat Transfer*, McGraw Hill Higher Education, tenth ed., 2010.
- [184] Bruckner, R., “The Chevron Foil Thrust Bearing: Improved Performance Through Passive Thermal Management and Effective Lubricant Mixing,” *World Tribology Congress*, Torino, Italy, September 2013.
- [185] Jahn, I. and Qin, K., “e3prepToFoam: a Mesh Generator for OpenFOAM,” Technical report 2015/04, The University of Queensland, June 2015.
- [186] Ryu, K. and San Andrés, L., “On the Failure of a Gas Foil Bearing: High Temperature Operation without Cooling Flow,” *ASME Journal of Engineering for Gas Turbines and Power*, Vol. 135, No. 11, 2013, pp. 112506.
- [187] San Andrés, L., Ryu, K., and Diemer, P., “Prediction of Gas Thrust Foil Bearing Performance for Oil-Free Automotive Turbochargers,” *ASME Journal of Engineering for Gas Turbines and Power*, Vol. 137, No. 3, 2015, pp. 032502.

## Discretisation of Reynolds equation

---

The generalized Reynolds equation is given by [8],

$$\frac{\partial}{\partial r}(\rho h^3 \frac{p}{r}) + \frac{1}{r} \rho h^3 \frac{\partial p}{\partial r} + \frac{1}{r^2} \frac{\partial}{\partial \theta}(\rho h^3 \frac{p}{\theta}) = 6 \eta \omega \frac{\partial(\rho h)}{\partial \theta} \quad (\text{A.1})$$

where  $\eta = \frac{\mu_0}{p_0} (\frac{R_0}{h_2})^2$ . The above equation can be expanded to:

- $\frac{\partial}{\partial r}(\rho h^3 \frac{p}{r})$
- $\frac{1}{r} \rho h^3 \frac{\partial p}{\partial r}$
- $\frac{1}{r^2} \frac{\partial}{\partial \theta}(\rho h^3 \frac{p}{\theta})$
- $6 \eta \omega \frac{\partial(\rho h)}{\partial \theta}$

Each part can be discretized as follows,

$$\begin{aligned} \frac{\partial}{\partial r}(\rho h^3 \frac{p}{r}) &= \rho h^3 \frac{\partial^2 p}{\partial r^2} + \frac{p}{r} \frac{\partial(\rho h^3)}{\partial r} \\ &= \rho h^3 \frac{\partial^2 p}{\partial r^2} + \frac{p}{r} (h^3 \frac{\partial \rho}{\partial r} + 3 h^2 \rho \frac{h}{r}) \\ &= a_1 \frac{\partial^2 p}{\partial r^2} + a_2 \frac{\partial p}{\partial r} \end{aligned} \quad (\text{A.2})$$

$$\frac{1}{r} \rho h^3 \frac{\partial p}{\partial r} = a_3 \frac{\partial p}{\partial r} \quad (\text{A.3})$$

$$\begin{aligned}
\frac{1}{r^2} \frac{\partial}{\partial \theta} (\rho h^3 \frac{p}{\theta}) &= \frac{1}{r^2} (\rho h^3 \frac{\partial^2 p}{\partial \theta^2} + \frac{p}{\theta} \frac{\partial(\rho h^3)}{\partial \theta}) \\
&= \frac{1}{r^2} (\rho h^3 \frac{\partial^2 p}{\partial \theta^2} + \frac{\partial p}{\partial \theta} (h^3 \frac{\rho}{\partial \theta} + 3 h^2 \rho \frac{\partial h}{\partial \theta})) \\
&= a_4 \frac{\partial^2 p}{\partial \theta^2} + a_5 \frac{p}{\theta}
\end{aligned} \tag{A.4}$$

$$\begin{aligned}
6 \eta \omega \frac{\partial(\rho h)}{\partial \theta} &= 6 \eta \omega (h \frac{\partial \rho}{\partial \theta} + \rho \frac{\partial h}{\partial \theta}) \\
&= a_6
\end{aligned} \tag{A.5}$$

where ,

$$a_1 = \rho h^3 \tag{A.6}$$

$$a_2 = h^3 \frac{\partial \rho}{\partial r} + 3 h^2 \rho \frac{h}{r} \tag{A.7}$$

$$a_3 = \frac{1}{r} \rho h^3 \tag{A.8}$$

$$a_4 = \frac{1}{r^2} \rho h^3 \tag{A.9}$$

$$a_5 = \frac{1}{r^2} (h^3 \frac{\partial \rho}{\partial \theta} + 3 h^2 \rho \frac{\partial h}{\partial \theta}) \tag{A.10}$$

$$a_6 = 6 \eta \omega (h \frac{\partial \rho}{\partial \theta} + \rho \frac{\partial h}{\partial \theta}) \tag{A.11}$$

The generalized Reynolds equation is,

$$a_1 \frac{\partial^2 p}{\partial r^2} + (a_2 + a_3) \frac{\partial p}{\partial r} + a_4 \frac{\partial^2 p}{\partial \theta^2} + a_5 \frac{\partial p}{\partial \theta} = a_6 \tag{A.12}$$

Using the central differencing method, and the following discretise partial derivatives,

$$\frac{\partial^2 p}{\partial r^2} = \frac{p_{(i,j+1)} + p_{(i,j-1)} - 2 + p_{(i,j)}}{\Delta r^2}, \tag{A.13}$$

$$\frac{\partial p}{\partial r} = \frac{p_{(i,j+1)} - p_{(i,j-1)}}{2\Delta r}, \tag{A.14}$$

$$\frac{\partial^2 p}{\partial \theta^2} = \frac{p_{(i+1,j)} + p_{(i-1,j)} - 2 + p_{(i,j)}}{\theta r^2}, \tag{A.15}$$

$$\frac{\partial p}{\partial \theta} = \frac{p_{(i+1,j)} - p_{(i-1,j)}}{2\Delta \theta}. \tag{A.16}$$

the discretised Reynolds equation takes the form,

$$A_1 p_{(i,j)} = A_2 p_{(i,j)} + A_3 p_{(i,j-1)} + A_4 p_{(i+1,j)} + A_5 p_{(i-1,j)} + A_6 \quad (\text{A.17})$$

where,

$$A_1 = \frac{2 a_1}{\Delta r^2} + \frac{2 a_4}{\Delta \theta^2} , \quad (\text{A.18})$$

$$A_2 = \frac{a_1}{\Delta r^2} + \frac{a_2 + a_3}{2 \Delta r} , \quad (\text{A.19})$$

$$A_3 = \frac{a_1}{\Delta r^2} - \frac{a_2 + a_3}{2 \Delta r} , \quad (\text{A.20})$$

$$A_4 = \frac{a_4}{\Delta \theta^2} + \frac{a_5}{2 \Delta \theta} , \quad (\text{A.21})$$

$$A_5 = \frac{a_4}{\Delta \theta^2} - \frac{a_5}{2 \Delta \theta} , \quad (\text{A.22})$$

$$A_6 = -a_6 . \quad (\text{A.23})$$

This equation can be solved over a grid in the  $r$  and  $\theta$  space using the Gauss-Seidel iteration method.



---

## Description of Eilmer

---

The compressible Navier-Stokes equations implemented in Eilmer can be expressed as [117],

$$\frac{\partial}{\partial t} \int_V \mathbf{U} dV = - \oint_S (\mathbf{F}_i - \mathbf{F}_v) \cdot \hat{\mathbf{n}} dA + \int_V \mathbf{Q} dV . \quad (\text{B.1})$$

For the thermal equilibrium models with a single-species, the conserved quantities  $\mathbf{U}$  are defined as,

$$\mathbf{U} = \begin{bmatrix} \rho \\ \rho u_x \\ \rho u_y \\ \rho u_z \\ \rho E \end{bmatrix} . \quad (\text{B.2})$$

The convective flux  $\mathbf{F}_i$  consists of mass flux  $G$ , momentum flux  $\mathbf{L}$  and energy flux  $H$ ,

$$\mathbf{F}_i = \begin{bmatrix} G \\ \mathbf{L} \\ H \end{bmatrix} = \begin{bmatrix} \rho \mathbf{u} \cdot \hat{\mathbf{n}} \\ \rho \mathbf{u} \mathbf{u} \cdot \hat{\mathbf{n}} + p \hat{\mathbf{n}} \\ \rho E \mathbf{u} \cdot \hat{\mathbf{n}} + p \mathbf{u} \cdot \hat{\mathbf{n}} \end{bmatrix} . \quad (\text{B.3})$$

The components of the viscous flux  $\mathbf{F}_v$  are,

$$\mathbf{F}_v = \begin{bmatrix} 0 \\ \tau_{xx} \\ \tau_{yx} \\ \tau_{zx} \\ \tau_{xx}u_x + \tau_{yx}u_y + \tau_{zx}u_z + q_x \end{bmatrix} \hat{i} + \begin{bmatrix} 0 \\ \tau_{xy} \\ \tau_{yy} \\ \tau_{zy} \\ \tau_{xy}u_x + \tau_{yy}u_y + \tau_{zy}u_z + q_y \end{bmatrix} \hat{j} + \begin{bmatrix} 0 \\ \tau_{xz} \\ \tau_{yz} \\ \tau_{zz} \\ \tau_{xz}u_x + \tau_{yz}u_y + \tau_{zz}u_z + q_z \end{bmatrix} \hat{k} . \quad (\text{B.4})$$

In three dimensions, the finite-volume cells are hexahedral, with 6 (possibly-nonplanar) quadrilateral surfaces interfacing to neighbouring cells. Flux values are estimated at midpoints of the cell interfaces and the integral conservation Equation B.1 is approximated by the algebraic expression,

$$\frac{d\mathbf{U}}{dt} = -\frac{1}{V} \sum_{\text{cell-surface}} (\mathbf{F}_i - \mathbf{F}_v) \cdot \hat{\mathbf{n}} dA + \mathbf{Q} . \quad (\text{B.5})$$

where  $\mathbf{U}$  and  $\mathbf{Q}$  now represent cell-average values.

The convective flux vector is estimated using a reconstruction-evolution approach. The viscous flux calculation is based on an estimate of spatial derivatives of flow quantities at the midpoint of cell-interfaces,

$$\nabla\phi = \frac{1}{V} \oint_S \phi \hat{\mathbf{n}} dA . \quad (\text{B.6})$$

Here, the surface  $S$  defines a secondary cell surrounding a primary-cell vertex, as shown in Ref. [117].

The discretised equations are integrated in a time-accurate manner using one of several explicit

update schemes: Euler, predictor-corrector or a 3-stage Runge-Kutta update. Within each stage of the selected time-integration process, Eilmer uses an operator-splitting approach, with the contributions from the convective and viscous transport processes being computed sequentially.



---

## Source Code

---

### C.1 Moving Wall Boundary Condition

---

```
110     case EAST:
111     i = bd.imax;
112     for (k = bd.kmin; k <= bd.kmax; ++k) {
113         for (j = bd.jmin; j <= bd.jmax; ++j) {
114             cell = bd.get_cell(i, j, k);
115             IFace = cell->iface[EAST];
116             FlowState &fs = *(IFace->fs);
117             fs.copy_values_from(*(cell->fs));
118             fs.vel = cross(r_omega, IFace->pos - centre) + v_trans;
119                 if (Twall_flag)
120                     {
121                         for ( size_t imode=0; imode < nmodes; ++imode ) fs.gas->T[
122                             imode] = Twall;
123                     }
124             fs.tke = 0.0;
125             fs.omega = ideal_omega_at_wall(cell);
126             if (bd.bcp[EAST]->wc_bc != NON_CATALYTIC) {
127                 cw->apply(*(cell->fs->gas), fs.gas->massf);
128             }
129         } // end j loop
130     } // for k
131     break;
```

---

## C.2 Periodic Boundary Condition

```

129     case BOTTOM:
130     k = bd.kmin;
131         for (i = bd.imin; i <= bd.imax; ++i) {
132             for (j = bd.jmin; j <= bd.jmax; ++j) {
133                 reorient_vector_quantities_in_cell(bd.get_cell(i,j,k-1), Rmatrix); // ghost
                    cell 1.
134                 reorient_vector_quantities_in_cell(bd.get_cell(i,j,k-2), Rmatrix); // ghost
                    cell 2.
135             } // end j loop
136         } // for i
137     } // end switch...
138
139     return SUCCESS;
140 }
141
142 // Helper functions
143 void apply_matrix_transform(const std::vector<double>& Rmatrix,
144     const std::vector<double>& oldv,
145     std::vector<double> &newv)
146 {
147     // Write out the matrix multiplication, long-hand.
148     newv[0] = Rmatrix[0]*oldv[0] + Rmatrix[1]*oldv[1] + Rmatrix[2]*oldv[2];
149     newv[1] = Rmatrix[3]*oldv[0] + Rmatrix[4]*oldv[1] + Rmatrix[5]*oldv[2];
150     newv[2] = Rmatrix[6]*oldv[0] + Rmatrix[7]*oldv[1] + Rmatrix[8]*oldv[2];
151 }
152
153 void reorient_vector_quantities_in_cell(FV_Cell *c, const std::vector<double>&
    Rmatrix)
154 {
155     global_data &G = *get_global_data_ptr();
156     std::vector<double>oldv(3);
157     std::vector<double>newv(3);
158     oldv[0] = c->fs->vel.x; oldv[1] = c->fs->vel.y; oldv[2] = c->fs->vel.z;

```

```
159     apply_matrix_transform(Rmatrix, oldv, newv);
160     c->fs->vel.x = newv[0]; c->fs->vel.y = newv[1]; c->fs->vel.z = newv[2];
161     if ( G.MHD ) {
162     oldv[0] = c->fs->B.x; oldv[1] = c->fs->B.y; oldv[2] = c->fs->B.z;
163     apply_matrix_transform(Rmatrix, oldv, newv);
164     c->fs->B.x = newv[0]; c->fs->B.y = newv[1]; c->fs->B.z = newv[2];
165     }
166 }
```

---

### C.3 Reconstruction

---

```
260  if ( interpolate_in_local_frame ) {
261      // Paul Petrie-Repar and Jason Qin have noted that the velocity needs
262      // to be reconstructed in the interface-local frame of reference so that
263      // the normal velocities are not messed up for mirror-image at walls.
264      // PJ 21-feb-2014
265      cL1.fs->vel.transform_to_local(IFace.n, IFace.t1, IFace.t2);
266      cL0.fs->vel.transform_to_local(IFace.n, IFace.t1, IFace.t2);
267      cR0.fs->vel.transform_to_local(IFace.n, IFace.t1, IFace.t2);
268      cR1.fs->vel.transform_to_local(IFace.n, IFace.t1, IFace.t2);
269  }
```

---



---

## Description of Wilcox's 2006 $k$ - $\omega$ model

---

Mass Conservation:

$$\frac{\partial \bar{\rho}}{\partial t} + \frac{\partial}{\partial x_i} (\bar{\rho} \tilde{u}_i) = 0 \quad (\text{D.1})$$

Momentum Conservation:

$$\frac{\partial}{\partial t} (\bar{\rho} \tilde{u}_i) + \frac{\partial}{\partial x_j} (\bar{\rho} \tilde{u}_j \tilde{u}_i) = -\frac{\partial P}{\partial x_i} + \frac{\partial}{\partial x_j} [\bar{t}_{ji} + \bar{\rho} \tau_{ji}] \quad (\text{D.2})$$

Energy Conservation:

$$\begin{aligned} & \frac{\partial}{\partial t} \left[ \bar{\rho} \left( \tilde{e} + \frac{\tilde{u}_i \tilde{u}_i}{2} + k \right) \right] + \frac{\partial}{\partial x_j} \left[ \bar{\rho} \tilde{u}_j \left( \tilde{h} + \frac{\tilde{u}_i \tilde{u}_i}{2} + k \right) \right] = \\ & \frac{\partial}{\partial x_j} \left[ \left( \frac{\mu}{Pr_L} + \frac{\mu_T}{Pr_T} \right) \frac{\partial \tilde{h}}{\partial x_j} + \left( \mu + \sigma^* \frac{\bar{\rho} k}{\omega} \right) \frac{\partial k}{\partial x_j} \right] + \frac{\partial}{\partial x_j} [\tilde{u}_i (\bar{t}_{ij} + \bar{\rho} \tau_{ij})] \end{aligned} \quad (\text{D.3})$$

Molecular and Reynolds-Stress Tensors:

$$\bar{t}_{ij} = 2\mu \bar{S}_{ij} \quad \bar{\rho} \tau_{ij} = 2\mu_T \bar{S}_{ij} - \frac{2}{3} \bar{\rho} k \delta_{ij} \quad \bar{S}_{ij} = S_{ij} - \frac{1}{3} \frac{\partial \tilde{u}_k}{\partial x_k} \delta_{ij} \quad (\text{D.4})$$

Eddy Viscosity:

$$\mu_T = \frac{\bar{\rho} k}{\tilde{\omega}} \quad \tilde{\omega} = \max \left\{ \omega, C_{lim} \sqrt{\frac{2\bar{S}_{ij} \bar{S}_{ij}}{\beta^*}} \right\} \quad C_{lim} = \frac{7}{8} \quad (\text{D.5})$$

Turbulence Kinetic Energy ( $k$ ):

$$\frac{\partial}{\partial t} (\bar{\rho} k) + \frac{\partial}{\partial x_j} (\bar{\rho} \tilde{u}_j k) = \bar{\rho} \tau_{ij} \frac{\partial \tilde{u}_i}{\partial x_j} - \beta^* \bar{\rho} k \omega + \frac{\partial}{\partial x_j} \left[ \left( \mu + \sigma^* \frac{\bar{\rho} k}{\omega} \right) \frac{\partial k}{\partial x_j} \right] \quad (\text{D.6})$$

Specific Dissipation Rate ( $\omega$ ):

$$\frac{\partial}{\partial t}(\bar{\rho}\omega) + \frac{\partial}{\partial x_j}(\bar{\rho}\tilde{u}_j\omega) = \alpha \frac{\omega}{k} \bar{\rho}\tau_{ij} \frac{\partial \tilde{u}_i}{\partial x_j} - \beta \bar{\rho}\omega^2 + \sigma_d \frac{\bar{\rho}}{\omega} \frac{\partial k}{\partial x_j} \frac{\partial \omega}{\partial x_j} + \frac{\partial}{\partial x_j} \left[ \left( \mu + \sigma \frac{\bar{\rho}k}{\omega} \right) \frac{\partial \omega}{\partial x_j} \right] \quad (\text{D.7})$$

Closure Coefficients:

$$\alpha = \frac{13}{25} \quad \beta = \beta_o f_\beta \quad \beta^* = \frac{9}{100} \quad \sigma = \frac{1}{2} \quad \sigma^* = \frac{3}{5} \quad \sigma_{do} = \frac{1}{8} \quad (\text{D.8})$$

$$\beta_o = 0.0708 \quad Pr_T = \frac{8}{9} \quad \sigma_d = \begin{cases} 0, & \frac{\partial k}{\partial x_j} \frac{\partial \omega}{\partial x_j} \leq 0 \\ \sigma_{do}, & \frac{\partial k}{\partial x_j} \frac{\partial \omega}{\partial x_j} > 0 \end{cases} \quad (\text{D.9})$$

$$f_\beta = \frac{1 + 85\chi_\omega}{1 + 100\chi_\omega} \quad \chi_\omega = \left| \frac{\Omega_{ij}\Omega_{jk}\hat{S}_{ki}}{(\beta^*\omega)^3} \right| \quad \hat{S}_{ki} = S_{ki} - \frac{1}{2} \frac{\partial \tilde{u}_m}{\partial x_m} \delta_{ki} \quad (\text{D.10})$$